UNIVERSITÉ DE MONTRÉAL

FATIGUE CRACK PROPAGATION AND FRACTOGRAPHY OF 3Y-TZP AND ZTA

par

Changzun ZHOU

DÉPARTEMENT DE MÉTALLURGIE ET GÉNIE DES MATÉRIAUX

ÉCOLE POLYTECHNIQUE

THÈSE PRÉSENTÉE EN VUE DE L'OBTENTION

DU GRADE DE PHILOSOPHIAE DOCTOR (Ph.D.)

(GÉNIE MÉTALLURGIQUE)

Octobre 1992

© droits réservés de Changzun ZHOU 1992.

National Library of Canada
Acquisitions and Bibliographic Services Branch
395 Wellington Street
Ottawa, Ontario
K1A 0N4

Bibliothèque nationale du Canada
Direction des acquisitions et des services bibliographiques
395, rue Wellington
Ottawa (Ontario)
K1A 0N4

Your file Votre référence

Our file Notre référence

e author has granted an evocable non-exclusive licence owing the National Library of nada to reproduce, loan, tribute or sell copies of /her thesis by any means and any form or format, making thesis available to interested sons.

L'auteur a accordé une licence irrévocable et non exclusive permettant à la Bibliothèque nationale du Canada de reproduire, prêter, distribuer ou vendre des copies de sa thèse de quelque manière et sous quelque forme que ce soit pour mettre des exemplaires de cette thèse à la disposition des personnes intéressées.

author retains ownership of copyright in his/her thesis. her the thesis nor substantial acts from it may be printed or erwise reproduced without her permission.

L'auteur conserve la propriété du droit d'auteur qui protège sa thèse. Ni la thèse ni des extraits substantiels de celle-ci ne doivent être imprimés ou autrement reproduits sans son autorisation.

ISBN 0-315-86561-X

Canada

UNIVERSITÉ DE MONTRÉAL

ÉCOLE POLYTECHNIQUE

Cette thèse intitulée:

FATIGUE CRACK PROPAGATION AND FRACTOGRAPHY

OF 3Y-TZP AND ZTA

presentée par: ZHOU Changzun

en vue de l'obtention du grade de: Philosophiae Doctor (Ph.D.)

a été dûment acceptée par le jury d'examen constitué de:

M. BAILON Jean-Paul, D.Sc.A. (Président)

M. DICKSON J.Ivan, Ph.D. (Membre et directeur de recherche)

M. NICHOLSON Patrick S., Ph.D. (Membre)

M. RIGAUD Michel, D.Sc.A. (Membre)

SOMMAIRE

Généralement les matériaux céramiques ne subissent pas de déformation plastique. Pour cette raison, on a cru longtemps que les céramiques n'étaient pas sujettes à une fissuration en fatigue. La taille critique de défaut qu'une pièce céramique peut tolérer pour une contrainte donnée est très petite à cause de la grande fragilité de ce type de matériau. Pour cette raison, une fissuration sous-critique par fatigue peut être très dangereuse parce que seulement un petit montant de propagation peut produire une fissure de taille critique, et donc, la rupture finale de la pièce à la contrainte de service.

De nombreuses questions se posent légitimement avant d'aborder l'étude da la fatigue des céramiques, même avancées! Comment les fissures de fatigue peuvent-elles se propager, à de faibles amplitudes du facteur d'intensité de contrainte? Existe-t-il un seuil critique de propagation? La loi de Paris pour la propagation des fissures de fatigue, peut-elle encore être appliquée dans de tels matériaux? Que se passe-t-il lors du passage de propagation lente à propagation rapide et brutale? Quels seraient les modifications à apporter à la microtexture de ces matériaux pour améliorer de façon significative leur comportement en fatigue? Peut-on prévenir la propagation brutale des fissures avant la rupture définitive de ces matériaux?

Du vue de fournir les premiers éléments de réponse à certaines de ces

questions, nous avons choisi d'étudier expérimentalement le comportement de deux types de matériaux, le premier une zircone de structure quadratique stabilisée avec 3% molaire d'oxyde d'yttrium et le second une alumine renforcée de particules de zircone. Nous désirions faire ressortir l'influence des différents mécanismes de renforcement, bien connus de par ailleurs, sur le comportement en fatigue, et c'est ce que nous avons réussi à faire.

Nous avons mesuré le comportement de ces matériaux en fatigue d'abord sous un cyclage de charges entièrement en compression, puis sous un cyclage de charges en flexion. Nous avons également déterminé les modules de rupture en flexion quatre points et la ténacité de ces matériaux.

Il est bon de préciser ici que les céramiques de haute technologie avec des résistances à la rupture élevées, de l'ordre de 1 à 2 gigapascales, ont été développées en utilisant des poudres de tailles submicroniques et en exerçant un contrôle serré de qualité, au niveau des mélanges, du compactage et de la cuisson. En ce faisant il a été possible de réduire la taille des plus grands défauts présent à une dimension inférieure à 5 à 10 microns (souvent des pores restant après frittage ou des agglomérats de particules de poudre). D'autres techniques ont été employées pour améliorer la ténacité à la rupture. Dans le cas des zircones partiellement stabilisées, un oxyde convenable est ajouté à la zircone pour empêcher la transformation de la forme tétragonale à monoclinique lors du refroidissement tout

en permettant que cette transformation se déroule lors de l'application d'une contrainte suffisamment élevée. Cette transformation de nature martensitique s'accompagne d'une augmentation de volume de l'ordre de 3%. Lorsque ceci se produit près du fond d'une fissure, cette transformation, après une certaine propagation, peut engendrer une contrainte résiduelle de compression conduisant à la fermeture du fond de fissure, ce qui réduit la contrainte efficace locale et sert à améliorer la ténacité.

Cependant cet effet de transformation ainsi que la plupart des autres mécanismes qui servent à améliorer la ténacité des matériaux céramiques ne sont pas réversibles. Il s'établit une boucle d'hystérésis contrainte-déformation en fond de fissure qui n'est pas complètement fermée, c'est à dire, qui ne correspond pas à un comportement élastique linéaire réversible. Donc à chaque cycle, un peu d'énergie est emmagasinée et le cumul de cet effet produit éventuellement une fissuration en fatigue.

Très peu a été publié sur l'aspect des surfaces de rupture produites par la fissuration en fatigue dans les céramiques. Nos travaux ont donné des résultats particulièrement intéressants sur l'aspect des surfaces de fatigue pour les polycrystaux de zircone stabilisés avec l'oxyde d'yttrium.

Dans le cas d'éprouvettes préentaillées, soumises à des contraintes cycliques

en compression, une fissuration en fatigue peut se produire lors d'un cyclage entre deux contraintes de compression. A cause de la présence de l'entaille et à cause des différents des modules d'élasticité entre grains voisins, ce cyclage produit des contraintes de tension en fond d'entaille, à certains endroits surtout près de certains joints de grains. Ceci permet l'initiation de microfissures dans la voisinage du fond d'entaille. La propagation de ces microfissures en compression cyclique détachent des particules du fond de la fissure, et la fissure qui se propage a donc réellement une forme d'une entaille aiguë. Les surfaces de rupture montrent surtout l'effet de "fermeture" en fond de fissure associé à ce type de cyclage en compression et au compactage des particules détachées. Cette fermeture qui croit en ampleur lorsque la fissure se propage donne une vitesse de propagation décroissante et finalement un arrêt de la fissure, du fait qu'en s'éloignant de l'entaille, la contrainte locale devient de plus en plus une contrainte de compression. Ceci retarde la rupture brutale et facilite le contrôle de l'essai.

La surface de fatigue en compression-compression pour le zircone stabilisée avec l'yttrie comporte quatre zones: une première zone de particules détachées qui ont été déplacées vers l'entaille, une deuxième zone de particules aplaties par la fermeture, une troisième zone de fermeture très importante où de grandes régions présentent un aspect indiquant que des particules ont été écrasées, aplaties et agglomérées ensemble par l'effet de la fermeture et une quatrième zone libre de signes de fermeture. Cette quatrième zone comprend probablement la zone

endommagée par la fatigue en compression-compression (champ lointain) qui est présenté lors de l'arrêt de la propagation. Cette zone est probablement en partie rupturée en traction qui suit la fatigue en compression. De plus, cette dernière zone a un aspect qui ressemble beaucoup celle des "stries" produites lors d'une propagation en fatigue tension-tension. Comme nous le soulignerons ultérieurement, cette quatrième zone a aussi une largeur semblable à celle prévue pour la zone transformée en fond de fissure. Cependant cette zone est aussi présente sur les éprouvettes d'alumine renforcée par des particules de zircone et est au moins en partie produite par la combinaison de la forme de fissure ressemblant une entaille et à la fermeture associée aux particules détachées. Pour ce type de cyclage, la fissure est plus longue sur les bords latéraux, du fait que les particules délogées de la surface de rupture peuvent sortir plus facilement sur les bords latéraux qu'à l'intérieur, réduisant les effets de fermeture à ces endroits. Ces effets de fermeture servent à ralentir la fissuration. Les observations montrent que lorsque la fissure se propage en profondeur, les effets de fermeture deviennent de plus en plus importants. Notons également que la fissuration en fatigue ainsi que la rupture finale sont intergranulaires, que la taille des grains est très fine ($\approx 0.25\ \mu m$) et qu'il est difficile de trouver des défauts dans le matériau.

Dans le cas d'un cyclage tension-tension sur une éprouvette préentaillée, nous avons obtenu un comportement typique d'une courbe de Woehler, et nous avons trouvé des petites zones de fissuration en fatigue produites avant la rupture finale

de l'éprouvette. Ces zones de fissuration en fatigue sont reconnaissables du fait que leur aspect est légèrement plus plat que la partie de la surface de rupture produite par rupture rapide.

Les résultats les plus intéressants ont été obtenus sur des éprouvettes préentaillées et finalement préfissurées en fatigue de type compression-compression et ensuite fissurées en fatigue sous un cyclage très bien contrôlé de type tension-tension. Sous ces conditions, la vitesse de fissuration devient suffisamment rapide pour que des bandes ou des stries indiquant des positions intermédiaires du front de fissure soient produites cycle par cycle sur les surfaces de rupture. Que cette propagation se produise de façon continue a été vérifiée en plaçant des microjauges de déformation en avant du fond de fissure sur les bords latéraux et en enregistrant les boucles contrainte appliquée-déformation mesurées lors des cycles de fatigue. Sur les deux surfaces opposées, ces lignes correspondent à deux dépressions de type image miroir. Ceci indique que ces stries sont le résultat de la transformation des grains de zircone en fond de fissure et qu'elles correspondent à des zones où le montant de transformation était relativement faible, très probablement à cause de la diminution de contrainte lors du cyclage qui a permis l'arrêt de la propagation près de la fin du cycle précédent. Nous avons noté sur les deux bords des stries, des lignes de rivières mais non en continuité l'une de l'autre de chaque côté des stries. Ceci indique un arrêt de la fissuration rapide près de chaque côté.

La présence de ces lignes d'arrêt permet de calculer la vitesse de fissuration en fonction du facteur d'intensité de contrainte cyclique, $\Delta K = K_{max} - K_{min}$, ou en fonction de K_{max}. Nous avons trouvé que c'est la valeur de K_{max} et non pas la valeur de ΔK, qui détermine la vitesse de propagation en fatigue.

A partir d'une microjauge placée sur le bords de la fissure un peu en avant du fond de fissure, nous avons pu montrer en synchronisant les courbes charge et déformation mesurées par la microjauge, lors de chaque cycle de propagation et à vitesse suffisamment élevée pour former des stries, que la fissure se propage premièrement lentement jusqu'à la charge maximale et que cette propagation est arrêtée au moment où débute le déchargement. Cependant un petit montant de diminution de charge provoque une propagation rapide, la fissure s'arrêtant toutefois après une diminution suffisante de la charge. La propagation lente correspond à la formation des stries. Une dépression se forme sur chaque surface de rupture, du fait que les montants de transformation et d'augmentation de volume sont inférieurs à ceux apparaissant lors de la propagation rapide. La propagation est initialement lente au début du cycle du fait que la transformation importante lors de la propagation dans le cycle précédent cause un effet de fermeture particulièrement important réduisant la valeur effective de ΔK. Cette transformation provoque donc une compression résiduelle en arrière du fond de fissure et probablement une tension résiduelle en avant du fond de fissures. Il est plus difficile à expliquer pourquoi qu'une petite diminution de la charge cause une fissuration

rapide, mais il semble probable que ceci est à cause que la contrainte de tension résiduelle en avant du fond de fissure augmente, ou que la contrainte résiduelle de compression en arrière du fond de fissure diminue, ce qui augmente la contrainte de tension effective en avant du fond de fissure. La cause de ces changements de contraintes résiduelles est probablement un renversement d'une partie de la transformation en déchargeant.

Un ralentissement de la propagation en fatigue a été observé à cause du maintien d'une charge constante. La cause de ce ralentissement est associé au moins en partie à un changement de l'orientation du plan macroscopique de propagation, suite au maintien de la charge constante. Aussi, une vitesse de propagation plus élevée que prévue fut obtenue suite à une diminution de ΔK. Cette accélération s'explique par le plus faible montant de transformation pendant le cyclage à faible ΔK, ce qui se traduit par une fermeture en fond de la fissure moins importante. Le comportement obtenu lors de variation de ΔK est donc compliqué, comme nos résultats l'indiquent, et ceci méritrait d'être étudié en détails.

La transformation produite lors de la fissuration a été étudiée par spectroscopie microscopique Raman et par diffraction de rayons-X. La spectroscopie microscopique Raman a donné des informations très utiles sur la transformation locale. Plus particulièrement, elle a montré que le montant de transformation était moins important dans les bandes foncées de fissuration lente

que dans les régions voisines de propagation rapide. De plus, le montant de transformation détectée augmentait avec l'augmentation de K_{max}.

Cette thèse a donc permis de confirmer qu'il était possible de faire propager des fissures de façon stable en fatigue, dans les céramiques fines, à base de zircone et d'alumine renforcée, tant en compression-compression qu'en tension-tension. L'aspect vraiment original de ce travail aura été de révéler les mécanismes agissant cycle par cycle, et d'expliquer de façon nette la formation de stries de fatigue dans la zircone stabilisée. Pour reproduire ce genre de travail il convient de préposer adéquatement les matériaux à tester, d'effectuer les pré-entailles avec soin et de mettre en charge les éprouvettes avec précaution. Les aspects les plus inattendus de ce travail auront été de révéler que: i) les fissures se propagent en deux temps à des vitesses très différentes, d'abord lentement jusqu'à la charge maximale, puis rapidement au tout début du déchargement avant de s'arrêter puis de reprendre le même rythme en deux temps au cycle suivant; ii) le comportement des matériaux testés, et principalement celui de la zircone stabilisée à l'oxyde d'yttrium, est affecté par une interruption de mise en charge.

Tous ces travaux ont été menés à température ambiante. En vue de continuer ce genre d'étude il conviendrait d'effectuer des mesures similaires à températures contrôlées, les plus élevées possibles.

ABSTRACT

Cyclic tensile fatigue as well as compression fatigue were investigated in 3 mol% yttria-stabilized tetragonal zirconia polycrystals (3Y-TZP) which is subjected to stress-induced transformation and zirconia-toughened alumina (ZTA).

Clear striation-like dark bands separated by larger bright zones were observed in tensile fatigue crack propagation of 3Y-TZP precracked specimens. These dark bands corresponded to matching depressions on the two opposite fracture surfaces and to regions of smaller amounts of transformation as confirmed by Raman spectroscopy. River or ridge lines often terminated on or near the first side (that closer to the precrack) of a dark band and restarted on the other side indicating a crack arrest site near each site of these bands.

Hysteresis loops from a strain gage, placed at the fatigue crack tip of 3Y-TZP, demonstrated that fatigue crack propagation in a single cycle occurred in three stages: slow propagation, very rapid propagation and another slow propagation. Occurrence of the rapid propagation was always associated with presence of visible striations on fatigue fracture surface. Moreover, it was shown that this rapid propagation was triggered by small amount of unloading in a load cycle, which indicates that unloading changes the residual stress distribution.

Analysis of information provided by the hysteresis loop and by the striation features for the same cycle permitted to explain fatigue crack propagation sequence in a load cycle.

Local exponent m of Paris' law on fatigue propagation curve exhibited an unusual change in 3Y-TZP, in that it gradually decreased with increasing stress intensity factor. This increased fatigue resistance is believed to result from that the transformation toughening effect became gradually stronger as cyclic stress intensity increased at the fatigue crack tip, when the fatigue crack propagation contained a slow propagation portion (the dark band) and a rapid propagation portion (the bright zone).

Fatigue crack propagation retardation was observed after a sustained load cycling, and fatigue crack propagation acceleration was observed during minor cycling which followed normal cycling in 3Y-TZP. Explanations are suggested for both effects. Fatigue crack propagation direction was found to oscillate about (i.e., fatigue crack deviation) the plane perpendicular to the loading axis during interruptions of load cycling.

Four different zones were observed on compression fatigue fracture surface of 3Y-TZP. The formations of these four zones were explained by considering migration of debris particles and crack closure effects.

Stress-induced transformation was characterized by Raman microscopy and X-ray diffraction. The amount of transformed particles was found to depend on the simultaneous stress intensity factor. Fracture toughness of 3Y-TZP was measured employing different techniques.

ACKNOWLEDGEMENTS

I sincerely thank professors J.Ivan Dickson and Michel Rigaud for their invaluable help during the course of this work through detailed discussions and for their suggestions in the correction of my manuscript. The financial support they provided was well appreciated.

I gratefully acknowledge useful discussions with Mrs Li Shiqiong and Mr Xia Jin, Li Xiangming, Gerardo Espinosa, Miao Huijun, Tong Zhaoxiong, Wang Ganlin and Wang Weixing. I also greatly appreciate assistance of Mr Louis Handfield, Yves Blanchette and Heberto Balmori. I also acknowledge useful discussions with Eric L'Esperance of Ecole des Mine de St-Etienne during his study at Ecole Polytechnique. The discussions with Ms Isabelle Bacon were also greatly appreciated.

I also thank Ms Céline Labelle, Carole Massicotte, Diane Tremblay, Julie Chamberlain, Lemire-Mercier Celine and Lyne Denommee and Mr Jacques Desrochers, Andre Desilets and Jean Claudinon for their technical and secretarial help during the course of this work and during preparation of this thesis.

Lastly, but not least, I acknowledge a great debt I owe to my wife and my daughter for giving up many weekends and evenings for my thesis.

CONTENTS

(*)SOMMAIRE iv

(*)ABSTRACT xiii

(*)ACKNOWLEDGEMENTS xvi

(*)TABLE OF CONTENTS xvii

(*)LIST OF FIGURES xxi

(*)LIST OF TABLES xxix

(*)LIST OF APPENDICES xxx

INTRODUCTION 1

PART I LITERATURE REVIEW

CHAPTER 1 STATIC FATIGUE IN BRITTLE MATERIALS 10

1.1 Static fatigue of materials 10
1.2 Fracture of ceramics 18
1.2.1 Macroscopic fracture aspects in ceramics 18
1.2.2 Microscopic fracture aspects in ceramics 21
1.2.3 Terrace-like fractographic aspect in alumina 24

CHAPTER 2 CYCLIC FATIGUE OF CERAMICS 26

2.1 Cyclic fatigue compared to cyclic manifestation of stress corrosion cracking 26
2.2 Investigations of fatigue life endurance 29
2.3 Fatigue crack propagation under tensile stress 31
2.3.1 Influence of the cycling frequency 36
2.3.2 Effects of the waveform on the fatigue life 37
2.3.3 Effect of stress intensity range 38
2.3.4 Effect of reversible cyclic load 38
2.3.5 Grain size effect on fatigue in ceramics 39
2.3.6 Discontinuous propagation during stress cycling 39
2.3.7 Fatigue striation 40

2.3.8 Crack closure and retardation 42
2.3.9 Fatigue deformation 44
2.3.10 Fatigue in non-transforming ceramics 45
2.3.11 Transformation associated with cyclic crack growth 45
2.5 Fatigue study using repeat indentation technique 46
2.6 Compression fatigue in ceramics 47

CHAPTER 3 ZIRCONIA 51

3.1 Phase relationship in pure zirconia 51
3.2 Stabilization of zirconia 56
3.3 Phase relationship in zirconia-yttria system 59
3.4 Stress induced martensitic transformation 61
3.5 Non-transformable tetragonal phase 63
3.6 Transformation toughening in ceramics 63
3.6.1 Crack closure model for transformation toughened ceramics 65
3.6.2 Energy dissipation model for the transforming ceramics . . 67
3.7 Determination of the transformation zone size 68

PART II EXPERIMENTAL RESULTS AND DISCUSSIONS

CHAPTER 4 MATERIALS AND SPECIMEN PREPARATION 75

4.1 Materials and specimen preparation of 3Y-TZP 75
4.2 Processing of zirconia-toughened alumina 76

CHAPTER 5 COMPRESSION FATIGUE OF YTTRIA-STABILIZED TETRAGONAL ZIRCONIA POLYCRYSTALS AND ZIRCONIA-TOUGHENED ALUMINA 80

5.1 Experimental procedures 80
5.2 Compression fatigue of 3Y-TZP 82
5.2.1 Crack propagation under far-field compressive cycling . . . 82
5.2.2 Fracture surface observations 85
5.2.3 The formation of the four zones on the compression fatigue fracture surface 93
5.3 Compression fatigue of zirconia-toughened alumina 97
5.3.1 Compressive fatigue crack propagation in ZTA 97
5.3.2 Observations on the lateral surface during compression fatigue 99
5.3.3 Fatigue fracture surface observations of ZTA 101
5.4 Compression fatigue in other ceramics 105

CHAPTER 6 FRACTURE TOUGHNESS MEASUREMENTS 111

6.1 Fracture toughness measurements employing four point bending . 111
6.2 Fracture toughness measured by indentation test 112
6.3 Differences in fracture toughness measurements 118

CHAPTER 7 FOUR POINT BENDING FATIGUE 122

7.1 Fatigue crack propagation under tensile stress in 3Y-TZP 122
7.1.1 Four point bending fatigue of notched specimens 122
7.1.2 Fatigue fractography of specimens fatigued precracked under far-field compression and then cycled under tension 127
7.1.3 Fatigue crack propagation behaviour of precracked 3Y-TZP specimens 134
7.1.4 Utilization of a microstrain gage for detection of fatigue crack propagation 137
7.1.5 Hysteresis loops from the crack-tip microstrain gage 138
7.1.6 The relationship between the fatigue crack increment and the displacement change on the hysteresis loop 142
7.1.7 Retardation effects of sustained load on fatigue cracking 145
7.1.8 Relationship between the slope of the hysteresis loop and the fatigue crack length 149
7.1.9 Fractographic aspects of 3Y-TZP produced at serial interruption of stress cycling 158
7.1.10 Crack velocity of 3Y-TZP in subcritical cracking 163
7.1.11 Crack deviation 170
7.1.12 Topography of the dark bands 176
7.1.13 The regression analysis of fatigue curves 177
7.2 Fatigue cracking in zirconia-toughened alumina 181
7.2.1 Crack propagation in ZTA under tensile stresses 181
7.2.2 Fracture surface observations of ZTA for tensile fatigue . 186

CHAPTER 8 CHARACTERIZATIONS OF STRESS-INDUCED TRANSFORMATION 190

8.1 X-ray diffraction measurement on stress-induced transformation in 3Y-TZP 190
8.1.1 X-ray diffraction on the lateral surface of compressed specimens 191
8.1.2 X-ray diffraction on the compressive and tensile surfaces in bending 194
8.1.3 X-ray measurement on fracture surface 195
8.2 Characterization of stress-induced transformation

by Raman microscopy 202

PART III DISCUSSION AND CONCLUSIONS

CHAPTER 9 DISCUSSION 212

9.1 Compression fatigue crack propagation and the related engineering significance 212
9.2 Occurrence of intergranular fracture 214
9.3 Crack-tip shielding and crack propagation curve 216
9.4 Sequence of fatigue crack propagation 229
9.5 Criteria for the visibility of striation-markings 234
9.6 Size of the transformation zone and study of the fatigue crack propagation sequence 238
9.7 Some suggestions on further fatigue study in ceramics 239

CHAPTER 10 CONCLUSIONS 242

REFERENCES 248

APPENDIX 1 260

APPENDIX 2 262

THE LIST OF FIGURES

Fig. 1.1 Typical curves of stress corrosion cracking [8] 11

Fig. 1.2 Sensitivity of slow crack growth behaviour in partially stabilized zirconia [3] 12

Fig. 1.3 Dependence of crack velocity on applied force. The percentage represents the relative humidity and Roman numerals identify the different regions of crack propagation [5] 15

Fig. 1.4 The order of severity for different fracture origin in ceramics, in which fibre inclusion was the most severe, then agglomerates, iron inclusions, pores and alumina inclusions [16] 23

Fig. 2.1 Fatigue crack propagation rate, da/dN, as a function of stress intensity range, ΔK, for Mg-PSZ [45] 35

Fig. 2.2 Illustrations of (A) wedging asperity and (B) sliding asperity [30] 35

Fig. 2.3 Fatigue crack propagation rate, da/dN, as a function of stress intensity range, ΔK, in 3Y-TZP [53] 41

Fig. 3.1 Zirconia-rich end of the yttria-zirconia phase equilibrium diagram [76] 52

Fig. 3.2 The amount of transformed particles and the corresponding temperature for monoclinc-tetragonal transformation in zirconia [64] 54

Fig. 3.3 Illustration of the stresses that arise in a dilatant transformation zone. Once the zone extends behind the crack tip, stresses in this zone will act in a direction to close the crack [130] 66

Fig. 5.1 Specimen geometry of 3Y-TZP and ZTA for compression fatigue. Exact dimensions are given in the related sections 81

Fig. 5.2 Crack profile observed on the lateral surface with the notch tip at the right. Spalls are observed on the lateral surface 84

Fig. 5.3 Fatigue crack length, a, measured from the notch-tip as a function of the compression cycle number, N, in 3Y-TZP 84

Fig. 5.4 Shape of the fatigue crack seen on the fracture surface with the notch surface and the final fracture surface on the left and right, respectively. Spalls on the compression fatigue surface are indicated by arrows 87

Fig. 5.5 General morphology of fracture surface presenting four different zones indicated by I to IV (propagation towards the top) 87

Fig. 5.6 Fatigue crack initiation has occurred in zone I, which is relatively free of debris. Zone II corresponds to a region of lightly-packed debris which has accumulated 88

Fig. 5.7 Grain agglomerates, A, have been extruded out of zone I into the notch tip 88

Fig. 5.8 Grains seen at the beginning of zone II with edges rounded by deformation and fretting 90

Fig. 5.9 Curved line-markings seen on a cake of debris near the start of zone III. The shape of some of the grains within this cake can still be observed 90

Fig. 5.10 In zone III, the debris has been tightly compressed into "cakes" which present lines marking produced by rubbing 91

Fig. 5.11 Two sets of line markings seen on a flattened cake in zone III (propagation towards the top) 91

Fig. 5.12 Zone IV, indicated by arrows, is immediately adjacent to the crack tip and relatively free of debris. The width of this zone is only 5 to 10 μm (propagation towards the left) 92

Fig. 5.13 Homogeneous grain size and intergranular fracture with presence of some aggregates on the region of final fracture surface produced during the K_{Ic} test 92

Fig. 5.14 Occasional apparently transgranular fracture (arrows) in the region of the final fracture surface 94

Fig. 5.15 Fatigue crack length, a, measured from the notch-tip as a function of the number of compression cycles, N, in ZTA. AN, AZ and AM refer to the different compositions of ZTA specimen employed 98

Fig. 5.16 Fatigue crack profile of specimen AMC1 (the ZTA-AM material) shows packing of extruded debris at the notch-tip 100

Fig. 5.17 Fatigue crack profile of the ZTA-AZ material shows extruded debris on the lateral surface 100

Fig. 5.18 The crack seen on the lateral surface of the ZTA-AN material at the end of the compression fatigue test 102

Fig. 5.19 Fracture surface produced by compressive fatigue in the ZTA-AZ material (crack growing towards the top). Three zones are associated with the compression fatigue. The middle zone which contains the agglomeration of debris particles is higher than the first and third zone and in some regions can be separated into two sub-zones 102

Fig. 5.20 The boundary between the compression and tension fatigue fracture surfaces (the ZTA-AM material, crack propagation towards the right) 104

Fig. 5.21 A portion of the boundary between the fracture surfaces produced by compressive and tensile fatigue (the ZTA-AM material, crack propagation towards the top) shows that the tensile fatigue crack initiated on a plane at different height from that of the compression fatigue crack. The compressive fatigue surface presents debris particles which are finer than the typical grain size 104

Fig. 5.22 Compression fatigue fracture surface produced in Al_2O_3 (notch is on top) 107

Fig. 5.23 Final fracture surface in Al_2O_3 showing the occurrence of terrace-like transgranular fracture in large grain 107

Fig. 5.24 The terrace-like transgranular facets observed in Al_2O_3 at large magnification 108

Fig. 5.25 Change of the profile of notch tip produced by compression fatigue ring. (a) before compression fatigue, (b) after compression fatigue,

the porous Mg-PSZ material shows no major fatigue crack at the notch tip but instead presents loosened particles 109

Fig. 6.1 Schematic illustration of an indentation impression and crack system produced by a Vickers indentation. (a) top view, (b) front view of section 114

Fig. 6.2 Typical indentations showing very well-behaved radial cracks obtained in 3Y-TZP at a load of 150 N 115

Fig. 6.3 Radial crack length, length of the indentation diagonals and measured fracture toughness obtained as a function of the applied load for 3Y-TZP, employing immersion oil on the test surface 117

Fig. 7.1 Specimen fixture for four-point bending fatigue test 124

Fig. 7.2 Relation between the maximum nominal stress intensity factor, K_{max}', and the number of cycles to failure, Nf, for notch specimens of 3Y-TZP fatigue under four point bending 126

Fig. 7.3 Relatively large fatigue cracking region (arrow) obtained for the notched specimen of 3Y-TZP material tested at low K_{max}' in tensile fatigue 128

Fig. 7.4 Relatively small fatigue cracking region (arrow) for the notched specimen of 3Y-TZP material tested at high K_{max}' in tensile fatigue 128

Fig. 7.5 The general aspects of the entire fracture surface for fatigued precrack specimens of 3Y-TZP under tensile cyclic stress. The regions a_{cf}, a_{b1}, a_{b2} and a_{ff} refer to compression-fatigue precrack, tensile fatigue crack without discernible striations, fatigue crack propagation with discernible striation, and the final fracture surface, respectively 132

Fig. 7.6 Typical aspect of the striation bands observed on the tensile fatigue fracture surface of 3Y-TZP 132

Fig. 7.7 Corresponding depressions observed at the striation sites on opposite fracture surfaces 133

Fig. 7.8 Fine ridge lines are observed to terminate often on one side of the striation, while new ridge lines tend to initiate on

the other side 133

Fig. 7.9 (a) crack growth rate da/dN versus ΔK for two R-ratios, as determined from the positions and spacings of the striation markings 135

Fig. 7.9 (b) crack growth rate da/dN versus K_{max} for two R-ratios, as determined from the positions and spacings of the striation markings. The fatigue growth behaviour under tensile stress is clearly controlled principally by K_{max} 136

Fig. 7.10 Hysteresis loops measured at the tensile fatigue crack tip with the microstrain gage on 3Y-TZP (specimen YSG1, the numbers on top indicate the cycle number). The measured strain increases gradually and stably with increasing cycle number 139

Fig. 7.11 Hysteresis loops measured at the tensile fatigue crack tip with the microstrain gage on 3Y-TZP (specimen YSG2, the numbers on top indicate the cycle number). The measured strain increases with increasing cycle number. Crack closure is observed near the minimum load value 140

Fig. 7.12 Correlation between the load cycle and the strain behaviour at the crack tip in tensile fatigue of 3Y-TZP 143

Fig. 7.13 A large number of striations observed on the fatigue fracture surface produced under cyclic tensile stress (Specimen YSG2) 147

Fig. 7.14 Two zones of striations produced before (bottom portion) and after (top portion) the cycling interruption which led to crack deviation and fatigue crack retardation on specimen YSG1 147

Fig. 7.15 Striations present in the region of crack deviation (specimen YSG1) 148

Fig. 7.16 Deeper and broader striation (arrow) produced by interruption of cycling on specimen YSG1 148

Fig. 7.17 Fatigue crack length determined from the striation position as a function of the cycle number (specimen YSG1) 150

Fig. 7.18 Fatigue crack length determined from the striation position as a function of the cycle number (specimen YSG2) 151

Fig. 7.19 Fatigue crack propagation rate da/dN versus the stress intensity range ΔK and versus the maximum stress intensity factor K_{max}, showing the crack retardation which resulted from the cycling suspension (specimen YSG1) 152

Fig. 7.20 Correlations between the maximum strain measured with the microstrain gage and fatigue crack length measured on the fracture surface corresponding to the same cycle number (specimens YSG1 and YSG2) 154

Fig. 7.21 Schematic illustration on the response of microstrain gage to fatigue crack propagation. Fatigue crack, when it propagates into the area covered by the microstrain gage, will bring an additional area to the coverage of the microstrain gage 156

Fig. 7.22 The microstrain gage response to a linearly slow unloading deviates from the preceding loop, which indicates some slow crack propagation during the slow unloading 160

Fig. 7.23 Fatigue fracture surface produced during cycling at initial constant load range (region A), during slowly decreasing load (region B), during cycling at four different smaller load ranges (regions C, D, E and F) and during the final load range (region G) (specimen YSB1) 162

Fig. 7.24 Fatigue crack propagation rate, da/dN, versus stress intensity range, ΔK, and versus the maximum stress intensity factor, K_{max}. The data points were obtained from different specimens and each of the low crack propagation rate was obtained following a cycling interruption 164

Fig. 7.25 Crack propagation velocity obtained in the bright zone of the striations in 3Y-TZP versus the instantaneous stress intensity factor. The data were obtained from YSP1 (square), YSP2 (triangle), YSG1 (circle) and YSB1 (inversed triangle). The dash line indicates regression of equation 7.6 167

Fig. 7.26 Schematic illustration for the determination of crack deviation 172

Fig. 7.27 Coupled micrographs for determination of the crack deviation angle. (a) micrograph at a tilt angle $\beta=0^{\circ}$, (b) micrograph of the same region at a tilt angle (clockwise) $\beta=35^{\circ}$ 174

Fig. 7.28 Striations are less visible near the lateral surface (to avoid the corner effect, the right edge of this micrograph was placed approximately 20 μm from the lateral surface) 178

Fig. 7.29 Hysteresis loops obtained in ZTA-AZ material with microstrain gage showing that the strain increased gradually with increasing cycle number during tensile fatigue 183

Fig. 7.30 The Strain, D, measured with the microstrain gage at the fatigue crack tip as a function of the cycle number during tensile fatigue (ZTA-AZ material) 185

Fig. 7.31 The relation between the crack propagation rate, da/dN, and the stress intensity range ΔK and maximum stress intensity factor, K_{max}, in ZTA (ZTA-AZ material) 187

Fig. 7.32 General fracture surface aspects in ZTA showing compression fatigue fracture surface (indicated by C), tensile fatigue fracture surface (T) and the final fracture surface (F) 189

Fig. 7.33 Some ridge lines present parallel to the crack front in ZTA (crack propagates from the left to the right) 189

Fig. 8.1 X-ray diffraction spectra obtained from the lateral surface after uniaxial compression. The $(11\bar{1})_m$ peak indicates the occurrence of the t- to m-phase transformation: (a) spectrum obtained on the free surface, (b) spectrum obtained after compression at 900 MPa, (c) spectrum obtained after compression at 3000 MPa 192

Fig. 8.2 X-ray diffraction spectra obtained from the fracture surface. (a) spectrum obtained on the free surface, (b) spectrum obtained on the fracture surface in which the peak $(11\bar{1})_m$ is clearly observed indicating the occurrence of the t- to m-phase transformation 196

Fig. 8.3 Illustration on the conversion from the particle distribution profile assumed by Kosmac et al [900] to that (a) more realistic distribution of transformed particles. The transformation volume is supposed to be equal in both areas. Therefore, area A in (a) is assumed equal to area B in (b) 199

Fig. 8.4 Typical Raman spectra. (A) Raman spectrum obtained from the tetragonal structure of ZrO_2, (B) Raman spectrum obtained from the monoclinic structure of ZrO_2 204

Fig. 8.5 Raman spectra of 3Y-TZP. Spectrum A from the free surface, B from the crack initiation region, C from the last bright zone, D from the last striation, E from the final fracture surface neighbouring the last striation, F from the final fracture surface far from the last striation 206

Fig. 8.6 The correspondence between the volume fraction of transformed particles, V_m, the instantaneous stress intensity factor, K, and the position on the fracture surface. The minimums in the volume fraction of transformed particles correspond to dark bands or striations 208

Fig. 9.1 Typical fatigue crack propagation curve, showing three stages propagation behaviour, consists of crack propagation near the threshold (region I), the power law crack propagation (region II) and the accelerated crack propagation (region III) 217

Fig. 9.2 Comparison of fatigue crack propagation curves obtained on 3Y-TZP in the present study and in the study of Liu and Chen [53] (solid line) as well as that obtained on Ce-TZP [34] (medium dash line) and Mg-PSZ [45] (dash line) 219

Fig. 9.3 Fatigue crack propagation rates, da/dN, which are obtained by measuring widths of dark bands (filled circle), bright zones (open triangle) as well as spacings between dark bands (open circle), are plotted as a function of the maximum stress intensity factor, K_{max} 222

Fig. 9.4 Schematic illustration on the relationship bewteen the load cycle, the topography of fracture surface and stress distributions at the crack tip. (a) load cycle, (b) fatigue fracture surface feature, (c) the topography of fracture surface (edge view) and (d) stress distributions at the crack tip 233

Fig. 9.5 Fatigue fracture surface showing two fine arrested lines of the fatigue crack 235

THE LIST OF TABLES

Table 4.1 Material composition of 3Y-TZP (wt%) 76

Table 4.2 The compositions of zirconia toughened alumina (wt%) 77

THE LIST OF APPENDICES

APPENDIX 1 The integration for subcritical crack propagation velocity . . . 260

APPENDIX 2 The development of equations for calculating the crack plane deviation angle 262

INTRODUCTION

Modern engineering applications place increasingly severe demands on material properties. For wear resistance, strength applications at high temperatures and oxidation resistance, metallic materials have very limited potentials. For such applications, advanced ceramics are becoming more and more attractive for the properties they can offer.

Advanced ceramics made of very fine powder and in high purity can exhibit extraordinary strength and improved fracture toughness. The important improvements which have been attained in the strength and toughness of advanced ceramics however can be offset if these ceramics are susceptible to some slow subcritical cracking, caused either by an environmental effect known as static fatigue or by a true fatigue effect associated with cyclic stress variations.

The true fatigue effect is the progressive failure or the progressive degradation in mechanical properties of an engineering component which occurs as a result of a cyclic variation in the applied stresses and strains. It is now well known that this fatigue process in an engineering component not containing a precrack consists of three stages: crack initiation caused by cyclic stresses or strains, crack propagation and the sudden overstress fracture of the remaining cross section. The fatigue life primarily depends on the crack initiation and crack propagation, with

crack initiation generally accounting for the majority of the fatigue life, when the fatigue life is long. Compared to the crack propagation behaviour, crack initiation exhibits considerable uncertainty, which results in difficulty in the reliable prediction of fatigue life.

In ceramics, the existence of preexisting flaws and defects can drastically decrease the portion of the crack initiation over the entire fatigue life or can even eliminate the crack initiation. This will result in severe decrease of the fatigue life. Therefore, service performance of ceramics depends strongly on the size of flaws present in the original material or component. It then is very important to be able to predict the rate of increase in flaw size during service and the resulting decrease in the fracture strength during service.

The fatigue crack propagation stage should be particularly important in advanced ceramics, since high strength materials with relatively low fracture toughness such as ceramics are more severely degraded by stable crack propagation than low strength materials. Excessive sensitivity to load variations can limit the potential of advanced ceramics for load-bearing applications in cases where the loads are variable.

In engineering applications, any type of failure or degradation will not be welcomed. Fatigue cracking in ceramics however is particularly unwelcomed because

of the small critical crack size which can make it difficult to detect the degradation. However, if one must chose between the possibility of sudden failure without any warning sign and gradual degradation with detectable warning, the latter would generally be chosen in most engineering applications, because the gradual degradation of service capability such as by fatigue can provide the opportunity to prevention of costly failures. The solution for this problem is to study the fatigue crack propagation behaviour in advanced ceramics. Advanced ceramics differ radically from other materials such as metals and organic materials in many aspects: processing, microstructure and properties. As a result, their fatigue behaviour will also differ greatly from other materials. Unfortunately, there have been very few studies available in this area. Even the occurrence of genuine fatigue crack propagation is not widely recognized in ceramics.

If fatigue crack propagation can really occur in ceramics, there are numerous questions to answer: How does the fatigue crack propagate at a low range of the applied stress intensity factor, does the threshold exist in advanced ceramics? Can the Paris law describe well the stable crack propagation? How does the final fracture occur? What are the fatigue fractographic features of ceramics? How does the fatigue crack propagate cycle by cycle? What difference will ceramics toughened with different process present during fatigue cracking? Is the fatigue crack propagation predictable and controllable? What kind of improvement in processing or in microstructure design should result in the greatest improvement in fatigue

resistance? Is it possible to predict the degradation rate in order to remove components from service before catastrophic failure occurs?

In order to attempt to begin to answer some of these questions, the main objective in the present study focused on the fatigue behaviour of the advanced ceramics. 3 mol% yttria-stabilized tetragonal zirconia polycrystals (3Y-TZP) and zirconia-toughened alumina (ZTA) were employed in the present study. The yttria-stabilized zirconia used is a fine grain ceramic and has potential for stress-induced transformation toughening. The yttria-stabilized zirconia has also very confined profile of transformation zone, the size of which can be of order of the amount of fatigue crack propagation expected in a single cycle. Therefore, this material is realistic for investigating the cycle-by-cycle mutual-influence between fatigue crack propagation and stress-induced transformation zone.

A study of the cycle-by-cycle fatigue propagation behaviour is of fundamental importance in correctly understanding fatigue crack propagation. Yet, very few details were known of the crack propagation sequence in ceramics within a single load cycle when the present study was initiated.

Fatigue testing under tensile stresses in ceramics requires great care and particularly close control of the test procedure in order to avoid small overloads which can produce fracture of these brittle materials. Moreover, when four point

bending is employed, which is often necessary because of the specimen sizes available for testing, the displacement in the loading direction will trigger a much large increment of tensile stress than loading in simple tension. Thus, to obtain information on the cycle-by-cycle propagation behaviour employed four point bending was expected to be particularly challenging. There was clearly a necessity to start the fatigue test at very low stress intensity factor. The use of microstrain gage positioned at the crack tip to obtain amplified load-strain signals was chosen to obtain information on the fatigue crack propagation in an individual cycle.

Striations associated with cyclic nature of fatigue crack propagation are commonly observed in metals as well as in some organic materials which exhibit considerably inelastic deformation during fatigue cycling. This feature of striations was not expected to be obtained in ceramics because of their very limited potential of inelastic deformation, particularly at room temperature. Nevertheless, there was some hope of finding striations in transformable ceramics, such as yttria-stabilized zirconia, because of the inelastic deformation associated with stress-induced transformation. Stress-induced transformation would be expected to play an important role in the fatigue crack propagation of transformable yttria-stabilized zirconia.

It was decided to also study fatigue behaviour on zirconia-toughened alumina, a material which is considered to demonstrate microcracking toughening behaviour.

Therefore, the present study focused on the fatigue behaviour of transformable yttria-stabilized zirconia, with some fatigue testing of other ceramics, in particular, zirconia-toughened alumina for comparison purpose.

The contents in this thesis are arranged as follow: As the main objective of this thesis is a study of stable fatigue crack propagation, chapter 1 and chapter 2 present a literature review on investigations of static fatigue and cyclic fatigue (i.e., true fatigue crack propagation) in ceramics, respectively. It is difficult to interpret the fatigue behaviour of a material without knowing its physical metallurgy. Phase relationships in zirconia, stabilization and transformation toughening are reviewed in chapter 3. Mechanical properties of ceramics are very sensitive to the processing. Chapter 4 describes the material processing and specimen preparation.

A compression cyclic load can cause fatigue crack propagation in prenotched specimens. Compression fatigue provides a convenient technique for study of the fatigue behaviour in ceramics, since most difficulties normally encountered in the study of the fatigue of brittle materials, such as poor machinability, brittleness, high requirement on perfect alignment of loading train during fatigue test, can be avoided. Chapter 5 describes the compression fatigue study performed and discusses the results obtained.

The fracture toughness is a mechanical property which should strongly affect

the fatigue properties of brittle materials, such as ceramics. After successful compression fatigue tests had been performed, precracked specimens were available for fracture toughness testing. The results from these precracked specimens were compared to results obtained by other techniques and to those obtained from non-precracked specimens. Chapter 6 describes the fracture toughness tests carried out, presents and discusses the results obtained.

The fracture toughness results provided key information for the preparation and control of fatigue tests under tensile stress which was achieved by four point bending. Chapter 7 describes and discusses fatigue crack propagation behaviour obtained under cyclic tensile stresses. Included is a presentation and explanation of the fractographic features as well as of crack tip strain measurements which provided key information in explaining the fatigue crack propagation sequence and the microfractographic features observed in yttria-stabilized zirconia.

Stress-induced transformation is expected to contribute to and to influence the fatigue crack propagation of ceramics which undergo stress-induced transformation. Chapter 8 focuses on the characterization of stress-induced transformation results in 3Y-TZP using X-ray diffraction and Raman microscopy. The Raman microscopy provided particularly localized analyses on the different microportions of fatigue fracture surface and helped confirm the proposed explanation of the striation-like markings observed in 3Y-TZP. The Raman

microscopic analyses also provided information on the dependence of stress-induced transformation on the instantaneous stress intensity factor.

Chapter 9 compares and discusses the results on 3Y-TZP with those reported in other studies on 3Y-TZP, on magnesia-partially stabilized zirconia and on ceria-stabilized tetragonal zirconia polycrystals. The type of fatigue crack propagation curve is also discussed in chapter 9. The conclusions are presented in chapter 10.

PART I LITERATURE REVIEW

CHAPTER 1 STATIC FATIGUE IN BRITTLE MATERIALS

The phenomenon of delayed failure associated with a steady stress is commonly termed static fatigue [1]. In static fatigue, crack propagation, which follows crack initiation and precedes final fracture, is usually termed subcritical crack propagation whether in the presence of moisture or not. The term stress corrosion cracking (SCC) is often employed specifically to describe static fatigue of a material in the presence of moisture [2]. Brittle fracture of ceramics is often preceded by subcritical crack growth and then occurs as a type of delayed failure without warning when a steady load is applied.

1.1 Static fatigue of brittle materials

A curve of the subcritical crack propagation (Figure 1.1), which is usually plotted in log-log base, consists of three regions: a linear portion at low applied stress intensity factor, K, corresponding to region I (usually with a steep slope), a plateau at medium K in region II and another linear portion at high K in region III (usually with steeper slope than that in region I).

Becher [3] has investigated stress corrosion cracking (SCC) in 7.2 mol% magnesia partially stabilized zirconia (Figure 1.2). For this transformable ceramic, the subcritical crack propagation gave a linear region I but the other two regions did

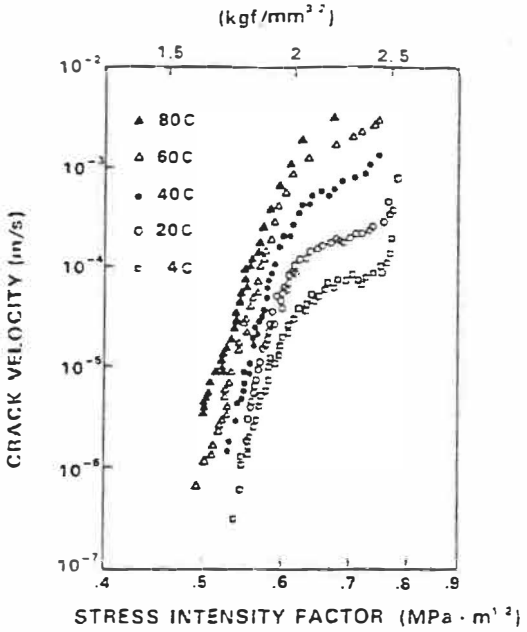

Fig. 1.1 Typical curves of stress corrosion cracking [8].

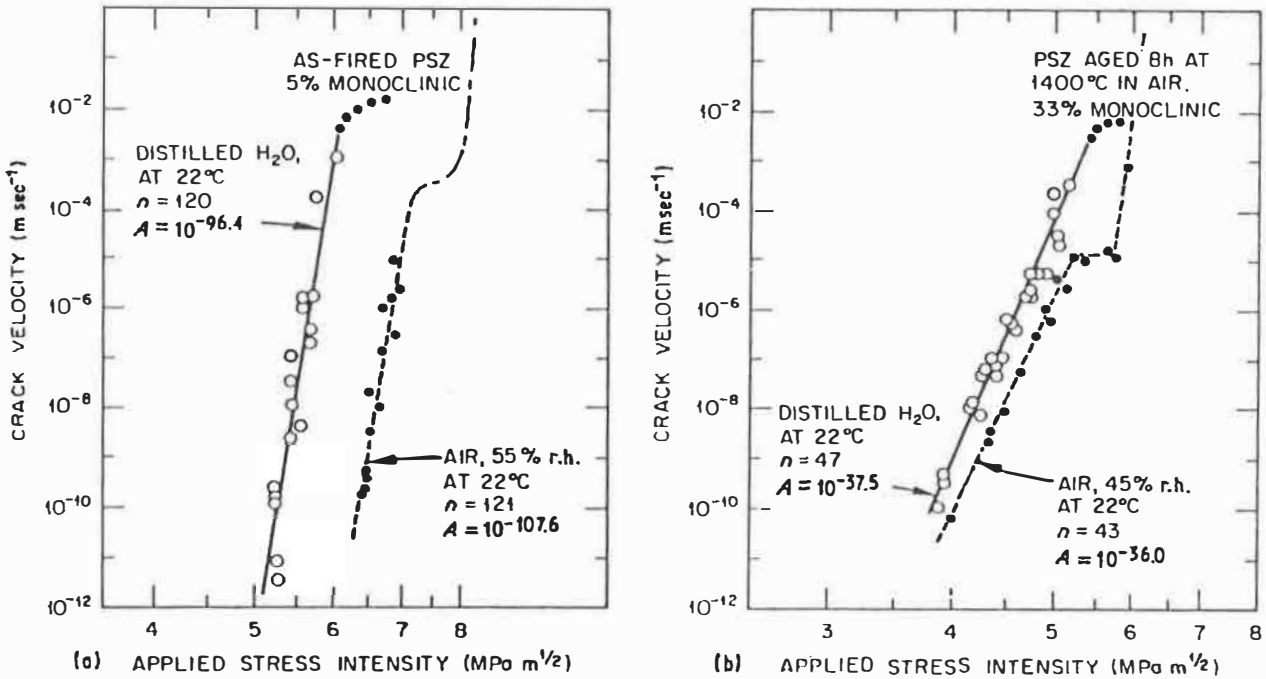

Fig. 1.2 Sensitivity of slow crack growth behaviour in partially stabilized zirconia [3].

not present clearly linear log-log behaviour. Region III did not even appear to be definitively present. As a result, the crack propagation curve consisted primarily of region I. It was also shown that the resistance to crack propagation was higher both in air (50% relative humidity) and in distilled water for the as-fired material than for the aged material. The decrease of the cracking resistance and of the fracture toughness in the aged condition was attributed to the formation of intergranular monoclinic precipitates during the aging process. In the as-fired material, crack growth occurred predominantly by transgranular fracture; whereas, in the aged material, the crack propagated intergranularly. This difference is attributed to tensile strains in the matrix adjacent to the precipitates produced in the aging process.

Comparison of crack propagation in different environments showed that subcritical crack propagation was sensitive to the environment for both the as-fired condition and the aged condition, with the as-fired condition being more sensitive [3]. The enviromental sensitivity of crack propagation in oxide ceramics is usually considered to result from reaction between water molecules and the oxygen bond [5,6].

Wiederhorn [5] investigated subcritical crack propagation in soda-lime glass. Glass is commonly regarded as resistant to chemical corrosion. Nevertheless, a small amount of water vapour, normally found in the atmosphere, can react with glass under stress to cause delayed failure. His investigation showed that the dependence

of crack velocity on applied force can be divided into three regions (Figure 1.3). In region I, the crack velocity varies exponentially with the applied force and all curves have similar slopes for different relative humidity levels. However, the curve is shifted to the higher velocity region with increasing relative humidity. In region II, the crack velocity is nearly independent of the stress intensity, the position of each plateau is shifted to lower velocities as the amount of water vapour in the environment is decreased. In region III, the crack velocity again varies exponentially with the applied force. However, the slope of the curve is considerably greater than that in region I. As well, all curves for the different relative humidity levels merge into a single curve in region III.

The cracking behaviour in regions I and II was explained by a theory of a heterogeneous chemical reaction between glass and the environment at the crack tip. It is suggested [5] that the reaction can be composed of five steps, the slowest of which will determine the rate of the overall process. The successive stages are the transport of gaseous reactants to the surface, the adsorption of gases, the reaction on the surface, and the desorption of products from the surface into the environment. Chemisorption is considered as the factor limiting the fracture process, because Van der Waals adsorption is physical in nature and will occur rapidly. Two factors mainly contribute to chemisorption: the water diffusion rate and applied force. The latter can change the ability of the surface for chemisorption. It is suggested that the applied force controls the cracking rate when it is low, as in the

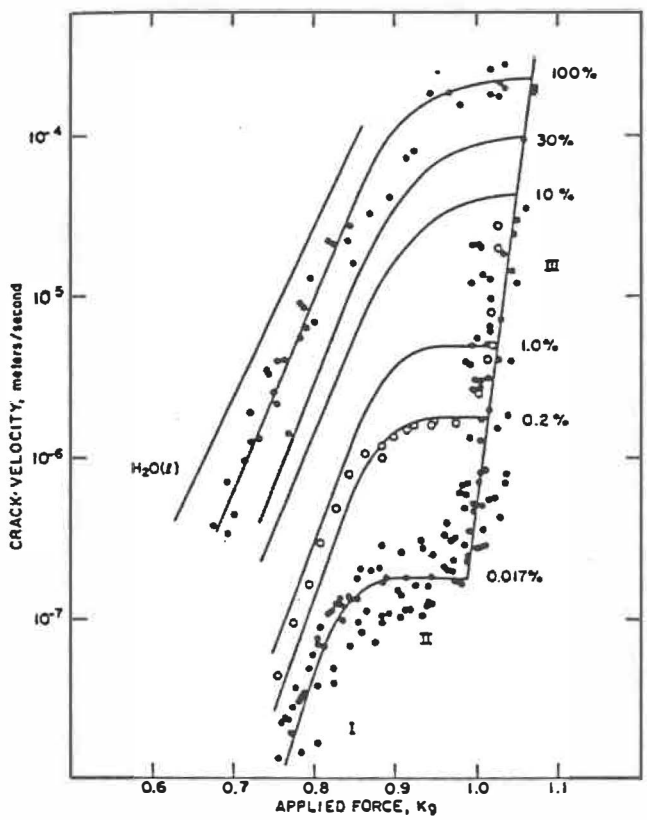

Fig. 1.3 Dependence of crack velocity on applied force. The percentage represents the relative humidity and Roman numerals identify the different regions of crack propagation [5].

case in region I. The water diffusion rate controls the cracking rate when the applied force is large, as in the K-independent stage.

Quantitative analysis based on a chemisorption model gives an equation for the cracking velocity. The analysis indicates that when load is small, the crack velocity depends exponentially on the applied force, as observed in region I. When the load is large, the velocity becomes independent of load, as the case in region II. But no satisfactory theory has been proposed to explain fracture in region III. A similar study has been conducted in vitreous silica, and has clarified the mechanism of how a water molecule reacts with the Si-O bond and breaks this bond [6].

To compare the effects of different solvents on static fatigue, White et al [7] studied static fatigue in vitreous silica tested in acidic and basic environments. The slope of the curve of the crack velocity versus the stress intensity is greater in the acidic environment than in the basic environment. The slope of the crack growth curve obtained in water is close to that obtained in acidic solutions.

An argument based on the expected chemical reactions [7] assumes that crack growth in acidic solution is a consequence of the reaction of the Si-O (siloxane) bonds with water; whereas, crack growth in basic solutions is a result of a reaction of Si-O bonds with hydroxide ions. When the hydroxide ions are removed from the immediate vicinity of the crack tip, crack growth behaviour reverts to that in acidic

solutions. The reaction at the crack tip is primarily that of the Si-O bonds with water molecules in the solutions. The manner in which water molecules or some other solvent molecules react with the Si-O bond in silica has been described in reference [6].

Similar results in silica have also been obtained by Yoshinori [8]. The crack growth velocity is markedly influenced by temperature and humidity. The slope of the log v-K curve in region I is independent of humidity. Compared to the results obtained in reference [7], however, the crack propagation velocity is shifted to higher values. The crack growth velocity in region II shows weaker dependence on stress intensity than in region I. Moreover, the transition from region I to region II seems to occur at a constant stress intensity and to be independent of temperature and humidity. The crack growth velocity at the transition point, however, depends significantly on temperature and humidity [8].

Krohn and Hasselman [9] investigated static and cyclic fatigue under tensile stress in alumina. Their data points of stress versus time-to-fracture (σ-t) showed very large scatter, i.e, the failure time varied greatly for different specimens under the same applied stress. One possibility for this data scatter may be (even though the authors did not this point out) variation in the size of the preexisting defects at which subcritical crack propagation initiated. In alumina, the crack propagates in differently in regions of large and small grains. In regions of small grains, the crack

propagates intergranularly; whereas, in large grains, the crack propagates transgranularly and produces terrace-like fractographic feature (this will be reviewed in the following section of this chapter).

Also as ceramics are brittle and very sensitive to bending, if bending arise during a tensile test due to imperfect aligment, this will also affect the results obtained from different tests.

1.2 Fracture of ceramics

Compared to metallic materials, fracture in ceramics exhibits many differences in both the macroscopic and microscopic features.

1.2.1 Macroscopic aspects of fracture in ceramics

A study on fracture in yttria-stabilized zirconia under tensile stress has shown [10] that the fracture surface was macroscopically flat and that crack propagated perpendicularly to the loading direction. These features are very common in brittle materials [11]. Since the most favourable flaw will propagate when the stress intensity exceeds its critical value, and no shear deformation can occur in such a brittle material, the fracture occurs under the effect of the maximum tensile stress and a flat fracture surface will develop perpendicularly to the maximum tensile

stress.

However, failure under a compressive load is more complex in brittle materials. Cracking associated with uniaxial compression can occur longitudinally, which is known as slabbing [11,12]. In slabbing, the cracking direction is parallel to the loading direction and the cracking plane is perpendicular to the dominant lateral surface of the specimen.

A study by Ashby and Hallam [11] on a rectangular plate specimen of PMMA with an angled main crack in its central portion has provided some clues in understanding the occurrence of slabbing. These authors have observed the cracking behaviour of an angled crack under uniaxial compression. The results showed that the angled crack reacted to the compression load by initiating two short cracks at its two extremities. At the initiation stage, these two short cracks were perpendicular to the angled crack, but gradually became parallel to the loading direction. From these observations, the authors concluded that sliding of the main crack resulted in the formation of wing cracks, and that further sliding of the main crack surfaces kept the wing cracks open and caused these to grow. The main crack sliding is believed to be promoted by the shear component of the applied compression load, and this sliding gives rise to a tensile stress field at the wing cracks. The propagation of the wing cracks results in the slabbing of the specimen. Therefore, it is always a tensile stress which causes slabbing in brittle materials.

Fracture in brittle materials strongly depends on the loading conditions. Uniaxial compression associated with a moderate lateral confinement might result in a macroscopic shear fracture, while uniaxial compression associated with important lateral confinement can cause the specimen to deform in a pseudo-ductile manner with large scale deformation.

Cracks produced by indentation in ceramics have attracted considerable research attention. In the initial stage of indentation, radial cracks form with the crack plane perpendicular to specimen surface and spread outwards from the periphery of the crater. As the indentation load increases, subsurface median circular cracks which are symmetric about the load axis form and extend. These median cracks which are perpendicular to the top surface merge with the radial cracks under coplanar conditions, or they grow as a separate entity. Finally, a series of lateral cracks with a crack plane parallel to the top surface initiate and propagate between the radial cracks.

Of these three type of cracks, the size of the radial crack is the more predictable and is often employed to evaluate the fracture toughness. The indentation technique has some advantages in measuring fracture toughness of ceramics, such as, simplicity and minimal material requirement. A number of semi-empirical equations for evaluation of the toughness have been developed by different authors [13,14].

1.2.2 Microscopic fracture aspects in ceramics

Attention paid to microscopic origins of cracks is often essential in understanding the fracture of ceramics. In ceramics, cracks originate generally at preexisting "defects", such as pores, inclusion agglomerates, and thermal cracks, etc [15,16,17]. Because of their limited potential for inelastic deformation, ceramics often response to a local stress concentration, such as that produced by residual thermal stresses by forming many microcracks. These microcracks can form a dense network at grain boundaries. The presence of microcracks which are carefully controlled in size and distribution can result in a dramatic increase in the toughness of ceramics by causing a reduction in the local or effective stress intensity [26,27,28].

An investigation on lead zirconate titanate with purposely-introduced spherical pores revealed that the fracture origins consisted typically of pores on or very near the tensile surface [15]. Evans et al [18] proposed that a partial equatorial crack around a spherical pore in ceramics would first propagate around the pore to form a complete equatorial crack and subsequently propagate outward to cause the failure of the specimen. In contrast, a study on pores in glass suggested [15] that cracks initiated at pores did not form an equatorial crack as an intermediate stage of failure. Even if the crack propagated around the periphery of pores, it almost never stayed on the same plane, and hence left fracture tails on the fracture surface.

To compare the effect of different fracture origins on the strength of ceramics, Sung and Nicholson [16] investigated the relationship between fracture stress and the size of different types of imperfections acting as the fracture origin in 4.5 wt% yttria partially stabilized zirconia. The defects identified in order of decreasing severity were as follows: fibre inclusions, agglomerates, iron inclusions, pores and alumina inclusions which existed in the material (Figure 1.4). The relative severity of these different types of fracture origin was explained by considering the residual stress fields developed at the defect-matrix interfaces. In particular, agglomerates which often exist in ceramics will cause serious degradation in strength, because the different local density between the agglomerate and the matrix can lead to a differential sintering effect and result in tensile residual stress. In addition to the stress intensification effect caused by the presence of the defect, the residual tensile stress will superimpose on the applied stress and result in fracture at lower stresses than that predicted by taking only the defect size into account [19].

Most ceramics are compounds which often have low crystallographic symmetry. It is believed that dislocation movements is usually unlikely to occur in most ceramics at ordinary temperatures. To study this possibility, Barber and Tighe [20] studied dislocations in alumina. They observed dislocations with $1/3\langle 11\bar{2}0\rangle$ Burgers vectors. By preventing dislocation from slipping on the basal plane, Gooch [21] observed that $\{11\bar{2}0\}\langle 1\bar{1}00\rangle$ dislocations slipped on the prismatic plane in sapphire at 1150°C. Gulden [22] also reported prismatic slip in alumina, but the

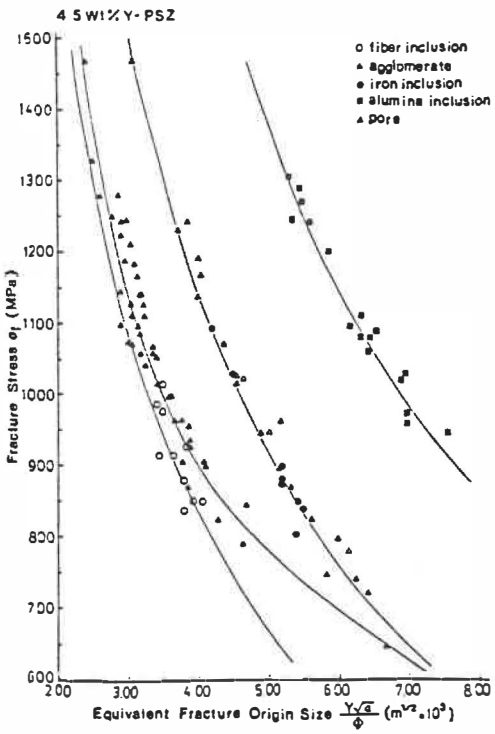

Fig. 8. $\sigma_f - Y\sqrt{a}/\phi$ plot for 4.5% Y-PSZ.

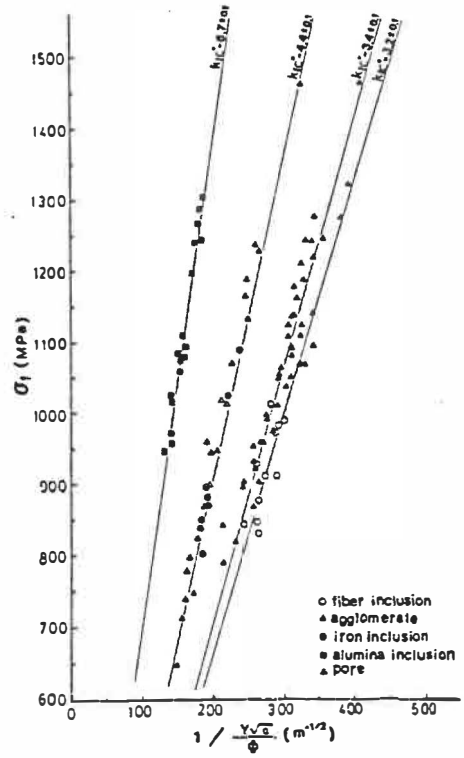

Fig. 9. $\sigma_f - 1/Y\sqrt{a}/\phi$ plot for 4.5 wt% Y-PSZ.

Fig. 1.4 The order of severity for different fracture origin in ceramics, in which fibre inclusion was the most severe, then agglomerates, iron inclusions, pores and alumina inclusions [16].

Burgers vector was reported to be 1/3<1011> rather than 1/3<11$\bar{2}$0>. This is somewhat surprising, since 1/3<11$\bar{2}$0> are the shortest Burgers vectors in this structure [22].

Probably, because of the great difficulty in obtaining large single crystals of monoclinic and tetragonal zirconia, very few publications are available on microscopic aspects of fracture in such zirconia. Cubic zirconia seems to cleave along {111} planes, this fracture involves in the breaking of a minimal number of anion-cation bonds per surface area. Metastable tetragonal zirconia crystals cleave probably along either {001} or {110} planes [23].

1.2.3 Terrace-like fractographic aspect in alumina

Although most fractures in ceramics occur intergranularly, transgranular fracture can also be observed occasionally in some ceramics, such as alumina. In alumina, particularly for large grain sizes which manifest more often cleavage features, the crack surface exhibits terrace-like transgranular fracture. The terrace-like feature occurs as numerous horizontal facets at different heights connected by vertical facets. Each horizontal portion has a flat surface on which many ridge lines are present; whereas, the vertical portions have slightly more prominent ridge lines and take the form of a winding prism surface. This terrace-like feature is believed

to result from alternative cracking on the basal and prismatic planes [24,25]. The terrace-like fracture occurs particularly in large grains, especially when these occasional large grains are surrounded by many small grains in which intergranular fracture is typically observed [25].

CHAPTER 2 CYCLIC FATIGUE OF CERAMICS

As mechanical properties of ceramics have been greatly improved, it has become feasible for ceramics to be employed for engineering components in which the variation of load is inevitable. Therefore, fatigue in ceramics has recently attracted more and more attention [29-36].

2.1 Cyclic fatigue compared to cyclic manifestation of stress corrosion cracking

The term cyclic fatigue has been employed to describe a variety of processes which lead to a degradation of mechanical properties due to cyclic loads. Cyclic fatigue in brittle materials is an interesting subject, because the occurrence of fatigue can dramatically influence the design philosophy employed for load-bearing components made of ceramic materials.

Generally, ceramics do not display the plastic or inelastic deformation with which fatigue propagation is usually associated, therefore, in the earlier studies, the failure of brittle materials under cyclic loading was considered as a cyclic manifestation of stress corrosion cracking rather than as a real fatigue effect [2,9,37,38].

The relationship of crack velocity, v, during stress corrosion cracking versus

stress intensity factor, K, is commonly expressed by equation (1.1). A problem with this expression is that the units of A depend on n which varies for different environments even for the same material. This makes the physical significance of this parameter A obscure. To overcome this problem, Sines [39] proposed an equation

$$v = \frac{da}{dt} = v_o \left(\frac{K}{K_c}\right)^n \qquad (2.1)$$

where v_o and n are constant parameters for a given material and environment. Then, v_o possesses a clear physical significance and is the stress corrosion cracking velocity when the stress intensity equals a critical value. As well, v_o then also possesses an unchangeable unit of length over time.

If fatigue effects are absent, an instantaneous crack growth velocity can be considered to result from stress corrosion cracking at each instantaneous load. Using equation 2.1 to integrate the differential crack growth distance with respect to time at each instantaneous load, Evans [2] analyzed time-to-failure under cyclic loads in glass and porcelain, and suggested that true fatigue effects were of minor significance in these materials, despite the cyclic nature of the applied stress. This is in agreement with the results obtained by Wiederhorn [5] for environment-enhanced subcritical crack propagation. Similar results are reported in reference

[40].

Nevertheless, some investigations [9,41,42] reveal the existence of a cyclic fatigue effect. A study by Krohn et al [9] on alumina demonstrated that a cyclic fatigue mechanism existed at a higher frequency (40 Hz) and higher amplitudes. The extensive data obtained by Chen and Knapp [43] on alumina, using a low frequency (0.3 Hz) tension cycle, also suggested a possible cyclic influence at room temperature, but no fatigue effect at 200°C and above.

Another method of identifying significant fatigue effects is to compare the time to failure at constant stress with those obtained for cyclic fatigue with the peak cyclic stress being the same as this constant stress [44], when the cyclic effect is rather significant. By this approach, Guin [44] obtained results on alumina in which the time to failure in the fatigue tests were considerably shorter than that in the quasi-static tests, which strongly suggested the existence of a true fatigue effect.

To demonstrate unequivocally that the crack growth observed is cyclically induced and that stress corrosion cracking mechanisms are not responsible, Dauskardt et al [45] monitored crack extension while the stress intensity was cyclically varied between K_{max} and K_{min} and while the stress intensity was held constant at the same value of K_{max}. The results revealed that crack propagation proceeded readily under cyclic loading. Upon removal of the cyclic stress

component by holding at the same K_{max}, no crack growth was detected. A study by Guin [44], using cylindrical non-precracked specimens, also obtained positive evidence for the existence of a cyclic cracking effect in pure alumina. When specimens were cyclically loaded with the maximum stress equal to the holding stress for the static fatigue test, the time to failure of these specimens was much shorter than that of static fatigue specimens.

As summarized above, both stress corrosion cracking and cyclic fatigue cracking exist in many ceramics. In many circumstances, crack propagation under cyclic loading consists of both of these effects. However, the threshold for static fatigue was higher than that for cyclic fatigue [30], therefore, at low stress intensity, crack propagation primarily resulted from the mechanical effect of the cyclic loading.

2.2 Investigations of fatigue life endurance

Traditional expectation on service endurance of engineering components has been based on studies of the number of cycles to failure on non-precracked specimens. Therefore, several studies have been carried out in ceramics on such endurance capability.

Recently, a study on the fatigue life of yttria-stabilized zirconia [46] has

shown that a higher mean stress is more damaging than a higher stress amplitude, when the maximum stress is the same. It was also shown that fatigue crack can initiate in both the mid-thickness section and at the surface of specimens in pull-push fatigue. Therefore, the surface condition does not have a very critical effect on the fatigue life of this material.

However, other results for push-pull tests show that fatigue behaviour is very sensitive to the condition of the specimen surface. Therefore, as far as the fatigue strength is concerned, the removal of surface flaws by annealing may be more beneficial than maintaining the machined layer of compressive residual stress [60].

Preexisting processing flaws are generally identified as the fracture origins in ceramics. Thus, crack initiation is a much easier process in ceramics than in metals. In metals, both the fatigue crack initiation and propagation are key factors in fatigue life. In ceramics, fatigue life is primarily controlled by crack propagation because crack initiation is facilitated by the presence of processing defects [46].

Endurance tests combined with periodic monitoring of surface crack propagation were performed on unnotched cantilever-beam specimens of MgO partially stabilized zirconia at room temperature [47]. The 9 mol% magnesia partially stabilized zirconia (Mg-PSZ) had a cubic structure with grain size of 50 μm in which 40 vol% of lens-shaped tetragonal precipitates were dispersed within the

matrix. These precipitates had a maximum size of 0.3 μm. Surface cracks were monitored by examining the top surface of the cantilever beam specimens.

Steffen et al [47] found that fatigue limit at 10^8 cycles with an R-ratio=-1 was about 50% of the tensile strength. Optical micrographic examination of specimen surface revealed a relatively large number of microcracks, which were observed to increase in both size and surface density with increasing alternating stress level or with increasing number of cycles. Although the majority of these microcracks were primarily orthogonal to the stress axis, some of them formed at angles up to approximately 45° to the stress axis particularly under tension-compression loading conditions.

The endurance tests performed in bending have drawbacks, since the fatigue crack always initiates at the specimen surface. This may simply be the result of the maximum stress being on the specimen surfaces. Under such test conditions, crack initiation at the specimen surface is not necessarily surface-related.

2.3 Fatigue crack propagation under tensile stress

Despite all of the experimental difficulties, particularly in obtaining bending free alignment, in performing a cyclic fatigue test in ceramics under tensile loading, several studies have been reported on fatigue under tensile stresses. Fatigue crack

propagation rates in the intermediate stress intensity region are a power-law function of the stress intensity range, in the same manner as the behaviour commonly observed for the fatigue of metals. The Paris law is therefore usually employed to describe the fatigue crack propagation in this region

$$\frac{da}{dN} = C\ (\Delta K)^m \qquad (2.6)$$

The exponent m in metals is typically of the order of 2 to 4. However, crack propagation rates in ceramics are far more sensitive to stress intensity range and much higher m values are obtained.

Dauskardt et al [45] investigated fatigue crack propagation in 9 mol% magnesia partially stabilized zirconia under tension-tension loading condition, and provided persuasive results of a true cyclic fatigue effects (Figure 2.1). Fatigue propagation curves at different toughness conditions exhibited different resistance to fatigue propagation, with the lowest fatigue resistance obtained for the overaged condition. Toughening due to transformable tetragonal particles could be estimated by comparing two curves for the peak toughness and for the lowest toughness conditions (the overaged condition), which gave approximately a 6 MPa$\sqrt{m}$ of transformation toughening.

Fatigue crack propagation showed a power-law dependence on the stress intensity range. The Paris law exponent was in the range 21 to 42 for 9 mol% magnesia partially stabilized zirconia. Dauskardt et al [45] pointed out that the unloading portion of the cycle results in enhanced microstructural damage ahead of the crack tip in Mg-PSZ, this localized damage could be microplasticity, or microcracking, particularly in the grain boundary and precipitate/matrix interface regions. Matrix microcracking associated with the formation of transformation shear bands has been well recognized in martensitic transformation. In response to cyclic loading, such microcracking could be enhanced by the cyclic movement of twin boundaries in transformed monoclinic particles, facilitating crack propagation under cyclic loading.

Moreover, Reece et al [30] suggest that crack surface asperities may act as a wedge between the two crack surfaces. Any possible microdeformation could result in the mismatch of such asperities on the two crack surfaces, which would induce Mode II and III cracking due to wedging action on unloading. The asperity mismatch was also observed in ceria-partially stabilized zirconia by Tsai et al [34]. Because of this mismatch, fatigue cracks retained an opened aspect when the applied load was removed completely compared to a subcritical crack. This retained crack opening may enhance fatigue crack propagation. Tsai et al [34] observed debris and edge-absent grain boundaries on fatigue fracture surfaces, which may have resulted from the wedging effect of asperities. As pointed out by Reece and

his coworkers [30], unloading in cyclic fatigue could produce a moment about an asperity, resulting in enhanced tensile stress at the crack tip (Figure 2.2). When fracture resulted in shape mismatch of the asperities on the two crack surfaces, the unloading would produce a moment as well as shear stresses.

Because of the poor thermal conductivity of ceramics, when fatigue tests are performed at a high frequency, such as 50 Hz, the crack tip temperature may increase, as a result of heat generation resulting from thermomechanical effects. Particularly, when a material shows nonlinear deformation (hysteresis behaviour) under cyclic loading, thermally activated processes [129] could also play an important role in fatigue crack propagation.

The fatigue threshold is the critical stress intensity factor below which there is no fatigue crack propagation. The fatigue threshold may signify the critical energy for crack propagation in materials with preexisting defects such as ceramics or the critical energy for crack initiation in materials free of preexisting defects. At very low K, the energy supplied from load cycling is well below that needed to break atomic bond during either one load cycle or by a build-up effect over several several cycles. At this circumstances, no fatigue crack propagation can be observed. The fatigue threshold should exist in ceramics as in metals. However, when this critical energy is very small, the threshold should be associated with very low stress intensity and at very low da/dN, as a result, it may not be observed even at a da/dN of 10^{-10}

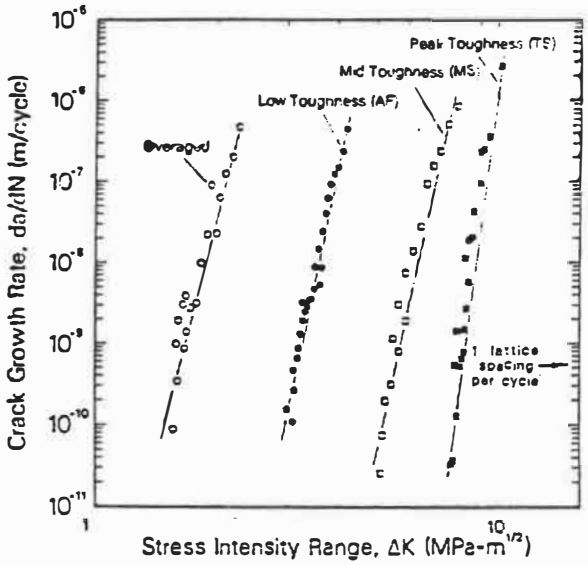

Fig. 2.1 Fatigue crack propagation rate, da/dN, as a function of stress intensity range, ΔK, for Mg-PSZ [45].

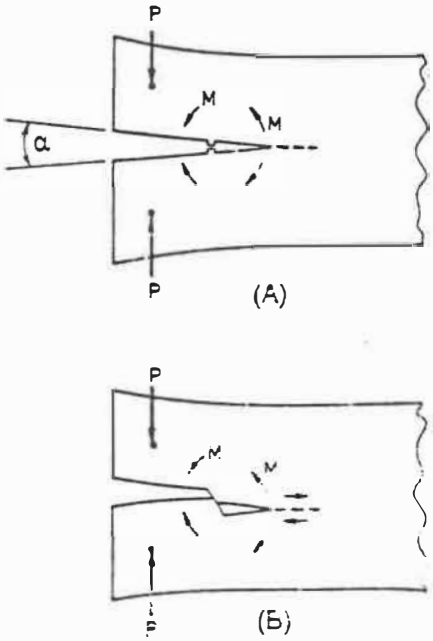

Fig. 2.2 Illustrations of (A) wedging asperity and (B) sliding asperity [30].

m/cycle [45].

In ceria-partially stabilized zirconia, Tsai et al [34] have shown that the stress-induced transformation zone size is large and the transformation toughening effect is strong. The fatigue threshold is high and associated with relatively high da/dN, which made it possible to discern the threshold at reasonable low crack propagation rate (between 10^{-8} m/cycle and 10^{-10} m/cycle,). When a lower critical stress for transformation was obtained by sintering at higher temperature than sintering at lower temperature, transformation toughening became stronger with respect to the material sintered at low temperature. As a result, the threshold became higher.

The exponent in the power-law correlation between log (da/dN) and log K increased slightly with increasing critical stress for the transformation. However, the critical stress intensity for fast fracture, K_c, was insensitive to this critical stress.

2.3.1 Influence of the cycling frequency

Dauskardt et al [45] examined the frequency dependence of the crack propagation rate, da/dN, for cyclic frequencies of 1, 10 and 50 Hz in 9 mol% MgO partially stabilized zirconia, employing compact tension specimens at room temperature. The cracking rate was found to be frequency independent.

Endurance tests performed by Grathwohl and Liu [49] on bend specimens (3.5x4.5x45 mm) of 3 mol% yttria-stabilized tetragonal zirconia polycrystals (3Y-TZP) showed a dependence on frequency. The specimens tested at 2 Hz exhibited comparatively lower numbers of cycles to failure than the specimens cycled at 200 Hz. This suggests a contribution of corrosion-assisted slow crack growth. As a result, zirconia ceramics exhibit significant subcritical crack growth caused by humidity, which is visible from the strong dependence of cracking on the loading rate. A cyclic fatigue effect also occurs in this material, which can be seen from the much shorter time to failure during cyclic fatigue compared to that under static load.

2.3.2 Effects of the waveform on the fatigue life

Tensile fatigue tests were performed by Lin and Socie [50] on cylindrical rods of 99.8% pure alumina with an average grain size of 6 μm. The tests were carried out at 1200°C in air employing three different loading waveforms, a sine wave, a square wave, and a trapezoidal wave. The cyclic lifetime was found to depend on the cycle shape and to be controlled by the duration of the hold time in a cycle at the maximum tensile stress. Cyclic loading with a higher strain rate and shorter duration at the maximum stress decreased the endurance life. As well, the fatigue life measured for the longer hold time at the maximum stress was very close to that for static loading [50].

2.3.3 Effect of stress intensity range

Rate of fatigue crack propagation in metals is generally more dependent on the range of stress intensity, ΔK, than on the mean or maximum stress intensity, K_{mean} or K_{max} [48]. Tests carried out by Dauskardt et al [45] on 9 mol% MgO partially stabilized zirconia, using compact tension specimens under a constant K_{max} (=4.2 MPa$\sqrt{m}$) with increasing K_{min}, demonstrated that crack propgation rate decreased with decreasing stress intensity range. This may indicate that certain reversible process occurred in ceramics during fatigue.

2.3.4 Effect of reversible cyclic load

Steffen et al [47] studied fatigue crack propagation study in 9 mol% MgO partially stabilized zirconia at room temperature. The crack was initiated at a wedge-shaped starter notch. Crack length was monitored with an electrical-resistance technique using NiCr films vapour-deposited on the specimen surface.

During the initial stages of crack propagation, for the same maximum tensile load, the propagation rates were somewhat slower for tension-tension than for tension-compression cycling. However, after only 20 μm of crack extension, crack propagation rates were similar for both cycling conditions. Since the total fatigue lives were invariably longer in tension-tension compared with corresponding tests in

tension-compression at the same maximum applied stress [47], this may indicate that tension-tension fatigue is less detrimental in engineering applications of ceramics.

2.3.5 Grain size effect on fatigue in ceramics

There is no many publication available for grain size effect on fatigue of ceramics. A study by Guin [44], on pure alumina at a frequency of 5 Hz under push-pull loading sequence, demonstrated that specimens with a grain size of 18 μm showed higher static fatigue resistance than those with a grain size of 29 μm.

2.3.6 Discontinuous propagation during stress cycling

A study of tension-tension fatigue in magnesia partially stabilized zirconia carried out by Sylva and Suresh [51] showed crack jumps or discontinuous propagation during fatigue cycling. The threshold stress intensity range for the occurrence of fatigue crack growth under tensile loads was approximately 3.4 MPa$\sqrt{m}$, almost the same value as found by Dauskardt et al [45]. A distinct aspect of the fatigue behaviour obtained was that the crack arrested after a small amount of rapid growth. The fatigue crack arrested completely after propagating a distance of between 10 to 36 μm, depending on the ΔK value. Further growth of the arrested crack could not be obtained, unless the stress intensity was raised. A model to rationalize the results obtained was proposed by these authors [51]. The threshold

stress intensity range, ΔK_{th}, for crack growth is reached when the maximum nominal stress intensity factor of the fatigue cycle, K_{Imax}, is equal to the fracture toughness of the fully stable cubic zirconia. Fatigue crack propagation occurs at a rapid rate over a distance, which is several times the width of the transformed zone. Maximum value for the distance is about five times that of the transformation zone size [52]. As the fatigue crack propagates, transformed material is left in the wake of the advancing crack. This transformed material forces the two crack surfaces together, producing crack closure and reducing the effective driving force for tensile fatigue cracking. Catastrophic failure occurs when the maximum stress intensity factor of the fatigue cycle approaches the steady state fracture toughness value.

2.3.7 Fatigue striations

Fatigue crack propagation has also been recently investigated in 3 mol% yttria-stabilized tetraganol zirconia polycrystals (3Y-TZP) by Liu and Chen [53]. Compared to MgO-PSZ, this material with a grain size of 0.38 μm has only limited transformation plasticity and relatively modest fracture toughness but very high strength. The results shows that the fatigue crack growth rate strongly depends on the maximum stress intensity factor. The relationship between the stress intensity factor and the crack propagation rate followed a power-law in which the exponent of ΔK in the crack propagation curve was reported as 21. The maximum crack growth rate obtained was approximately 40 to 65 μm per cycle (Figure 2.3).

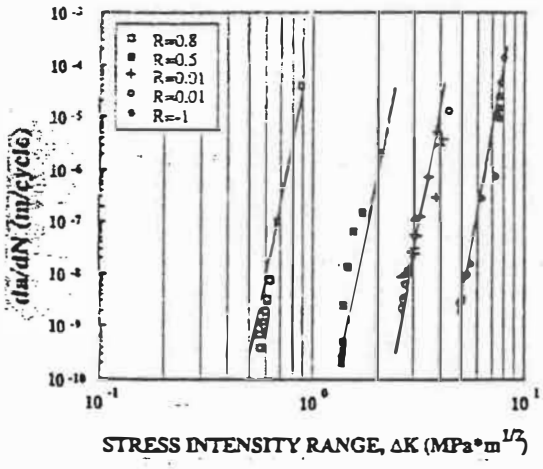

Fig. 2.3 Fatigue crack propagation rate, da/dN, as a function of stress intensity range, ΔK, in 3Y-TZP [53].

These authors observed light zones and dark bands on the fatigue fracture surface and argued that the light and dark bands were associated respectively with fatigue and overload fracture, respectively. When crack growth was entirely in the fatigue regime (i.e., in the absence of a contribution of overload propagation), they did not detect any striation-like light and dark bands [53].

They also found that the striations were present at K_{max} between 4.3 and 5.0 and that from observations made on the matching fracture surfaces, the striation features were symmetric in appearance (black on one surface corresponded to black on the other and white corresponded white).

According to the comparison made between the crack resistance curve in terms of K and the stress intensity factors at which the striations were produced, they suggested that the striations were observed only when the peak stress intensity factor exceeded the critical crack resistance, K_r, on the R-curve [53].

2.3.8 Crack closure and retardation

Dauskardt et al [54] studied fatigue crack propagation in 9 mol% magnesia-partially-stabilized zirconia using CT specimens. This material contains cubic zirconia with a grain size of approximately 50 μm with 40 vol% of lens-shaped tetragonal precipitates having a maximum size of 300 nm. A back-face strain gage was

employed to detect changes in the compliance during the fatigue crack propagation.

In this study, most test pieces were 3 mm in thickness, although specimens with thicknesses of 1.5 and 7.8 mm were also tested at room temperature in air to examine the role of through-thickness constraint. Precracking was achieved by machining a wedge-shaped notch and carefully growing the crack approximately 2 mm by fatigue under displacement control [54].

The fracture surface under cyclic loading was reported as nominally identical to that under monotonic loading. No evidence of fatigue striations or of crack arrest markings were found on the fatigue fracture surfaces [54]. The threshold for fatigue crack propagation was 50% of K_{Ic}.

Crack closure effects were also found from the response of back-face strain gage. The crack closure resulted primarily from the wedging action of fracture surface asperities. This is consistent with the progressively higher levels of crack closure seen in the higher toughness microstructures, which exhibit the roughest crack paths. Moreover, the volume expansion resulting from the transformation acts to reduce the crack opening displacements, which further encourages premature crack-surface contact on unloading [54].

Retardation immediately followed high-low block overloads. Transient

acceleration immediately followed low-high block overloads. Delayed retardation followed single tensile overloads. Such behaviour is analogous to that commonly reported for metallic materials and consistent with expectations of crack-tip shielding due to the transformation in the crack tip region. The region affected by retardation was approximately 500 μm, approximately 5 times the measured transformation zone width [54].

2.3.9 Fatigue deformation

Two distinct fatigue mechanisms, microcracking and transformation plasticity, have been identified in 3Y-TZP and 9 mol% Mg-PSZ. Liu and Chen [55] have carried out push-pull fatigue on 6 mm diameter cylindrical bars. Axial strain and radial strain were simultaneously recorded. If there are open microcracks, their presence will cause a significant change in the curvature of the hysteresis loop. By analyzing the shape of hysteresis loop of push-pull fatigue, microcracking was found to be dominant in 3Y-TZP, while transformation plasticity was more evident in Mg-PSZ. However, the proportion of these two mechanisms depends on the frequency and stress amplitude, with transformation plasticity favoured at low frequency and high stress. Generally, microcracks form in the tensile half cycle and partly close in the compression half-cycle [55].

Since a volume increase due to microcracking is not expected for

compression load and can come only from t- to m-phase transformation, and such a volume increase was observed to occur gradually during both in compression and in tension loading, therefore, transformation must have taken place both in tension and in compression [55].

2.3.10 Fatigue in non-transforming ceramics

Fatigue behaviour has also been studied in silicon nitride and silicon carbide [56], which are not transformable ceramics. Cyclic crack growth was observed in the intergranular-fracture type materials but not in the transgranular-fracture type materials, silicon carbide and HIPed silicon nitride. For intergranular-fracture type, micro-scale crack branching or crack path deflection, grain-boundary particle debonding, and crack surface asperity are considered as the factors contributing to the crack propagation.

2.3.11 Transformation associated with cyclic crack growth

Dauskardt et al [57] performed Raman spectroscopic mapping on the lateral surface of fatigue cracking region in 9 mol% MgO partially stabilized zirconia with a grain size of 50 μm. Both the fraction of transformed monoclinic phase adjacent to the crack and the width of the transformation zone varied in response to the applied loading. A decrease in the transformation zone size was observed following

a load reduction and an increase in the size of the transformation region was found associated with a single overload [57].

2.4 Fatigue study using repeat indentation technique

A low cycle fatigue study has been performed by Reece and Guin [59] on high purity alumina bioceramics with a grain size of 2 μm by using a repeated indentation technique. This technique involves making repeat indentations on the same impression. The measurements focused on identifying the number of indentations required to cause the occurrence of chipping in different fluid environments. Reece and Guin found that water was the active agent in all of the environments and that the presence of salt ions and proteins did not influence very much the fatigue behaviour of the tested materials [59].

The mechanism of fatigue cracking has been compared by Guin et al [60] for different types of fatigue tests on ceramics. Under push-pull loading, fatigue is attributed to short surface cracks. For cyclic loading tests, the fatigue crack advances as bridging ligaments are broken behind the crack tip. The cyclic loading helps to break these ligaments, either by repeated fretting, shear or crushing. For indentation tests, chipping is caused by subsurface cracks which lie and propagate in a direction parallel to the specimen surface [60].

2.5 Compression fatigue in ceramics

Ewart et al [61] performed crack propagation tests under pure compressive loads and demonstrated that a fatigue crack propagated from a notch under far-field cyclic compression in alumina. The crack initiated uniformly at the notch tip, propagated progressively at a decreasing average velocity and grew intergranularly in a plane perpendicular to the applied compressive loads.

The crack front in ceramics under cyclic compressive loads was straight in the mid-thickness regions; however, the crack grew faster near the two lateral surfaces. Thus the longest crack length was present at the lateral surfaces, rather than in the mid-thickness region, which is the opposite of typical case in metallic materials. Another distinct characteristic of the compression fatigue of ceramic materials is that a large amount of debris particles can be found on the fatigue fracture surfaces.

To explain their experimental results, these authors proposed a model to rationalize the existence of fatigue crack propagation under far-field cyclic compression in ceramics. Experimental observations [37] of the side surfaces revealed a population of grain boundary microcracks near the notch tip. These microcracks lead to a reduction in the elastic modulus in the process zone. This zone is partly shielded from the far-field compressive stress by the surrounding material which is strained elastically. The difference in the compliance within the

process zone and that outside the zone can induce residual tensile stresses during unloading. During compression loading, microcracks initiate and open. Upon unloading the compliance in the process zone will become the same as the original compliance, once all microcracks close completely. If the microcracks remain completely open, the compliance in the process zone will be less than the original compliance. In the intermediate situation which is that expected, the microcracks close partially, and the compliance shows a slight decrease. This compliance change in the process zone results in residual stresses during the fatigue cycling.

More experimental results and explanations on the crack propagation under fully compressive loads have been reported by Suresh and his co-workers [61]. They observed that grain boundary microcracks were introduced during loading, and suggested that compliance was changed by the grain boundary microcracking. The compliance change creates a tensile stress upon unloading and this residual tensile stress promotes fatigue crack propagation. The start of the fatigue cracking is observed on the side surface during unloading. Acoustic emission signals coming from both the surface and the interior reveal that fatigue crack growth occurs during the unloading portion of the compression fatigue cycle [61].

The reported results strongly indicate an important role of grain boundary microcracks. In the compression fatigue of brittle solids, the fracture occurs along grain boundaries, and after the first compression cycle, grain boundary microcracks

are observed on the two lateral surfaces at the notch-tip [61]. Some other results indirectly support the grain boundary microcracking in the fatigue cracking. When a notched single crystal of alumina is subjected to uniaxial cyclic compression, no fatigue cracking is obtained. Fatigue cracking is also not observed in notched plates and rods of glass [61] in which no grain boundaries exist.

Experiments conducted by Kossowsky [36] on hot-pressed Si_3N_4 and on Si_3N_4-reinforced with 10, 20 and 30 vol% SiC whiskers showed that the pull-out of whiskers in the ceramic composite occurs under fully compressive loads, which strongly indicated the existence of residual stresses at the notch-tip.

In compressive fatigue cracking of brittle materials, debris commonly forms on the fatigue fracture surface [37,61]. The effect of this debris on fatigue cracking must be considered. Ewart and Suresh [37] argued that the debris particles was not the primary cause of fatigue under far- field cyclic compression, but the wedging effect of debris could lead to some further crack propagation. This argument seems contrary to the result that fatigue crack growth distance is larger when debris is removed from the fatigue crack tip.

In transforming ceramics, the residual stress induced by martensitic transformation from the metastable tetragonal to the monoclinic phase also plays an important role. A finite element analysis carried out by Suresh and

Brockenbrough [61] on magnesia partially stabilized zirconia showed that the zone of maximum tensile stress did not occur directly ahead of the notch-tip, but was situated at an angle of approximately 20° from the notch plane and at a distance of approximately 0.02 mm ahead of the notch-tip. The accompanying test gave results which agreed well with this analysis. After one cycle of fatigue, crack extended about 0.02 mm at an angle of 20° to the notch plane.

CHAPTER 3 ZIRCONIA

Stabilized zirconia are attractive ceramics because of the stress-induced transformation which results in a considerable improvement in their fracture toughness. Since an important portion of the present was performed on yttria-stabilized zirconia, a review of the stabilization of zirconia, of phase relationships in zirconia and of yttria stress-induced transformation will therefore be important in understanding the mechanical behaviour of the stabilized zirconia.

3.1 Phase relationship in pure zirconia

Zirconia, ZrO_2, named baddeleyite in honour of Baddeley who first found this mineral on Ceylon (Sri Lanka) in 1890, is often obtained by the thermal decomposition of zirconium salts (e.g., zircon, $ZrSiO_4$) [62]. There exist three solid phases in pure zirconia at atmospheric pressure: the monoclinic phase (the m-phase), the tetragonal phase (the t-phase which has the rutile structure), and the cubic phase (the c-phase which has the fluorite structure).

The phase relationship in zirconia-yttria system is shown in Figure 3.1. The critical temperatures of transformations of pure zirconia can be found by tracing a vertical line at yttria-0% composition. On cooling, the liquid phase of zirconia will transform to the c-phase at 2710°C. The transformation from the c- to the t-phase

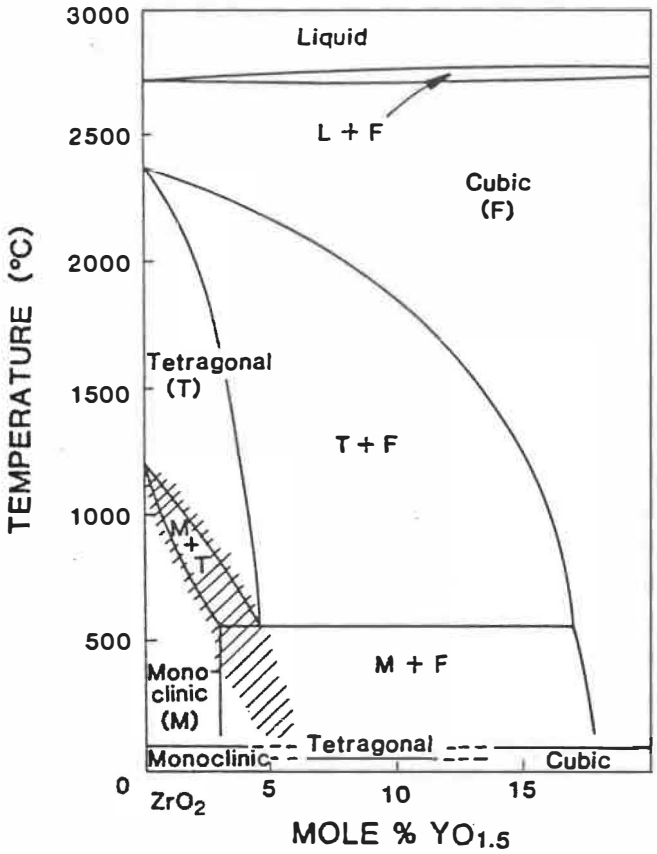

Fig. 3.1 Zirconia-rich end of the yttria-zirconia phase equilibrium diagram [76].

occurs at 2370°C. The transformation from the t- to m-phase occurs between 1000 and 850°C. The transformation from the t- to m-phase is martensitic in nature, and a volume expansion of approximately 3.5% results from this transformation [63].

Wolten [64] investigated the t- to m-phase and the m- to t-phase transformations in pure zirconia using high temperature diffractometry. He found that the transformation from the t- to m-phase on cooling and from the m- to t-phase on heating occurred in a region of temperature rather than at a critical temperature (Figure 3.2). He also found that compared to the transformation from the t- to m-phase during cooling, the transformation from the m- to t-phase on heating occurred at higher temperature region (it started at 1000°C and finished at 1120°C). As a result, a considerable hysteresis could be observed for a cycled transformation from the t- to m-phase and from the m- to t-phase (Figure 3.2).

Maiti et al [65] studied pure polycrystalline zirconia and found that the tetragonal to monoclinic phase transformation occurred at the region of 850 to 1000°C, the amount of transformation was tempreature-dependent in this region of 150°C. However, the monoclinic to tetragonal phase transformation occurred at 1170°C without significant temperature-dependence.

Smith et al [66] studied the tetragonal to cubic phase transformation by using high temperature X-ray diffraction. They found that only the cubic (200) peak was

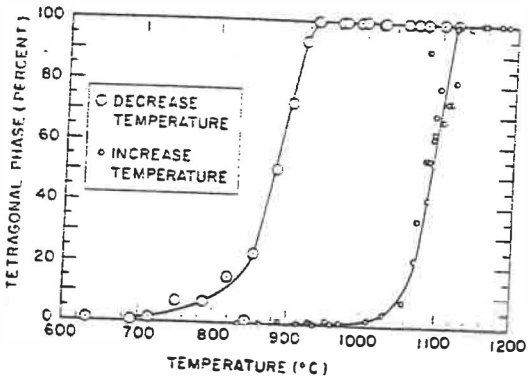

Fig. 3.2 The amount of transformed particles and the corresponding temperature for monoclinc-tetragonal transformation in zirconia [64].

present at temperatures above 2285°C and that the transformation was reversible with a hysteresis less than 15°C.

Solid-state transformation temperatures will vary with the purity, thermal history, and crystal perfection of the material. By using Raman spectroscopy, Perry et al [67] investigated the transformation temperatures from the t- to m-phase in pure zirconia and yttria-partially stabilized zirconia containing less than 20 wt% of yttria. The transformation both from the t- to m-phase (on cooling) and from the m- to t-phases (on heating) occurred in a range of temperature. For single crystals of pure zirconia, the transformation from the m- to t-phase (on heating) started at 1179°C and finished at 1190°C; whereas, the transformation from the t- to m-phase (on cooling) started at 1000°C and finished at 950°C without detectable retained tetragonal phase.

By using thermal expansion measurements, Adams et al [68] observed that the transformation from the m- to t-phase occurred from 1179 to 1190°C and the transformation from the t- to m-phase occurred from 1048 to 920°C.

The transformation of the monoclinic to tetragonal phase is martensitic in nature, which was first suggested by Wolten [64]. Clear metallographic evidence for this martensitic transformation has been presented by Bansal et al [69,70]. In the transformation temperature range, holding at any temperature will not change the

relative proportion of the two phases. The crystal structure analysis confirmed that the transformation had been diffusionless [64]. These features also indicate that the t- to m-phase transformation is martensitic.

3.2 Stabilization of zirconia

Because of its low strength and poor toughness [71], pure zirconia is often alloyed with yttria, magnesia, calcia and other oxides to improve its properties. Early studies on alloyed zirconia showed that under standard atmospheric pressure, the transition temperatures from the cubic to the tetragonal phase and from the tetragonal to the monoclinic phase are lowered by addition of the oxides [72]. If sufficient alloying elements are added to zirconia, the transformation temperatures both from the cubic to the tetragonal phase and from the tetragonal to the monoclinic phase can be decreased below room temperature. The single phase cubic zirconia, obtained at room temperature by the addition of a stabilizer, is commonly referred to as fully stabilized zirconia (FSZ). Either single phase metastable tetragonal zirconia or a mixture of metastable tetragonal and cubic phase zirconia, obtained in the same manner, is referred as the partially stabilized zirconia (PSZ). When a suitable stabilizer of metallic oxide is added into zirconia, the metallic atom will replace zirconium atom, which introduces deformation into the crystal structure, inhibits normal transformations, and results in stabilization of zirconia.

When yttria, Y_2O_3, is added to zirconia, additions of 8 mol% and 3 mol% will be sufficient to obtain fully stabilized and partially stabilized zirconia, respectively [73,74].

Stabilization, the process and theory for obtaining tetragonal zirconia polycrystals (TZP) below the equilibrium transition temperature of the t- to m-phase, can be achieved primarily with the addition of oxide stabilizers (such as magnesia, calcia, yttria etc). The stabilization will also be influenced by the grain size and cooling rate.

By using hydrous gel precipitation techniques, Winnubst et al [75] studied stabilization effects of yttria. The gel were dried at 390 K and calcined at 820 K for two hours to obtain the powders. The powders, with a grain size less than 0.2 μm, were isostatically pressed at 400 MPa and sintered at 1380 to 1660 K. Finally they obtained 100% tetragonal phase for zirconia containing 4-8.9 mol% yttria.

This result is in considerable conflict with the equilibrium phase diagram given by Scott [76]. In that phase diagram, the occurrence of the cubic phase is inevitable, if zirconia-yttria alloys contain more than 4 mol% of yttria. This cubic structure will transform into t'-phase on cooling (t'-phase is the tetragonal phase which is non-transformable even under stress), provided that the cooling rate is sufficient high. As a result, a mixture of the t- and t'-phases will be obtained at room

temperature instead of only the t-phase.

Lio et al [77] studied zirconia containing 2 mol% of yttria. The powders were pressed at 150 MPa and sintered at 1550°C in air. They obtained 100% tetragonal structure. According to Scott's phase diagram [76], 2 mol% yttria-zirconia has a completely t-phase structure at the sintering temperature, and this t-phase will be retained after cooling. As a result, 100% tetragonal zirconia polycrystal will be obtained. Lio also found that the stabilized tetragonal phase did not transform to the monoclinic phase even at a temperature as low as liquid helium temperature (4.2 K). Nonetheless, the monoclinic phase became present in this material after aging at 300°C for several hours. The authors argued that the Ms (martensitic transformation starting temperature), if it exists, would be lower than the liquid helium temperature.

The effect of the sintering temperature on the stabilization of partially stabilized zirconia containing a low percentage of yttria was investigated by Gupta et al [78]. After sintering at 1400 to 1450°C, nearly 100% tetragonal phase was obtained. There was a sudden decrease in the tetragonal phase and a corresponding increase in the monoclinic phase, when the sintering temperature was raised to and above 1500°C. This behaviour was believed to be associated with a change in grain size. A large amount of t-phase was observed for stabilized zirconia with a small grain size, while a large amount of monoclinic phase was observed for that with a

large grain size.

Different degrees of stabilization at the specimen surface and in the bulk of specimen were also observed. Specimens with an apparent high proportion of t-phase was observed to have a larger amount of monoclinic phase at the surface than in the bulk [78].

Pujari and his coworkers [79] investigated effects of the sintering process on ZrO_2 powder containing 3.5 mol% yttria with a grain size of 0.94 μm (crystallite size was 0.02 to 0.03 μm). The green specimens were isostatically pressed at 310 MPa. Sintering was carried out at a pressure of 830 MPa for 2 to 5 hours at 1400°C. A pressureless sintering was performed at 1550°C for 3 hours. They found the pressureless-sintered specimen contained a much larger amount of m-phase than the pressure-sintered specimen. On grinding, both types of specimens showed partial t- to m-phase transformation; however, the transformation in the pressure-sintered specimen was much less than in the pressureless-sintered specimen. This may be attributed to the volume expansion associated with the transformation from the t- to m-phase. Residual compression in the pressure-sintered specimens will then tend to inhibit the transformation.

3.3 Phase relationships in zirconia-yttria system

A good understanding of the phase equilibria in the zirconia-yttria system (Figure 3.1) is fundamental to the prediction of phase transformation in yttria-containing zirconia.

Complications in phase relationship research arise out of large temperature range which is encountered in establishing a complete phase diagram. Very long times will be required to reach equilibrium at relatively low temperature, and inhomogeneity of composition will result in less reproducible results fot the phase relationships.

Srivastava et al [80] carried out a literature review of phase relationships in the zirconia-yttria system. Since then, several new studies have appeared. Scott [76,81] studied the phase relationship in the zirconia-yttria system in the high zirconia content region [76] as well as in the yttria-rich region [81]. Pascual et al [82] studied subsolidus phase equilibria. Ruh et al [83] studied phase relationships at low yttria contents.

Some conflicting results were reported in these studies. The phase diagram by Scott [76] has been considered to be the most reliable diagram, in particular, the region of low yttria which is that of great interest.

The most important feature of the zirconia-yttria phase diagram established

by Scott is the decrease in the temperature of the tetragonal-monoclinic phase transformation with increasing yttria concentrations in the region in which the yttria content is less than 5 mol%. This phenomenon has important implications both for the design and for use of stabilized zirconia. In most engineering service conditions, the transformation of the monoclinic to tetragonal phase is very undesirable. Therefore, the upper temperature limit for some engineering applications will be determined by the transformation temperature of the monoclinic to tetragonal phase.

The c- to t-phase transformation could also be martensitic in nature [76]. Above 2200°C, zirconia containing 6 mol% yttria will have a single phase cubic structure and will undergo a diffusionless transformation to the tetragonal phase on quenching. At 2000°C, the equilibrium is a two-phase mixture of tetragonal phase containing 2 mol% yttria and cubic phase containing 8 mol% yttria. On quenching, this tetragonal phase transforms to the monoclinic phase and this cubic phase to the tetragonal phase. At 1400°C, the equilibrium again involves the same two phases. On quenching, the tetragonal phase transforms to the monoclinic phase, but the cubic phase, since it contains sufficient yttria, remains cubic at room temperature [76]. The phase diagram established by Scott [76] indicates that 14 mol% of yttria in the cubic phase is sufficient to obtain fully stabilized zirconia.

3.4 Stress-induced martensitic transformation

When the critical temperature is attained, zirconia tends to transform. This transformation in stabilized zirconia is inhibited by a stabilizer because of the greater activation energy required. This extra activation energy can be supplied by an external inducement, such as applied stress. In stabilized zirconia, stress-induced transformation has been observed and well studied.

The stress induced martensitic transformation in yttria partially stabilized has been studied by measuring the difference in the ratio of t- to m-phase both on tensile and on compressive surfaces of bending specimen in ZrO_2-3 mol%Y_2O_3 at 200°C [84]. Using localized electron beam heating, Heuer et al [85,86] studied the transformation induced by thermal mechanical stresses. They found that transformation occurred and was reversible.

Some studies revealed that some preconditions must be satisfied to permit the stress-induced transformation to occur [87-89]. A threshold stress must be exceeded to induce the transformation, its typical value in zirconia has been shown to be the order of 450 MPa [87,88]. A short report [89] on stress-induced transformation under compression at high temperatures in yttria (4 mol%) partially stabilized zirconia showed that some critical stress and/or strain must be reached to induce the transformation from the metastable tetragonal to the monoclinic phase. The critical values of stress and strain were respectively the yield stress and 1%. A tensile stress was more favourable to the transformation than a compressive stress,

because more transformed particles were found on the surface stressed in tension than that stressed in compression in a pure bending test.

3.5 Non-transformable tetragonal phase

When partially stabilized zirconia is processed by plasma spraying in which rapid cooling can be achieved, a nonequilibrium tetragonal phase containing a high yttria concentration can be obtained [90]. This structure has been termed as t'-phase (denoted as "non-transformable tetragonal phase"), because it will not transform on cooling to room temperature. The t'-phase is unstable with respect to diffusion at high temperatures. Further phase separation into the equilibrium high-yttria cubic and low-yttria tetragonal phases can be expected with increasing exposure time at high temperature [90,91].

By using TEM in ZrO_2-Y_2O_3 alloys containing 3 to 5 mol% Y_2O_3 prepared by arc-melting, Sakuma [92] has studied the morphology of the non-transformable tetragonal phase. Heuer et al [93] have analyzed the c- to t'-phase transformation criteria.

3.6 Transformation toughening in ceramics

Although transformation toughening can occur in several ceramics [64,94],

zirconia is generally chosen as a typical example. The understanding of transformation toughening is primarily based on studies of stabilized or partially stabilized zirconia.

Partially stabilized zirconia is metastable and transformation from the metastable t-phase to the monoclinic phase can occur under extrinsic inducement [74]. The toughness of the partially stabilized zirconia (PSZ) is higher than that of other zirconia structures [71,74]. It is generally accepted that the increased fracture toughness can be attributed mainly to a process of stress-induced martensitic transformation from the t-phase to the m-phase which occurs in the region of the crack tip [95,96]. Moreover, not only an applied mechanical stress, but also stresses resulting from polishing, grinding [97] or even high voltage electron beams [85,86] can induce the transformation.

Shimbo and his coworkers [74] studied strengthening and toughening associated with metastable t-phase in yttria-stabilized zirconia by correlating the strength and toughness with the volume of the t-phases before and after bending. This study confirmed the occurrence of stress-induced transformation and transformation toughening effects.

Relationships between the toughness and the volume fraction of t-phase have been studied on yttria-stabilized zirconia [89]. The materials with larger volume

fraction of the metastable tetragonal phase gave higher flexural strength and higher fracture toughness values, and a larger amount of phase transformation was obtained for a higher t-phase content than for a lower t-phase content. The transmission electron microscopy study of Porter and Heuer [98] on stress-induced transformation in magnesia-partially stabilized zirconia suggested that only those particles located around crack tip transformed under stress inducement and that the primary contribution to the toughness was associated with the number of transformed particles within the transformation zone adjacent to the propagating crack. A study by Swain [99] also showed that fracture toughness in partially stabilized zirconia increased linearly with increasing transformed zone depth. All of these results indicate that it is the transformation process that toughens these materials rather than only the presence of tetragonal particles.

3.6.1 Crack closure model for transformation toughened ceramics

Many studies have proposed mechanisms by which the martensitic transformation toughens the ceramic materials. McMeeking and Evans [52] proposed a crack closure model. The residual compression strain field associated with volume expansion during stress-induced transformation tends to squeeze the two crack surfaces together at the crack tip (Figure 3.3). According to their model, the increased toughness could be estimated from the crack tip stress intensity change induced by the volume expansion of transformed material. For mathematical

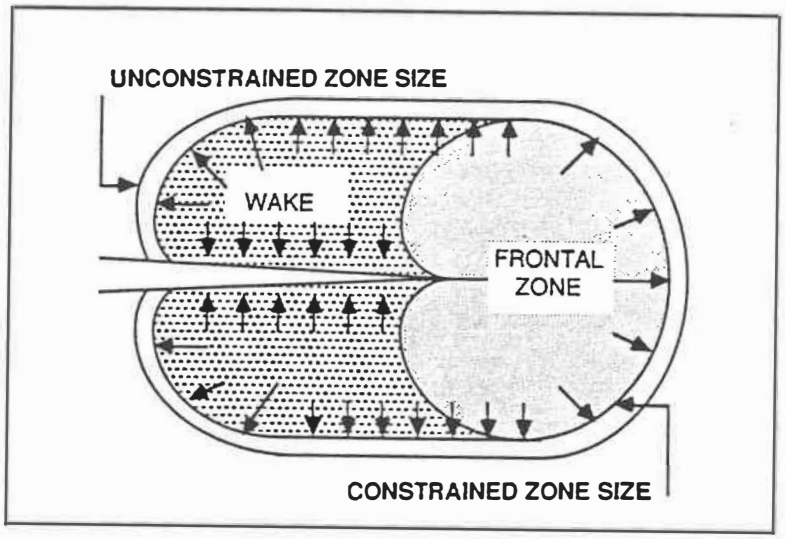

Fig. 3.3 Illustration of the stresses that arise in a dilatant transformation zone. Once the zone extends behind the crack tip, stresses in this zone will act in a direction to close the crack [130].

simplification, it was assumed that this transformation was irreversible and that the portion of the crack which extends into transformed materials was larger than 5 times the thickness of the transformation zone on the fracture surface. According to this model, the increment of fracture toughness introduced by the stress-induced transformation will be proportional to the strain associated with the martensitic transformation, the volumetric fraction of transformed particles and the square root of the transformation zone size. A weakness in this model is the assumption of irreversibility of the transformation [85,86,100].

3.6.2 Energy dissipation model for the transforming ceramics

The reversibility of the martensitic transformation in transforming ceramics has been reported [85,86,100]. This reversibility has been taken into account in a model proposed by Lange [101]. The transformation triggered by stress will absorb strain energy and will relieve the stress and strain concentration. It is assumed that only those particles which remain transformed after the crack advances will contribute to the dissipation of the non-recoverable energy and that the transformation zone size is as large as the particle size [101]. The transformation zone size, Young's modulus, and the volumetric fraction of retained transformed particles will contribute proportionately to the increment of fracture toughness. The problems with this model are associated with the difficulty in the direct calculation of the toughness increment, the equality between the transformation zone and

particle sizes, the non-consideration of the variation of the volumetric fraction of transformed particles with depth in going from the crack tip into the matrix and the non-consideration of the contribution of re-transformed particles.

3.7 Determination of the transformation zone size

The transformation zone size is believed to be a key factor influencing toughening. The determination of the transformation zone size has been widely studied, however, a realistic determination of this size remains difficult. Transmission electron microscopy, X-ray diffraction, and Raman microprobe techniques have been employed in this determination.

Based on X-ray intensity calibrations in stabilized and unstabilized ZrO_2 systems, Adam [102] studied the relationship between the integral X-ray intensities of the monoclinic and the tetragonal phases. The relationship was expressed as

$$I_m(111) + I_m(11\bar{1}) = I_t(111) \qquad (3.1)$$

where $I_m(111)$, $I_m(11\bar{1})$, and $I_t(111)$ are the integral intensities for the (111), $(11\bar{1})$ peaks of the monoclinic phase and the (111) peak of the tetragonal phase, respectively. The integral intensities for the monoclinic phase were obtained after

martensitic transformation; whereas, the intensity for the tetragonal phase was obtained before the transformation during which the tetragonal phase totally transformed into the monoclinic structure.

Garvie and Nicholson [41] have studied a more common situation in which some tetragonal particles remained untransformed. According to their study, the fraction of the monoclinic structure transformed from the tetragonal phase will be

$$X_m = \frac{I_m(111) + I_m(11\bar{1})}{I_m(111) + I_m(11\bar{1}) + I_t(111)} \qquad (3.2)$$

where X_m is the volume fraction of transformed monoclinic particles. This equation has become a basic relation employed in the calculation of the transformation zone size on the fracture surfaces of zirconia.

Raman microscopy has been employed in characterizing the amount of transformed particles in ceramics [103-105]. In order to perform a quantitative analysis, the relationship determined by Garvie and Nicholson [41] has been adapted to Raman microscopic analysis by Clarke and Adar [107], where a similar calculation is required for measurement of the volume fraction of transformed particles.

Assuming that the fraction of the transformed tetragonal particles, X_{trans}, is constant and equal to 1 (100% transformation obtained) to a depth a below the fracture surface and that the fraction of the m-phase outside the transformation zone remains the same as that before fracture, Kosmac et al [42] proposed the following expression for the transformation zone size:

$$a = \frac{\sin\theta}{2\mu}\ln\frac{X_{bulk} - X_{trans}}{X_{meas} - X_{trans}} \qquad (3.3)$$

where X_{trans} is the fraction of the tetragonal particles which transform within this zone, and is assumed equal to 1; X_{bulk} is the fraction of the monoclinic phase before the fracture test; X_{meas} is the measured fraction of the monoclinic phase after the fracture test, calculated by using expression (2-1); θ is the diffraction angle which is approximately 15°; μ is the absorption coefficient. The transformation depths calculated using this expression were between 1 to 4 microns for different ceramic materials, which is considered to be reasonable compared to the direct observations performed by transmission electron microscopy by Porter et al [98].

Nevertheless, it should be noted that there are some unrealistic simplifications in this model. First, during the integration for the intensity of the monoclinic phase, the sum of X_{trans} and X_{bulk} should be used over the transformation depth instead of only X_{trans}, because both X_{trans} and X_{bulk} will contribute to the measured diffracted

intensity of monoclinic particles. Secondly, the assumption that X_{trans} is equal to 1 is not consistent with the experimental results [107,108]. The fraction of transformed tetragonal particles across the transformation zone should not be a constant but rather a function of zone depth.

Based on similar considerations as Kosmac but without the assumption that X_{trans} is equal to 1, Garvie et al [109] proposed a two wavelength method which permits to calculate the transformation zone size without knowing X_{bulk}. They obtained an equation

$$\frac{X_{m1}}{X_{m2}} = \frac{1 - \exp(\frac{-2a\mu_1}{\sin\theta_1})}{1 - \exp(\frac{-2a\mu_2}{\sin\theta_2})} \qquad (3.4)$$

where X_{m1} and X_{m2} are the monoclinic fractions measured using two X-rays with different wavelengths; μ_1 and μ_2, the absorption coefficients for the two X-rays, respectively, and θ_1 and θ_2, the corresponding diffraction angles.

Also realizing that the fraction of transformed tetragonal particles is not a constant, Mori et al [108] considered this fraction to be a function of the depth and defined the transformation zone size, d, as the depth at which the monoclinic phase

fraction is equal to 1/e (e is the base of natural logarithms) times that at the fracture surface. This study gave the transformation zone a more realistic depiction but did not give the real distribution of the transformed tetragonal particles over the depth of the transformation zone [108].

Using transmission electron microscopy, Porter et al [98] directly observed transformed particles in the vicinity of cracks which were introduced by microhardness indentation. This method is tedious and time consuming. It is also difficult to employ in measuring the transformation zone size on a fatigue fracture surface, because of the difficulties in cutting a small foil containing the fatigue crack tip and in preventing the entire foil from breaking off during polishing.

Another feasible method to determine the transformation zone size is the Raman microprobe technique. The monoclinic and tetragonal phases of zirconia have distinct and characteristic Raman scattering spectra [107,110], which makes it possible to distinguish these two phases and to calculate their fractions from the spectra obtained [107,108]. The results indicated that even when the laser beam was positioned on the crack itself, some of the zirconia remained in the tetragonal structure. On the fracture surface only about 20% of the t-phase transformed. Even in the centre of the indentation where more transformed particles were expected, less than 40% of tetragonal particles had transformed. This technique can detect the amount of transformation either on a lateral surface or on the fracture surface but

cannot directly detect the transformation into the depth.

PART II EXPERIMENTAL PROCEDURE AND RESULTS

CHAPTER 4 MATERIALS AND SPECIMEN PREPARATIONS

Any material for engineering applications will be subjected to variable loads. By employing advanced materials processing technology, such as, hot isostatic pressing (HIP) and using ultra fine powders, some promising ceramics have been developed for engineering applications. Comprehensive studies of mechanical behaviour of high performance ceramics have become important for evaluating their service capabilities and for improving their mechanical properties. Since fatigue resistance is one of the important mechanical properties, the present study focused on the fatigue behaviour of hot isostatically pressed zirconia stabilized with 3 mol% yttria (3 mol% yttria-stabilized tetragonal zirconia polycrystals, 3Y-TZP), of zirconia-toughened alumina, and to a less extent of a few other ceramics. The study of fatigue crack propagation behaviour of 3Y-TZP also led to the consideration of the effect of stress-induced transformation on this behaviour.

4.1 Materials and specimen preparation of 3Y-TZP

Hot isostatically pressing is a very effective method to reduce defects, such as pores, and eventually to improve material properties. The HIPed 3Y-TZP used in the present study was ordered from and manufactured by Gorham International Inc. The material obtained has the composition presented in Table 4.1.

Table 4.1 Material composition of 3Y-TZP (wt%)

ZrO_2	Y_2O_3	Al_2O_3	SiO_2	Fe_2O_3	Na_2O
balance	5.15	0.067	0.002	0.003	0.008

The specific gravity was 6.08 g/cm^3, the grain size was highly homogeneous and approximately 0.25 μm. The specimens were sintered and then HIPed by Gorham International Inc. The sintering procedure employed by the manufacturer was as follows: ramp from room temperature to 700°C under vacuum in 0.5 hour, hold for 0.5 hour, fill with nitrogen to a pressure of 0.45 MPa; then ramp from 700 to 1400°C in 70 minutes, hold for 1 hour, and furnace cool.

The HIP cycle employed immediately after sintering was as follows: ramp from room temperature to 700°C under vacuum in 0.5 hour, hold for 0.5 hour, then ramp to 1500°C in 1 hour while simultaneously pressuring to 150 MPa under nitrogen, hold for 1 hour and then furnace cool.

4.2 Processing of zirconia-toughened alumina

Compared to the HIP technique, cold isostatic pressing is much easier to perform, but does not improve material properties as strongly as the former technique. Cold isostatically pressed zirconia-toughened alumina (ZTA) was

employed in the present study. Three different compositions were chosen to study the fatigue behaviour of ZTA. Their compositions are presented in Table 4.2.

Table 4.2 The compositions of zirconia-toughened alumina (wt%)

Material	Al_2O_3	ZrO_2 (MgO)	ZrO_2 (m)
AM	85	15	-
AN	80	20	-
AZ	90	5	5

The average diameter of the different powders, in angular morphology, was approximately 0.6 μm. Zirconia (MgO) indicates zirconia-magnesia alloy which consisted of approximately 93.1(wt)% ZrO_2, 3.61% MgO and 1.7% HfO_2. Zirconia (m) indicates pure zirconia in the monoclinic structure.

Plaster-cast green specimens of ZTA were prepared by Heberto Balmori [111]. The processing employed by him were as follows: prepare slurry of 65 wt% of solid power and 35 wt% liquid solvent which contained 1.9 vol% of Darvan 7. Deionized and double distilled water was employed in preparing the liquid solvent. Milling in rotatory miller with balls made up of partially stabilized zirconia (PSZ). Pour the slurry prepared into plaster mould to fabricate rectangular plate. Remove the mould in 3 H then dry in air for 24 H. For reducing porosity in specimens, cold isostatic pressing was employed at 350 MPa. Calcination at 400°C for 1 h, to reduce

the porosity produced by polymer which were burned out during the calcination, another isostatic pressing at 350 MPa was employed.

The green specimens were manually cut to a proper size by the present author in order to fit into the cylindrical chamber of an Autoclave cold isostatic press. Cold isostatic pressing (CIP) was performed at 350 MPa. Right after the CIP process, specimens were calcinated in a calcination furnace. The calcination process was as follows: the temperature was gradually increased to 400°C in 4 hours, held for 1 hour, then gradually cooled to room temperature in 4 hours. Another identical CIP process followed the calcination. The sintering processes finally applied to the specimens were as follows: the temperature was gradually increased to 1600°C in 5 hours and held for 1 hour, then cooled to 1200°C at 13°C/min. This temperature was held for 10 min, then cooled at 3°C/min to room temperature. According to the diagram of ZrO_2-MgO system, there is little or no solubility of MgO in monoclinic zirconia up to the tetragonal transformation temperature. Hold at any temperature below 1400°C will lead MgO precipitate, therefore, specimens were held at 1200°C for only 10 min to obtain an even temperature distribution.

Specimen machining, grinding, and cutting, were conducted on a Clausing machine. The transverse advance rate and feeding rate of the operation disk employed in grinding were 20 μm and 5 μm, respectively. The feeding rate was 10 μm for cutting. Specimens were annealed at 1200°C after machining.

The details of specimen geometries employed will be given in those chapters which deal with the particular type of the experiment.

CHAPTER 5 COMPRESSION FATIGUE OF YTTRIA-STABILIZED TETRAGONAL ZIRCONIA POLYCRYSTALS AND ZIRCONIA-TOUGHENED ALUMINA

Investigations have shown that stable fatigue crack growth in polycrystalline alumina can occur on notched specimens under far-field compressive cyclic loads [37]. This result provides a convenient method to study fatigue behaviour in ceramics, since it permits to avoid most of the difficulties associated with the brittleness of the specimen during fatigue. Compression fatigue can also be used to introduce a sharp crack in a ceramic specimen in order to perform more complicated fatigue cracking studies.

5.1 Experimental procedures

Far-field compression fatigue was performed in 3 mol% yttria-stabilized tetragonal zirconia polycrystals (3Y-TZP), zirconia toughened-alumina (ZTA), magnesia-stabilized zirconia and pure alumina by employing single edged-notched specimens. The specimen geometry is schematized in Figure 5.1. A notch was introduced with a circular diamond low-speed saw which produced a notch tip radius of 0.17 mm in the specimens. The fatigue tests were carried out at room temperature on an Instron electromechanical testing machine (model 1362). Constant amplitude compressive load cycling was applied to the specimens at a frequency of 0.5 Hz. The nominal stress ratios of minimum to maximum nominal

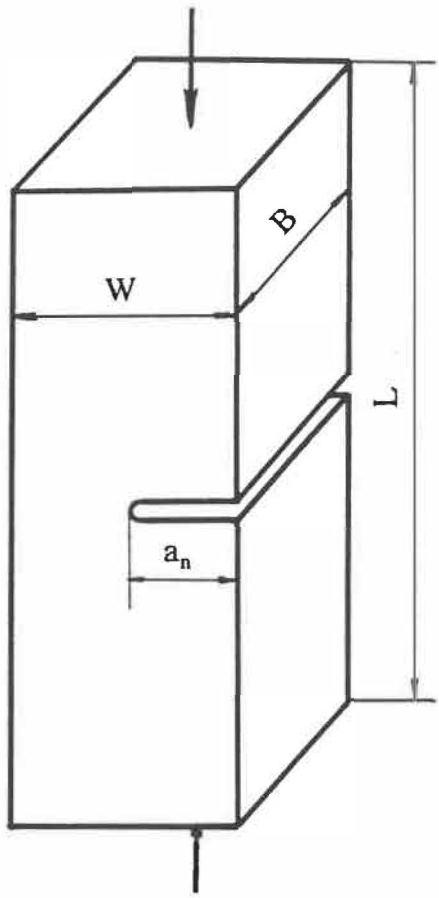

Fig. 5.1 Specimen geometry of 3Y-TZP and ZTA for compression fatigue. Exact dimensions are given in the related sections.

stresses were chosen in order to prevent the specimens from moving in the test fixture as well as to create as a large a variation in the stress intensity at notch tip as possible without fracturing the specimens. Crack growth was monitored on the side surface using a travelling microscope.

5.2 Compression fatigue of 3Y-TZP

Yttria-stabilized zirconia can give a good combination of strength and toughness by virtue of its transformable structure, fine grain size, and advanced processing techniques employed. Studies on compression fatigue was carried out on this material employing specimens with a length of 40 mm, a width and a thickness of 5 mm. The notch depth employed was 2.5 mm.

5.2.1 Crack propagation under far-field compressive cycling

The crack profiles observed on the lateral surfaces as a result of compression fatigue are shown in Figure 5.2. Although some spalling sites can be seen, the crack is straight and well-defined. Observations of the crack on the lateral surface in the SEM show that the crack appears to be opened in the unloaded condition and that the separation between the fracture surfaces is quite wide and easily observed. Debris particles are seen to have been extruded out into the notch, on the lateral surface as well as in the spalls produced at these surfaces. Figure 5.2 also shows that

the fatigue crack has initiated in the form of a notch which becomes increasingly sharp as the crack propagates.

The relationships between the fatigue crack length and stress cycle number are presented in Figure 5.3. This relationships indicate that the crack growth occurred in a reasonably continuous manner. The compression fatigue crack propagation behaviour can be characterized by three different stages. First, the fatigue crack length increases approximately linearly with increasing cycle number. As the crack propagated away from the notch tip, a gradual decrease in crack propagation rate was noted. Finally, the crack propagation stopped, and a plateau in the curve of crack length, a, versus number of cycles, N, was obtained for each specimen.

The cycle numbers required for fatigue crack initiation and for obtaining the plateau on the crack length versus cycle number curve are different for each specimen. The crack initiation might depend mainly on nominal stress, and the crack length at which propagation terminated appeared to depend both on the radius of the notch and on the nominal stress.

After the far-field compressive stress cycling, the maximum compressive stress was increased by 25 MPa (about 5%) for two specimens in order to verify the overload effect on compressive fatigue cracking behaviour. This load increment led

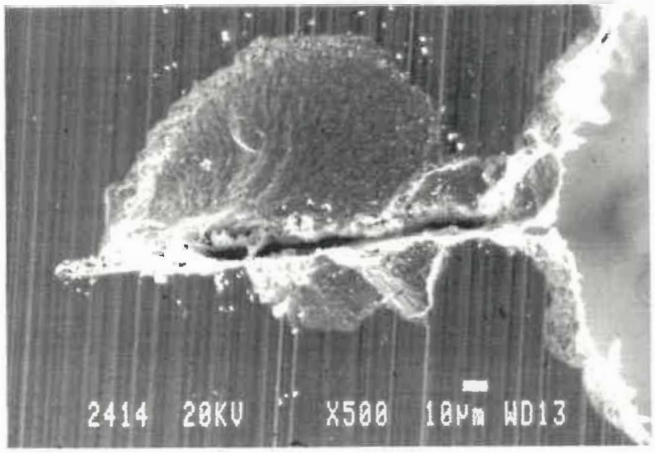

Fig. 5.2 Crack profile observed on the lateral surface with the notch tip at the right. Spalls are observed on the lateral surface.

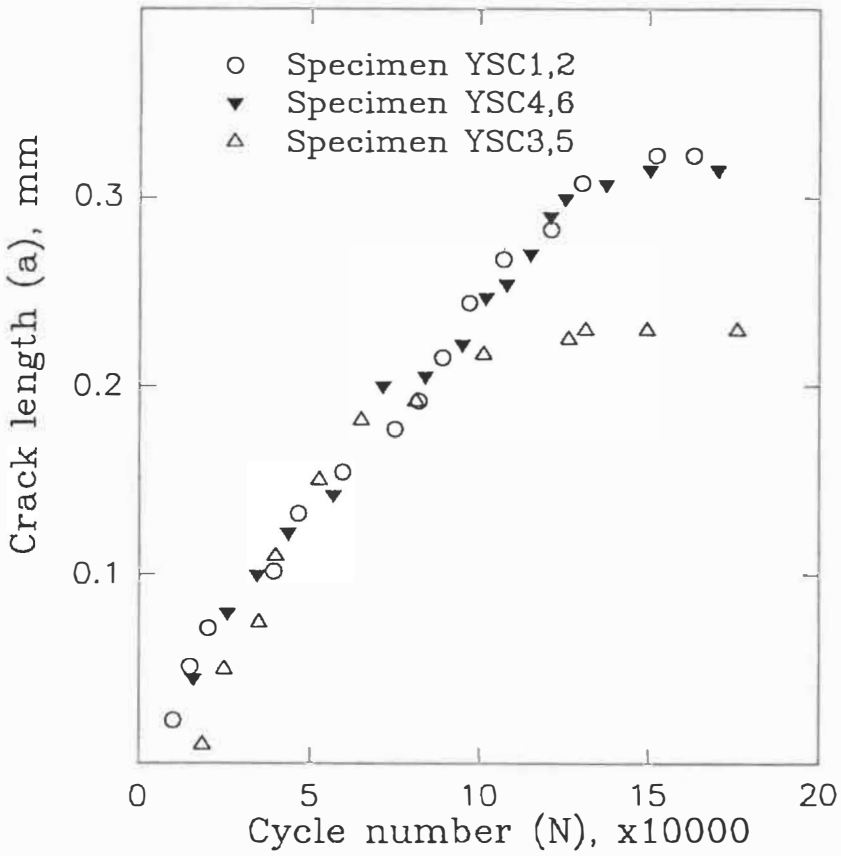

Fig. 5.3 Fatigue crack length, a, measured from the notch-tip as a function of the compression cycle number, N, in 3Y-TZP.

to catastrophic failure of these specimens which split longitudinally. These results indicated that for the specimen geometry employed HIPed 3Y-TZP is very sensitive to the critical cyclic stress. When cycled below the critical stress, hardly any fatigue cracking occurred. Slightly above this critical stress, the specimen would fracture in a catastrophic manner.

A study on a fully bainitic steel [37] showed that the amplitude of the first compression cycle had a pronounced influence on the total distance of crack propagation under far-field cyclic compression. An increase by a factor of three in the stress in first cycle alone led to an increase in the fatigue crack length by a factor of fourteen. However, the threshold value of stress for crack growth in ceramics is very critical, therefore, the overload approach can not be used easily to obtain larger amounts of fatigue crack growth in ceramic materials.

5.2.2 Fracture surface observations

Compressive fatigue specimens were fractured under four point bending. The typical compressive fatigue crack observed on the fracture surface is shown in Figure 5.4. Along the notch front across the specimen thickness, several spall sites can be seen. In the region of these spalls, the fatigue crack propagated a longer distance than in the neighbouring region. Observations indicated that the spalls were produced after the crack had propagated in that region, since the spalls observed

on one surface were not present at the matching site on the opposite surface, and the spalls never extended to the fatigue crack tip. The fractographic observations indicated that the crack length in the interior region during compression fatigue was approximately two times shorter than that near the lateral surfaces. The boundary between the fatigue crack and the zone of final fracture was a winding frontier rather than a straight interface. Different initial crack origins resulted in the formation of ridge lines parallel to the crack propagation direction.

At large magnifications, four different zones could be discerned on the compressive fatigue fracture surface (Figure 5.5). The first zone was narrow (approximately 10 μm in width) and contained some debris particles. This zone, in which the fatigue crack initiated, was immediately adjacent to the notch tip. A large number of aggregates, most containing at least a dozen grains, could be seen to have been extruded or cleared out of the first zone into the notch (Figure 5.6). In some cases, the debris particles which had been cleared out of the crack appeared to match neighbouring depressions on the fracture surface (Figure 5.7), which suggests that these debris particles were detached and cleared out of the fracture surface.

The second zone was characterized by important debris accumulation on the fracture surface (Figure 5.6). This debris consisted of individual grains as well as small aggregates. Grains as well as some of the debris particles in this zone started

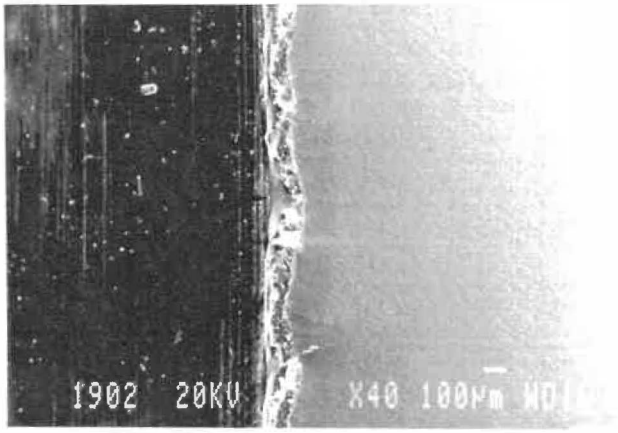

Fig. 5.4 Shape of the fatigue crack seen on the fracture surface with the notch surface and the final fracture surface on the left and right, respectively. Spalls on the compression fatigue surface are indicated by arrows.

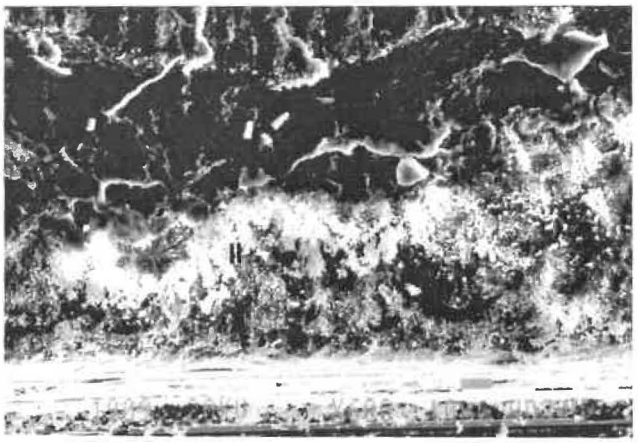

Fig. 5.5 General morphology of fracture surface presenting four different zones indicated by I to IV (propagation towards the top).

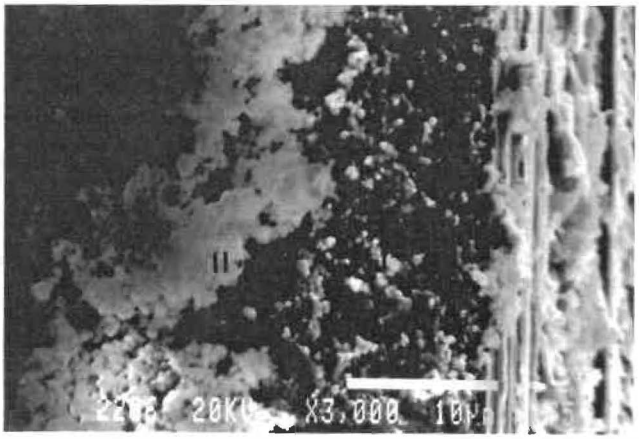

Fig. 5.6 Fatigue crack initiation has occurred in zone I, which is relatively free of debris. Zone II corresponds to a region of lightly-packed debris which has accumulated.

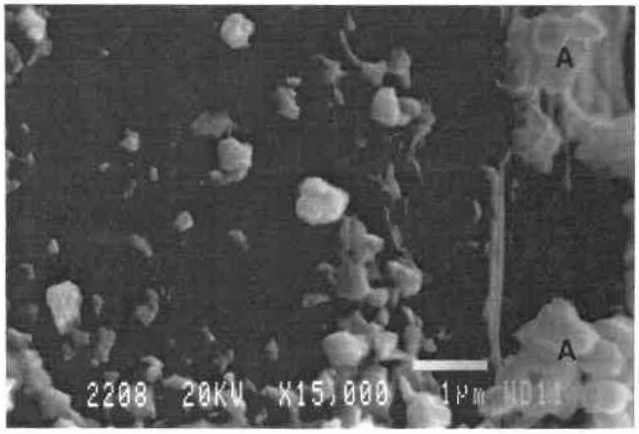

Fig. 5.7 Grain agglomerates, A, have been extruded out of zone I into the notch tip.

to present round edges (Figure 5.8). Their aspects indicate that it was the contact and friction effects during fatigue cycling that deformed these particles, removed the sharp edges, and broke them into smaller debris particles which accumulated on the fracture surface.

The third zone contained flattened "cakes" formed apparently by debris particles having been pressed together by the cyclic compression stresses (Figure 5.9). At the start of this zone, the flattened cakes were small, with a morphology similar to that of the aggregates, but increased in size as the crack propagated. On the flattened cakes, line markings were present both approximately parallel to (Figure 5.9) and approximately perpendicular to (Figure 5.10) the crack propagation direction. Some of the cakes simultaneously presented both sets of line markings, some of which at times appeared curved (Figure 5.11). The fourth zone was very narrow (approximately 5 to 10 μm in the width, the order of magnitude of the expected width of transformation zone ahead of the crack tip) and was situated immediately adjacent to the final fracture zone on the fracture surface. This last zone was free of the flattened cakes but not completely free of debris particles (Figure 5.12).

The region of final fracture (i.e., the fracture surface produced during the subsequent K_{Ic} test) presented primarily intergranular facets (Figure 5.13). On the final fracture surface, the grains were homogeneous in size and well-defined.

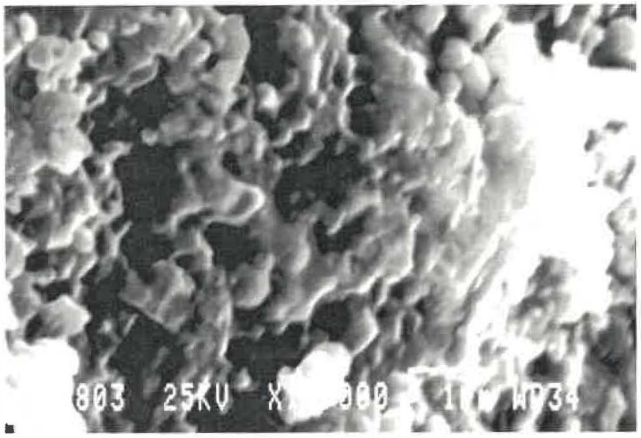

Fig. 5.8 Grains seen at the beginning of zone II with edges rounded by deformation and fretting.

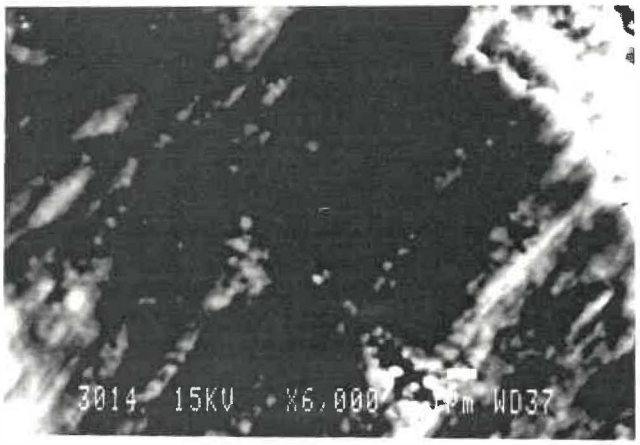

Fig. 5.9 Curved line-markings seen on a cake of debris near the start of zone III. The shape of some of the grains within this cake can still be observed.

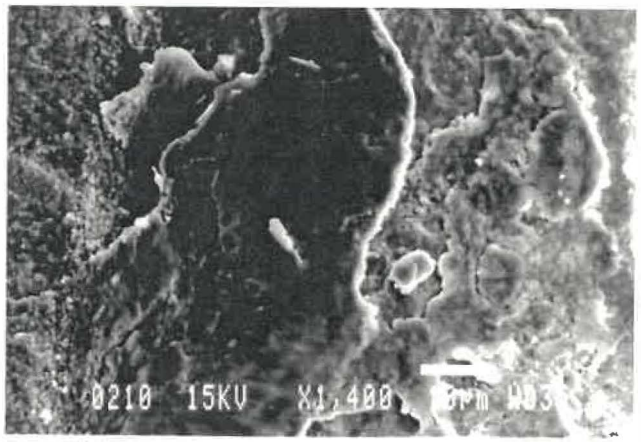

Fig. 5.10 In zone III, the debris has been tightly compressed into "cakes" which present lines marking produced by rubbing.

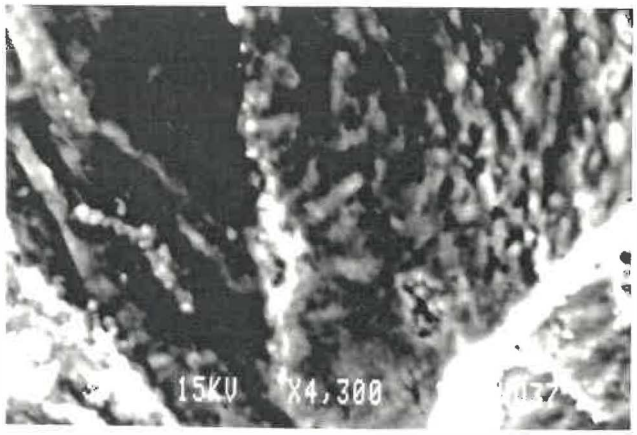

Fig. 5.11 Two sets of line markings seen on a flattened cake in zone III (propagation towards the top).

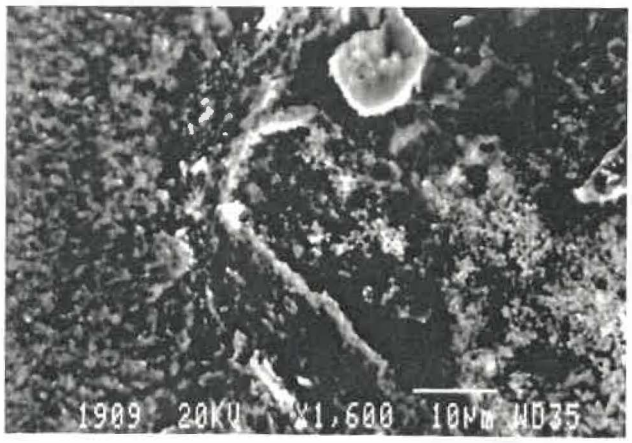

Fig. 5.12 Zone IV, indicated by arrows, is immediately adjacent to the crack tip and relatively free of debris. The width of this zone is only 5 to 10 μm (propagation towards the left).

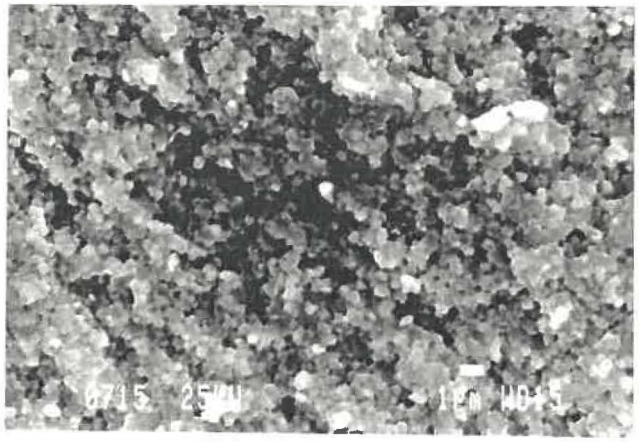

Fig. 5.13 Homogeneous grain size and intergranular fracture with presence of some aggregates on the region of final fracture surface produced during the K_{Ic} test.

Although there were a large amount of debris on the fatigue fracture surface, the final fracture surface was completely free of debris particles. Intergranular fracture mode was dominant on this part fracture surface, but some occasional transgranular fractures were also observed in the present study (Figure 5.14). An investigation by Michel and his coworkers [23] on the fracture of single-phase metastable tetragonal zirconia suggests that the cleavage plane in that material is either {001} or {110}. Because of the very fine grain size, in the present study, the crystallographic details were difficult to resolve by scanning electron microscopy, and it was even difficult to clearly show the presence of cleavage facets.

5.2.3 The formation of the four zones on the compression fatigue fracture surface

Tensile residual stresses and crack closure effects can be expected to have the opposite influence during compression fatigue propagation. Tensile residual stresses will be a driving force for crack propagation, but crack closure will tend to inhibit crack propagation. The fractographic observations clearly showed the role of crack closure in influencing the fatigue propagation under far-field compression. The average crack growth rate decreased as the crack propagated away from the notch, which can be attributed to the crack closure become increasingly evident and important in going from the first zone to the start of the fourth zone on the fatigue fracture surface. Any factor increasing the crack closure will decrease the crack

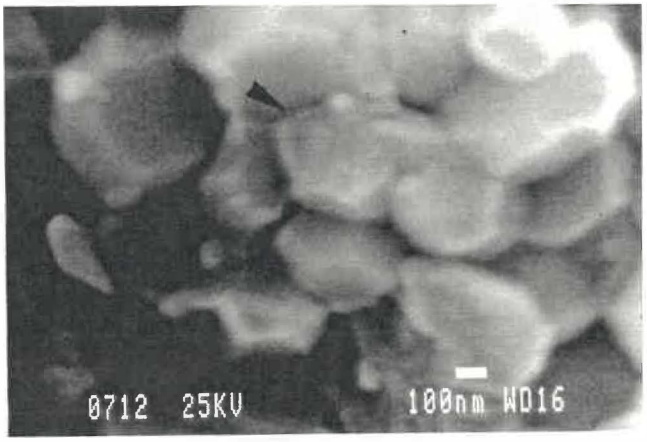

Fig. 5.14 Occasional apparently transgranular fracture (arrows) in the region of the final fracture surface.

propagation. In the region where spalls formed and where debris have been extruded out of the fracture surface, decreased crack closure and increased crack propagation are expected locally. The larger amount of fatigue crack propagation near the spalls can also be explained by this argument. At the crack tip near the lateral surface, spalls can easily form and the debris can be easily extruded out, therefore, the crack closure will be less strong locally. As a result, the fatigue crack propagates a larger distance near the lateral surface than away from these surfaces.

The four distinct zones on the fracture surface are associated with differences in the amount of crack closure and of debris movement. At the beginning of fatigue cycling, the debris are easily extruded out of the fracture surface, which results in a relatively clean zone. As the crack propagates, fewer and fewer debris particles are extruded out of the fracture surface. As a result, the debris particles are packed together on the fracture surface, which forms the second zone. In this zone, some of packed debris present rounded edges, which indicate the occurrence of fretting and crack closure.

The important amount of crack closure which occurred in the third zone is very evident fractographically. The compression associated with this closure presses the debris particles tightly together into large flattened cakes, in which the grain features are no longer evident, indicating the considerable deformation and fretting to which these debris particles have been subjected. The observations indicate that

the line markings on these flattened cakes form behind the crack tip, as a result of the high local stresses associated with crack closure. The aspects and orientations of the lines suggest that the fracture surfaces slide somewhat on each other parallel to these lines, which therefore indicate shear stress components acting in the fracture plane. These stresses act both parallel and perpendicular to the crack propagation direction. Such shear stresses acting parallel to the crack propagation direction are also suggested by the debris particles being displaced away from their initial sites. These shear stresses possibly resulted from the premature contact of the fracture surfaces. The contact effects forced the fracture surfaces to rub together as the local stresses become more compressive.

The observations indicate that crack propagates by forming a small notch at the prenotch tip. The depth of this small notch extends and its tip becomes increasingly sharp as the fatigue cycling continues. This was particularly clear for the results obtained from the zirconia-toughened alumina which will be described in section 5.3. The amount of particles being chipped off at the notch-like crack tip decreases progressively, because the open surface at this notch-like crack tip decreases during compression fatigue. Finally, the compression fatigue crack with a process zone at its tip stops propagating. The final fracture which was carried out after compression fatigue by using four-point bending revealed this process zone on the fracture surface which has been recognized as the fourth zone. This zone presents some grains which are surrounded by microcracks along their grain

boundaries, which indicates that in addition to transformation residual stress, microcracks along grain boundaries developed at the notch-like crack tip during compression fatigue.

5.3 Compression fatigue of zirconia-toughened alumina

Zirconia-toughened alumina (ZTA) is a promising ceramic material, and Balmori [111] proved recently that cold isostatic pressing was a relatively easy technique to reduce some of the defects and to improve material properties. To examine its fatigue properties, compression fatigue was carried out on cold isostatically pressed alumina toughened with zirconia.

5.3.1 Compressive fatigue crack propagation in ZTA

The same loading train was used for zirconia-toughened alumina as for 3Y-TZP, but the notch length was 3.6 mm and the minimum and the maximum nominal stresses were -250 MPa and -50 MPa, respectively.

Specimens of three different compositions (defined in Table 4.2) designated as AM, AN, and AZ were fatigued under far-field cyclic compressive loads. All three materials showed fatigue crack propagation (Figure 5.15), but the crack growth behaviour differed greatly. Crack initiation in the AM material occurred late, the

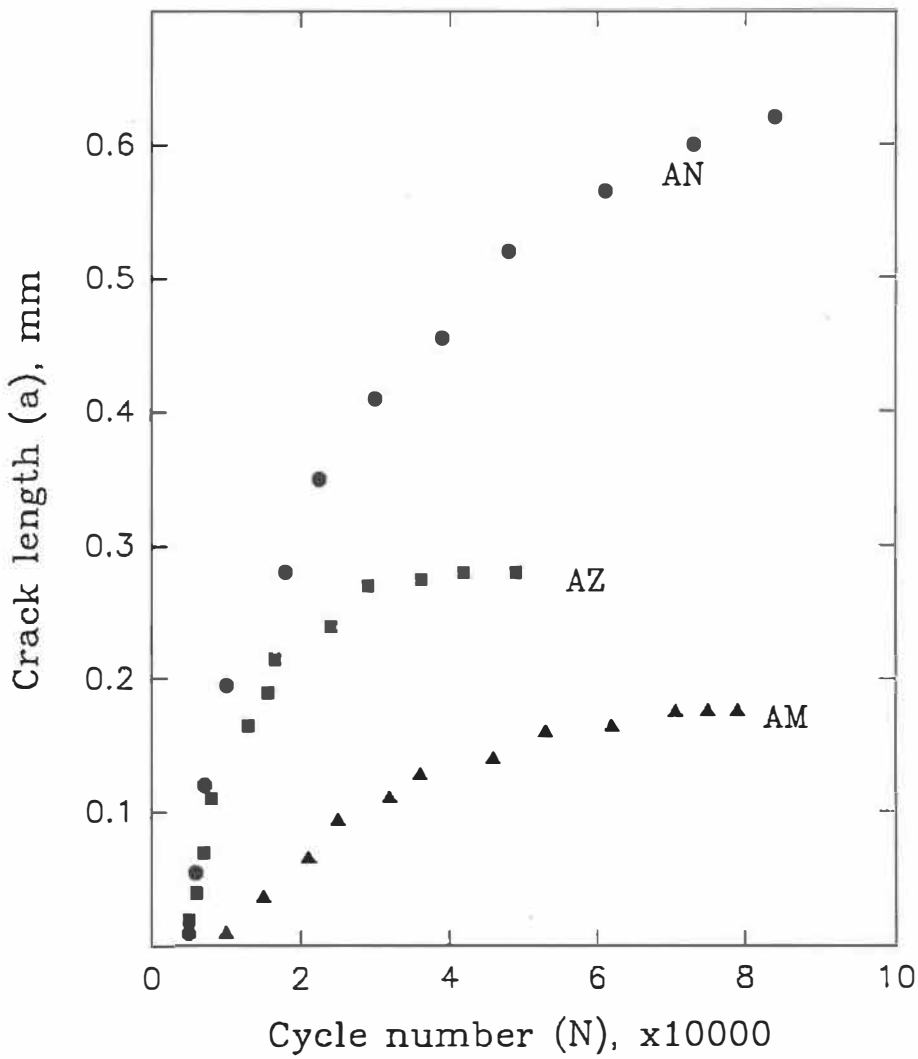

Fig. 5.15 Fatigue crack length, a, measured from the notch-tip as a function of the number of compression cycles, N, in ZTA. AN, AZ and AM refer to the different compositions of ZTA specimen employed.

crack propagated more slowly, and amount of fatigue crack propagation observed was also much shorter than the other two materials. This result indicated that the AM material showed the highest resistance to crack propagation of these three ceramics. The AN material showed the largest crack propagation of these three materials. The AZ material was very similar to the AN material in the crack initiation stage, but the crack arrested much earlier in the AZ material.

5.3.2 Observations on the lateral surface during compression fatigue

The crack profile and cracking behaviour observed at the lateral surface in zirconia-toughened alumina exhibited considerable similarities with those observed for yttria-stabilized zirconia. Clusters of debris were observed at the notch tip during crack initiation and propagation (Figure 5.16). The fatigue crack observed on the lateral surface appeared filled with debris, which is an indication that debris also play an important role in the compression fatigue behaviour of ZTA.

Large spalling sites were also observed on the lateral surface with clusters of debris particles extruding out of the crack into the spalls (Figure 5.17). This debris must have been extruded out of the crack after spalling. If it has been extruded out prior to the spalling, it would have been removed from the lateral surface together with the spalls as these fractured off. This suggests that the debris forms quite continuously and is extruded out of the crack surface. Figures 5.16, 5.17, and 5.18 also

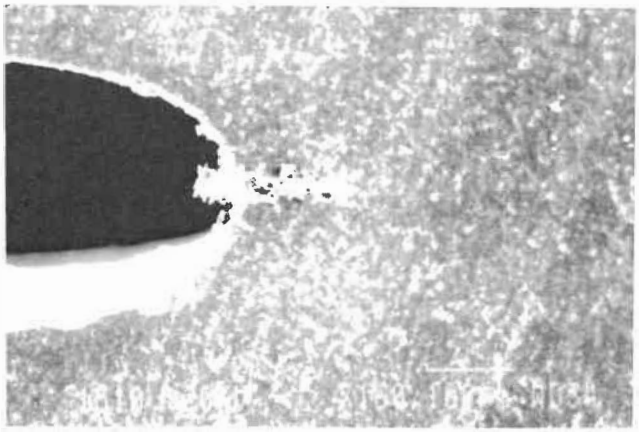

Fig. 5.16 Fatigue crack profile of specimen AMC1 (the ZTA-AM material) shows packing of extruded debris at the notch-tip.

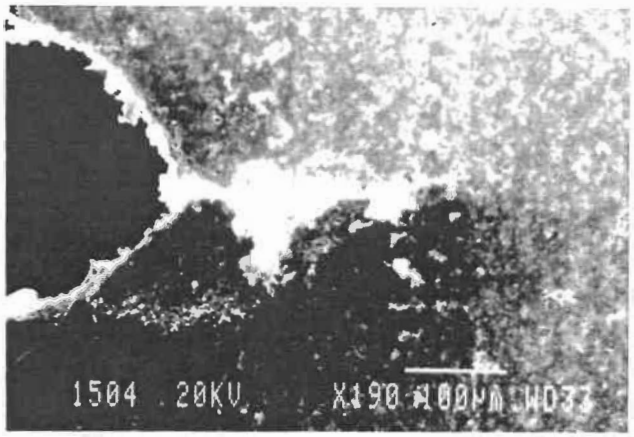

Fig. 5.17 Fatigue crack profile of the ZTA-AZ material shows extruded debris on the lateral surface

show the final crack lengths obtained after compressive fatigue at the same amplitudes of load for the different materials. The crack propagation obtained was greatest in the AN material and shortest in the AM material. The initial compressive cycling produced a crack in the form of a sharper notch at the pre-notch tip and this "notch-crack" progressively became sharper as it propagated.

5.3.3 Fatigue fracture surface observations of ZTA

Typical features of the fatigue fracture surface are shown in Figure 5.19. Compared to 3Y-TZP, only three different zones with distinct aspects can be observed. The first zone, next to the notch, is relatively clean, and presents only a few individual debris particles. The second zone shows mainly aggregates. Each of these aggregates contains a number of grains. In some regions of this zone, cakes of flattened particles have started forming near the third zone, separating the second zone into two sub-zones. In this regions, the fractography is closer to those observed in 3Y-TZP in which four different zones were obtained. The aggregates in the cakes observed in ZTA, however, were more loosely compacted than those observed in the cakes in 3Y-TZP.

The third zone in Y-TZA had a width of approximately 20 μm and consisted of a depression on the two opposite fracture surfaces. It is similar to, although considerably larger than, the fourth zone observed in 3Y-TZP which has a width of

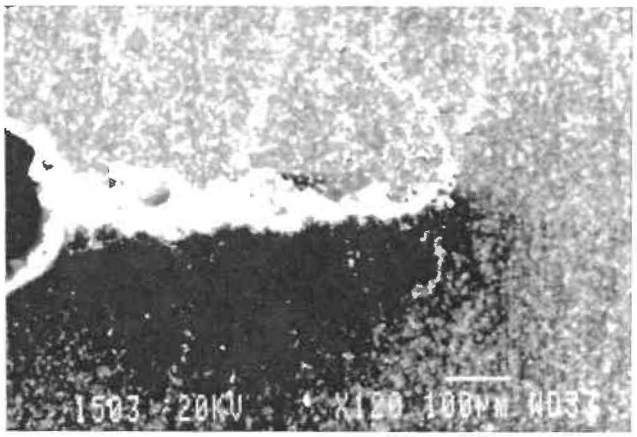

Fig. 5.18 The crack seen on the lateral surface of the ZTA-AN material at the end of the compression fatigue test.

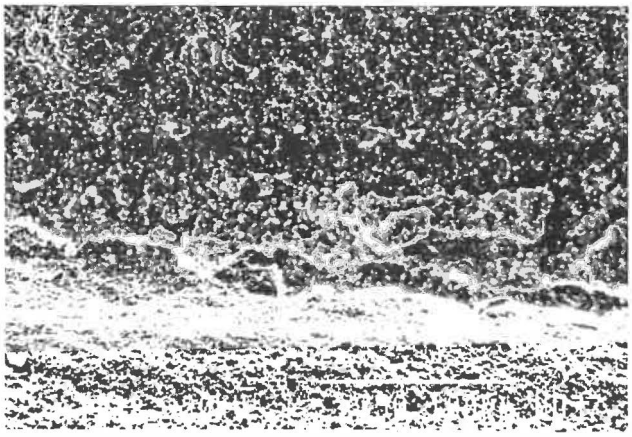

Fig. 5.19 Fracture surface produced by compressive fatigue in the ZTA-AZ material (crack growing towards the top). Three zones are associated with the compression fatigue. The middle zone which contains the agglomeration of debris particles is higher than the first and third zone and in some regions can be separated into two sub-zones.

the order of 5 to 10 μm.

Tensile fatigue was performed on a specimen of the AM material. At the boundary of compression fatigue-tensile fatigue fracture surfaces, some features of compressive fatigue can be seen (Figure 5.20). There are particles with a somewhat compressed flattened aspect, which indicates that the portion of fracture surface was produced in compression fatigue. This zone also usually contains some small debris. These small detached debris particles can be seen more clearly in the region near the boundary of compression fatigue-tensile fatigue surfaces. The very small size of some of these particles indicates that some grain size particles have been fractured into smaller debris particles. Most of the particles seen in the third compression fatigue zone in this figure have rounded edges. The presence of such round particles indicates the occurrence of some fretting and rubbing.

Figure 5.21 also presents the boundary between the compression fatigue zone (the bottom part) and the tensile fatigue zone (the top part). Compared to the top part, a number of particles of different sizes are loosely packed on the fracture surface in the bottom part, indicating that the particles have been crushed, rubbed and moved from somewhere to their present location during compressive cycling. Compared to the features shown in Figure 5.20, the debris particles in Figure 5.21 show less of a fretting effect, which preserved clearer edges of the particles.

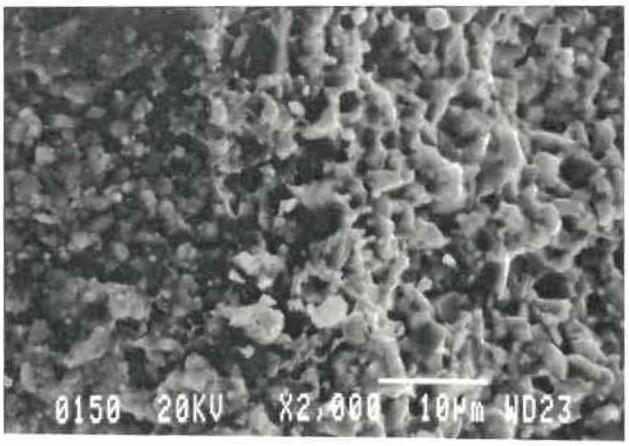

Fig. 5.20 The boundary between the compression and tension fatigue fracture surfaces (the ZTA-AM material, crack propagation towards the right).

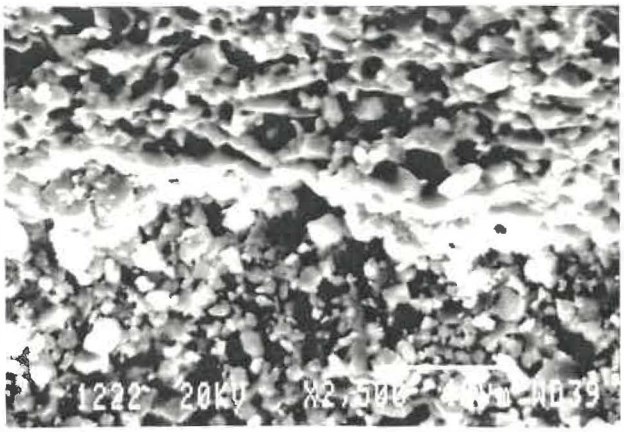

Fig. 5.21 A portion of the boundary between the fracture surfaces produced by compressive and tensile fatigue (the ZTA-AM material, crack propagation towards the top) shows that the tensile fatigue crack initiated on a plane at different height from that of the compression fatigue crack. The compressive fatigue surface presents debris particles which are finer than the typical grain size.

In ZTA, there existed more pores where particles could take refuge, therefore, the grains could not be greatly pressed by the crack closure effect. As a result, the aggregates seen on the fatigue fracture surface were not as flattened as in zone III of the compression fatigue fracture surface of 3Y-TZP.

5.4 Compression fatigue in other ceramics

Compression fatigue tests were also performed on several other ceramics. Prenotched specimens of pure alumina with a grain size of 15 μm were tested under cyclic compression at a frequency of 0.5 Hz. The specimen dimensions were a thickness of 5 mm, a width of 10 mm, and a length of 30 mm. The notch length for all specimens was 2.5 mm. Various peak nominal stresses were employed for different specimens, which were from -100 to -200 MPa, the R-ratio was 10. No fatigue cracking was observed at the notch tip on the lateral surface. Specimens either sustained a very large cycle number without breaking at a low nominal stress or broke abruptly by extending the notch plane through the thickness of specimen. Due to the brittleness of these specimens, grinding of the two ends for obtaining better parallelism was difficult to perform. Therefore, the failure in obtaining fatigue crack propagation could be attributed partly to the poor parallelism between two end surfaces of the specimen and partly to the large grain size and the brittleness of this material.

The fracture surface observations showed clear intergranular facets immediately next to the prenotch tip. Debris particles, which are a common feature of compression fatigue, were only observed locally (Figure 5.22). At large magnification, some transgranular fracture could be observed occasionally in some large individual grains (Figure 5.23). This transgranular fracture presented a terrace-like topography (Figure 5.24), a characteristic feature of transgranular fracture of alumina [24,25]. This terrace-like aspect should be the result of cleavage occurred alternately between the basal and prismatic planes.

Notched specimens of magnesia-stabilized zirconia with a grain size of 10 μm was also tested under cyclic compression at a frequency of 0.5 Hz. The specimen dimensions were a thickness of 5 mm, a width of 10 mm, and a length of 25 mm. The notch length for all specimens was 2.5 mm. The peak nominal stresses employed for different specimens were from -80 to -120 MPa; the R-ratio was also 10. This material contained a large amount of pores and loosely packed agglomerates. As a result, the particles were easily detached from the prenotch tip during stress cycling. The prenotch tip changed its shape by forming a large and more porous zone, instead of transforming into a sharper notch and into a crack (Figure 5.25). Migration of particles from the notch tip to the notch during the stress cycling could be seen clearly to have occurred.

The present author provided assistance to Eric L'Esperance of Ecole des

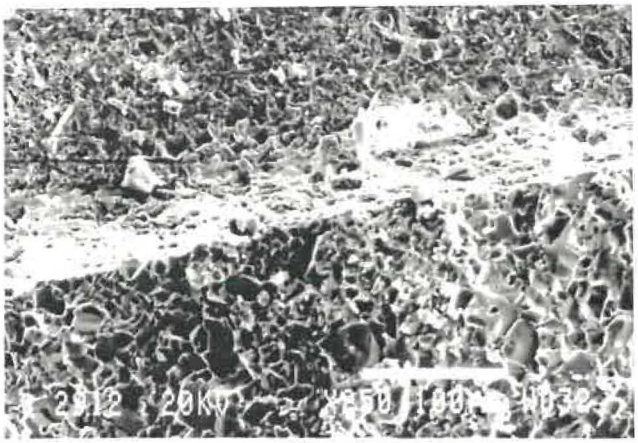

Fig. 5.22 Compression fatigue fracture surface produced in Al_2O_3 (notch is on top).

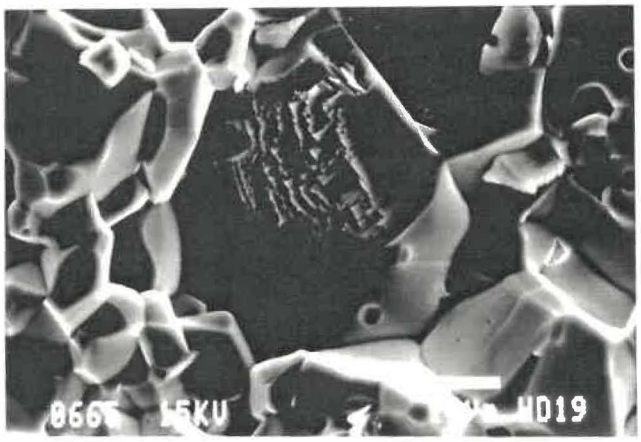

Fig. 5.23 Final fracture surface in Al_2O_3 showing the occurrence of terrace-like transgranular fracture in large grain.

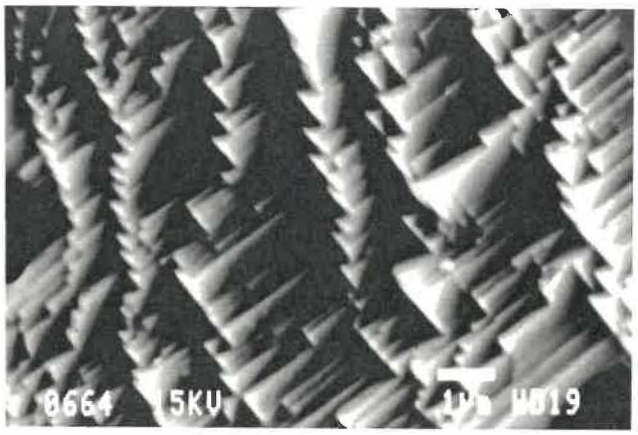

Fig. 5.24 The terrace-like transgranular facets observed in Al_2O_3 at large magnification.

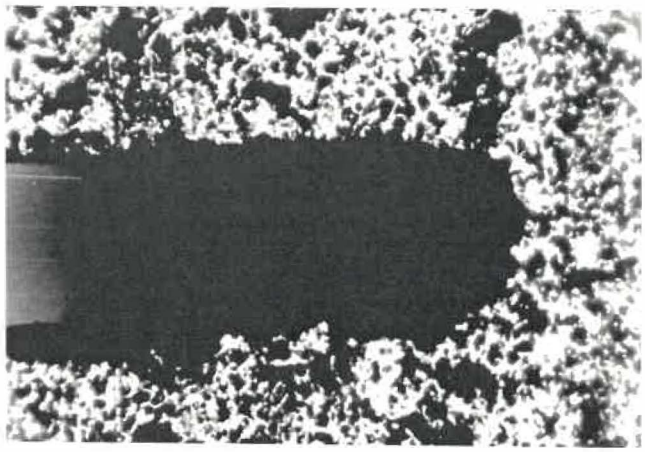

(a)

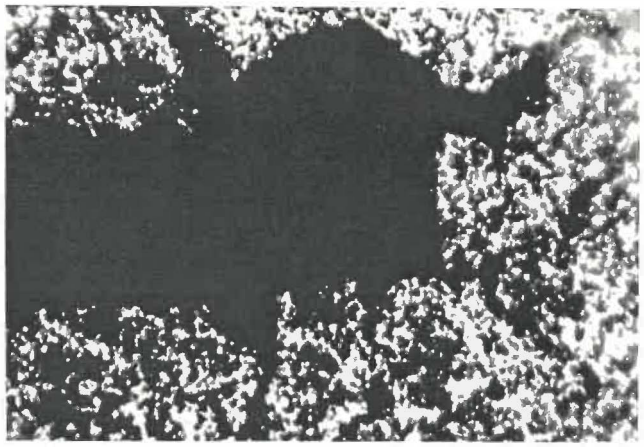

(b)

Fig. 5.25 Change of the profile of notch tip produced by compression fatigue ring. (a) before compression fatigue, (b) after compression fatigue, the porous Mg-PSZ material shows no major fatigue crack at the notch tip but instead presents loosened particles.

Mine de St-Etienne during his study at Ecole Polytechnique for performing compression fatigue tests on prenotched specimens of SiALON which consists of AlON, SiC, SiAlON, and Al_2O_3. Specimen dimensions were a length of 42 mm, a thickness of 5 mm, and a width of 7 mm. The length of prenotch was 3 mm.

Observations at the notch tip during stress cycling was performed employing a video camera and a travelling microscope. Particles were observed to be projected radially from the notch tip to the notch surfaces as soon as the stress cycling started. The speed of the particle projection was so high that the particles were observed on the video tape to fly out of the notch tip. The particles which flew out were especially numerous during approximately the first 20 cycles. This striking manner of particle ejection can be considered as an extreme case of the migration of particles during compression fatigue.

CHAPTER 6 FRACTURE TOUGHNESS MEASUREMENTS

Although various techniques have been employed in different investigations, there is no standard technique to determine the fracture toughness of ceramic materials at the present time. As a result, measurements obtained in different studies are not always easily comparable. Therefore, the determination of the fracture toughness of ceramics may still be considered as a challenge in characterizing their mechanical properties.

By means of the compression fatigue studies described in the previous chapter, we were able to obtain a sharp precrack, which allowed us to obtain reliable fracture toughness measurements. This further permitted the study of factors influencing the toughness values. Different techniques and specimen geometries have been employed in the present study. The results showed considerable variability, in particular, in comparing toughness results obtained without first employing a sharp precrack with those obtained on specimens with a sharp precrack.

6.1 Fracture toughness measurements employing four point bending

A notch can be easily introduced into ceramic specimens. Many earlier fracture tests, therefore, were performed on specimens containing a notch rather

than a precrack. The fracture toughness of 3 mol% yttria-stabilized tetragonal zirconia polycrystal (3Y-TZP) was also estimated on notch specimens in the present study. The notch was produced with a diamond saw and had a radius of 0.17 mm. The tests were performed in four point bending employing the same geometry as for the four point bending fatigue tests. These tests on the notched specimens gave a K_{Ic} fracture toughness value of 10.4 MPa$\sqrt{m}$.

Since a notch cannot be considered as a real crack, three specimens precracked in compression fatigue were fractured under four point bending. The K_{Ic} values measured on these specimens were 5.0, 5.3 and 5.5 MPa$\sqrt{m}$. As will be discussed in section 6.3, these values should not be considered as corresponding to K_{Ic} values.

After tensile fatigue on specimens precracked in compression, the fatigue crack lengths at which final failure occurred were measured. From the measured crack lengths and associated loads, the stress intensity factor which caused final fracture was calculated. This technique gave fatigue fracture toughness values of 4.3, 4.3, 4.4, and 4.5 MPa$\sqrt{m}$ (see chapter 7).

5.2 Fracture toughness measured by indentation test

When an indentation is made in ceramics, radial, lateral and median cracks

will form in most cases [13,112-115]. The radial crack length obtained, which is usually well-defined on the specimen surface and can be easily measured, has been correlated for a given load to the fracture toughness of the material by different authors. A schematic illustration of crack system for indentation is shown in Figure 6.1.

The indentation technique was also employed in the present study to measure the fracture toughness. The Vickers indentations were made using a micro-hardness tester. Specimens were mounted on a glass plate with plasticine. The indentation axis was maintained perpendicular to the specimen surface. The specimen surface were polished with diamond paste from 16 to 1 μm to obtain mirror smooth surfaces. The loads used were 50, 100, and 150 N. The impressions were so arranged that spacings between indentations were approximately 10 times the indentation size.

The impressions obtained exhibited an almost perfect geometry (Figure 6.2). These indentations did not result in undesirable crushing, spalling, or irregular cracks, which are common problems encountered in indentation tests on brittle materials [14]. The indentations obtained satisfied usual recommendations which are that the crack dimensions be smaller than one-tenth of the thickness of the specimen, and the half length of the radial crack be larger than or equal to the diagonal length of the impression. Deviation of the data obtained for the same applied load was very small (less than 5%).

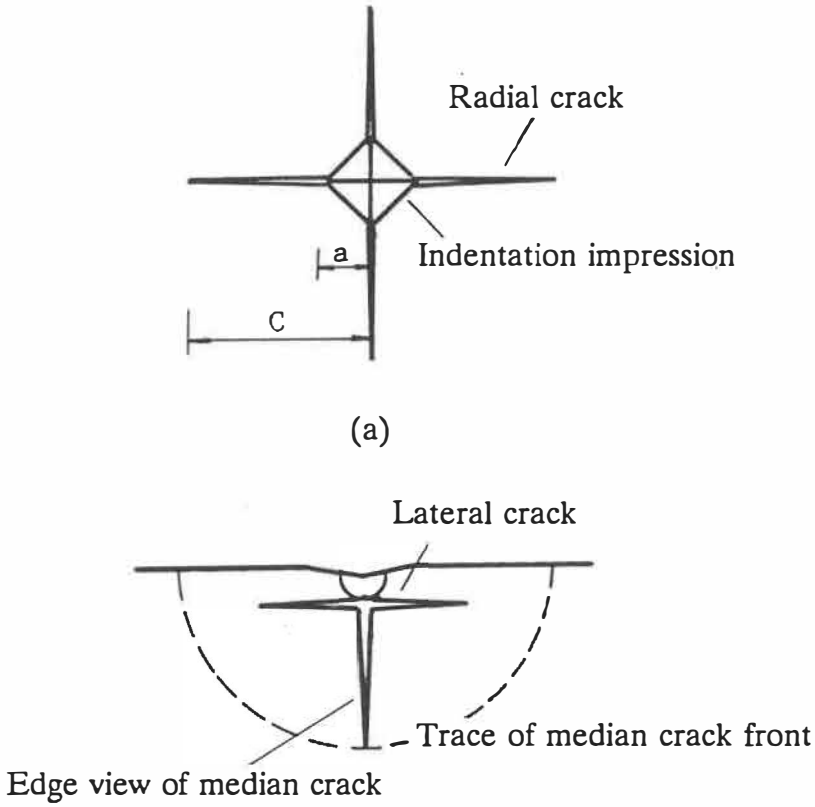

Fig. 6.1 Schematic illustration of an indentation impression and crack system produced by a Vickers indentation. (a) top view, (b) front view of section.

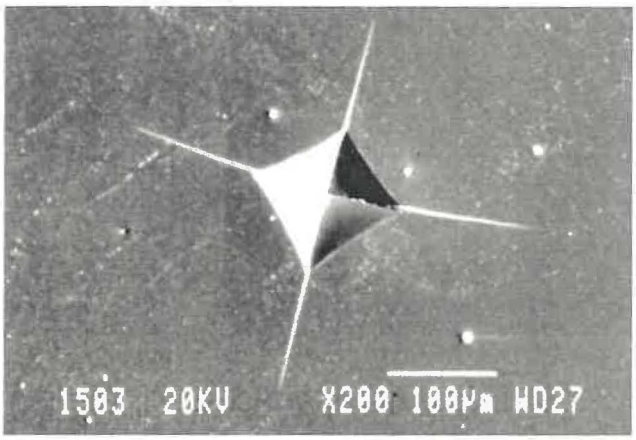

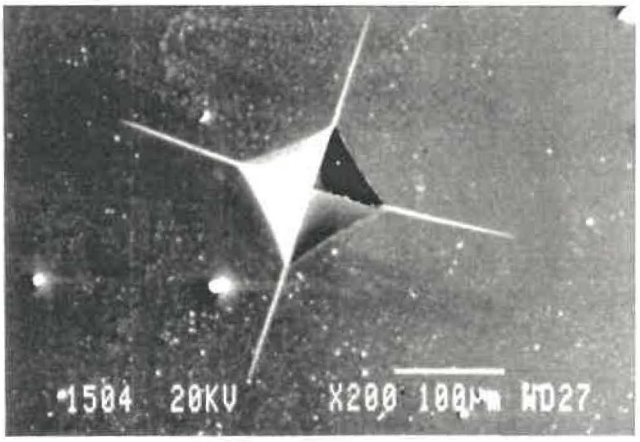

Fig. 6.2 Typical indentations showing very well-behaved radial cracks obtained in 3Y-TZP at a load of 150 N.

The measurements are presented in Figure 6.3. Two formulae were employed to determine the indentation toughness. The first was from reference [14]

$$K_c = k \sqrt{\frac{E}{H}} \left(\frac{P}{C^{3/2}}\right) \qquad (6.1)$$

where k is a constant approximately equal to 0.016±0.004; E is Young's modulus (=200 GPa); H is the Vickers hardness number, determined by equation (4-2); P is the load; C is the half length of radial crack; and a is the half diagonal length of the indentation.

The second equation employed, taken from reference [13], is the following:

$$K_c = \frac{0.15\ k\ H\ \sqrt{a}}{\phi} \left(\frac{a}{C}\right)^{3/2} \qquad (6.2)$$

where k is a constant approximately equal to 2.6; ϕ is also a constant approximately equal to 3; H is the Vickers hardness number; a is half diagonal length of the impression; and C is half length of radial crack.

Each data point listed in Figure 6.3 was obtained as an average value from

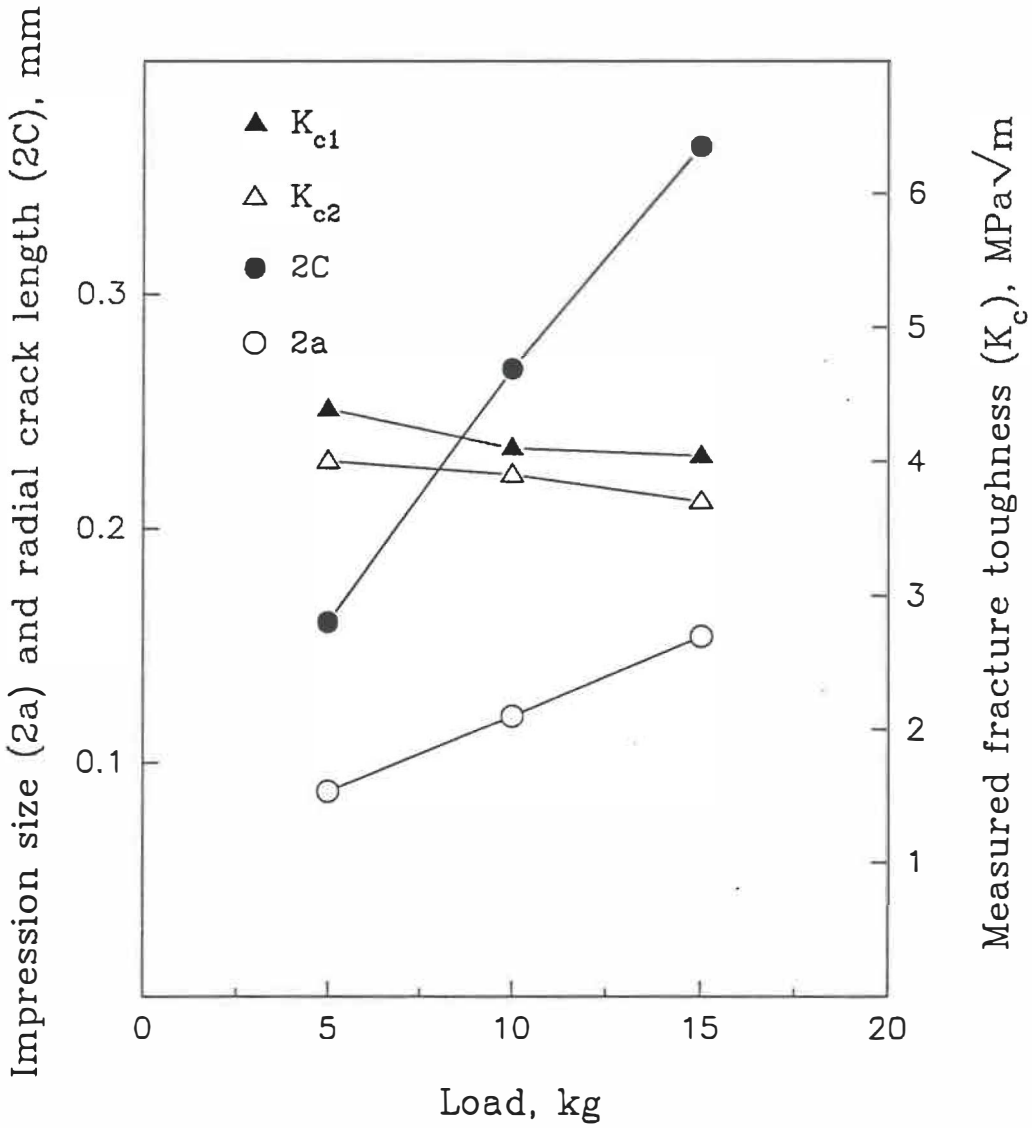

Fig. 6.3 Radial crack length, length of the indentation diagonals and measured fracture toughness obtained as a function of the applied load for 3Y-TZP, employing immersion oil on the test surface.

at least 20 indentations. From Figure 6.3, it is seen that the tests employing smaller loads tended to give slightly higher toughness values.

To compare the slow cracking effect from stress-corrosion cracking caused by moisture in the atmosphere, surfaces covered with immersion oil were also tested. Measurements of indentation size and crack length were conducted right on the micro-hardness tester, and the indented surfaces were examined by optical microscopy and subsequently by scanning electron microscopy.

To examine the effect of slow crack propagation, measurements without immersion oil were also made after two days of exposure to the laboratory environment following the introduction of the indentations. These results showed less than 2% of additional crack propagation compared to the measurements made immediately after the indentation.

6.3 Differences in fracture toughness measurements

The three different techniques employed in the present study gave different results for the fracture toughness of 3Y-TZP. As can be expected, the notched specimens tested under four point bending gave the highest toughness value of 11 MPa$\sqrt{m}$. Specimens precracked by compression fatigue and tested under four point bending gave an average value of 5.3 MPa$\sqrt{m}$. The fracture toughness measured by

microhardness indentation gave the lowest values of 3.8-4.2 MPa√m.

As a notch with a radius 0.17 mm is much blunter than a crack, the notched specimen will give a considerable over-estimation of the fracture toughness. The present results show that the fracture toughness can be overestimated by the order of 100% in comparison to the value obtained for the specimens precracked in compression fatigue. For the specimen fatigued under cyclic compression, a certain amount of residual stresses should exist in the crack tip region due to the cyclic fatigue. The residual stresses from phase transformation would be compressive stresses. A compressive stress applied to a notched specimen, however, also tends to result in tensile residual stresses, which appears responsible for the cracking in compression fatigue. The present results indicates that the compression fatigue precrack actually has the form of a very sharp notch rather than of a true precrack. On the other hand, some intergranular microcracks have been introduced by this cyclic compression at the tip of this sharp notch, so this notch should indeed act like a true precrack. Considering all these effects, it appears probable that the specimens precracked in compression fatigue gave the fracture toughness closest to the true value.

The toughness values obtained during the tensile fatigue test were slightly lower than for the specimens simply precracked in compression fatigue. The result that we did get fatigue cracking in this material did show that subcritical crack

propagation could occur below K_{max}. This fatigue fracture toughness value therefore corresponds to that required to transform a propagating subcritical crack into a critical crack. The values obtained in this manner therefore do not correspond to true K_{Ic} values but are underestimations. The lack of scatter in these toughness values is striking.

That the toughness values measured from indentation tests do not agree perfectly with those obtained on precracked specimens is not surprising. The equations employed to obtain these toughness values are largely empirical. These equations have been obtained partly from theoretical considerations and partly from curve-fitting. The data employed for this curve-fitting have been invariably taken from different sources and are not necessarily highly comparable. Another factor which affects the toughness value obtained from indentation tests is stress corrosion cracking (SCC). A noticeable SCC effect was not found by interrupting cycling in the compression fatigue. In indentation testing, after the release of the indenter from the specimen surface, the radial cracks still extended a small distance even when immersion oil was employed to prevent SCC from occurring. With immersion oil, there was about 5% difference between the immediate measurement of the radial crack length and the reading taken one day later.

Some materials from which the equations to obtain indentation toughness values were developed present very often irregular crack orientations, crack

branching or crack deviation. As a result, the radial crack measured in a straight direction is not necessarily very long, even if the material is very brittle. As a result, the cracks employed to calibrate a brittle material are often shorter than they should be. When the equation is then employed to characterize a tougher material presenting a straight radial crack, an under-estimation of the fracture toughness will tend to be obtained. In the present study, the radial crack was almost perfectly straight, so the fracture toughness obtained from the empirical indentation equations was relatively low. The magnitude of the applied load also affects toughness measurements, a smaller load tended to give a higher fracture toughness.

The major difficulty in obtaining reliable fracture toughness measurements in ceramics is to obtain a sharp precrack free of residual stresses. The ideal specimens to employ for these measurements would have been those containing a precrack produced in cyclic tension at a relatively low stress intensity value. Ideally, the test should have been interrupted to perform the fracture toughness measurement. The fatigue toughness values obtained during the cyclic tension fatigue tests, by producing a rapidly propagating crack at the start of the unloading cycle, very probably gave toughness values which are slightly lower than the true K_{Ic} values. This suggests that the most accurate K_{Ic} values obtained were probably the slightly higher values obtained on the specimens precracked in compression fatigue.

CHAPTER 7 FOUR POINT BENDING FATIGUE

Compared to fatigue crack propagation under compressive stresses, the crack which is subjected to a cyclic tensile stress presents a greater danger to engineering components. However, because of the considerable difficulties associated with the tensile fatigue testing of brittle materials, the literature on the tensile fatigue behaviour of ceramics is very limited.

7.1 Fatigue crack propagation under tensile stress in 3Y-TZP

3 mol% yttria-stabilized tetragonal zirconia polycrystals (3Y-TZP) shows very good potential in engineering applications due to its excellent resistance to oxidation and to wear at high temperature. However, very few studies have been carried out on the fatigue crack propagation resistance of 3Y-TZP. To understand the fatigue behaviour in this material, fatigue cracking under tensile stress was studied by employing four point bending. Tests were carried out on notched specimens with and without a precrack.

7.1.1 Four point bending fatigue of notched specimens

Fatigue crack propagation studies were conducted on notched specimens of 3Y-TZP. The specimen dimensions were a length of 40 mm, a thickness and a width

of 5 mm. A through-thickness notch with a width of 0.34 mm was introduced with a diamond circular saw. The notch length was 2.25 mm for all specimens. The specimens were fatigued with a sinusoidal waveform at 0.5 Hz at different stress intensity levels. The R-ratio of stress intensity (K_{min}'/K_{max}') for all specimens was 0.1, where K_{max}' and $\Delta K'$ are nominal stress intensity value obtained by treating the notch as a crack.

The specimen fixture was a commercial Instron Ltd fixture (Figure 7.1). The outer and inner spans of the fixture are 36 and 20 mm, respectively. There is a ruby ball in the fixture for precise alignment. The displacement can be measured by monitoring the mobile rod movement relative to the fixed reference on the fixture. To protect all accessories and the fixture from the load shock associated with fracture of the specimen, a protection plate was also mounted on the fixture. The tests were run on an Instron electromechanical machine (model 1362) employing a high precision load cell with a maximum capacity of 1000 N. The crack length at a lateral surface was monitored closely with a travelling microscope, providing a magnification of 70X.

During fatigue testing, no visible cracks were observed at the notch tip on the lateral surfaces. Specimens cycled at different load ranges failed after different number of cycles. The number of cycles to failure, N_f, versus K_{max}' and versus $\Delta K'$

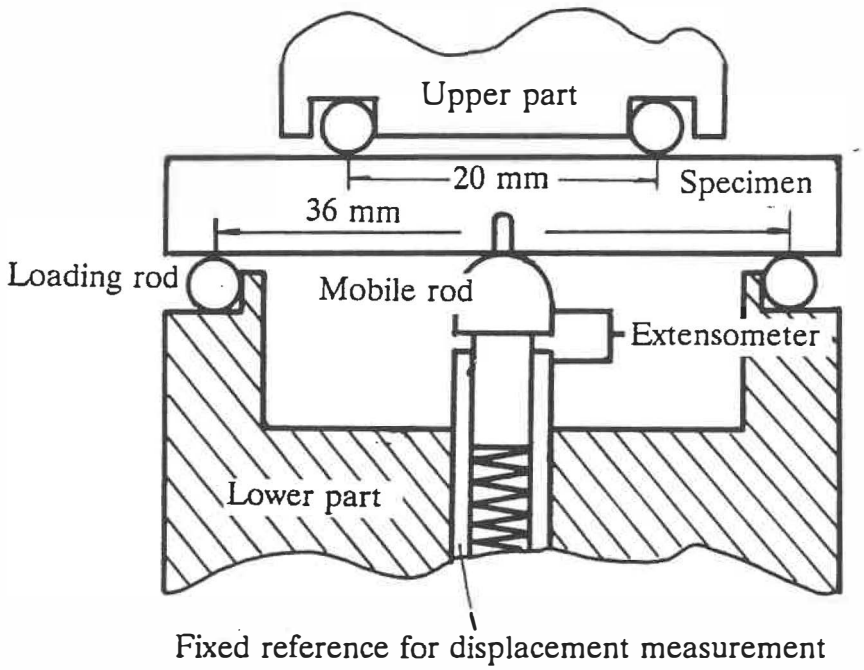

Fig. 7.1 Specimen fixture for four-point bending fatigue test.

are presented in Figure 7.2. This S-N or endurance type curve shows a typical fatigue effect of decreased specimen life with increasing stress amplitude.

On the curve of K_{max}' versus N_f, the K_{max}' value (10.4 MPa√m) plotted at N_f=1 corresponds to the fracture toughness of the notch specimen, which was much higher than the average fracture toughness of 5.2 MPa√m obtained on compression precracked specimens. Some authors have employed this type of test on notched specimen to measure material fracture toughness, but it can be expected that the measurement made on notched specimens does not correspond to the true value, but overestimates considerably the fracture toughness of the material.

As the nominal stress intensity values applied decreased, the number of cycles to failure increased rapidly. At K_{max}'=7.0 MPa√m, the specimen was cycled 100,000 cycles without failing. A plateau was reached on this curve, which indicated a fatigue limit had been reached. Therefore, the endurance limit expressed as K_{max}' for notched specimen with a/W=0.45 should be approximately 7.0 MPa√m which is still approximately 2.0 MPa√m higher than the fracture toughness obtained on precracked specimens.

Detailed fractographic observations allowed to recognize the fatigue cracking regions which led to final fracture. For specimens that were cycled at low ΔK' values, a single, large fatigue crack could be found at the notch tip near the mid-

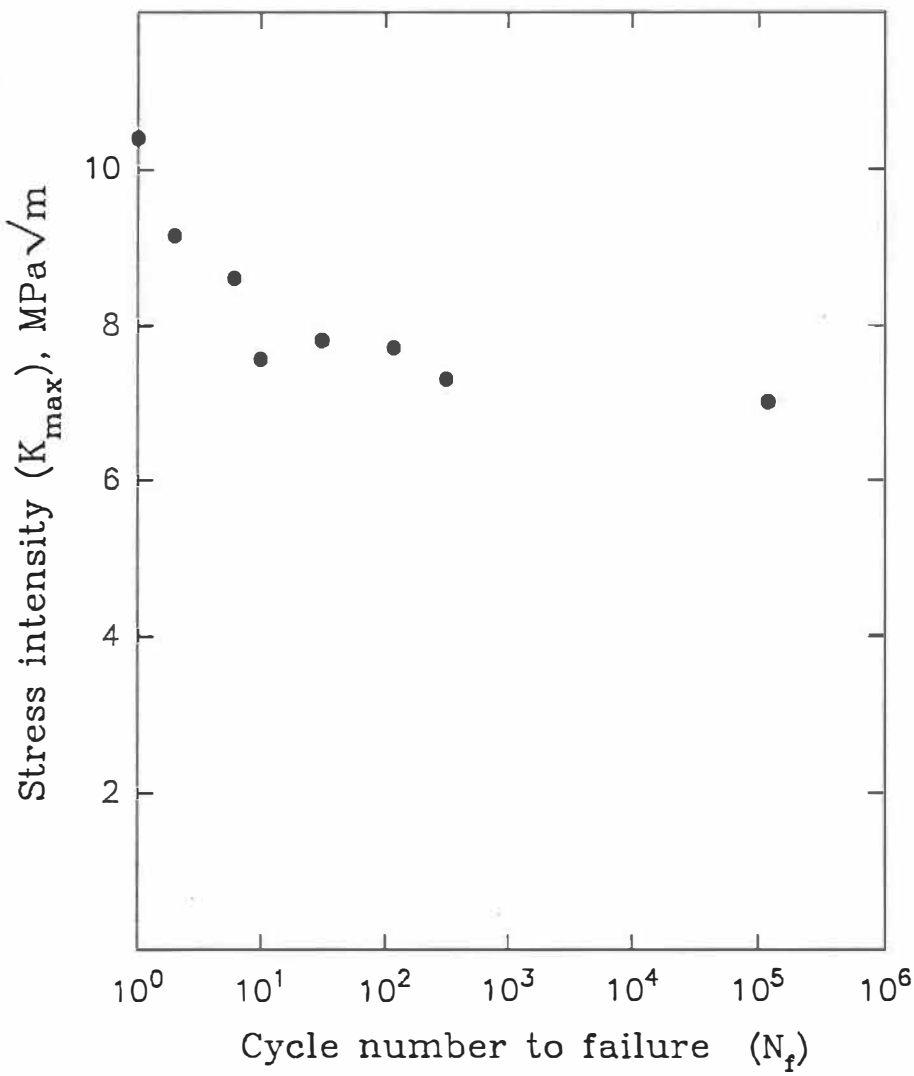

Fig. 7.2 Relation between the maximum nominal stress intensity factor, K_{max}', and the number of cycles to failure, Nf, for notch specimens of 3Y-TZP fatigue under four point bending.

thickness of the specimens (Figure 7.3). For specimens cycled at high $\Delta K'$ values, these fatigue cracking regions were small in size (Figure 7.4). For very high $\Delta K'$ values, fracture occurred catastrophically, and multiple fatigue cracking regions could be found. The fatigue cracking regions were darker in colour than the neighbouring area, and stretched out partly into notch, which was probably associated with the volumetric change caused by the stress-induced transformation.

7.1.2 Fatigue fractography of specimens fatigue-precracked under far-field compression and then cycled under tension

Crack propagation of 3Y-TZP under four point bending was investigated on specimens fatigue precracked in compression (see chapter 5). The specimens had a thickness and a width of 5 mm and a length of 40 mm. A through-thickness notch with a width of 0.34 mm was introduced with a diamond circular saw. The notch length a_n was 2.25 mm for all specimens and the precrack length a_{cf} was approximately 0.2 mm. Specimens were fatigued with a sinusoidal waveform at a frequency of 0.5 Hz. The test fixture was the same commercial Instron fixture. For the first several specimens, the stress intensity factor of the tensile fatigue cycling was started at a K_{max} of approximately 0.5 MPa$\sqrt{m}$ in order to avoid specimen fracture from starting at too high a K_{max} value. If no fatigue cracking was noticed in 3000 cycles, the stress intensity factor was increased by 0.2 MPa$\sqrt{m}$ and the procedure was repeated.

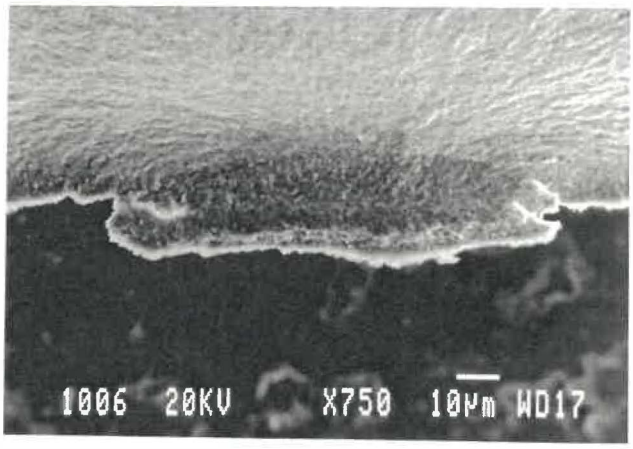

Fig. 7.3 Relatively large fatigue cracking region (arrow) obtained for the notched specimen of 3Y-TZP material tested at low K_{max}' in tensile fatigue.

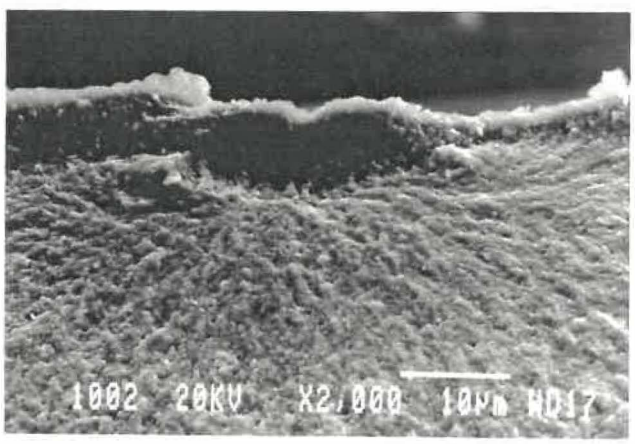

Fig. 7.4 Relatively small fatigue cracking region (arrow) for the notched specimen of 3Y-TZP material tested at high K_{max}' in tensile fatigue.

Careful observations at the precrack tip were made with a travelling microscope during fatigue cycling, but no visible crack propagation was observed in this manner for specimens YSP1 and YSP2. The fracture surface produced during tensile fatigue cycling gave particularly useful information concerning fatigue crack propagation under cyclic tensile stresses.

Figure 7.5 shows the fracture surface obtained after final fracture. The fracture surface of these specimens could be divided into four portions with the middle two portions corresponding to those produced in tensile fatigue. The first portion, a_{cf}, immediately adjacent to the notch tip, corresponds to the fracture surface developed during compression fatigue precracking. In order not to risk unexpected specimen fracture, smaller nominal compressive stresses and a smaller cycle number were employed during precracking, in comparison to those employed for compression fatigue testing. Although its morphology was, as expected, very similar to that obtained in the compression fatigue test, a few differences were observed. Compared to those in the compression fatigue tests, the four fracture surface zones, especially the third and the fourth zones were less well developed.

The two fracture surface zones produced in tensile fatigue consisted of a first zone a_{b1} without visible striations and a second zone a_{b2} with visible striations. The crack front of these tensile fatigue portions had a convex curvature in the crack propagation direction near the lateral surfaces, with the crack front at the lateral

surface having propagated slightly slower than in the mid-thickness region. This curvature of the crack front was essentially the opposite of that obtained in compression fatigue, where the fatigue crack obtained was longer in the region near the lateral surfaces than near the mid-thickness. Therefore, although the fatigue crack under tensile cycling already grew more rapidly in the mid-thickness region, the growing crack still could not be seen on the lateral surface for most of its propagation, because of the presence of the precrack produced in far-field compression fatigue which was longer near the lateral surface.

Under a constant load amplitude, the applied stress intensity increases with increasing crack length. Finally the crack grew sufficiently large that the critical crack length was reached for the applied load level. This led to the final fracture of the specimen and produced the final portion of the fracture surface. This final fracture portion, a_{ff} presented predominantly intergranular fracture, with the intergranular facets showing little evidence of deformation.

Particularly interesting features were obtained on the middle portions of the fracture surface, which corresponded to the crack propagation zone produced in four point bending under far-field tension. In contrast to the fracture surface morphology obtained in compression fatigue, in addition to the difference in the crack front curvature, this tensile fatigue surface did not present any debris particles, nor any agglomeration of such particles into cakes, nor any spalling at the lateral

surface, all of which were common characteristics of the fatigue fracture surface produced under fully compressive loads.

In the second portion of the tensile fatigue region of the fracture surface, clear striation-like dark bands, approximately 10 μm in width, separated by larger more lightly coloured regions were observed (Figure 7.6). Stereographic observations showed that these dark bands corresponded to matching depressions on the two opposite fracture surfaces (Figure 7.7). The lighter-coloured zones between the striation-like markings increased in width with increasing crack length. Nevertheless, the width of the darkish bands did not change as greatly as those of the brighter zones (Figures 7.8).

Some of the river or small ridge lines, which were associated with and approximately perpendicular to the striation markings, could be discerned at large magnification (Fig.7.8). These river lines, which were approximately parallel to each other, often terminated on or near the first side (that closer to the precrack) of a dark band and restarted on the other side. Groups of small river lines merged into more prominent lines as the crack propagated away from a striation marking. Some of the fine river lines gradually faded away in reaching the centre of the dark band, sometimes to reappear on the other side of the dark band. The manner in which these striation markings interacted with the fine river lines or ridge lines on the

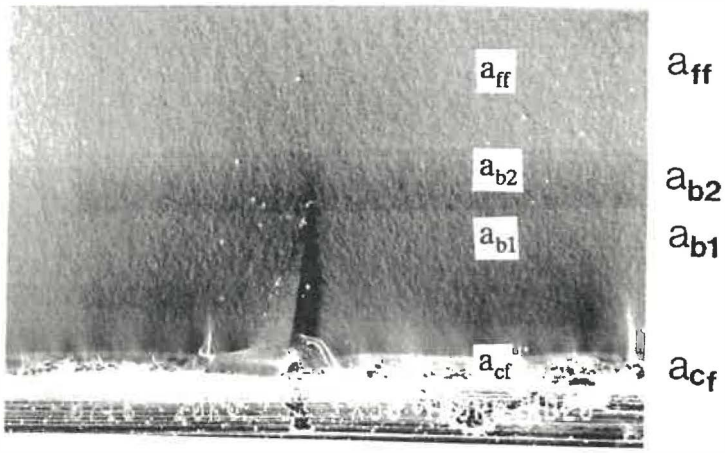

Fig. 7.5 The general aspects of the entire fracture surface for fatigued precrack specimens of 3Y-TZP under tensile cyclic stress. The regions a_{cf}, a_{b1}, a_{b2} and a_{ff} refer to compression-fatigue precrack, tensile fatigue crack without discernible striations, fatigue crack propagation with discernible striation, and the final fracture surface, respectively.

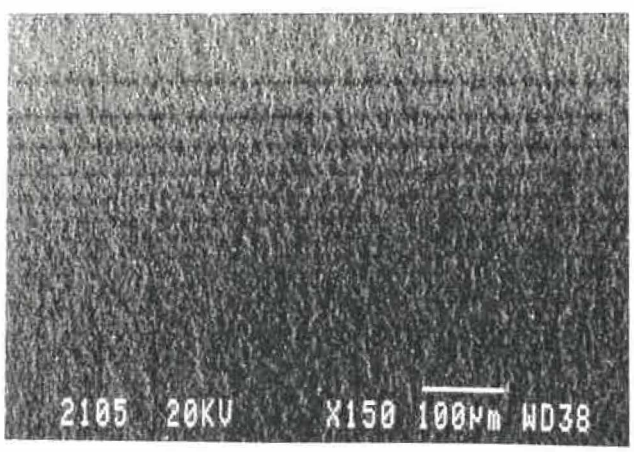

Fig. 7.6 Typical aspect of the striation bands observed on the tensile fatigue fracture surface of 3Y-TZP.

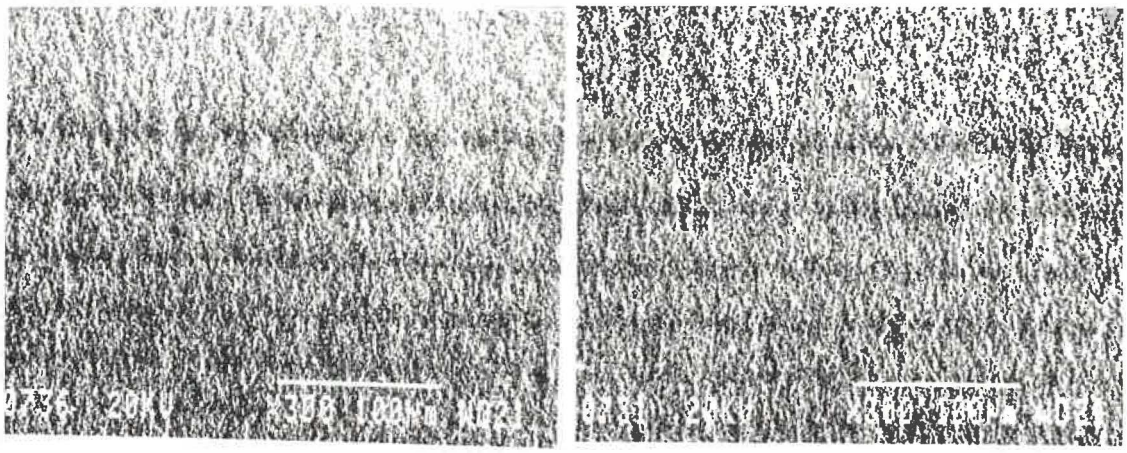

Fig. 7.7 Corresponding depressions observed at the striation sites on opposite fracture surfaces.

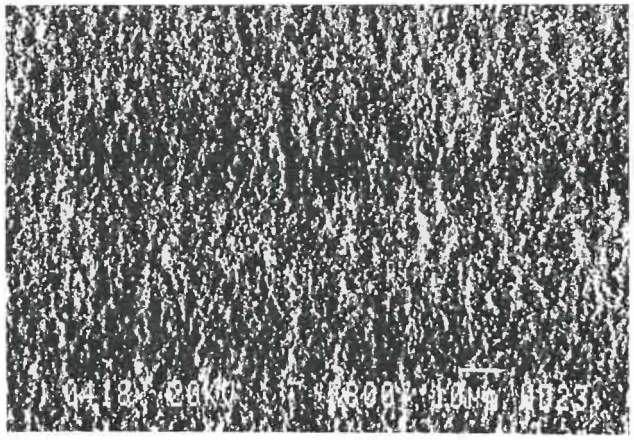

Fig. 7.8 Fine ridge lines are observed to terminate often on one side of the striation, while new ridge lines tend to initiate on the other side.

fracture surface clearly indicated that the first side of these dark bands corresponded to a site of crack arrest and the other side to a site of the start of rapid propagation.

7.1.3 Fatigue crack propagation behaviour of precracked 3Y-TZP specimens

For all specimens fatigued under tensile stresses, the general aspect of the fracture surfaces was the same as schematically illustrated in Figure 7.6. For a typical specimen (YSP1), a_n, a_{cf}, a_{bf}, and a_{ff} were 2.20, 0.11, 0.71, and 1.98 mm, respectively. Measurements related to the striation positions and spacings between the dark bands were carried out on the fracture surface. These spacings were employed to obtain crack growth rates by assuming that each band was produced during a successive stress cycle. By correlating the position of each dark band on the fracture surface (which gives the crack length) with the constant cyclic load, the corresponding stress intensity factor could be obtained without ambiguity.

The curves of fatigue crack propagation rate, da/dN, versus the range of stress intensity factor, ΔK, and versus K_{max} obtained from the measurement of striation spacings for specimens YSP1 and YSP2 are presented in Figure 7.9. On a ΔK basis, the crack propagated at a higher rate for the larger load ratio (R=0.33) than that for the smaller load ratio (R=0.14). The highest crack growth rate obtained for this material was approximately 50 μm/cycle under four point bending, which is relatively high compared to that generally obtained for metallic materials.

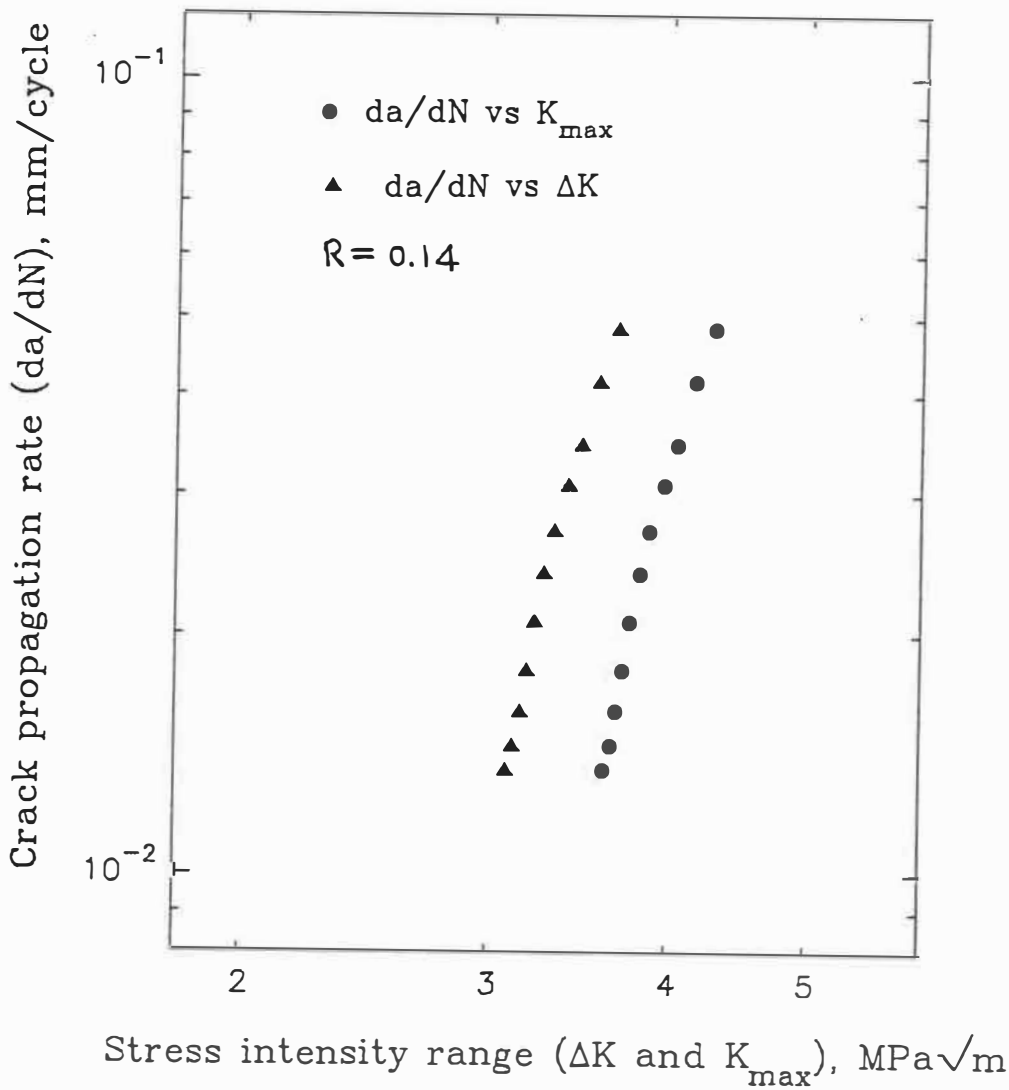

Fig. 7.9 Crack growth rate da/dN versus ΔK and versus K_{max} for two R-ratios, as determined from the positions and spacings of the striation markings. The fatigue growth behaviour under tensile stress is clearly controlled principally by K_{max}.

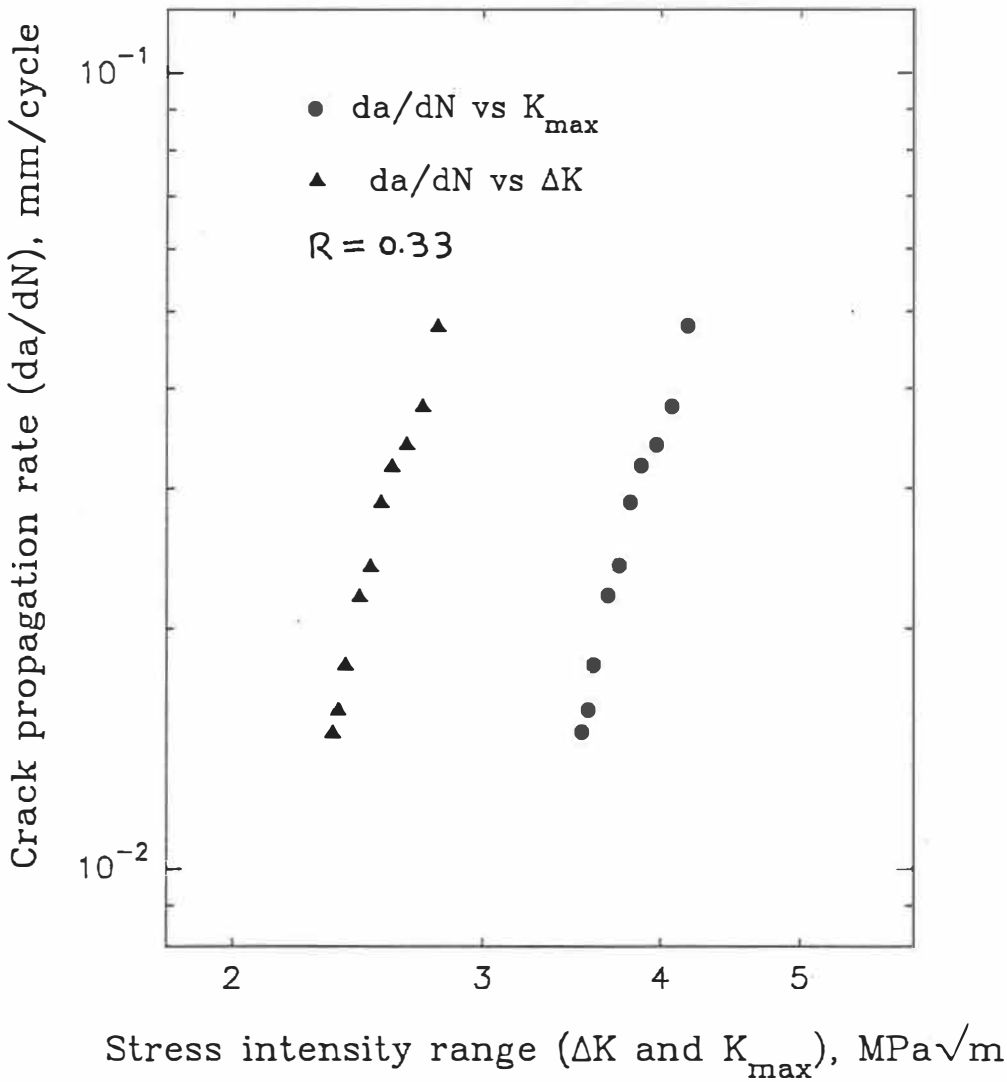

Fig. 7.9 (b) crack growth rate da/dN versus K_{max} for two R-ratios, as determined from the positions and spacings of the striation markings. The fatigue growth behaviour under tensile stress is clearly controlled principally by K_{max}.

The curves of da/dN versus K_{max} for two specimens were very similar. At the same K_{max} level, da/dN was only slightly higher for the larger mean stress or R-ratio than for the smaller mean stress. This result indicates that the principle driving force for fatigue crack propagation in this ceramic is K_{max} and not ΔK.

For specimen YSP1 tested at R=0.33, fatigue cycling was started at K_{max}=2.7 MPa√m and final fracture occurred at K_{max}=4.3 MPa√m. For specimen YSP2 tested at R=0.14, fatigue cycling was started at K_{max}=2.6 MPa√m and final fracture occurred at K_{max}=4.5 MPa√m.

7.1.4 Utilization of a microstrain gage for detection of fatigue crack propagation

As fatigue crack propagation was very difficult to observe with a travelling microscope during tensile fatigue, microstrain gages were employed to detect fatigue crack propagation. Microstrain gages from Intertechnology Inc., model EA-06-015DJ-120, were installed at the precrack tip in two tests (specimens YSG1 and YSG2) with the centre of the gage being approximately 0.7 mm from the crack tip. The gage length was 0.38 mm, the grid width was 0.51 mm, and the gage factor was 2.09. A conditioner (Intertechnology Inc. model 2120) was employed for each gage for conditioning the microstrain gage signals into high level voltage output. The bridge excitation voltage employed was 2 volts. To obtain temperature

compensation, a reference gage of the same type was installed on a reference specimen of the same material.

Hysteresis loops from the strain gages were recorded at an interval of approximately every 20 cycles during the initial phase of the test. Once a detectable change in loop slope could be noted, recording was performed every few cycles or finally every cycle. The cyclic loading was started at a K_{max} value of approximately 1.0 MPa$\sqrt{}$/m. If no crack propagation was observed after 6000 cycles, the K_{max} value was increased by 0.2 MPa$\sqrt{}$/m.

7.1.5 Hysteresis loops from the crack-tip microstrain gage

For the fatigue cracking monitored with a microstrain gage ahead of the precrack tip, typical responses of the microstrain gage to fatigue cracking are presented in Figures 7.10 and 7.11. The response is plotted in terms of the far-field applied load as a function of the average displacement in the crack opening direction over the area covered by the gage.

The hysteresis loops were observed after different number of cycles to examine the decrease in their slope. At the start of cycling, the decrease in their slope was very small, and, there was not a discernible difference in the slope of the loading and unloading portions of the same loop, (i.e., the gage response for loading

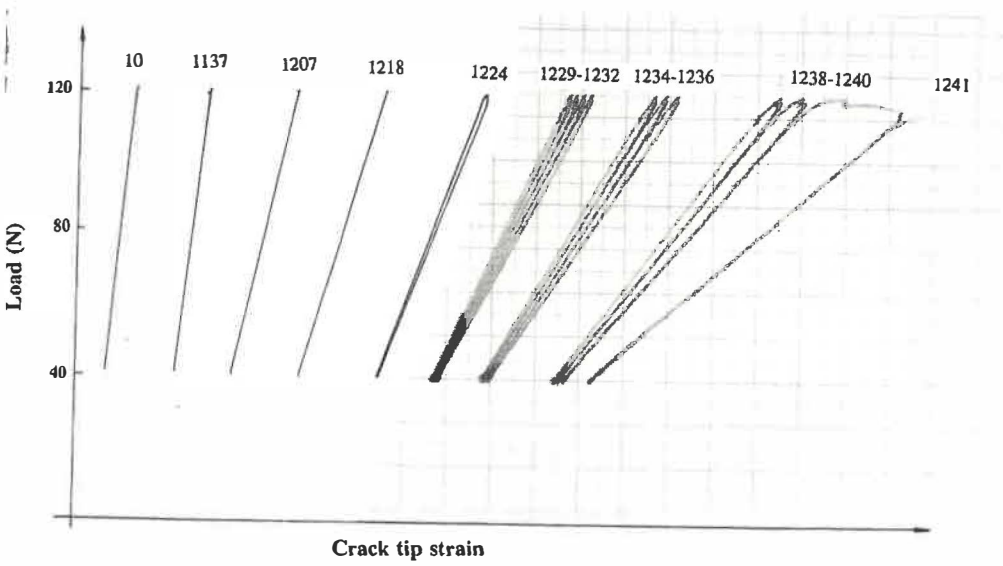

Fig. 7.10 Hysteresis loops measured at the tensile fatigue crack tip with the microstrain gage on 3Y-TZP (specimen YSG1, the numbers on top indicate the cycle number). The measured strain increases gradually and stably with increasing cycle number.

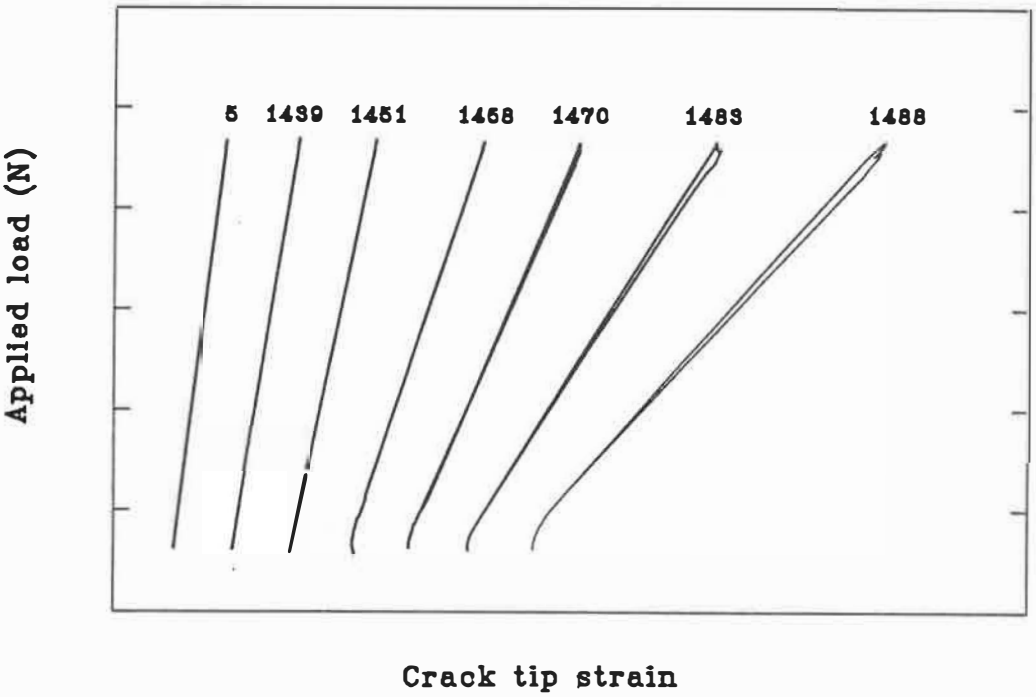

Fig. 7.11 Hysteresis loops measured at the tensile fatigue crack tip with the microstrain gage on 3Y-TZP (specimen YSG2). The measured strain increases with increasing cycle number. Crack closure is observed near the minimum load value.

nd unloading portions appeared to follow the same path). As the crack grew nger, not only did the slope of the loops decrease, but also the loading and nloading portions of the loops became separated. The two portions of the loop no nger followed the same path, but instead the unloading path had a slightly lower ope than the loading path. The difference in the slopes between the two paths ould correspond primarily to crack growth in the same cycle.

The loading portion of the hysteresis loop in the following cycle was initially rallel to the unloading portion in the previous cycle, until it deviated from earity. This result indicates that no discernible crack growth occurred in the linear rtions of the unloading ramp in one cycle and of the loading ramp in the following cle (Figure 7.10).

After a certain number of cycles, for the tests performed at R= 0.1, the slope the load hysteresis loop increased as the load decreased and approached the nimum load. The same high slope was maintained during the initial load reasing portion of the next stress cycle before returning to the slope for linear stic behaviour. With this effect of an increased slope near K_{min}, the specimen aves as if the crack has been shortened, which is typical of a crack closure effect gure 7.11). Such a crack closure effect was not observed or was very small at =0.3, which also is typical crack closure behaviour where the closure effect reases in magnitude or disappears with increasing R-ratio (Figure 7.10).

1.6 The relationship between the fatigue crack increment and the displacement ıange on the hysteresis loop

The correspondence between the load cycle and the gage response in the last 'o cycles of specimen YSG1 is presented in Figure 7.12. Points of interest were :termined first on the load-displacement curve obtained from the strain gage, then e corresponding points were determined on the applied load cycle assumed from e waveform by translating the load value on the hysteresis loop to the load cycle. ıe load starts to increase at point A. Linear load displacement behaviour is tained until point B, indicating that no or very little propagation has occurred ring this portion of the load cycle. The gradual deviation from linearity between int B and the maximum load point C indicates that stable crack propagation is tained in this portion of the load cycle. As unloading begins, the hysteresis loop ɔws a small portion CD in which the load-displacement curve has a slope slightly ver than the initial slope between A and B. This indicates that very little ɔpagation is occurring during this portion of the cycle or that the crack has 'ested. This is followed by portion DE of the hysteresis loop, in which the placement increases rapidly with time while the load is approximately constant can even appear to increase. This indicates that an amount of rapid propagation ; occurred. The slope of the hysteresis loop becomes approximately linear elastic point F, indicating some slower propagation between E and F, but the slope ıtinues to decrease slightly until approximately point G which indicates some even

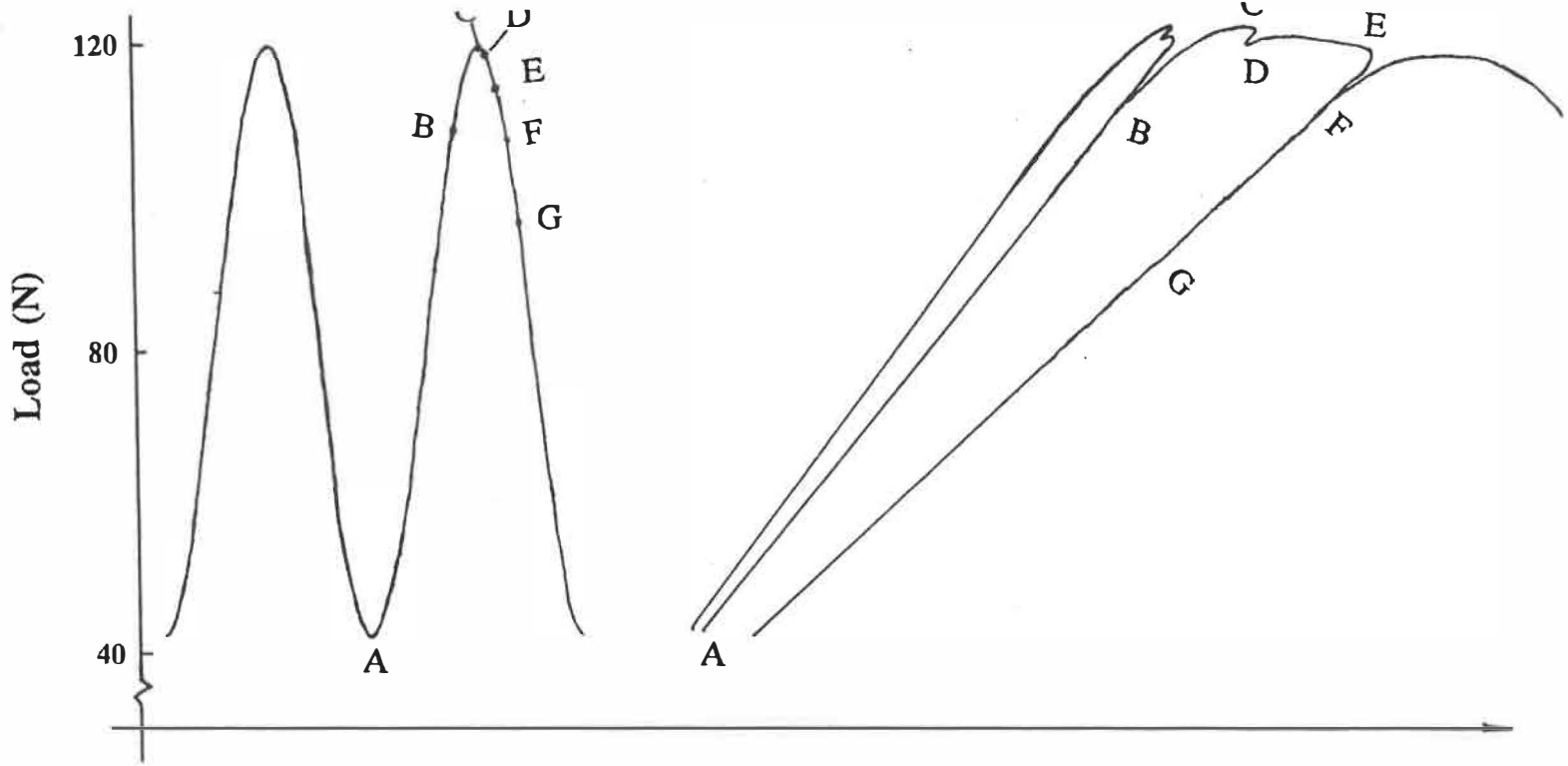

Fig. 7.12 Correlation between the load cycle and the strain behaviour at the fatigue crack tip.

ower propagation between points F and G. The crack then arrests approximately point G. A change in slope is again observed near the minimum load associated th the occurrence of crack closure.

In the case of very small increment of fatigue crack length, a proportional ationship between the crack increment and the displacement increment in the steresis loop can be assumed for an individual cycle. As a result, the proportion the crack increments in the portions of BD and DE of the loop can be estimated comparing the relative displacement proportion of BD and DE. On the other nd, the widths of the striation-like markings in the form of dark bands and bright nes on the fracture surface between these bands provide information on the ount of propagation for each zone for that same cycle. The comparison of the ain gage results with the fractographic observations indicates that the dark band l the bright zone for one cycle are developed during the portions of BD and DE the hysteresis loop, respectively.

In addition to the description of the formation of dark bands and bright es proposed in section 7.1.2, there is another possibility to explain the tographic features of the dark band followed by a larger bright zone. The crack ests with a small transformation zone as K decreases, but as K increases during next half cycle the crack tip transformation zone increases. When a critical K ne is attained, the crack starts propagating rapidly, but this is done by initiating

new crack on the other side of the transformation zone. In other words, rapid rack propagation is not initiated at the previous crack tip but at the interface of the ransformation zone ahead of the previous crack tip. This appears in agreement with he new river lines initiating at the end of the wide striations and with the old river nes appearing to terminate within the dark band. The manner in which these actographic features form will be considered in further detail in chapter 9.

The striations appear to be clearly associated with a difference in the ansformation zone size between the crack arrest site and the sites where the crack propagating rapidly. It is particularly interesting to note that a certain decrease load is necessary to cause the crack to propagate rapidly which produces the right zone between dark bands. Therefore, the formation of the bright zone etween dark bands requires that the applied K_{max} be greater than a certain value nd that a certain value of unloading ΔP or ΔK follow the attainment of K_{max}.

Fatigue fracture surface of specimen YSG2 (Figure 7.13) exhibited very nilar striation-like markings as in the previous tests of specimens YSP1 and YSP2. his suggests that the markings are highly reproducible. Such markings were also ported on 3Y-TZP by Liu and Chen [53].

1.7 Retardation effects of sustained load on fatigue cracking

Bending fatigue was also performed on specimen YSG1 which was tested th a microstrain gage at the precrack tip. Fatigue cracking was discerned after ndreds of cycles, then an intensive recording of individual hysteresis loop was tained on an X-Y plotter. However, the recording paper ran out, and in order to load the plotting paper, the load cycling was interrupted. The load was kept at the ean level during the interruption which lasted approximately 10 seconds. After this spension of 10 seconds, the load cycling was resumed with exactly the same cycling nditions as before. Cycle-by-cycle plotting was performed in order to obtain a mplete recording. Fatigue cracking resumed as soon as the cycling restarted and opagated in a stable manner until final failure.

When the fatigue fracture surface was observed in the SEM, two fatigue nes separated by a dark line were seen with clear striation-like markings present both sides of this boundary line (Figures 7.14 and 7.15). At large magnifications, boundary line between the two zones appeared as a broader and deeper pression on both fracture surfaces than other markings (Figure 7.16).

The striation markings faded away in approaching the precrack (Figure 7.14). the initial stage of fatigue cycling (K_{max}≈1.8 MPa√m). Although the fatigue cking had already started, no striation-like bands could be observed. In this ion, the crack growth expected from the fatigue crack propagation curve would less than the width of a dark band in each cycle. As a result, the crack arrest

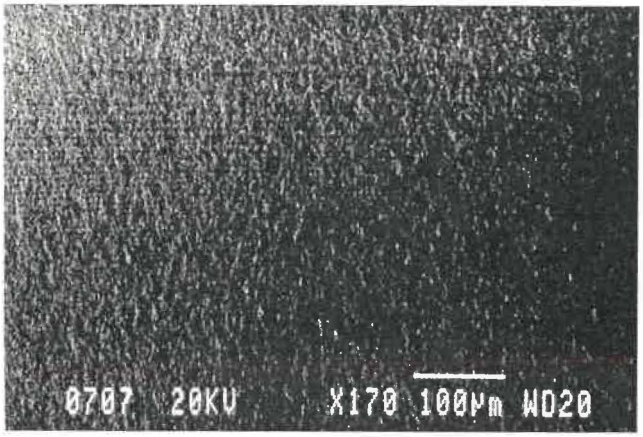

Fig. 7.13 A large number of striations observed on the fatigue fracture surface produced under cyclic tensile stress (Specimen YSG2).

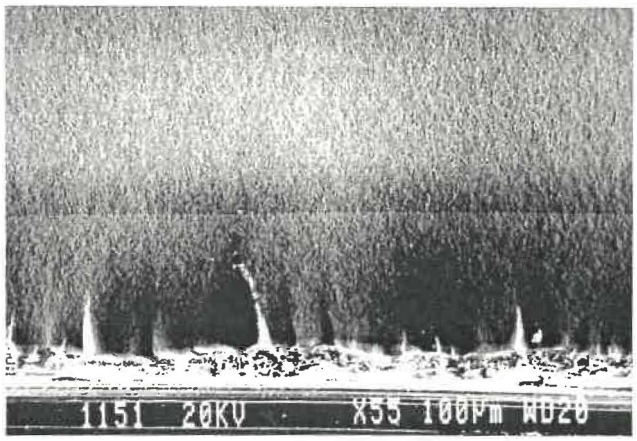

Fig. 7.14 Two zones of striations produced before (bottom portion) and after (top portion) the cycling interruption which led to crack deviation and fatigue crack retardation on specimen YSG1.

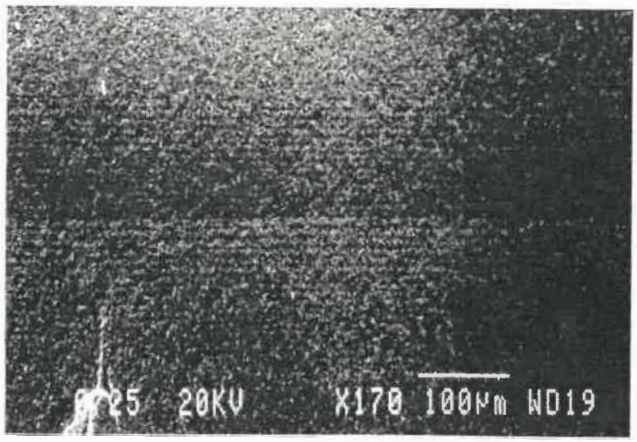

Fig. 7.15 Striations present in the region of crack deviation (specimen YSG1).

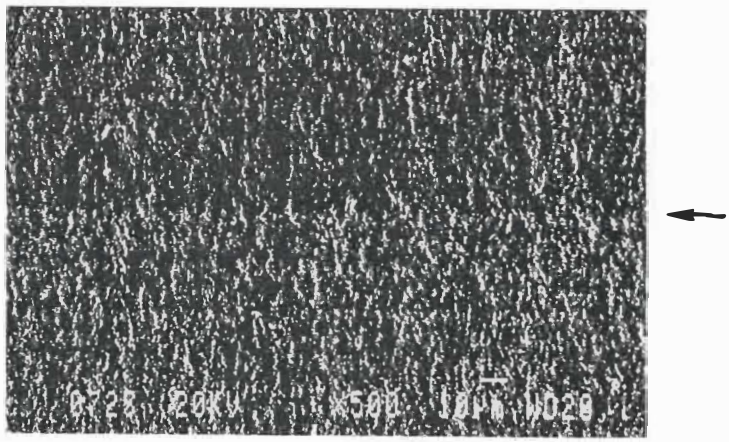

Fig. 7.16 Deeper and broader striation (arrow) produced by interruption of cycling on specimen YSG1.

tes cannot be distinguished. They only became distinguishable after 1200 cycles at K_{max} value of 2.18 MPa√m.

An inflection point can be seen near 1225 cycles in the crack length versus 'cle number curve of specimen YSG1 (Figure 7.17), which indicates a retardation 'fect as a result of the cycling interruption performed during the testing. However,) such inflection point was found for specimen YSG2 which was not subjected to ıy load interruption (Figure 7.18). The crack propagation curve obtained on ›ecimen YSG1 show clearly two parallel curves (Figure 7.19), one for zone A and e other one for zone B. The crack propagation rate increased gradually with crack ngth in zone A, but it decreased abruptly after the interruption of the cycling. It en reincreased gradually to form a curve parallel to that obtained for zone A. The ırallelism suggests that a crack tip stress shielding effect was introduced by the terruption of the cycling, and that this stress shielding effect continued to operate r the entire width of zone B.

l.8 Relationship between the slope of the hysteresis loop and the fatigue crack ıgth

By correlating the crack length, a, and the average strain, D, measured by crostrain gage for the same cycle number, the relations between a and D were tablished for specimens YSG1 and YSG2. This was performed by starting from

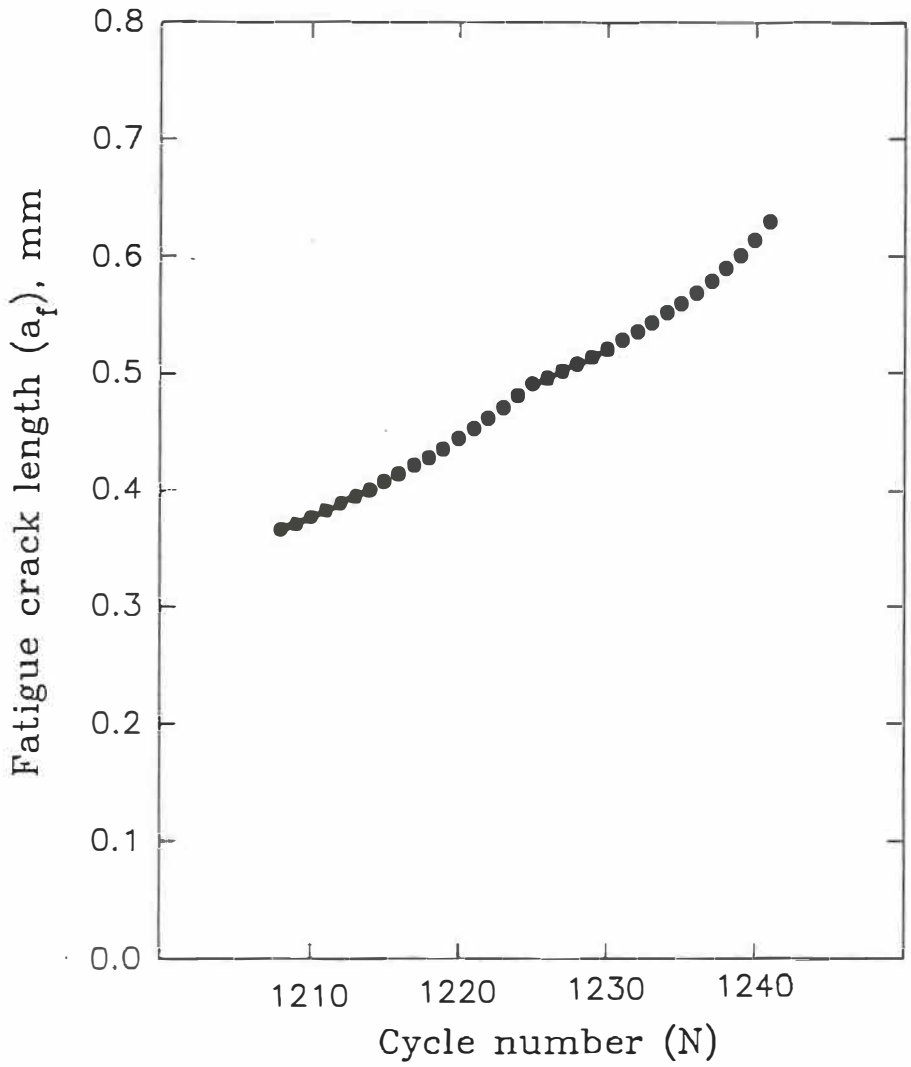

g. 7.17 Fatigue crack length determined from the striation position as a function of the cycle number (specimen YSG1).

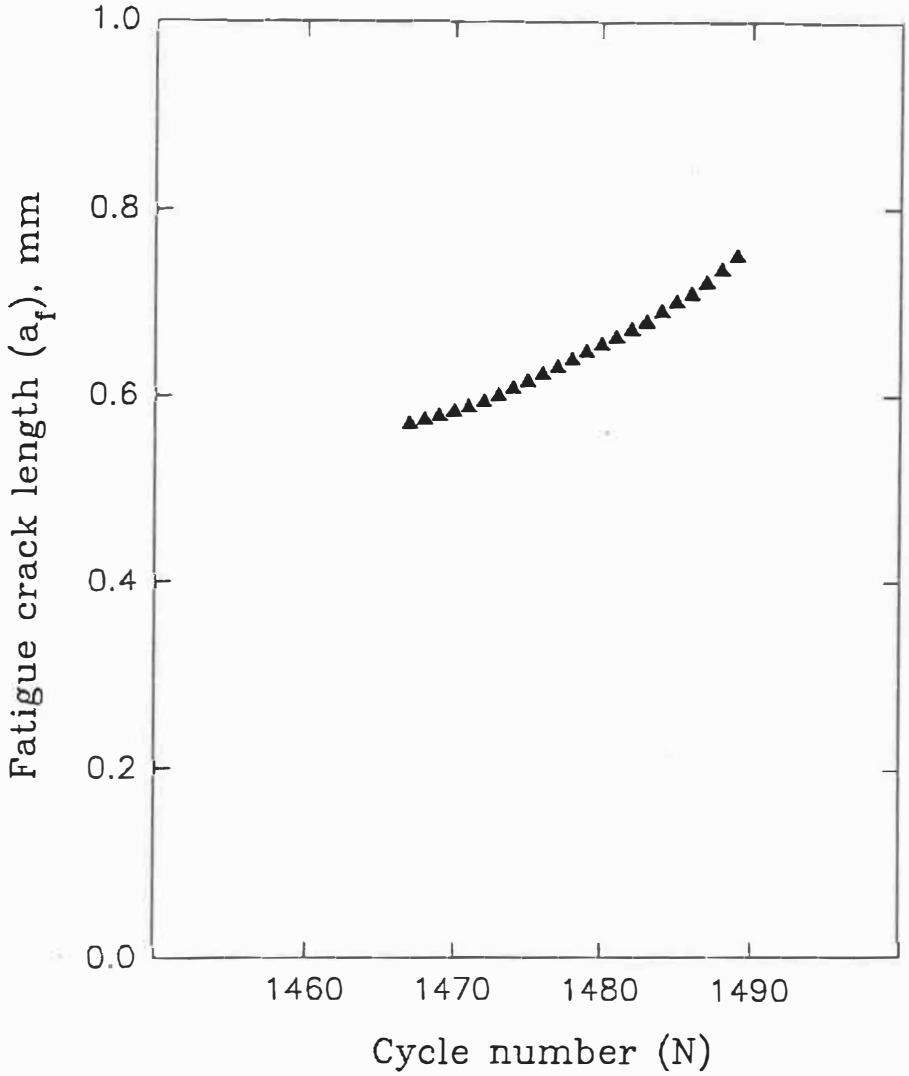

Fig. 7.18 Fatigue crack length determined from the striation position as a function of the cycle number (specimen YSG2).

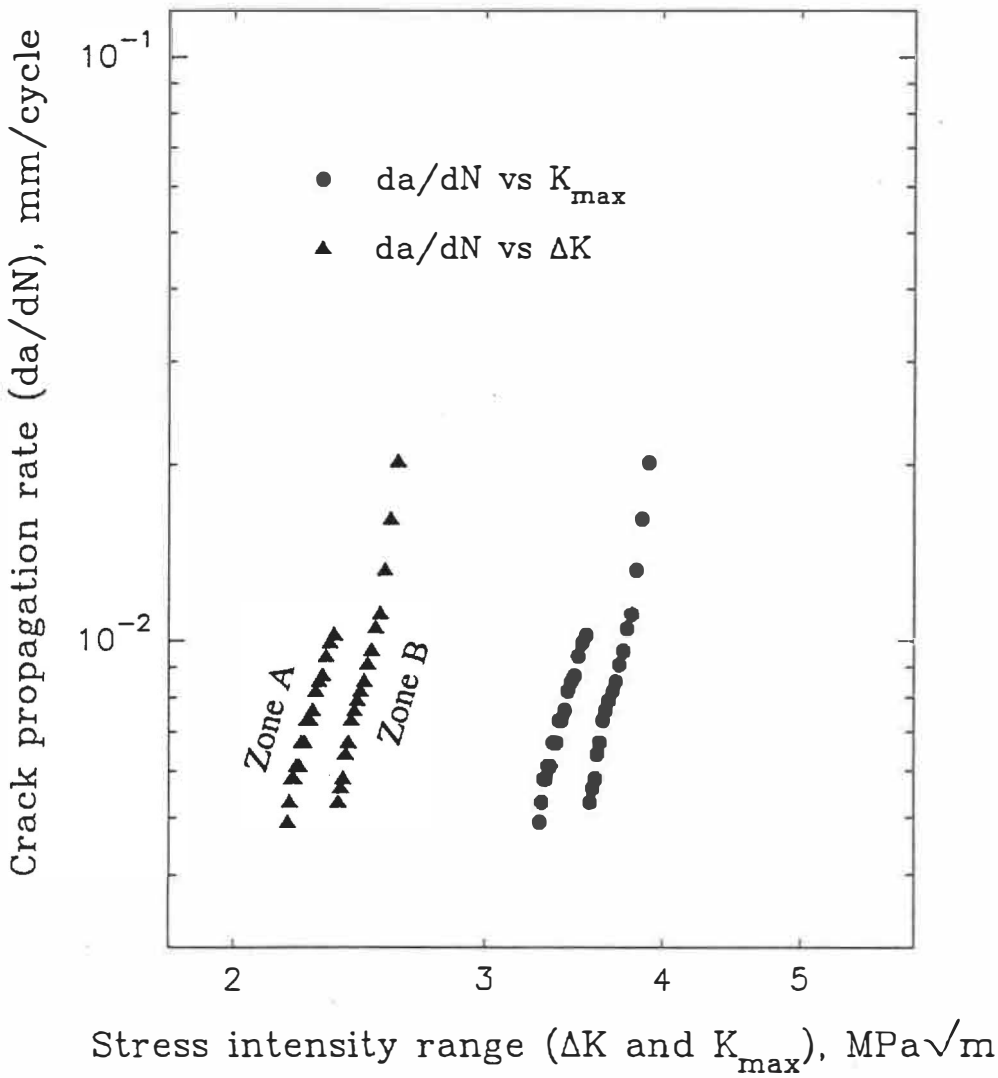

ig. 7.19 Fatigue crack propagation rate da/dN versus the stress intensity range ΔK and versus the maximum stress intensity factor K_{max} showing the crack retardation which resulted from the cycling suspension (specimen YSG1).

ıe last loop and the last dark band. As a result, relationships of fatigue crack length ınd the average strain measured with a microstrain gage were obtained (Figure 20). From regression analysis, the average strain could be expressed as a parabolic ınction of the crack length, particularly for a large fatigue crack length. Both the ack length and crack increment can be used in this context. These two terms can : converted by involving a coordinate translation. As the crack length will be quired for calculation of stress intensity factor, the crack length is preferred in the llowing discussion.

The parabolic relationships for specimens YSG1 and YSG2 are the following, spectively:

$$a = 241D^2 + 0.40 \qquad (7.1)$$

$$a = 212D^2 + 0.56 \qquad (7.2)$$

here a is the crack increment in mm, D is the average strain measured with crack-strain gage in percentage.

By considering the crack profile covered by the gage and the manner in ich the gage reacts to the presence of the crack, the parabolic function between : crack length and the average strain measured with a gage can be obtained ılytically.

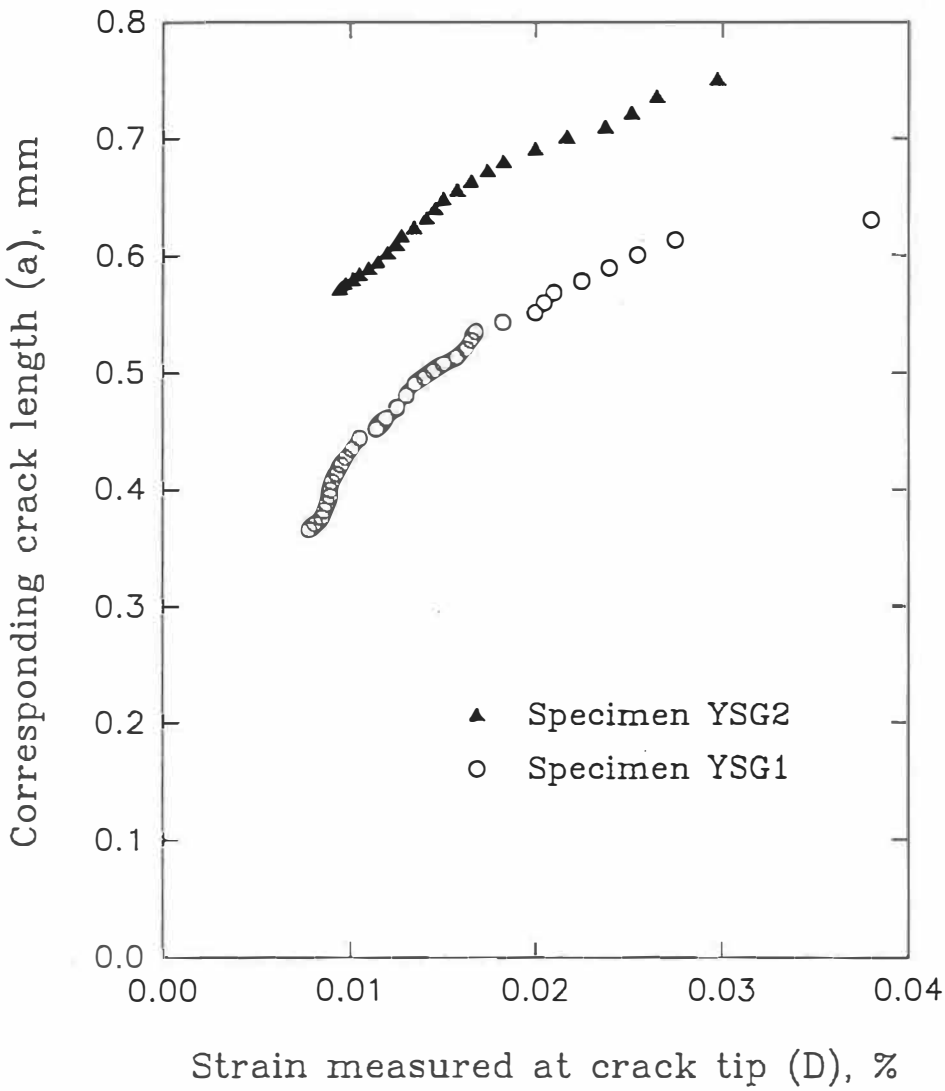

g. 7.20 Correlations between the maximum strain measured with the microstrain gage and fatigue crack length measured on the fracture surface corresponding to the same cycle number (specimens YSG1 and YSG2).

When the gage is far from the crack tip, it covers neither the crack tip nor ıe transformation zone. The average displacement field measured by the gage is quite uniform displacement field developed under the uniform tensile stress ɔnsidered to be very similar to the stress in far-field. As the crack moves gradually ›wards the gage, the transformed zone will first move into the gage area. ventually, not only the transformed zone but the crack tip will also be situated ıder the gage.

When the fatigue crack is partially covered under the strain gage, the fatigue ack should take a profile approximately like an isosceles triangle, as indicated in gure 7.21. By starting from this assumption of the isosceles triangle configuration, e are able to obtain geometrically the parabolic relationship between the fatigue ack length and the average strain measured by the strain gage.

For simplicity of analysis, the coordinate origin is taken to be always at the ansformation zone tip. The average strain measured by the strain gage is nsidered as an extra displacement field brought by the crack increment which is ıder the coverage of the strain gage. As far as the gage is concerned, this extra splacement exists only after the process zone ahead of the crack moves into the ge area. Because the gage reacts to the extra displacement field by measuring an crease in the displacement in the Y direction over the entire width in the X ·ection. The extra area brought in by the crack is the area of the isosceles triangle

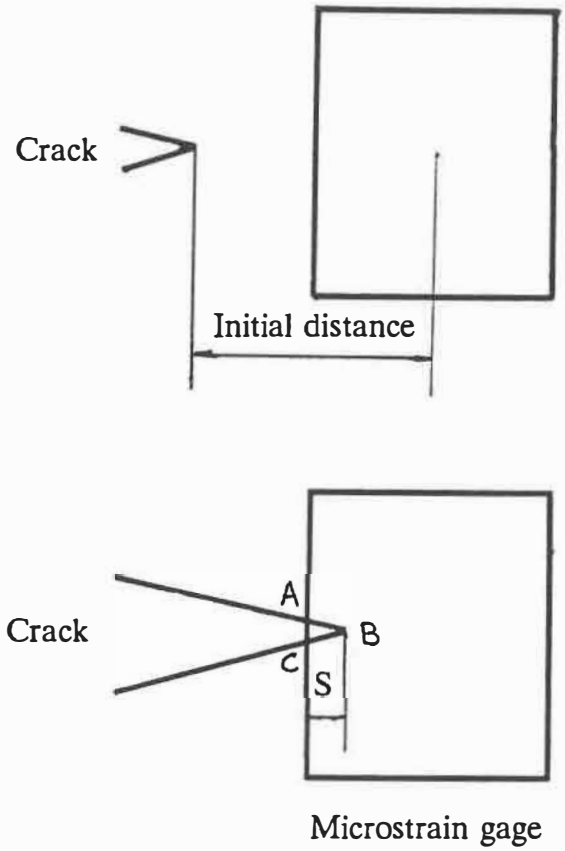

Fig. 7.21 Schematic illustration on the response of microstrain gage to fatigue crack propagation. Fatigue crack, when it propagates

BC. The base AC is proportional to the height, a. On the other hand, the area of BC equals half of the base multiplied by the height. Therefore,

$$\Delta ABC = AC \cdot a/2 \qquad (7.3)$$

$$AC = k \cdot a \qquad (7.4)$$

ıbstituting equation (7.4) into equation (7.3) yields

$$\Delta ABC = k \cdot a^2/2 \qquad (7.5)$$

ıerefore, the response of the strain gage, corresponding to area ΔABC, is a rabolic function of the crack length, a.

This approximation of the isosceles triangle configuration will be closer to ılity, when the crack increment covered by the strain gage is much larger with ;pect to the size of the transformation zone, which will not take the form of an ·sceles triangle. Figure 7.20 indicates this effect in which the relationship between : average strain and the crack increment deviates from the parabolic relation for 'ery small crack increment.

A possible problem with the consideration discussed above is over-durability the strain gage with respect to the crack length. If the strain gage is still working ter the crack propagates through the entire area of the gage, the extra area vered by the gage will be no longer an isosceles triangle but a trapezoid. In the esent study, the final failure of the specimen occurred when the fatigue crack tip ıs still under the coverage of the strain gage. This indicates that the assumption the isosceles triangle configuration is applicable till the end of fatigue crack opagation and that correspondence between the last dark band and the last steresis loop is certainly correct.

.9 Fractographic aspects of 3Y-TZP produced at serial interruption of stress :ling

In order to detect crack propagation by measuring the change in the npliance of the specimen, a microstrain gage was installed on the back face of the :cimen in two other tests (specimens YSB1 and YSB2). The strain gage model, ıditioner, exciting voltage, as well as calibration employed were identical to that ployed in the previous experiments. The R-ratio for these two tests was kept at during the entire experimental process.

An effort was made to measure crack propagation rates at low stress intensity tors on specimen YSB1 by decreasing the stress intensity factor after some crack

rowth had been detected by this gage. This specimen was cycled at a maximum ›ad of 150 N for 480 cycles, a visible change in the slope of the hysteresis loop was bserved. The cycling was then interrupted by decreasing the load linearly from 150 to 15 N in 30 seconds. Then cycling was performed successively at a maximum ›ad of 70 N for 950 cycles, at 80 N for 600 cycles, at 90 N for 500 cycles, at 100 N ›r 200 cycles, at 110 N for 30 cycles where the specimen broke.

The R-ratio was kept constant (=0.1) during the cycling interruptions. etween each change in load amplitude, the load was maintained constant at the inimum load for approximately 10 seconds. A new change in slope of the 'steresis loop was not detected by the back face strain gage until the fourth crease in load.

Figure 7.22 shows the hysteresis loops of specimen YSB1 for cycle #480 at maximum load of 150 N and for a few cycles immediately preceding. Cycle #480 as followed by the cycling interruption described above. A change in the slope of e hysteresis loops was already discernible in the preceding cycles, and a crack osure effect also became visible on these loops. The increased displacement in the steresis loops due to crack propagation became visible only at upper tip of these ops. Compared to the strain gage installed at the crack tip, the response of the ain gage on the back face was much less sensitive to crack propagation. When the igue crack became sufficient large, all the information concerning fatigue crack

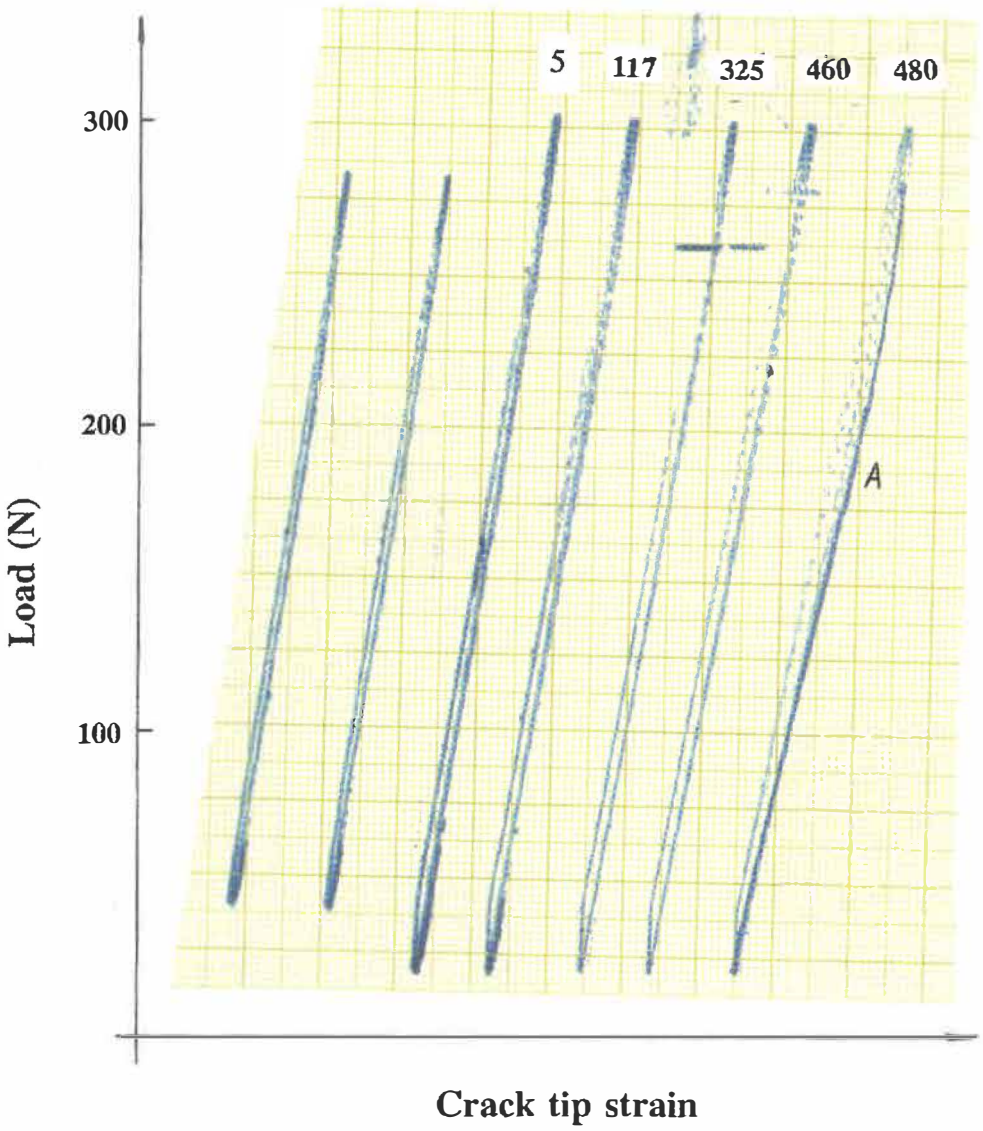

Fig. 7.22 The microstrain gage response to a linearly slow unloading deviates from the preceding loop, which indicates some slow crack propagation during the slow unloading.

opagation could be obtained by using the strain gage on the back face. From the steresis loops measured with the back face strain gage, small amounts of crack opagation could be difficult to detect, which makes the monitoring of the initial tigue crack propagation with this method more difficult.

The dark line segment A, which is bowed towards the right side of these ops, in Figure 7.22 is the record of the linear unloading that followed cycle #480. ie unloading path A deviated considerably from the hysteresis loop of cycle #480, iich indicated that the fatigue crack propagated significantly during this linear loading.

Figure 7.23 shows the fractographic features observed for this test. Large nds presenting different grey levels are present, with clear striations observed on th sides of these bands. A large bright zone, approximately 200 μm, immediately ecedes these bands, with this bright zone preceded by a region of striation-like rk bands separated by larger brighter bands. According to the fatigue cycling tory, the cycle number corresponding to each interruption of stress cycling and characteristics of the hysteresis loops (particularly, that of the line segment A Figure 7.22 which exhibits deviation from the normal loop) indicates that the iation region indicated A in Figure 7.23 formed preceding the cycling interruption, ght zone B was produced during the slow unloading in the interruption, and nds C, D, E, F resulted from each of the increases in cyclic stress which followed

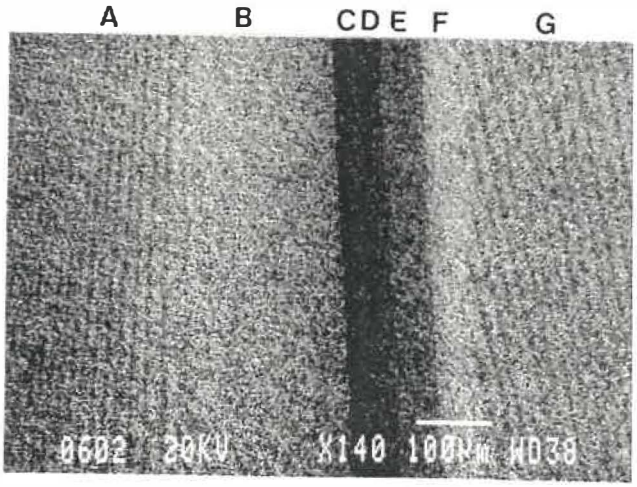

Fig. 7.23 Fatigue fracture surface produced during cycling at initial constant load range (region A), during slowly decreasing load (region B), during cycling at four different smaller load ranges (regions C, D, E and F) and during the final load range (region G) (specimen YSB1).

ıis interruption. Striation region G was produced during the final cycling orresponding to the fifth increase in the cyclic load amplitude after the ıterruption.

The average crack propagation rates in bands B, C, D, E were estimated by ividing each band width by the number of cycles associated with the corresponding ›ad range. The crack propagation rates thus obtained are presented in Figure 7.24. ompared to that obtained by extrapolating the crack propagation curve in the :gion of high stress intensity, the crack propagation rate obtained from the bands ›r low stress intensity is very high. Very probably, this can be attributed to the fluence of the transformation on the fatigue cracking. At low stress intensity, ress-induced transformation will occur only on a very small scale. In this case, its ›tential in impeding the fatigue crack propagation is limited. As a result, the tigue crack will propagate more rapidly than expected from the results obtained high stress intensity factors.

1.10 Crack velocity of 3Y-TZP in subcritical cracking

The total crack advance measured on the fracture surface which rresponded to cycle 1241 of specimen YSG1 was 24 μm, with the dark band ving a width of approximately 7 μm, and the bright zone a width of approximately μm. The fraction of the time period T of the sinusoidal load cycle spent in

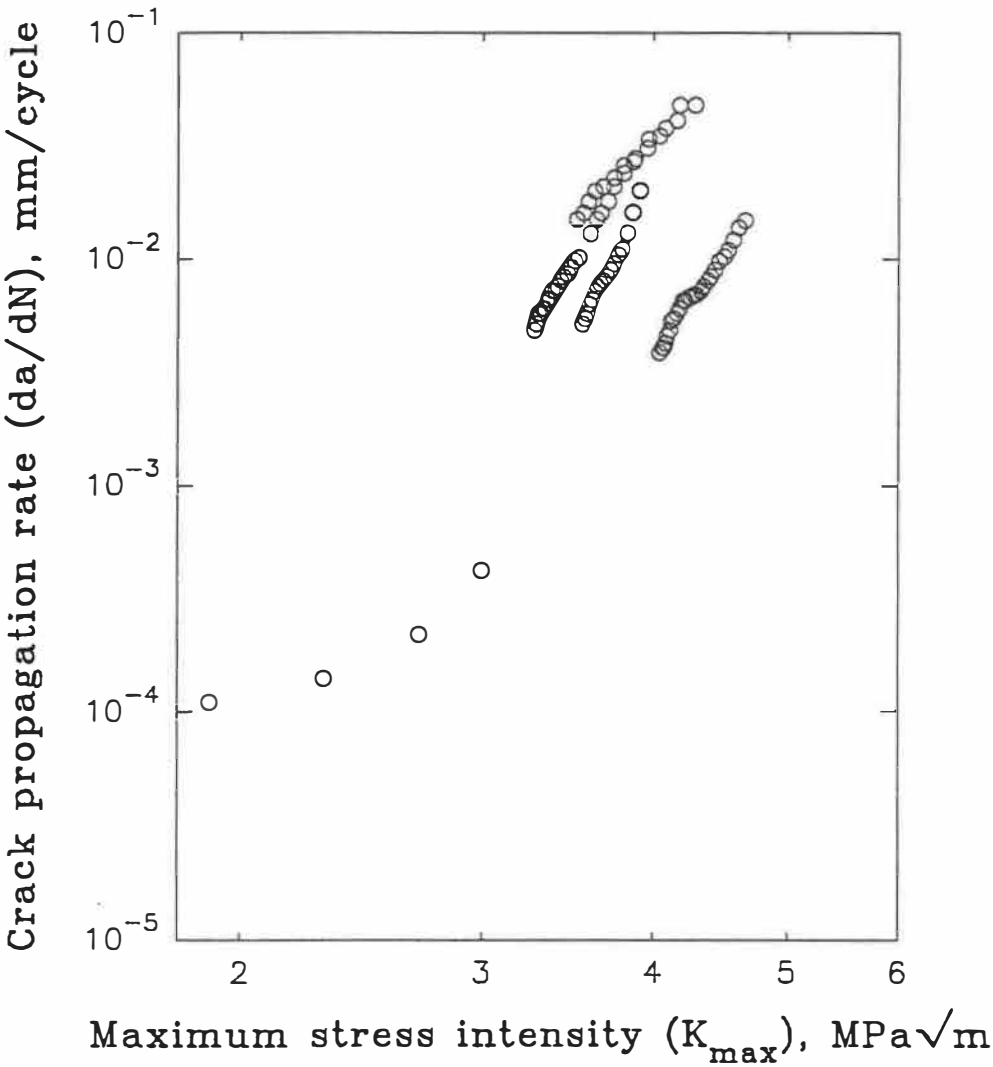

'ig. 7.24 Fatigue crack propagation rate, da/dN, versus stress intensity range, ΔK, and versus the maximum stress intensity factor, K_{max}. The data points were obtained from different specimens and each of the low crack propagation rate was obtained following a cycling interruption.

vancing the crack was approximately T/4 for the dark band and T/30 for the ght zone, as measured from the load sequence presented in Figure 7.12. The :le period T was 2 seconds in this test. Therefore, we are able to estimate the ɜrage crack velocities both in the dark band and in the bright zone for all ɜcimens by using the same method.

The cracking velocity estimated in this manner not only exhibited a very ɔng dependence on the stress intensity, but also varied in a considerable range :he same stress intensity factor for different specimens. The highest crack velocity ıproximately 0.57 mm/s) was obtained from the last bright zone (corresponding an instantaneous stress intensity of 4.5 MPa√m) of specimens YSP1 and YSP2.

The lowest velocity (approximately 0.19 mm/s) occurred in the last bright ıe of specimen YSG2 and corresponded to an instantaneous stress intensity of 4.3 'a√m. The crack velocity on the last bright zone of specimen YSG1 was estimated 0.26 mm/s. The cracking velocity in the dark band varied less for all specimens, l was approximately 0.014 mm/s. These estimations indicate that the average ck velocity in the bright zone was approximately 14 to 36 times faster than that he dark band.

As discussed above, the bright zones between the dark bands were produced ɜn the stress intensity factor acting at the crack tip was at or near its peak value.

When the peak value of stress intensity increases, the width of the bright zones increases rapidly. This appears not to be related to the stress cycling, but related to the propagation velocity. This propagation although rapid can be considered as subcritical since the crack can be arrested in the load decreasing portion. Moreover, its initiation is triggered by the start of the load decrease.

Cracking velocity is often employed to characterize this subcritical propagation. The relationship between the crack propagation velocity da/dt and the stress intensity factor K was obtained by analyzing the cracking velocities in the bright zones and the corresponding instantaneous stress intensity factors. Figure 7.25 represents the curve fitting results for the data obtained on specimen YSB1. The crack velocity da/dt is obtained by dividing each bright zone width with the associated time period, the stress intensity is the corresponding instantaneous value at which this bright zone has been produced. This analysis permitted to obtain the following relationship for specimen YSB1

$$\frac{da}{dt} = 1.97 \times 10^{-9} (K)^{12} \qquad (7.6)$$

where da/dt is the cracking velocity in mm/s and K is the stress intensity factor in Pa√m.

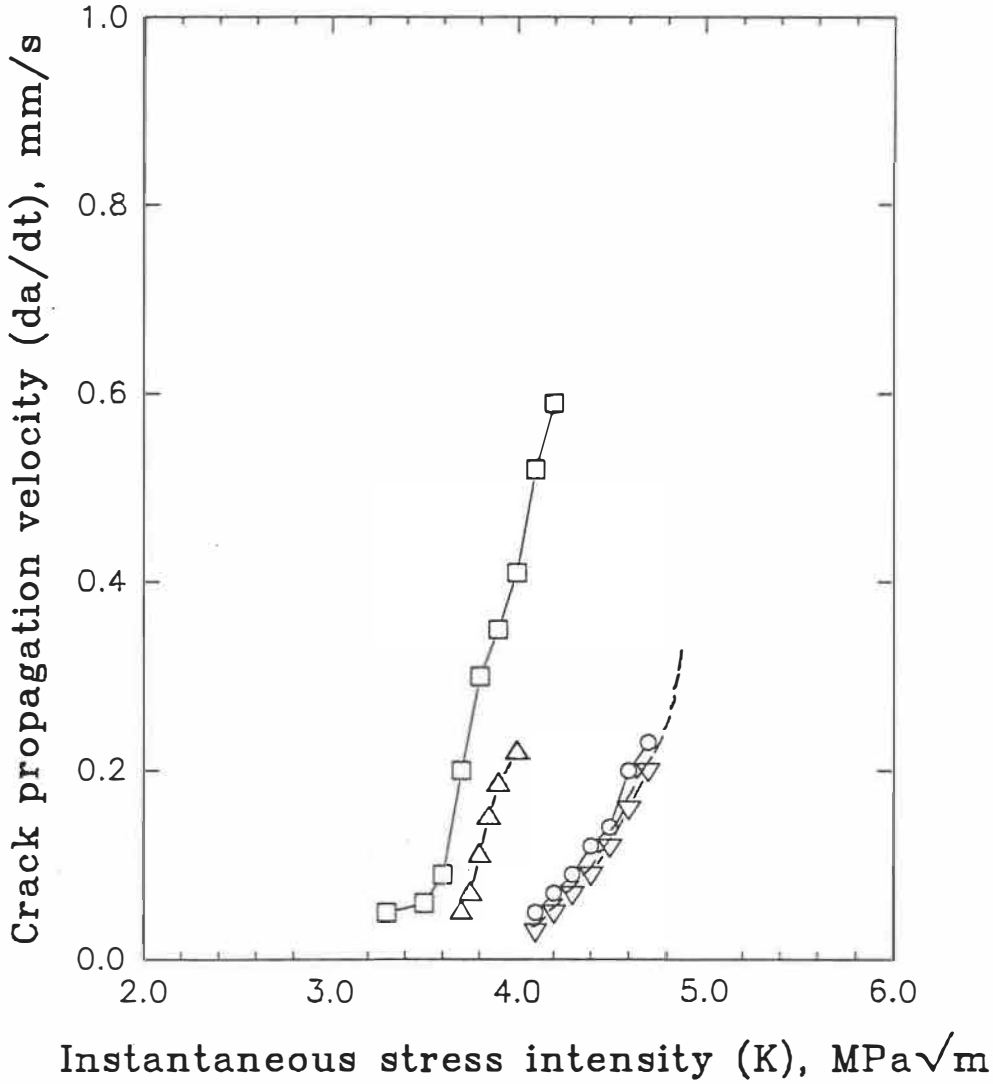

g. 7.25 Crack propagation velocity obtained in the bright zone of the striations in 3Y-TZP versus the instantaneous stress intensity factor. The data were obtained from YSP1 (square), YSP2 (triangle), YSG1 (circle) and YSB1 (inversed triangle). The dash line indicates regression of equation 7.6.

Zone B on the fracture surface of specimen YSB1, which has a width of ıpproximately 200 μm (Figure 7.23), is believed to have been produced during the ınloading performed during the cycling interruption. This unloading proceeded inearly from 4.3 to 0.43 MPa$\sqrt{m}$ in 30 seconds. This portion of fracture surface is .lso believed to have developed in a very similar manner as the bright zones in the triation regions. To verify this assumption, the integration on the increment in crack ɜngth during these 30 seconds of unloading was calculated by integrating equation .6.

$$\Delta a = \int_0^{30} 1.97 \times 10^{-9} (K)^{12} \, dt \qquad (7.7)$$

Vhich yields

$$\Delta a = 0.20 \text{ mm} \qquad (7.8)$$

This result for which the calculation details are given in Appendix 1 is in very ɔod agreement with the measurement (approximately 200 μm) made on the ıicrographs of the fracture surface. This agreement indicates that equation (7.6) ɔes adequately describe the relationship for the crack velocity as a function of K, ıce the crack has started to propagate relatively rapidly. This relationship however ınnot be expected to apply to the propagation within the dark band.

It is worth noting that the unloading time period during the interruption of 'cling is much longer than that associated with unloading in the normal cycle. The ne periods for the former and latter are 30 and 1 seconds, respectively. From the sults discussed in the previous sections, it was clearly shown that the most of the ack propagation in fatigue at high stress intensity factors occurred in a very short ne period near the peak stress intensity and that as soon as a visible change in ɔpe was observed on the hysteresis loop, a considerable amount of crack 'opagation already had occurred. During the normal tensile fatigue cycle, the stress tensity will decrease to four-fifth of its maximum value in a very short time period : 0.15 second), but it took approximately 6 seconds for the same amount of ıloading in the interruption of cycling. Therefore, in the latter case, the specimen ıs subjected to a near critical stress intensity for a relatively long time period, ıich resulted in a greater amount of crack propagation. This indicates that the cling frequency and the cyclic waveform influences the amount of fatigue crack opagation, particularly for the region of high stress intensity factor for which the ight zone is produced between striations in the form of dark bands.

The striations obtained on specimen YSB1 after the four series of cycles at ver load amplitudes were seen to be inclined with respect to the bands produced lower ΔK (Figure 7.23). It appears that in specimen YSB1 the fatigue crack nitiated in the region near the lateral surface after the bands produced at low ΔK.

his result can be considered as supporting our argument that fatigue crack initiation must occur each time that cracking resumes.

1.11 Crack deviation

After each interruption of stress cycling or change in stress cycling conditions, e average crack plane could deviate a certain angle from its preceding orientation. ıch deviation is a fairly common feature of fatigue crack propagation of metallic aterials following overloads, but such crack deviation behaviour has not been ported for ceramics.

Associated with the changes in the load amplitudes, the shade of the regions oduced on the fracture surface changed considerably. This difference in colour on e fracture surface might very probably result from changes in the crack plane ientation, i. e., from crack deviation.

By virtue of its extraordinary depth of field, SEM can be employed to aracterize the deviation angle without necessitating the destruction of the fracture face, if the deviation is sufficiently distinguishable.

When the specimen stage is tilted a certain angle, the projected distance tween two features on a crack surface will change an amount which depends on

: tilt angle and on the inclination of the crack surface to the base. Combined with : tilt angle, the projected distances before and after the tilting can be employed calculate the inclination, as long as after tilting, the two interested features are l in focus at the magnification employed.

The deviation angle, the angular difference between the average crack ›pagation planes before and after the interruption, is an important parameter in cribing and understanding the crack deviation behaviour. To obtain the deviation ;le, it is preferable to choose a reference plane and to calculate the angle ween both cracking planes of interest and this reference plane. As long as the ;le between both cracking planes and the reference plane are known, the iation angle between these two cracking planes can be easily obtained. Figure 5 schematically illustrates this consideration.

The angle between a crack plane and the reference plane, α, can be :ulated by the following equation

$$\alpha = \mathrm{Arctg}(\Delta Z/\Delta Y) \qquad (7.9)$$

:re ΔY, the projected distance between the two features, can be measured :ctly on a micrograph obtained before the tilting operation, and ΔZ is the height ɜrence, with respect to the reference plane, between these two features. This

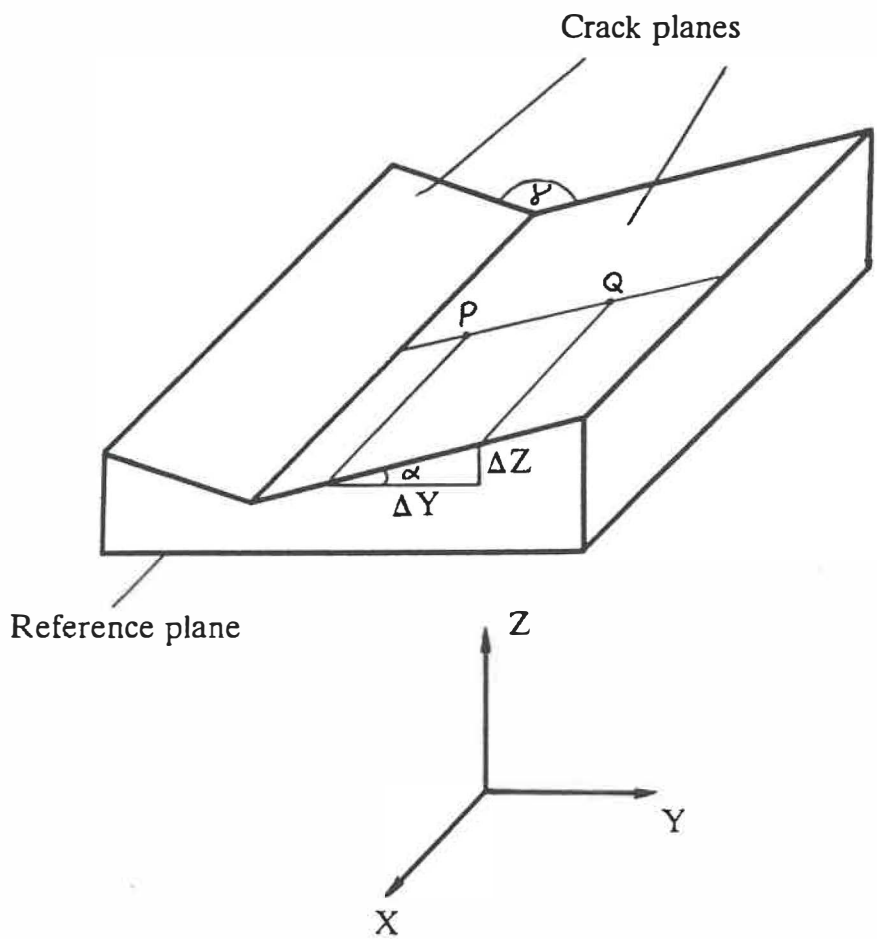

Fig. 7.26 Schematic illustration for the determination of crack deviation.

eight difference cannot be measured directly on a micrograph, but can be alculated from:

$$\Delta Z = \frac{\Delta Y' - \Delta Y \cos\beta}{\sin\beta} \qquad (7.10)$$

here $\Delta Y'$ is the projected distance on the micrographs obtained after the tilting, nd β is the tilt angle. The development of these equations is given in Appendix 2.

Figure 7.27 shows a pair of micrographs which have been taken from band nes of specimen YSB1 before and after the specimen stage was tilted an angle of) clockwise. Analyses were carried out on this portion of fatigue fracture surface ing equation (7.9). Measurements were performed on many pairs of features on ch zone, the results indicated that a shorter projection distance starting from a undary tended to give a larger deviation angle. The inclination of the average ack plane to the reference plane was found to be approximately 10° for the mbined crack plane of zones C and D, the first two zones produced after the crease in load amplitude. Because of small size of zone C, zones C and D were ken as one zone. Zone E was inclinded approximately 5° to the reference plane, d the inclination of zone F to the reference plane was approximately -5° ockwise).

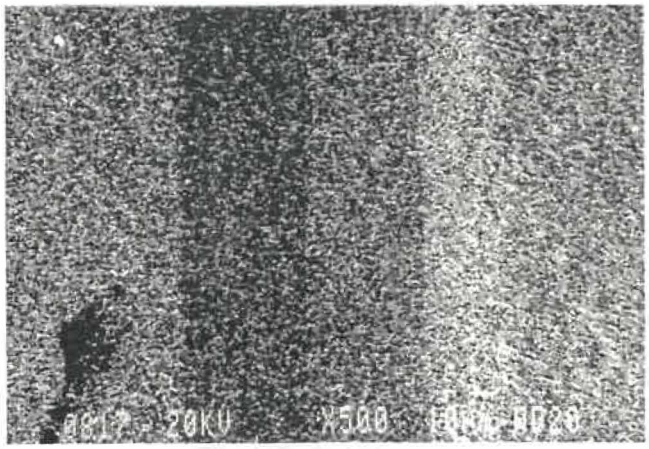

A

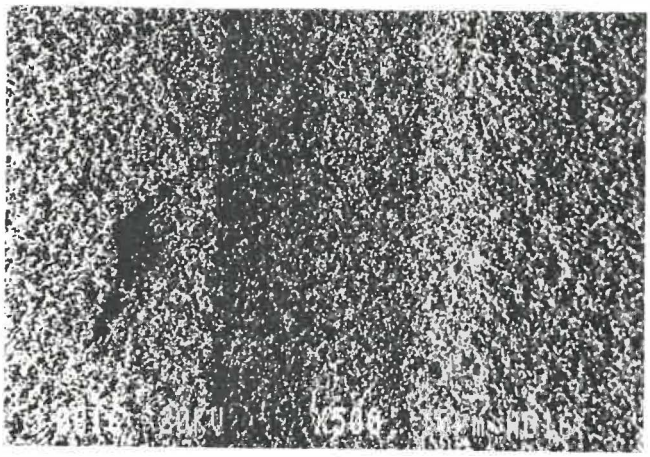

B

Fig. 7.27 Coupled micrographs for determination of the crack deviation angle. (a) micrograph at a tilt angle $\beta=0^{\circ}$, (b) micrograph of the same region at a tilt angle (clockwise) $\beta=35^{\circ}$.

The deviation angles obtained appear smaller than that observed under :reoscope. This might result from the crack plane deviating from its previous ientation due to the cycling interruption, but gradually returning towards its evious orientation as cycling continued after the interruption. As a result, a small erage crack deviation angle measured is smaller than the initial deviation angle.

Analyzing the stress cycling history for each zone suggests that the difference tween the stress intensity factors which were acting on two sides of the boundary ring fatigue should play an important role in fatigue crack deviation. It should be ted that there are two boundaries for each zone, but the boundary considered in : present discussion is the boundary by which the zone of interest connects with : preceding crack plane. The stress intensity factor at the end of zone B which inects with zone C was 0.43 MPa√m; whereas, the stress intensity factor for the ginning of zone C was 2.1 MPa√m. The difference in stress intensity factors is proximately 1.6 MPa√m at the boundary of zones B and C at which a large riation was obtained. The difference of the stress intensity factors at the indaries of the other zones was in all cases approximately 0.3 MPa√m. Another eresting feature in the crack deviation is that the fatigue crack was always inclined the reference plane, which indicates that the fatigue crack never propagated fectly perpendicular to the loading direction following the interruptions.

1.12 Topography of the dark bands

Since the striation-like dark band on the fatigue fracture surface corresponds depressions on both surfaces, it should then be produced because of a difference volume expansion. This volume expansion is caused by the difference in the size transformation zone as well as the difference in the amount of transformed rticles within this zone between the site at which the crack arrested in the evious stress cycle and the site at which rapid or temporarily unstable crack owth started.

In support of this proposal, the region at which the band appeared to be epest from observations of stereographic pairs of micrographs generally appeared be near the side of the band facing the precrack. This feature indicates an ymmetrical distribution of transformed particles with respect to the geometrically nmetrical axis of this band. A substantial amount of fatigue crack propagation in e present study resulted from stable crack growth during which only the dark band s produced.

Because of the very fine grain size ($\approx 0.25\ \mu m$), the fracture surfaces were ficiently flat to perform Nomarski interference microscopy. Measurements were rformed of the depth of the depressions associated with the dark bands by using on different microregions of the fracture surface and reading the height of

ıe objective with the vernier scale. Although these measurements showed onsiderable scatter, which appeared to result partly from variations in the depth nd partly from scatter associated with this technique, the observations indicated ıat the depth of the depression associated with the bands increased with increasing rack length and that the ratio of depression depth to the width of the length was pproximately constant. The depression depth for the last band prior to the region f final fracture was approximately 0.7 μm, while its width was approximately 10 μm.

It was also noted that the crack front markings were less visible near the teral edges (Figure 7.28). This aspect appears to be the result of the volume pansion associated with the phase transformation near the lateral surface being ıle to occur freely in the direction towards the lateral surfaces, which results in a ıaller difference in expansion between the dark band and the bright zone.

The results indicated that crack propagation under cyclic tensile stress in the ecracked specimens occurred in a continuous manner. Striation-like markings rmed on the fracture surface during fatigue crack propagation at high da/dN. The acing between striations gradually increased with increasing stress intensity factor. e width of striations also increased slightly.

.13 The regression analyses of fatigue curves

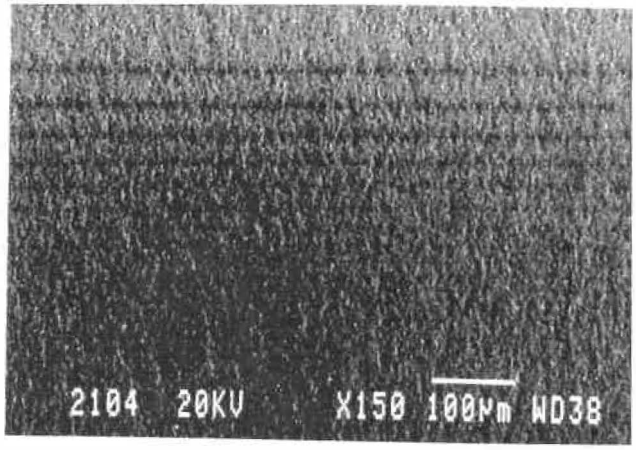

Fig. 7.28 Striations are less visible near the lateral surface (to avoid the corner effect, the right edge of this micrograph was placed approximately 20 μm from the lateral surface).

By using the similar method as for specimens YSP1 in the previous section, the fatigue crack propagation per cycle da/dN for specimens YSG2, YSP2, YSB1, YSB2 are plotted as a function of ΔK or K_{max}.

Linear regression analysis, employing the least square method, was applied o the log-log curves of crack rates determined from the interstriation spacings as ı function of the corresponding stress intensity. The following results were obtained:

'or specimen YSP1,

$$da/dN = 5.7x10^{-5}(\Delta K)^{6.6} \quad (7.11)$$

$$da/dN = 4.1x10^{-6}(K_{max})^{6.6} \quad (7.12)$$

'or specimen YSP2,

$$da/dN = 3.7x10^{-6}(\Delta K)^{7.5} \quad (7.13)$$

$$da/dN = 1.0x10^{-6}(K_{max})^{7.5} \quad (7.14)$$

or specimen YSG1,

$$da/dN = 4x10^{-11}(\Delta K)^{11} \quad (7.15)$$

$$da/dN = 4.6x10^{-12}(K_{max})^{11} \quad (7.16)$$

or specimen YSG2,

$$da/dN = 1x10^{-14}(\Delta K)^{12} \quad (7.17)$$

$$da/dN = 1x10^{-14.7}(K_{max})^{12} \quad (7.18)$$

or specimen YSB1

$$da/dN = 5x10^{-9}(\Delta K)^{11} \quad (7.19)$$

$$da/dN = 4x10^{-10}(K_{max})^{11} \quad (7.20)$$

r specimen YSB2

$$da/dN = 2x10^{-9}(\Delta K)^{10} \quad (7.21)$$

$$da/dN = 1x10^{-10}(K_{max})^{10} \quad (7.22)$$

e correlation coefficients obtained for these analyses were all greater than 0.94. :an therefore be seen that the Paris law expresses well the relationships between : crack propagation rate and the applied stress intensity factor. However, the ›onents m for different specimens of 3Y-TZP showed considerable variation. This y result from that the prenotch plane was not perfectly parallel to the loading ɜction or from that the curvature, which was produced by circular diamond saw,

at the prenotch tip across the thickness of specimen was different for each specimen.

7.2 Fatigue cracking in zirconia-toughened alumina under cyclic tensile stress

Fatigue crack propagation was also investigated on compressively fatigue-precracked specimens of zirconia toughened alumina (ZTA).

The same loading train as for the tensile fatigue of 3Y-TZP was used. A constant load amplitude was employed at a frequency of 0.5 Hz. For detection of cracking under tensile stresses, microstrain gages were installed at the precrack tip. The strain gage responses were monitored and recorded on an X-Y plotter.

7.2.1 Crack propagation in ZTA under tensile stresses

The fatigue cracking under cyclic tensile stresses in ZTA was successfully obtained only in the material designated as AZ containing Al_2O_3 (90 wt%), MgO-stabilized ZrO_2 (5 wt%), and pure ZrO_2 in the monoclinic structure (5 wt%). In the other two type of materials AM and AN, the cyclic tensile fatigue was also performed, but specimens all fractured prematurely along processing defects. Otherwise, the fatigue cracking under tensile stress should exist in such materials

ecause of their better toughness. Specimen dimensions were a length of 42 mm, a ickness of 5 mm, and a width of 7 mm. The notch length introduced was 3.5 mm.

The hysteresis loops measured from the microstrain gage indicated that the igue cracking occurred in a continuous and stable manner for the ZTA-AZ aterial (Figure 7.29). The slope of the hysteresis loops decreased with increasing cle number, which suggests that the fatigue crack grew continuously with reasing cycle number. The area encircled by the loop also increased with reasing cycle number.

It was found that the slope obtained under decreasing load was steeper in the portion of the loop than near the middle of the loop where this slope was proximately linear. This behaviour indicates that some crack propagation, even nor, is occurring while the load was starting to decrease. The slope obtained der increasing load was steeper in the bottom portion of the loop than near the idle portion. This is a typical of a crack closure effect.

Figure 7.29 also shows the last few cycles immediately prior to the final ture. The hysteresis loop next to the last cycle shows very similar behaviour to t obtained in the 3Y-TZP material.

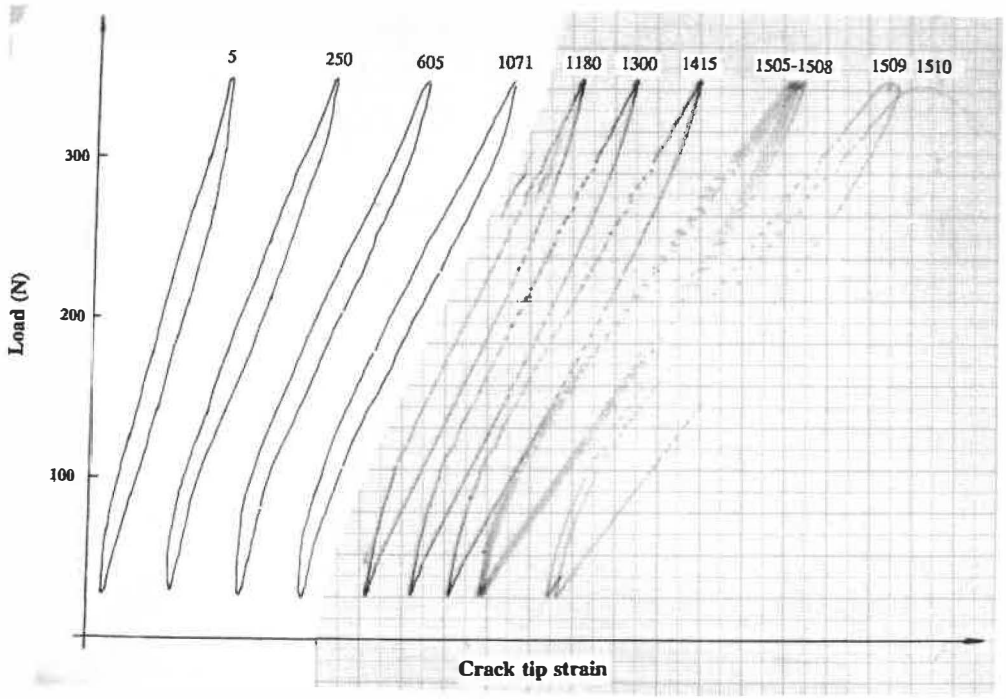

Fig. 7.29 Hysteresis loops obtained in ZTA-AZ material with microstrain gage showing that the strain increased gradually with increasing cycle number during tensile fatigue.

The relationship between the average strain measured with the microstrain gage and the number of load cycles shows clearly a continuous increase in the displacement (Figure 7.30). In the beginning of fatigue, the displacement increased rapidly, which very probably resulted from residual tensile stresses produced by the compression fatigue. If a certain zone is already damaged during compressive fatigue, fatigue crack under tensile stresses could propagate more rapidly than the normal rate in this zone. The crack propagation gradually became more stable with increasing cycle number. The strain measured by the crack tip strain gage increased linearly with increasing cycle number. Finally, the fatigue crack near its critical size grew very rapidly until final fracture.

According to the modelling mentioned previously in section 7.1.8, the crack tip strain D is a parabolic function of the crack length, a, produced in tensile fatigue. When the symmetrical axis is parallel to the horizontal axis of the coordinate system, which is the case in the present study, the parabolic function takes a simple form,

$$D = A\,a^2 + C \qquad (7.23)$$

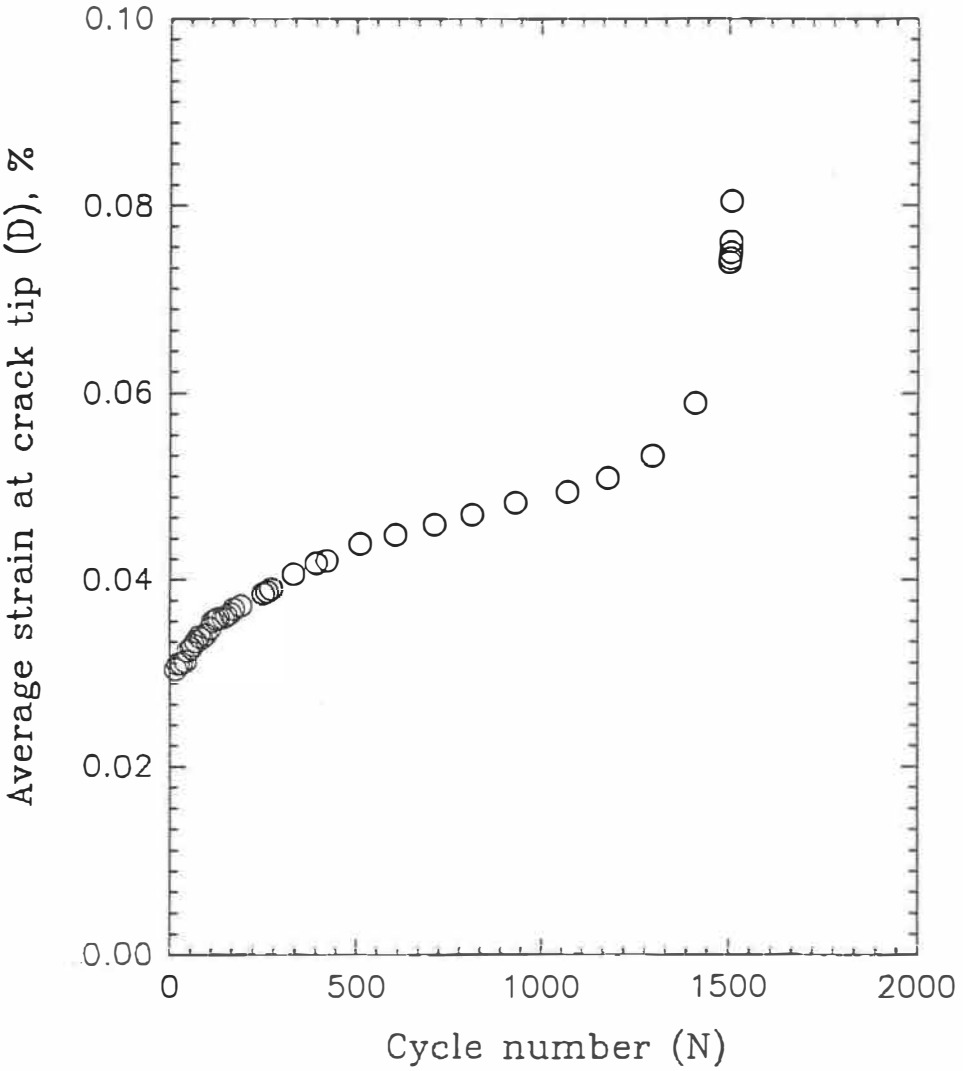

Fig. 7.30 The Strain, D, measured with the microstrain gage at the fatigue crack tip as a function of the cycle number during tensile fatigue (ZTA-AZ material).

) measured on the first cycle was taken as corresponding to the beginning of fatigue racking where the crack length increment produced in tensile fatigue was zero, hile D measured on the last cycle corresponded to the final fatigue crack length hich could be measured on the fractograph and this measurement indicated 0.7 ım of propagation in tensile fatigue. With these two sets of boundary conditions, ɔnstants A and C were obtained. The crack length for each cycle during the test ın be calculated from D by rearranging equation (7.23) and using the obtained ɔnstants A and C.

The cyclic stress intensity range, ΔK, and the maximum stress intensity factor, $_{max}$, could be obtained for each cycle by using specimen geometry, loading ırameters, and the calculated fatigue crack length for each cycle. Therefore, the ack propagation rate da/dN as a function of the stress intensity factor can also be ɔtained (Figure 7.31). The results show that fatigue crack propagated slower in ΓA-AZ than in 3Y-TZP and that the critical stress intensity factor below which tigue cracking occurs slightly higher in ZTA-AZ than in 3Y-TZP.

2.2 Fracture surface observations of ZTA for tensile fatigue

Observations were carried out by scanning electron microscopy on the fatigue ıcture surfaces. The general aspects of the entire fracture surface is presented in gure 7.32. A transition zone (approximately 50 μm in width) was observed at the

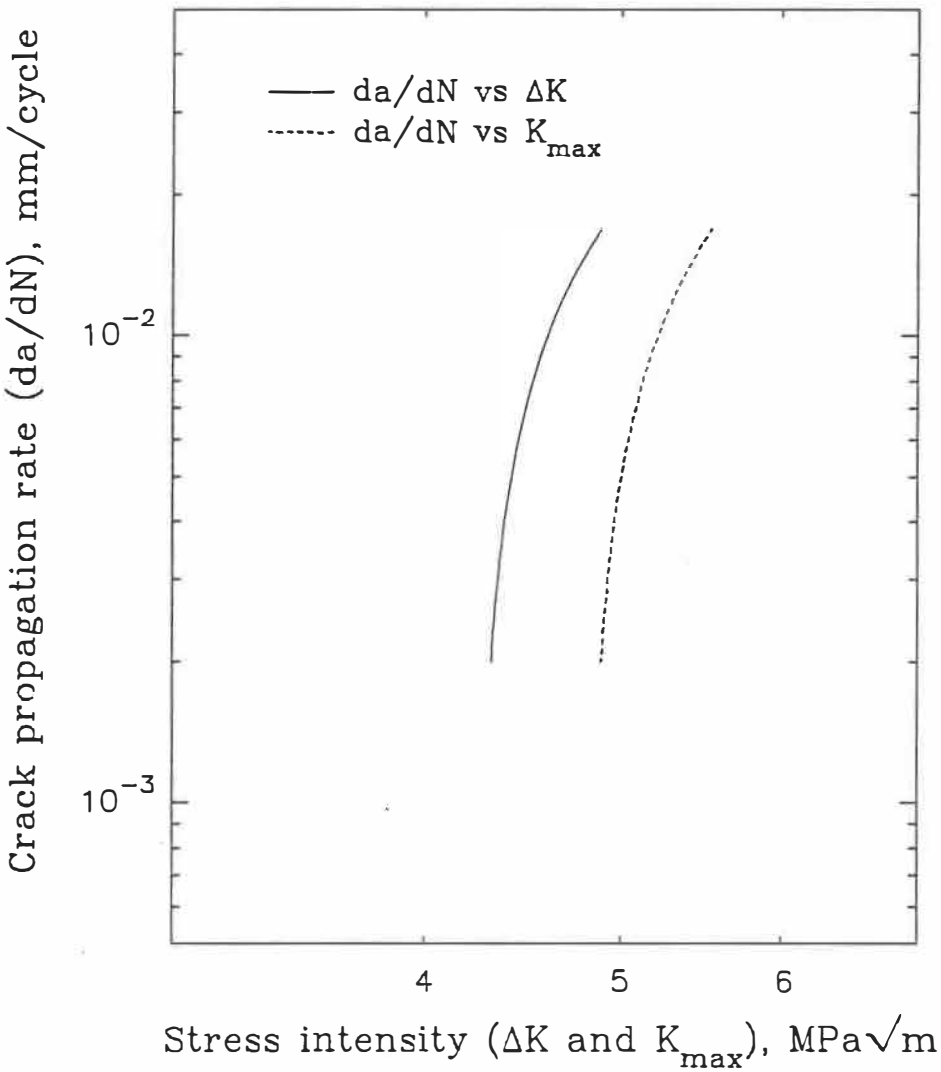

Fig. 7.31 The relation between the crack propagation rate, da/dN, and the stress intensity range ΔK and maximum stress intensity factor, K_{max}, in ZTA (ZTA-AZ material).

oundary between the compression fatigue and the tensile fatigue. Figure 5.20 btained at large magnification shows another portion of the transition zone which onsisted primarily of intergranular fracture, occasional of transgranular facets and artly of fragmented particles which were detached from the fracture surface. The mount of detached particles observed decreased with increase in the fatigue crack ngth.

The typical aspect at the boundary between the compression and the tension tigue is presented in Figure 5.21. A amount of small particles can be observed on e side of compression fatigue fracture surface, and a large difference in height can so be seen at this boundary. Tension fatigue crack appears to initiate more dependently in this area than in other areas.

Although no well-defined striations were observed on the fatigue fracture rfaces, some lines were present (Figure 7.33) perpendicular to the crack opagation direction. These lines correspond to changes in height of the crack ane and therefore to probable intermediate positions of the crack front.

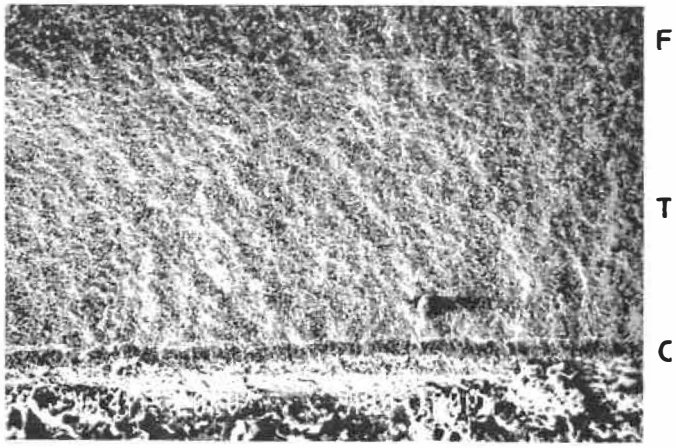

Fig. 7.32 General fracture surface aspects in ZTA showing compression fatigue fracture surface (indicated by C), tensile fatigue fracture surface (T) and the final fracture surface (F).

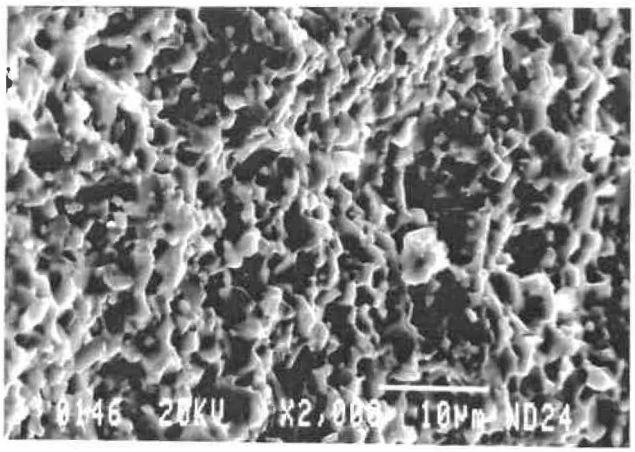

Fig. 7.33 Some ridge lines present parallel to the crack front in ZTA (crack propagates from the left to the right).

CHAPTER 8 CHARACTERIZATIONS OF STRESS-INDUCED TRANSFORMATION

In the present study, 3 mol% yttria-stabilized tetragonal zirconia polycrystals ;Y-TZP) has been employed. This ceramics consists of metastable tetragonal phase ıd is subject to stress-induced transformation which occurred by transforming the tragonal phase to monoclinic phase. The detection of its occurrence and the easurement its magnitude are essential to understanding transformation-related ıcture behaviour. Although limited to macro-analysis, X-ray diffraction (XRD) is widely used technique in the measurement of the transformation. For local analysis ı an order of 1 μm), Raman microscopy has been employed by different authors)7,103,104,105]. Therefore, XRD and Raman microscope were employed in the esent study to detect and measure the stress-induced transformation.

X-ray diffraction measurement on stress-induced transformation in 3Y-TZP

X-ray diffraction measurements were performed in a Phillips diffractometer, V1015. The X-ray incident beam was 3 mm by 7 mm. To obtain monochromatized Kα radiation, a graphite monochromator was used. The step-scanning fraction technique was employed, with a rotation speed about the symmetrical s of $2\theta=1^{\circ}$/min. Diffraction measurements were started at $2\theta=15^{\circ}$ and finished $2\theta=45^{\circ}$.

Specimen was attached to the holder by a small, a thin layer of glue to inimize the noise coming from the material (normally plasticine) holding the ecimen. This method reduced the noise dramatically compared to holding the ecimen with plasticine.

To decrease broadening of the target peaks and to favour obtaining well-parated peaks, portions of fracture surfaces, 2 mm in width and 5 mm in length, re also analyzed by the diffractometer.

.1 X-ray diffraction on the lateral surface of compressed specimens

X-ray diffraction was performed on the lateral surface of specimen mpressed uniaxially on the two end surfaces. Specimen was loaded to a certain mpressive stress level, held for approximately 10 seconds, released from the ding train, and diffracted on diffractometer. If there was no detectable nsformation on the lateral surfaces of the specimens, the compressive stress was reased by 200 MPa. Transformation was detectable from 900 MPa to 3000 MPa compressive stress. At the latter stress, the specimen fractured in a longitudinal it manner (Figure 8.1).

Results of these tests showed that some transformation had occurred as a ult of the compressive loading. Compared to the free surface before the

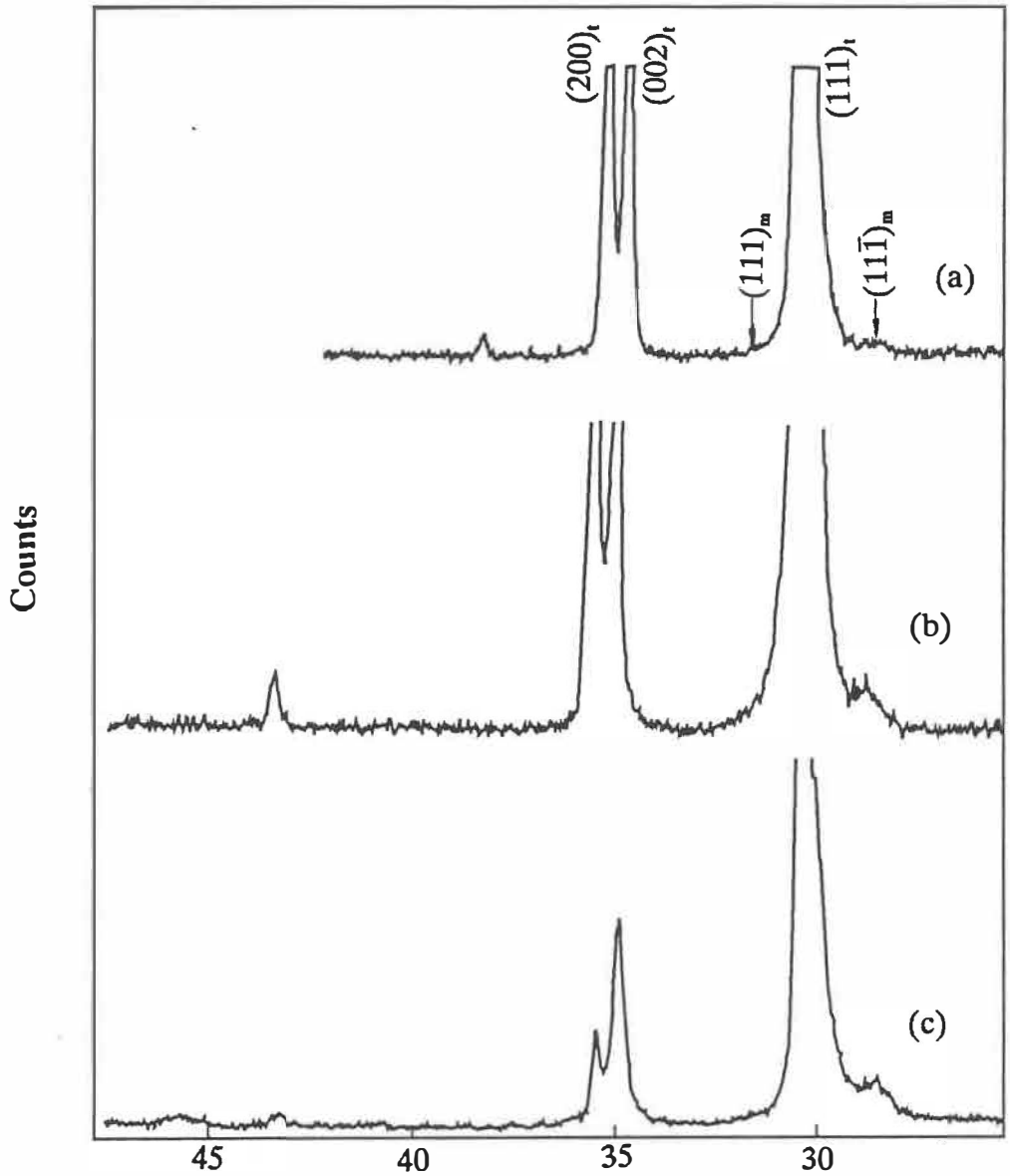

Fig. 8.1 X-ray diffraction spectra obtained from the lateral surface after uniaxial compression. The $(11\bar{1})_m$ peak indicates the occurrence of the t- to m-phase transformation: (a) spectrum obtained on the free surface, (b) spectrum obtained after compression at 900 MPa, (c) spectrum obtained after compression at 3000 MPa.

ɔmpression test, which was almost pure tetragonal phase, when the transformation ccurred, the intensity for $(111)_t$ decreased. The intensity for $(11\bar{1})_m$ and $(11\bar{1})_m$ also ıcreased, but the $(111)_m$ peak was too small to be discerned. One can see that the tensity for $(11\bar{1})_m$ was slightly higher for a compressive stress 3000 MPa than for)0 MPa.

When a mixture of the tetragonal and monoclinic phases is detected, which commonly encountered in most studies, a mixed spectrum of these two phases is ɔtained. The $(200)_t$ (relative intensity from standard index, R.I.60%) and $(002)_t$;.I.20%) peaks in the region 2θ=34-36° overlap with the $(200)_m$ (R.I.14%) and $20)_m$ (R.I.12%) peaks. These two peaks are very sensitive to tetragonal to ɔnoclinic phase transformation. When transformation occurs, $(200)_t$ intensity will op much more than that for $(002)_t$ due to their relative intensity ratios. The ensity of $(002)_m$ peak which overlaps the $(200)_t$ will increase almost the same as ıt of the $(020)_m$ which overlaps the $(002)_t$. This is the probable reason that the ensity of the $(200)_t$ peak has become much smaller than that of $(002)_t$.

It should be mentioned that the condition in which X-ray diffraction indices d been obtained on the monoclinic (card 13-307) and the tetragonal (card 14-543) ases of zirconia would be a little different from the material used in the present dy. First, the composition was not the pure zirconia in the present study. Second, the pure zirconia, tetragonal phase does not exist at room temperature, the index

or this structure has been supplied by either calculation (card 24-1164) or a special echnique (card 14-534) [106].

.1.2 X-ray diffraction on the compressive and tensile surfaces in bending

In order to detect transformation on specimen being loaded, a miniature antilever grip which could be installed in the chamber of diffractometer was esigned. Sliced specimens (40 mm in length, 5 mm in width, and 1.5 mm in ıickness) were examined by using this grip. XRD was carried out both on the ɔmpressive and on the tensile surfaces of the sliced specimen in bending with the ıalyses made on the original surfaces rather than on the surfaces produced during icing. On the later surface, some transformed particles will be introduced during icing.

Results obtained on these specimens showed that stress-induced ansformation was not detected before specimen failure. Since it is improbable that versible stress-induced transformation could be obtained at room temperature, this sult indicates that the stress applied was still inferior to the threshold stress which minimum stress to induce a detectable amount of transformation. In bending, the plied load cannot be applied too high due to relative low tensile strength mpared to the compression strength of ceramics. In bending, the applied stress ıich initiates fracture at the tensile surface is still relatively low with respect to the

ompressive strength. As well, slicing the specimen introduce microcracks at the rface, facilitating the failure of the specimen in bending.

1.3 X-ray measurement on fracture surface

To verify the transformation associated with fracture, the fracture surfaces ere analyzed by X-ray diffraction. Figure 8.2 shows a typical spectrum from a acture surface. It presents several differences with respect to the spectrum from free surface. The $(11\bar{1})_m$ peak, which indicates the occurrence of the nsformation, is present. The $(111)_m$ peak also could be discerned, even if very all. The intensities of $(200)_t$ and $(002)_t$ decreased but that of the smaller peak creased more. The relative amount of transformed particles can be calculated m the integrated intensity,

Kosmac et al [42] have proposed a very simplified model for the calculation the transformation zone size. They supposed the volumetric fraction of nsformed particles in this zone, X_{trans}, was 1 (i.e., full transformation), but outside zone the volumetric fraction of transformed particles was equal to that in the k before the test, X_{bulk}. They obtained an equation,

$$a = \frac{\sin\theta}{2\mu} \ln \frac{X_{bulk} - X_{trans}}{X_{meas} - X_{trans}} \qquad (8.1)$$

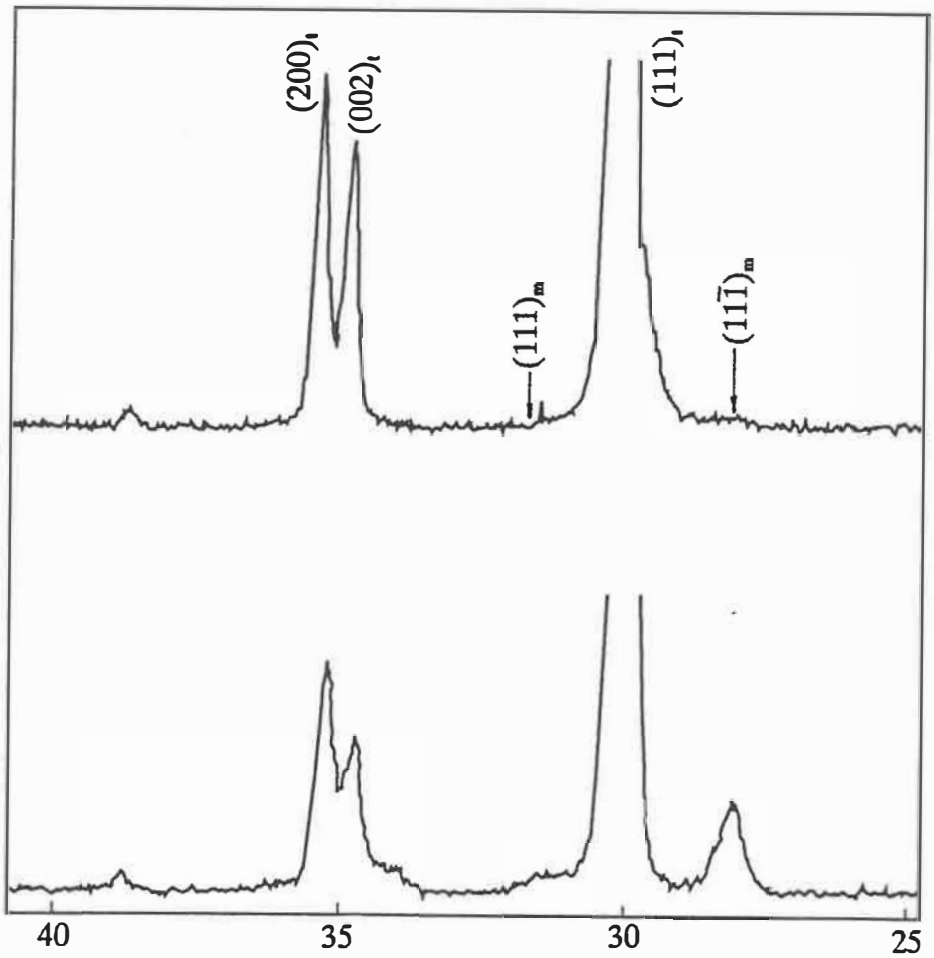

Fig. 8.2 X-ray diffraction spectra obtained from the fracture surface. (a) spectrum obtained on the free surface, (b) spectrum obtained on the fracture surface in which the peak $(11\bar{1})_m$ is clearly observed indicating the occurrence of the t- to m-phase transformation.

ere X_{trans} is the fraction of the transformed tetragonal particles (assumed equal 1) in the transformation zone; X_{bulk} is the volumetric fraction of monoclinic phase fore the fracture test; X_{meas} is the measured fraction of monoclinic phase after the cture test, as calculated by equation (2.2); θ is the diffraction angle which is 15°; s the absorption coefficient.

Several other models have been proposed, which also differ from the real tribution of transformed particles across the zone depth of the transformation ıe. Direct measurements by Raman microscopy showed that the volumetric portion of transformed particles gradually decreased from the fracture surface ards the interior of specimens.

The present author analyzed a measured distribution of transformed particles a function of the distance obtained by Raman spectroscopy on yttria-stabilized onia in reference [108] and found that a power cosine expression give a better vith the measured data. This expression is the following:

$$F_v = \cos^n(bx) \qquad (8.2)$$

re F_v is the volumetric fraction of transformed particles over the total volume,

is the depth measured from fracture surface into the bulk, and n and b are ›nstants. For a fracture surface on which particles highly transformed n will be gh. For the data considered from reference [108], n was found to be approximately Accordingly,

$$F_v = \cos^8(bx) \qquad (8.3)$$

ppose F_v is 1 on the fracture surface, and F_v is 0 outside of the transformation ne (Figure 8.3). Accordingly, X_{bulk} will be 0 and X_{trans} will 1, if Kosmac's model employed to describe this situation. Make the two areas A and B equal (Figure ›), so that

$$\int_0^{\frac{\pi}{2b}} F_v \, dx = 1 \times a \qquad (8.4)$$

bstituting $\cos^8(bx)$ for F_v in equation (8.4), then yields

$$\int_0^{\frac{\pi}{2b}} \cos^8(bx) \, dx = a \qquad (8.5)$$

›ceeding with this integration, one obtains,

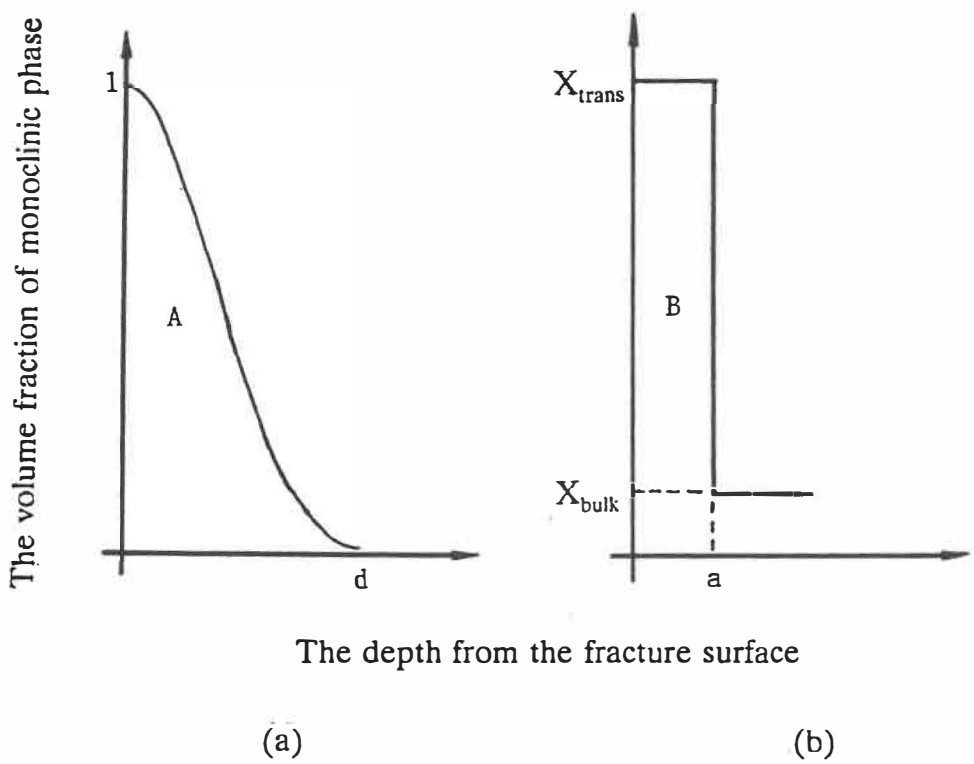

Fig. 8.3 a) more realistic distribution profile of transformation particles assumed in the present study is compared to b) that assumed by Kosmac et al [900]. The transformation volume is supposed to be equal in both areas. Therefore, area A in (a) is assumed equal to area B in (b).

$$b = \frac{105\ \pi}{768\ a} \qquad (8.6)$$

ubstituting equation (8.6) for b in equation (8.5), yields,

$$F_v = \cos^8\left(\frac{105\ \pi\ x}{768\ a}\right) \qquad (8.7)$$

ıe transformation zone size is then given by the x value at $F_v = 0$. For $F_v = 0$, ıuation (8.7) permits to obtain,

$$\frac{105\ \pi\ x}{768\ a} = \frac{\pi}{2} \qquad (8.8)$$

ım which,

$$x \approx 4\ a \qquad (8.9)$$

e transformed zone size, x calculated in this manner, is approximately 3.7 times large as Kosmac's transformation zone size, a.

In the present study, θ is 15°, X_{bulk} is zero, X_{trans} is assumed to be 1. The ear absorption coefficient, μ, is 661.87/cm, X_{meas} calculated by equation (2-2) with egrated intensities of $(11\bar{1})_m$, $(111)_m$ and $(111)_t$ is 0.30. The transformation zone e a calculated by equation (8.1) (Kosmac's model) is approximately 1 micron. ith the more realistic transformation distribution assumed in the present study, **x**, m equation (8.9) is approximately 3.5 microns.

The observations made of the fourth zone on the fracture surface produced compression fatigue and on the dark band in cyclic tensile fatigue indicate that ir width is approximately 5 to 10 μm. The width of the striation-like dark bands uld be related in some manner to the size of the stress-induced transformation ne. This relationship however should not be simple, since the results indicate that re is some stable crack growth while at the same time the transformation zone the moving crack tip increases in size. The similar width of the fourth ctographic zone produced in 3Y-TZP by compression fatigue to that of these dark nd however appears fortuitous. This is indicated by the larger size of the responding zone observed for the ZTA materials. Since compression fatigue pagates the crack in these ceramic materials as a notch which progressively omes sharper, the size of the final fractographic zone produced by compression gue appears to be determined by sufficient debris particle-induced crack closure urring beyond this notch-crack tip to stop the compression fatigue propagation. size of the fourth zone will therefore also be influenced by the width or opening

of the notch tip. The larger final fractographic zone obtained for the ZTA material hould therefore be related to the crack in this material propagating as a wider notch. The widths of these dark bands are in reasonable agreement but as expected arger than the present estimation of the transformation zone size from the X-ray iffraction data.

.2 Characterization of the phase transformation by Raman microscopy

The monoclinic and tetragonal phases are reported to have distinct and haracteristic Raman spectra [110,116,117]. Raman microscopy has specific dvantages for the detection of this phase transformation. In particular, it provides emarkable spatial resolution, and spontaneous transformation does not occur during e measurements.

Raman microscopy was carried out with an argon ion laser with a wavelength 514 nm at the Ontario Laser and Lightwave Research Centre (OLLRC). The cident laser beam was focused on the spot to be characterized using an optical icroscope. The diameter of the focused laser beam on the specimen can be easured on the microscope and was approximately 8 μm. As the intensity of the ser beam has a Gaussian distribution with respect to the distance from the centre beam, Raman scattering emissions detected by the sensor come primarily from e central region which has a diameter of less than 5 μm. The spectral output is

amplified and displayed as intensity versus Raman shift. To have a more distinguishable spectrum, the duration of detection on each spot was set to 20 minutes. Data acquisition and processing were accomplished by a computer.

Typical Raman spectra obtained from the tetragonal and monoclinic structures [107] are presented in Figure 8.4. Two prominent peaks for the pure etragonal structure are the peaks obtained at Raman shifts of 148/cm and 264/cm which are the deviation from the incident beam and are measured by the number of the wavelength of the incident beam par centimetre. Two major peaks for the pure monoclinic structure are those obtained at Raman shifts of 181/cm and 192/cm. The latter two peaks will present between the two prominent peaks of the pure etragonal structure, in case of the characterization of a mixture of these two tructures.

A spectrum obtained from the free surface which contains almost pure tragonal phase is presented as intensity versus Raman shift in Figure 8.5. There some overlap of the monoclinic and tetragonal lines for Raman shift greater than 00/cm. The spectrum of the pure monoclinic phase is given in reference [107]. Two eaks at Raman shift numbers 261/cm and 149/cm are very strong and are aracteristic of the tetragonal phase. When transformation of the tetragonal to the onoclinic phase occurs, two characteristic peaks 181/cm and 192/cm of the onoclinic phase will be present between the Raman shift 261/cm and 149/cm.

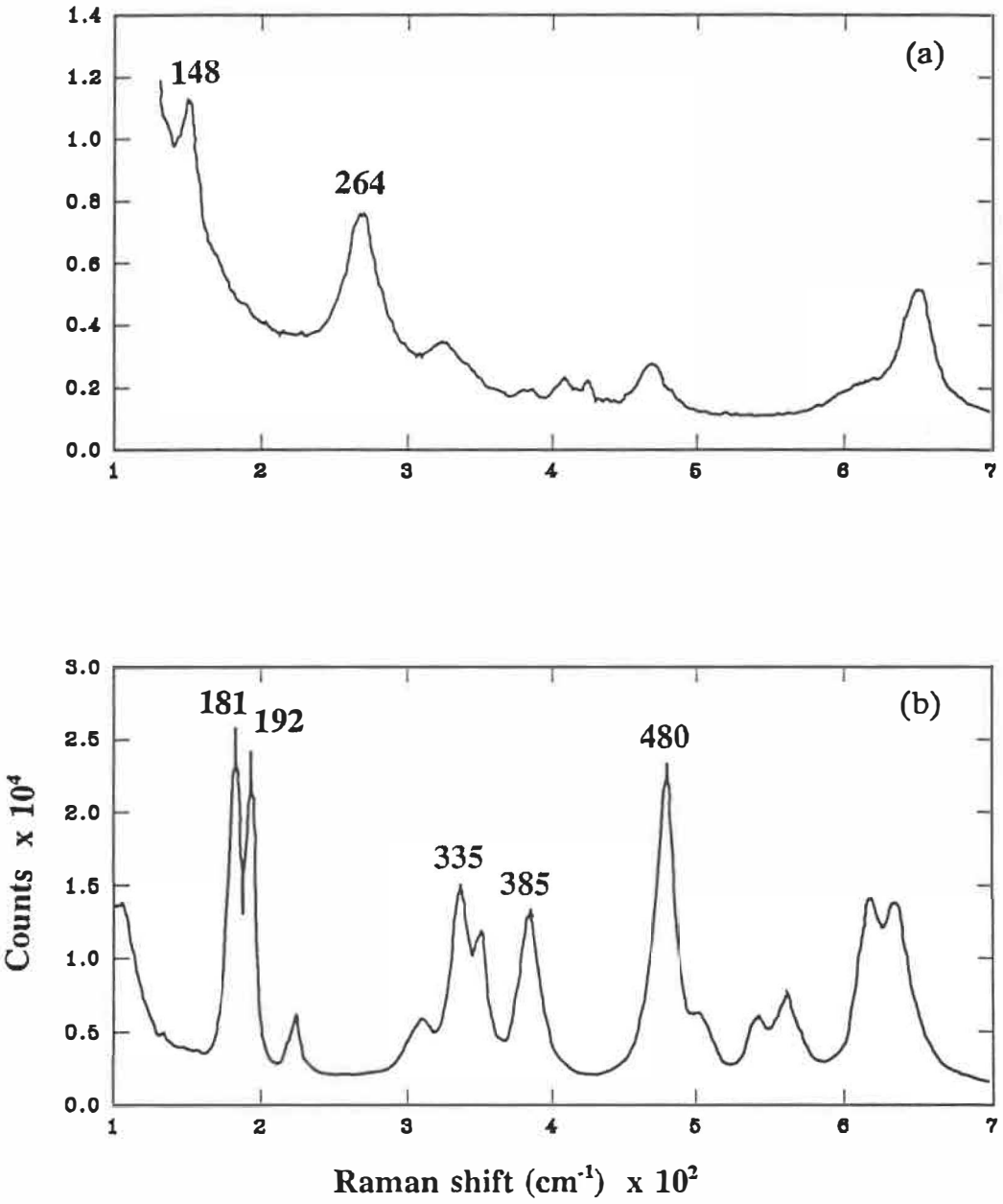

ig. 8.4 Typical Raman spectra. (A) Raman spectrum obtained from the tetragonal structure of ZrO_2, (B) Raman spectrum obtained from the monoclinic structure of ZrO_2.

Special attention will therefore be given to these 181/cm and 192/cm peaks in the following analyses.

Measurements were carried out on many successive striations on the fracture surface as well as in the bright spacings between striations.

Spectra obtained on the last striation and that obtained on the last bright zone (the zone just before the last striation) on specimen YSP1 showed a considerable difference in the intensity of the overlapped peaks of 181/cm and 192/cm (Figure 8.5). When more transformed particles are present, the contribution of these particles will result in an increase in the intensities of the 181/cm and 192/cm peaks as well as of the background intensity. Therefore, the real increase in the amount of transformed particles will be greater than that observed by the change of relative intensities. Comparison made on the spectra of the last spacing and part of final fracture surface (at a distance of 10 microns from the last dark band) indicated that the amount of transformed particles in these two regions were very similar. The intensity of the (181) peak in the last dark band or striation which is in between the last bright zone and the final fracture region was considerably smaller.

Clarke and Adar [107] have transfered an equation given by Garvie and Nicholson [41] for X-ray volume fraction analysis into Raman microscopic analysis.

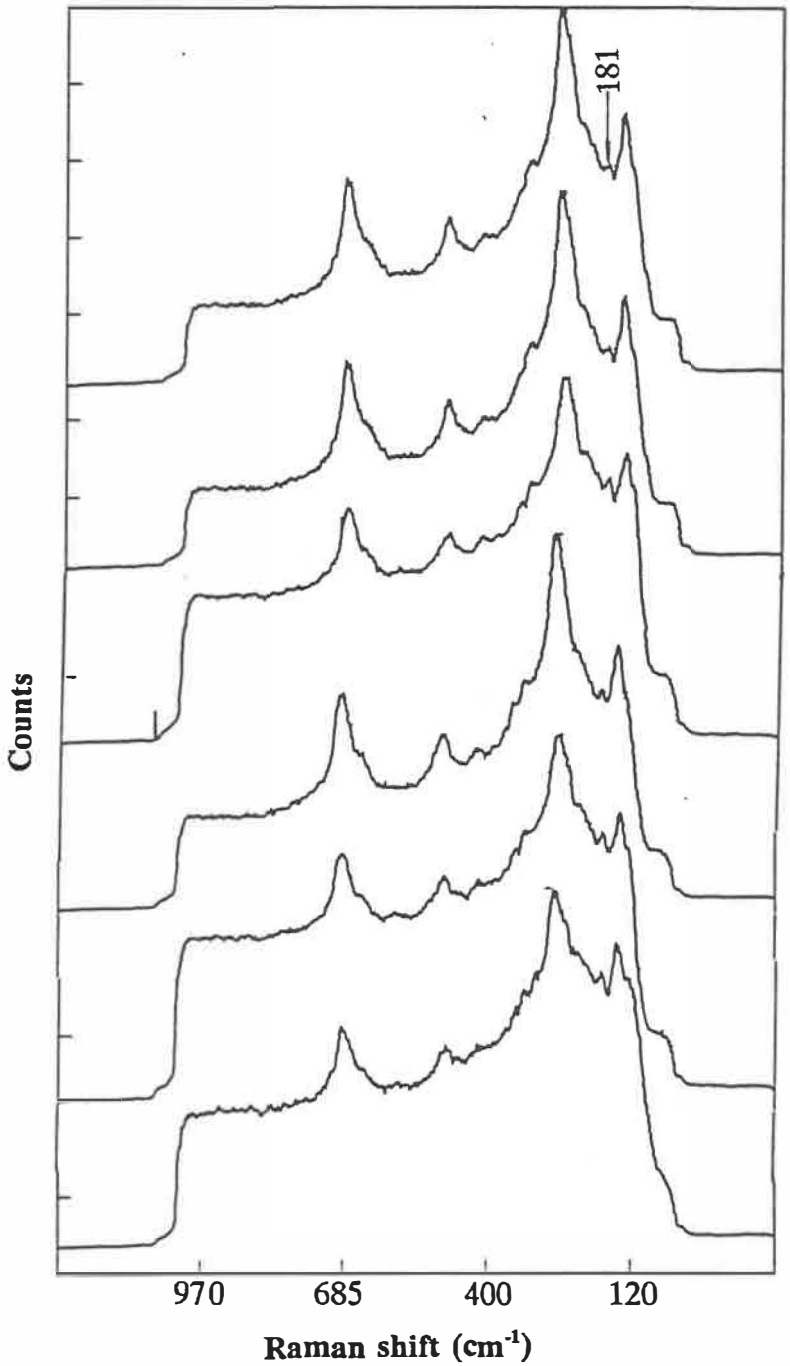

Fig. 8.5 Raman spectra of 3Y-TZP. Spectrum A from the free surface, B from the crack initiation region, C from the last bright zone, D from the last striation, E from the final fracture surface neighbouring the last striation, F from the final fracture surface far from the last striation.

The spectra obtained was analyzed using the equation transfered by Clarke and Adar [107]. This equation for C_m, the volume fraction of monoclinic phase or of transformed particles, is as follows:

$$C_m = \frac{I_m^{181} + I_m^{192}}{F(I_t^{148} + I_t^{264}) + I_m^{181} + I_m^{192}} \qquad (8.10)$$

where I is the intensity of the particular peak, F was found by these authors to be 97, and m and t refer to the monoclinic and tetragonal phases, respectively. Each number refers to the corresponding peak present at that wave number. This analysis results indicated that there was 3 percent of transformed particles on the free surface, 15 percent in the initial region of tensile fatigue crack propagation, 30 percent in the last bright region just before the last striation, approximately 15 percent on the last striation, 30 percent in the region of final fracture surface near the last striation, 45 percent near the very end of the final fracture region.

A schematic illustration of the volumetric fraction of transformed particles obtained from these analyses as a function of the position on fatigue fracture surface is presented in Figure 8.6. A fluctuation of the volumetric fraction with respect to the position on the fatigue fracture surface is a striking feature obtained from the above analyses. Generally, this variation in amount of transformed particles is found

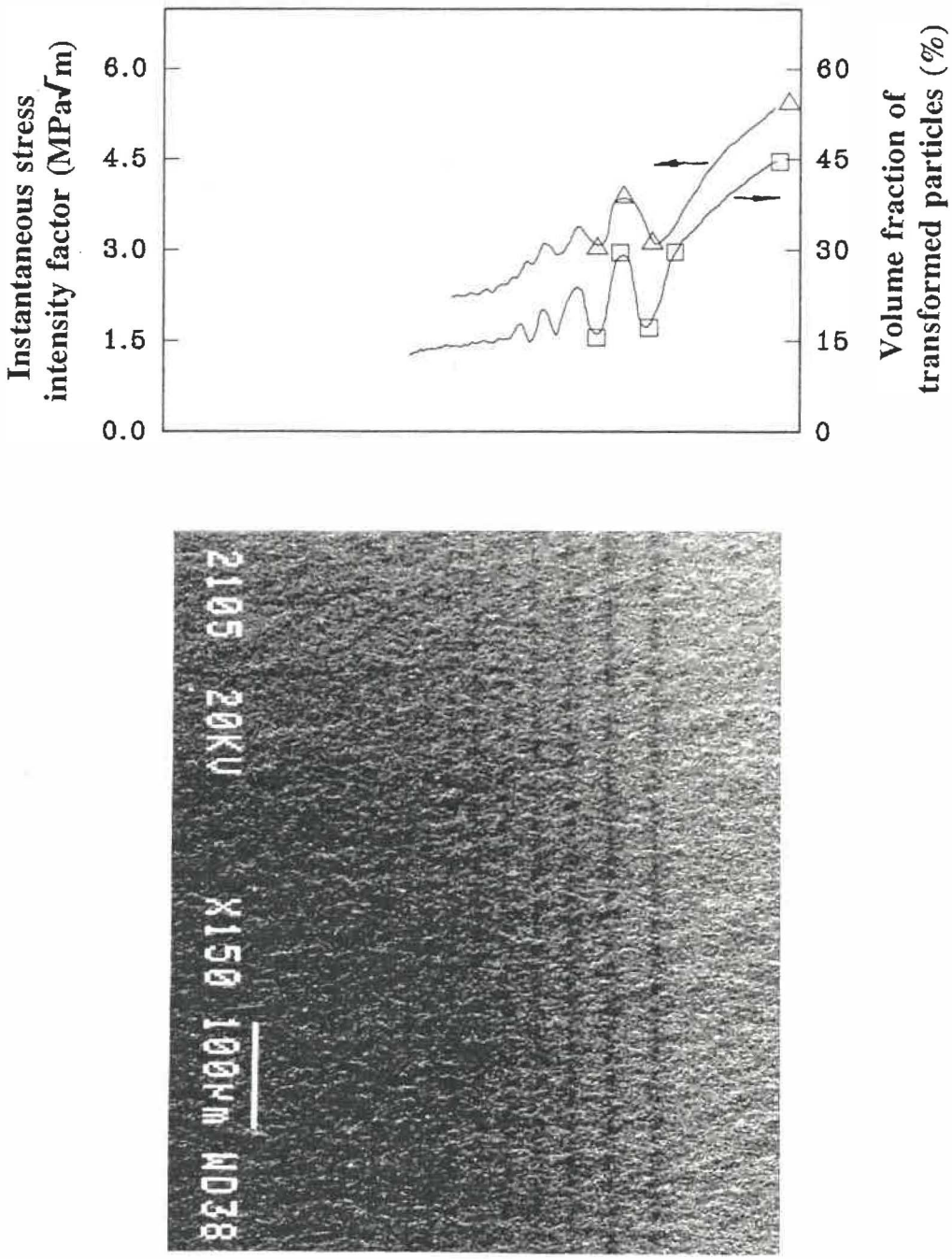

Fig. 8.6 The correspondence between the volume fraction of transformed particles, V_m, the instantaneous stress intensity factor, K, and the position on the fracture surface. The minimums in the volume fraction of transformed particles correspond to dark bands or striations.

be associated with the alternative presence of dark striations separated by bright and, with the latter presenting considerably more particles transformed than the ark bands.

The results presented above clearly demonstrate that there was more ansformed particles in the spacing between dark bands than on the successive dark nds. As well, there was a very similar amount of transformed particles in the acing between the last two dark bands and in the initial region of the final fracture rface, both of which were produced at very similar stress intensity factors. This es strong and direct support for our argument that the dark bands, which are esent as depressions on the both fracture surfaces, form as a result of the esence of less stress-induced transformation in these bands than in the bright nes between bands. These Raman spectroscopy results indicate that there are re transformed particles in the spacings between the bands than in the dark nds and that the amount of transformed particles present on a region of the cture surface depends on stress intensity at which that part of fracture surface s produced (Figure 8.7).

The Raman spectroscopy measurements therefore complement very well the ormation obtained from the analyses of the hysteresis loops obtained from the ck tip strain gage and from the microfractographic observations.

A major uncertainty in Raman microprobe analysis arises from polarization fects, since the spectral intensity contributed by an individual particle depends on crystal orientation. In the present study, grain size is very small (0.25 μm), and e size of transformed crystallites should be smaller than the grain size by an order magnitude. Thus, the transformed crystallite size will be approximately 0.025 μm. ierefore, the area analyzed by the laser beam, which has a diameter of proximately 8 μm, will contain at least hundreds of crystallites, when the netration depth (approximately 0.4 μm) of the laser beam is also taken into :ount. As well, the initial material having been produced by powder metallurgy ›uld not have any preferred orientations. The crystallites produced by the rtensitic transformation should therefore have a random orientation and arization effects should be insignificant.

PART III DISCUSSION AND CONCLUSIONS

CHAPTER 9 DISCUSSION

The investigation of fatigue crack propagation carried out in the present study has provided important information on the fatigue crack propagation behaviour, the fatigue fractography and some associated fracture aspects in some ceramics. The present chapter will further discuss how the fractographic features form and how they are related to the fatigue propagation behaviour. As well, the significance of the present results to ceramic processing and to engineering applications will be briefly considered.

9.1 Compression fatigue crack propagation and the related engineering significance

In compression fatigue, the formation and migration of debris particles have been found to affect crack propagation [37]. The presence of debris particles may increase the crack closure effects, but the migration of debris particles will move the crack closure site further back from the crack tip and create an opening at the notch-like crack tip. The opening will accommodate more debris particles and facilitate notch-like crack propagation.

Although compression fatigue caused crack propagation in the ceramics studied, cyclic compression did not impose as great damage as cyclic tension. In compression fatigue at a constant load range, the crack propagates at a decreasing

ıte with increasing cycle number, and finally the crack arrests automatically. An crease in load range can only increase the crack propagation slightly. If slabbing prevented, it appears difficult to obtain a large amount of propagation under ›mpression fatigue. This indicates that advanced ceramics are more suitable to ithstand compressive fatigue loading than tensile fatigue loading.

Fatigue crack propagation in prenotched specimens under cyclic compression also mechanistically different from that produced under cyclic tension. In mpression fatigue, fatigue cracking occurred by forming a notch-like crack which came progressively sharper during load cycling. Unlike tensile fatigue in which :igue cracks initiate preferably at crack-like preexisting defects, the compression :igue cracks initiated at a prenotch tip. The crack propagated by breaking off ıall particles from the notch or crack tip, and the total crack propagation obtained pears dependent upon the diameter of the semi-circle prenotch tip. Such a ɜnotch can be considered as resembling more volume-dominant defects rather ın surface-dominant defects, such as, cracks. In engineering components of ·amics which are subjected to cyclic compression, such notch-like cracks could m preferably at some large diameter spherical defects instead of at large sized ɜet-like or penny-shaped crack-like defects. Fortunately, by virtue of the manner which advanced ceramics are processed, spherical defects are much easier to ıtrol by using advanced techniques, such as HIP and CIP, than sheet-like or ınıy-shaped crack-like defects.

9.2 Occurrence of intergranular fracture

The intergranular fracture mode was dominant in the present study as in nost other investigations dealing with fatigue and fracture of ceramics [53,112,113]. Because of their poor capacity for deformation, the fracture behaviour of ceramics s affected strongly by the elastic properties (for instance, by Young's modulus) and by their elastic anisotropy. In polycrystalline ceramics, although the mechanical behaviour shows isotropic behaviour as a result of the large number of grains of lifferent orientations, the elastic properties can vary considerably between neighbouring grains due to the inherent anisotropy of such grains. For example, the lastic modulus of a single crystal of cubic zirconia can vary by a factor of two with rystallographic direction [38]. The elastic modulus in the soft [110] direction is only 80 GPa, while in the hard [010] direction it is 360 GPa.

Due to the continuity of deformation before the cracking of a specimen, the ame amount of deformation must be obtained in the adjacent grains on both sides f the grain boundaries. Considering the elastic anisotropies mentioned above, grains aving different orientations in different crystal directions relative to the loading axis ill be subjected to different stresses near the grain boundaries. Even if the average ress is low, the local stress at some grain boundaries can be considerably higher.

Moreover, analyses for stress distribution at grain boundaries indicate that the stress intensity near a triple grain junction exhibits a logarithmic singularity [40,43], therefore, it can be assumed that the highest stresses exist at triple grain junctions. It is these stresses which should be responsible for the breaking off of small particles at the notch tip which causes compression fatigue crack propagation.

It can be predicted that an improvement in the cohesion at the grain boundaries would increase the strength and the toughness as well as resistance to compression fatigue in ceramics, and if the anisotropies in elastic constants could be decreased by proper control of the composition, the local stress concentration would be reduced significantly.

Ewart and Suresh [38] have proposed the existence of tensile residual stress at the notch tip of specimen tested under cyclic compression fatigue. The opening of a population of grain-boundary microcracks within the process zone at the notch tip leads to a reduction in the elastic modulus of the material in the microcracked zone. The difference in the compliance of the material within the process zone and that of the surrounding material can then induce residual tensile stresses during unloading from the maximum compressive condition over a distance of the order of the size of the process zone. In the fourth zone of compression fatigue nearest the crack tip, some semi-detached particles are present and indicate the existence of

nicrocracks. This proposed role of the residual tensile stresses in compression atigue crack propagation appears in agreement with the present observations.

.3 Crack-tip shielding and crack propagation curve

According to studies performed in metals [118], the full curve of fatigue crack ropagation rate as a function of the stress intensity factor generally exhibits three egions: the threshold region, the region of stable crack propagation and the region f final crack propagation (Figure 9.1). In region I, the behaviour of a long fatigue rack exhibits a fatigue crack growth threshold, ΔK_{th}, which corresponds to the stress ıtensity factor range below which cracks do not propagate. However, fatigue crack ropagation curves in ceramics often do not exhibit well these three stages of crack ropagation.

Compared to Liu and Chen's study [53] on a similar ceramic, our results were ɔncentrated in the region of high crack propagation rates at high K_{max} values. As ıown in Figure 9.2, fatigue crack propagation rates obtained in the present study ere in good agreement with those obtained by Liu and Chen [53] who introduced precrack by hardness indentation.

When Paris' law (equation 2.6, chapter 2) is employed to analyze fatigue ack propagation in 3Y-TZP, the exponent m is an important parameter in

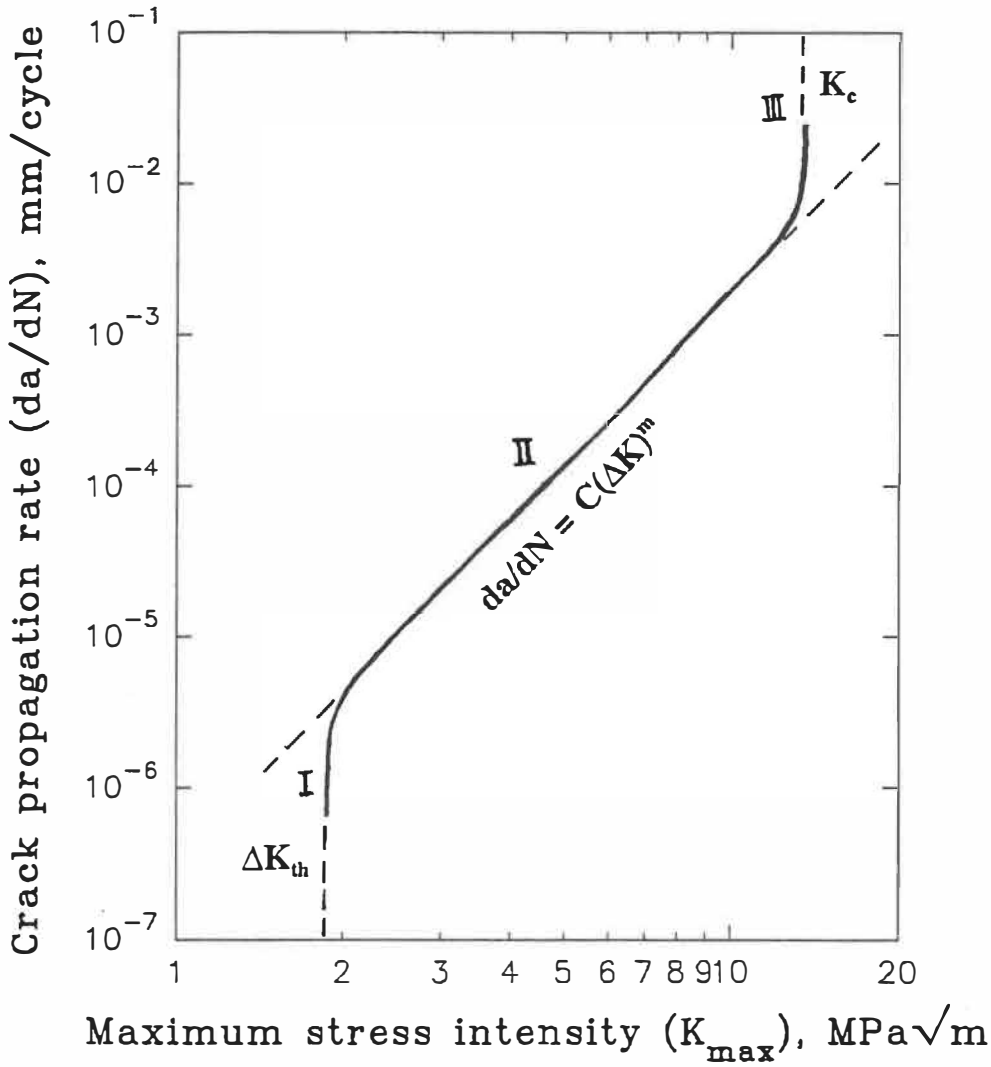

g. 9.1 Typical fatigue crack propagation curve, showing three stages propagation behaviour, consists of crack propagation near the threshold (region I), the power law crack propagation (region II) and the accelerated crack propagation (region III).

escribing the fatigue propagation behaviour. The average value of the exponent m eported by Liu and Chen is approximately 21. The exponents obtained from the resent study were 7 to 12 which are considerably smaller than theirs. Moreover, the xponent m of Paris' law exhibits an unusual change in 3Y-TZP, since the local xponent m appears to gradually decrease with increasing stress intensity factor Figure 9.2).

When a phase transformation involving shear and dilatational strains occurs the crack tip region, the stress distribution in this region will be affected. The ansformation zone is always confined within untransformed matrix, this constraint ill induce stresses. By imaging the transformed zone in the crack tip region being essed back to its original volume size before the transformation, transformation ughening has been modelled by considering the effect on the local stresses [52]. or purely dilatational transformation, these calculations have indicated that there ould be no toughening effect in the zone in front of the crack tip and that there isted tensile residual stresses in the region $\theta \leq 60^{\circ}$ ahead of the crack tip. As the ack propagates through the transformation zone, transformed particles are left hind the crack tip, unless the transformation is fully reversed on unloading . In the ake" of an advancing crack, residual compressive stresses then act to close the ack, giving rise to a toughening effect, which increases with the width of the nsformation zone. Its size depends primarily on the applied stress intensity factor, , but more exactly on the local stress or strain ahead of the crack tip. Therefore,

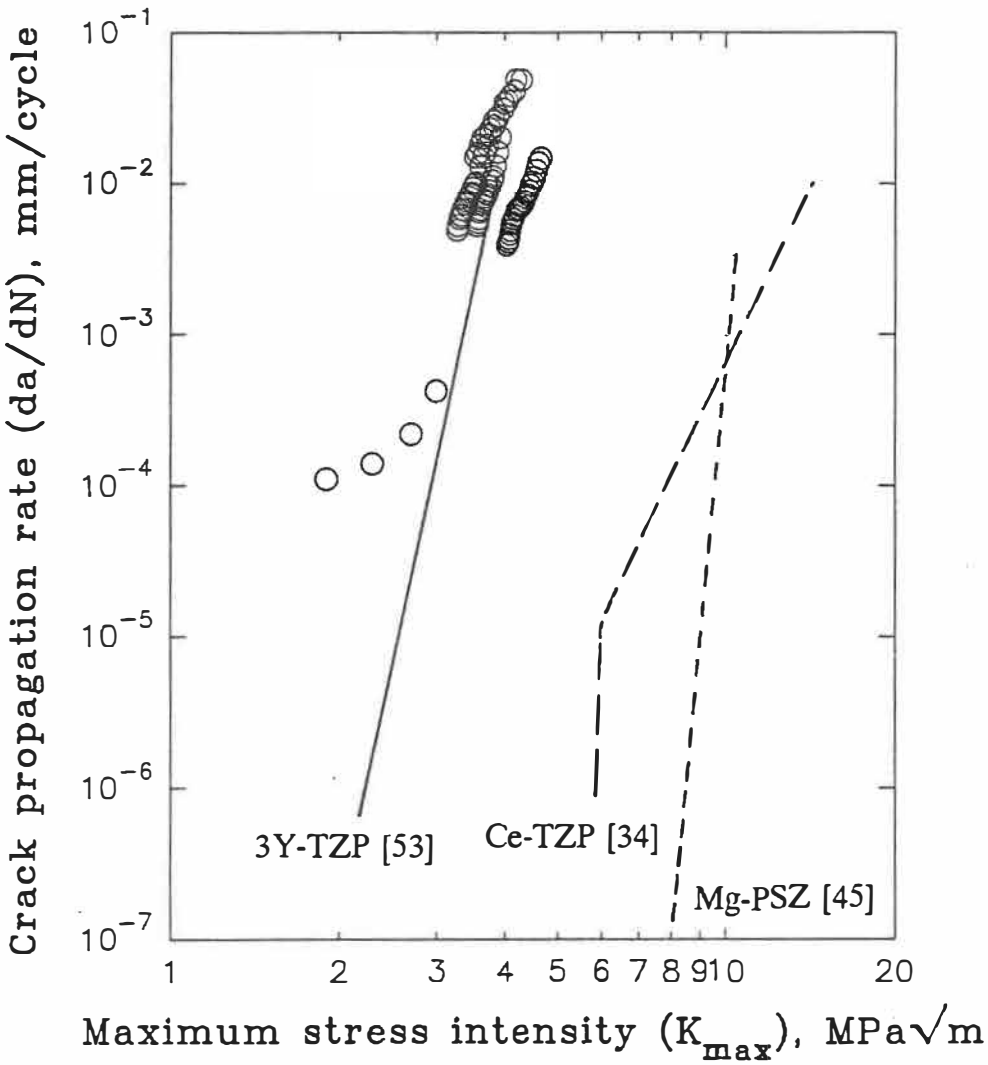

g. 9.2 Comparison of fatigue crack propagation curves obtained on 3Y-TZP in the present study and in the study of Liu and Chen [53] (solid line) as well as that obtained on Ce-TZP [34] (medium dash line) and Mg-PSZ [45] (dash line).

the degree of shielding is diminished if crack growth occurs below a critical K value, for example, at $K_a < K_c$ (slow crack propagation), and shielding is enhanced, if crack growth occurs at $K_a > K_c$ (unstable crack propagation) [131].

At low ΔK or K_{max}, the transformation zone size is small, the amount of transformed particles is also small and da/dN is very low. There is only a small increase in transformation zone per cycle, which results in a weak crack-tip shielding effect. If it is the increase in transformation zone per cycle which principally controls the fatigue propagation resistance, fatigue crack propagation in low shielding encounters low fatigue resistance. Furthermore, at low stress intensity factor, only a small amount of stress-induced transformation is expected. Therefore, the gradual increase in the stress intensity factor should not result in an important effect of transformation toughening as long as the transformation zone size remains small. This is indeed indicated by the results of Liu and Chen, who found a high exponent n (≈ 21) at low stress intensity. Moreover their results also tend to suggest that this exponent decreases as K increases.

At high ΔK or K_{max}, the fractographic features of dark bands and bright zones was obtained, and the exponent m is surprisingly low for a ceramic. In this portion, the transformation zone size increases as K increases. As well, there is a large difference between the transformation zone size at crack arrest at low K in the receding cycle and that produced near K_{max}. The degree of crack tip shielding from

e crack closure stresses in the wake of the crack should be particularly important ter the rapid propagation, i.e., during the formation of the dark band. The crack- shielding at this stage will oppose slow crack propagation in the dark band igure 9.3). Crack propagation rates measured as the width of the bright zone, the dth of the dark band and the spacing between the dark bands are plotted as a nction of K_{max} in Figure 9.3. In this log-log plot, the crack propagation rates easured as the width of the bright zone (the amount of rapid propagation per cle) and as the spacing between successive dark bands (the total amount of opagation per cycle) versus K_{max} exhibit a similar slope, which decreases slightly th increasing K_{max}. The slope for the curve of the widths of the dark bands (the ount of slow propagation per cycle) plotted versus K_{max} on the log-log plot creases considerably more with increasing K_{max}. This can be attributed to the reased crack closure resulting from the more important amount of transformation oduced during the rapid propagation in the preceding cycle. The m value for the id propagation in the bright zone is nevertheless quite similar to that in the dark ne. As the rapid propagation occurs in the bright zone, a large transformation ne develops and causes compressive stresses in the wake of the crack, contributing the low m value for this zone. Because of the log-log scale employed, the m value the total crack growth per cycle depends mainly on the larger contribution, and refore is similar to the m value for the rapid propagation.

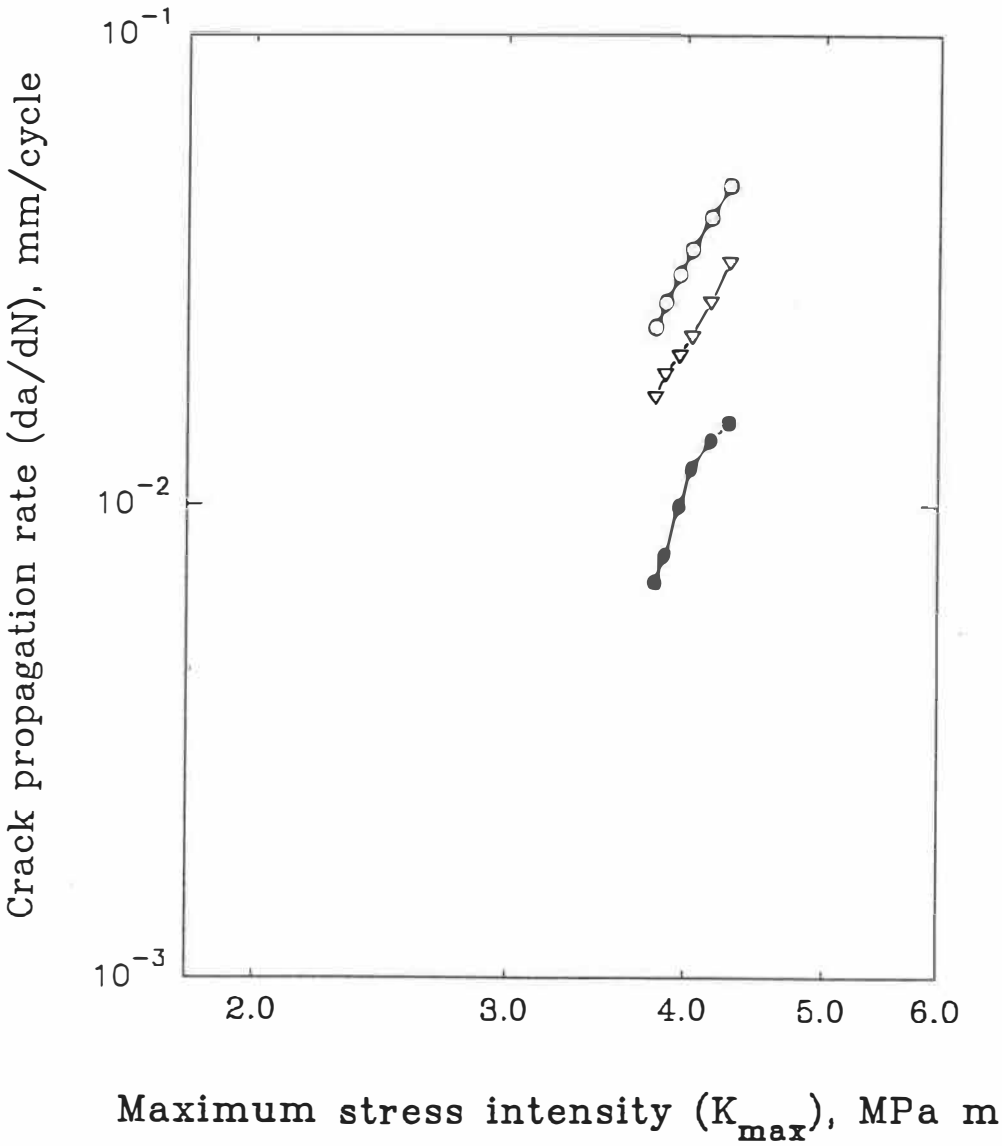

Fig. 9.3 Fatigue crack propagation rates, da/dN, which are obtained by measuring widths of dark bands (filled circle), bright zones (open triangle) as well as spacings between dark bands (open circle), are plotted as a function of the maximum stress intensity factor, K_{max}.

From the relatively low values of m which we obtained for the region resenting striations, the results indicate that the value of m actually decreases once riations form (Figure 7.9). Although they did not point this out, this is also seen om the results of Liu and Chen [53] since their data points obtained for the region ith striations give a considerable lower slope than the remainder of their curve.

We have estimated the exponent m for the results reported by Liu and Chen 3]. Their exponent m for the plot of crack propagation rate measured from the acing between the slow propagation dark bands (i.e., the total amount of opagation per cycle) versus K_{max} has a value of approximately 3.4. This low value fers considerably from our results which indicate a value of approximately 10. The ason for this difference is not clear at the present time, but their lower m value ggests that they had a larger transformation zone width, producing more crack tip ielding at high K_{max} than obtained in our specimens. Their exponent m for the plot crack propagation rate measured from the width of their slow propagation bands rsus K_{max} has a value of approximately 9.4, which is similar to that for the steepest rtion of our corresponding curve. It should be noted that their white bands respond to our dark bands and vice versa, indicating that they employed optical croscopic observations, which makes it more difficult to measure the width of the w propagation band accurately.

Two load history effects were noted during the crack propagation tests. One ccurred at high K during the formation of striations when cycling was interrupted : K_{min} to change X-Y plotter paper. This resulted in a decrease in crack ropagation rates with the new log da/dN versus log K_{max} curve being parallel to the riginal curve but displaced to a higher K_{max} value (Figure 7.19). This previous 'cling history effect indicates that the cycling interruption resulted in an additional crement of crack tip shielding. This effect can be explained by the crack deviation hich resulted, combined with the crack tip closure stresses acting on the fracture rface bright zone immediately before this crack deviation site. The crack tip ielding which resulted was important since the new portion of crack propagation rve did not tend to realign with the old portion, in spite of the quite large amount new propagation produced.

The other load history effect observed was propagation acceleration which curred during several blocks of low load amplitude cycling. During normal cycling, was noted that rapid propagation was occurring and the load was slowly decreased the K_{min} value, then several blocks of low load amplitude cycling were performed.

The average fatigue crack propagation rate for these blocks of low amplitude :les was found (Figure 9.2) to give higher propagation rates compared to that ɔected from the results of Liu and Chen [53], who, by employing an indentation a precrack, were able to follow the fatigue crack propagation at low propagation

tes. The difference between these data points and the curve of Liu and Chen owever decreased for each successive block. As well, these points appear to adually merge into the curve obtained under normal load cycling by Liu and Chen 3] as the load amplitude increases. The propagation rates in these blocks also erged into the extrapolation of our curve obtained from the striation spacing. owever, the fatigue crack propagation rates obtained for the blocks at the lowest ess intensity factor were also considerably higher than that expected by trapolating our fatigue crack propagation curves obtained from the striation acing. Our results therefore suggest crack propagation acceleration associated with e cycling history employed.

The fracture surface produced under decreasing load showed an increasingly rkish colour, followed by a very dark band. A crack arrest site is seen within this rk band which has a width of approximately 5 to 10 μm. This arrest site is situated er the darkest portion this band. This indicates that the propagation produced der decreasing load stopped at this arrest line and that only light crack closure esses were present in the darkest fracture surface region behind the crack tip on rting the new propagation at low ΔK. The accelerated cracking compared to the ve of Liu and Chen can be attributed to the low crack closure stresses near the ck tip until sufficient new propagation was produced to increase the crack closure esses to their level in the absence of unloading effects. In agreement with this

xplanation, the crack growth rate for the subsequent blocks of cycles became creasingly closer to those expected from the results of Liu and Chen.

A study on ceria-partially stabilized zirconia by Tsai et al [34] showed (Figure 2) that the existence of a threshold in region I, followed by power law propagation stage II and by unstable fatigue crack propagation in region III (even if only a few ıta points were available in this last region). Considering that the Ce-TZP nployed by Tsai et al has a relatively high fracture toughness (approximately 16 Pa√m), it can be suggested that when the fatigue crack propagates at very low te in ceramics with relatively moderate toughness, such as 3Y-TZP and Mg-PSZ, threshold value should logically still exist but should be very low.

At intermediate values of ΔK (region II), a straight line usually is obtained a log-log plot of fatigue crack propagation curve. This is described by the well-own Paris law (equation 2.6). The exponent m in equation 2.6 is usually between o 4 for metals. However, this exponent shows great variation in ceramics even for e same material. The exponents obtained in the present study from different ecimens of 3Y-TZP varied between 7 and 12 for crack propagation determined ım the striation-like markings on the fatigue fracture surfaces.

It appears that whether or not fatigue crack propagation is stable depends the fatigue resistance from the previous transformation zone but does not

ecessarily depend on the presence of visible striations. Even if the crack ropagation exhibits temporary instability in the bright zone, the combined ehaviour in a complete cycle still corresponds to quite stable crack advance. The pid propagation occurred during the unloading portion of the cycle and increased e transformation zone size and therefore the transformation- induced crack tip ielding. These factors acted to keep the rapid propagation sufficiently stable to rm the alternating dark and light bands for a small number of cycles, although the crease in load during the major portion of the rapid propagation was small from e hysteresis loops measured. In fact, this behaviour indicates an advantage of ansformable ceramics subjected to cyclic loads.

Crack propagation rates are generally expected to increase rapidly at high ΔK lues (region III, Figure 9.1). In this region, fatigue cracking commonly exhibits stable or accelerated crack propagation [34]. This unstable propagation will ntinue just prior to complete failure of the specimens. The fractography features dark bands and bright zones in the present study showed a slow and stable rease in the width of the dark bands, and a more rapid but also apparently stable rease in the width of the bright zone. The total crack advance in a cycle primarily pended on the width of bright zone. This width of bright zone, which should rrespond to less stable propagation, strongly depended on the K_{max} value.

By measuring spacings between striations and calculating the related stress ntensity factors, we are able to determine well the fatigue crack propagation which ›ccurs from the formation of the first visible striations to the final fracture. Only for he last few cycles immediately prior to the final fracture, did the exponent m for atigue crack propagation indicate an increase. This accelerated crack propagation ypical of region III would therefore be able to account for only a very small portion ›f the complete crack propagation curve.

The stages of crack propagation in 3Y-TZP cannot be well defined since it ›ppears that in stage II m decreases progressively and the appearance of striation-ike dark and bright bands results in a more pronounced decrease in m. Comparison ›f the present results with those of Liu and Chen indicate that a stage II is .pproximated and that stage III corresponds to the appearance of the striation-like ›ands. Whether the threshold region with a well-defined threshold value can be ›btained in region I may depend on the fracture toughness properties and on the nicrostructure. In the case of high toughness, such as in Ce-TZP, a threshold value ›as reported [34], and fatigue crack propagation occurred only when the range of he stress intensity factor, ΔK, exceeded this value, ΔK_{th}. Stable crack propagation n region II has been well demonstrated for transformation-toughening advanced eramics, such as, 3Y-TZP [53], Mg-PSZ [45] and Ce-TZP [34]. The fatigue crack ›ropagation rate is then predictable even if the accuracy with which it can be

redicted is not high. This inaccuracy results from the considerable variation in the ey parameters of the Paris law, particularly that of the exponent, m.

.4 Sequence of fatigue crack propagation

Crack advance in a single cycle produced at high stress intensity factor results ı two different microportions of crack propagation, the dark band and bright zone. he bright zone resulted from rapid crack propagation which occurred (except at mes for the last cycle) after a small portion of unloading. This rapid propagation as usually triggered by unloading. This indicates that the transition from the ading to unloading portion of a loading cycle has a very important effect on the tigue crack propagation.

It is reasonable that the effective or total stress distribution at the crack tip l be changed due to transformation which produces residual stresses. This residual sses will depend on the dilation and shear strain resulting from transformation, size, shape of the transformation zone and particle distribution in this zone. If the dilation effect is taken into account, and certain zone shape is assumed, rous calculation can be performed for schematizing transformation toughening to such dilation effect. The calculations of McMeeking and Evans [52] indicate these residual stresses are tensile in crack tip region for θ value from $-\pi/3$ to In the exterior of this region, transformed particles will impose compressive

stress. This calculation also shows that toughening effect results from the compressive stresses acting on crack surfaces at the wake of the crack.

In the present study, a striking result was that rapid crack propagation was riggered by slight unloading. On K_{eff} basis, this result indicates that the maximum ffective tensile stress ahead of the crack tip in the $\theta=0$ region is increased by the nloading. Two possibilities are envisaged to give rise to this increase in maximum ffetive tensile stress, one being a decrease in the shielding stresses and the other eing an increase in the tensile residual stresses ahead of the crack tip. The former ould result logically from some reversible transformation on unloading. Marshall nd James [100] have observed reversible transformation at room temperature at w stresses in Mg-PSZ.

Another possibility could be that the start of unloading does not completely rest the crack but slows it down, with rapid propagation then being triggered by e relatively low crack closure stresses near the crack tip as a result of the presence f the depressions in the dark bands. This possibility however does not agree well ith the fractographic evidence that crack arrest occurs close to the end of the dark and. Of these possibilities, the most probable appears to be that rapid propagation iggered by unloading results from reversed transformation, decreasing the crack-tip ielding during the start of unloading and increasing the maximum tensile stress fficiently to initiate rapid propagation.

In the transformable 3Y-TZP, the transformation zone at the fatigue crack ɔ keeps changing and developing during a load cycle. According to hysteresis loops : crack-tip microstrain gage and fracture surface observations, it appears that the tigue crack arrested in the dark band near the edge facing the fatigue crack during e unloading portion of the preceding cycle.

Crack-tip shielding occurring at the wake of the arrested crack can ɔnsiderably affect fatigue crack propagation. As the applied load increases, fatigue acking begins to occur gradually. In this stage, both the shielding effect and the ack driving force are increasing with increasing applied load, but with the driving rce having a slight advantage, causing the crack to grow slowly. After the applied ad attained the maximum value and began to decrease, with respect to the crack iving force, the shielding acquired a slight advantage. Therefore, the fatigue crack ɔpped propagating.

When the applied load began to decrease, reverse transformation might occur the zone outside of the $\theta \leq 60^\circ$ region, which would decrease the crack tip ielding and increase the effect of the residual tensile stresses in the region $\theta \leq 60^\circ$ ıead of the crack tip. If this increase in the effective maximum stress ahead of the ack tip allows it to attain locally the critical stress for brittle fracture, rapid acking would initiate in the zone of maximum tensile stress. This cracking would opagate rapidly back towards the original crack as well as forwards. This rapid

opagation and its associated large crack tip effective stress would induce a large ıount of transformation, making two crack surfaces come in contact in the crack ıke after a small amount of propagation. Therefore, the crack tip shielding form ɜ crack closure stresses rebuilds up, tending to slow down the propagation and rmitting the crack to be arrested again if K becomes sufficiently low. The large ıount of transformed particles produced by the rapid propagation zone may be ributed to either a high effective tensile stress in the crack tip region or to the ınsformation being sensitive to the strain rate. That unloading triggered rapid ɔpagation indicates that it caused an increase in the effective crack tip stresses. ıce twinning is associated with the transformation [130], the amount of nsformation obtained could be strain rate sensitive.

Figure 9.4 schematically illustrates the relationship between total stress tribution at the crack tip, fracture surface topography, crack propagation ɟuence and load cycle. As the loading increases from the minimum value, the igue crack starts to propagate slowly producing the dark band. After the ximum load has been attained and unloading begins, the fatigue crack ɔpagation arrests because fatigue crack driving force decreases and the degree of elding at the wake of the crack is high.

Careful examination of the fracture surface shows that this bright zone ɔears to contain a line at which river lines stop or start, with this line situated a

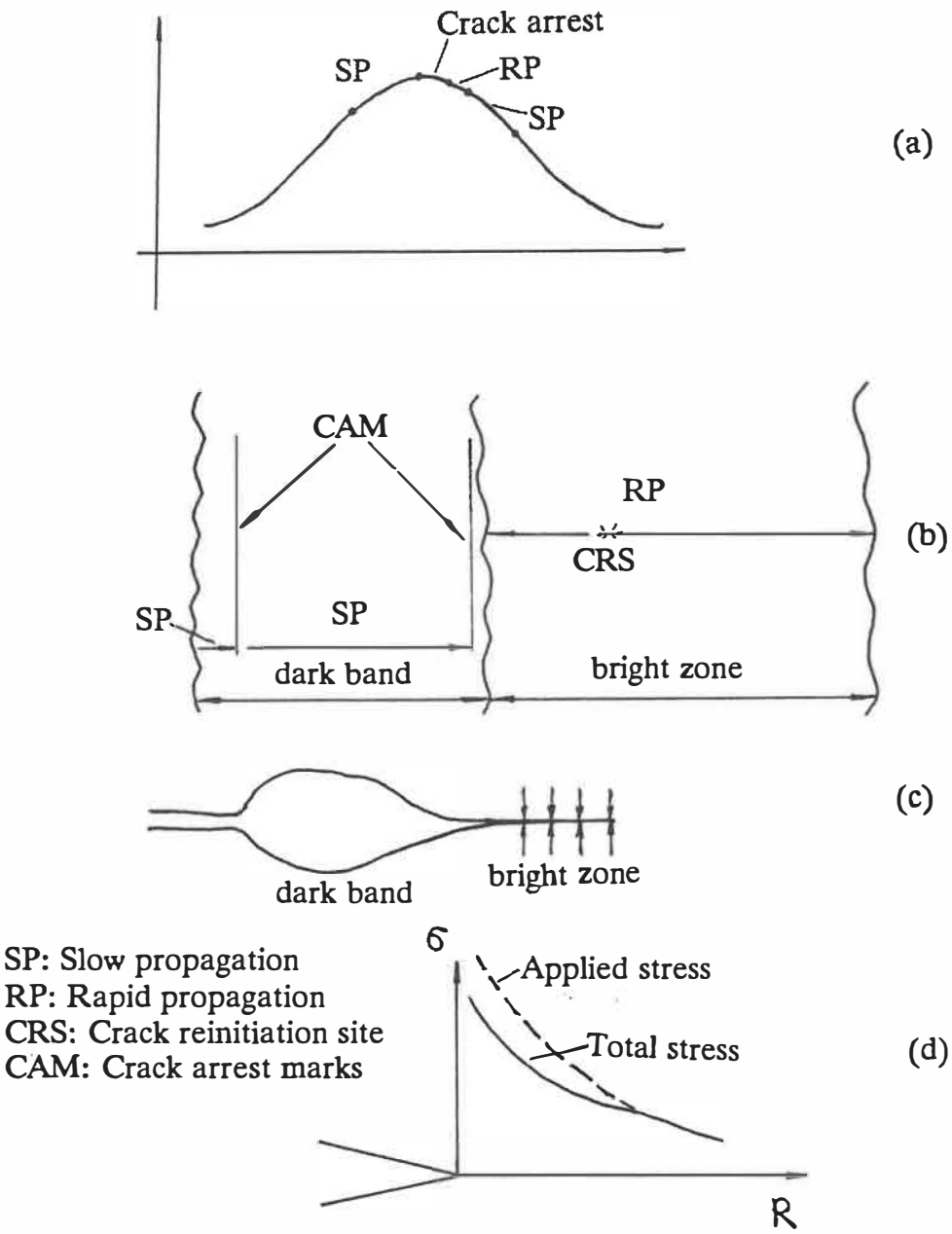

Fig. 9.4 Schematic illustration on the relationship bewteen the load cycle, the topography of fracture surface and stress distributions at the crack tip. (a) load cycle, (b) fatigue fracture surface feature, (c) the topography of fracture surface (edge view) and (d) stress distributions at the crack tip.

similar distance ahead of the dark band as the width of this band (Figure 9.5). This suggest that it may be at this line that rapid propagation initiates, which would indicate that the maximum effective tensile stress is obtained somewhat ahead of the crack tip. This line however is not as clearly observed as the two arrest lines within the dark bands, but this would be expected since it does not correspond to an arrest line but to a line of approximate reinitiation sites.

It however is not clear whether crack reinitiation does occur ahead of the crack tip or not. If it does not occur at the light line suggested by the fractographic observations, the observations would then suggest that it occurs at or very close to the arrest line produced by the start of unloading.

As the unloading continues after the rapid crack propagation, the fatigue crack propagates an additional small distance, which can be seen on hysteresis loops obtained with crack tip microstrain gage (see chapter 7). This small additional propagation leads the fatigue crack to arrest slightly inside the next dark band at the side of the darkest portion of this band, which indicates that this last portion of propagation produced only a small transformation zone at the crack tip.

.5 Criteria for the visibility of striation-markings

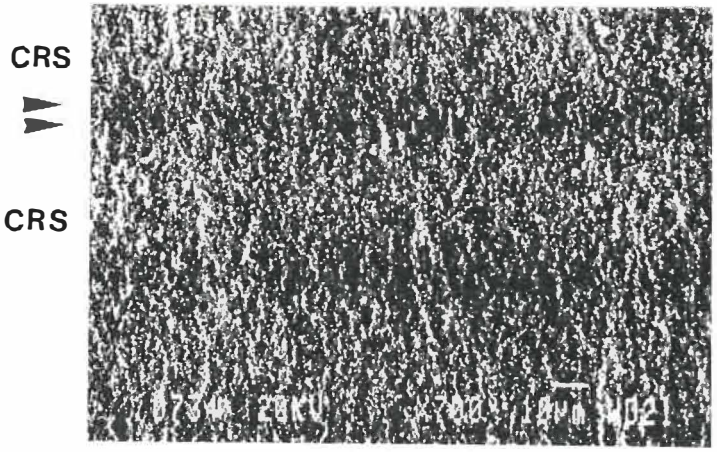

Fig. 9.5 Fatigue fracture surface showing two fine arrested lines of the fatigue crack.

The presence of striation-like markings is an important feature of the fatigue f 3Y-TZP at high propagation rates. Liu and Chen [53] proposed that fatigue crack ropagated rapidly when the stress intensity factor exceeded the crack resistance, $_r$, obtained from the determination of an R-curve. They explained the alternating and striations as resulting from K_{max} intercepting the R-curve twice in each cycle, ith fatigue crack growth continuing for the portion of the cycle when the stress ıtensity factor falls below K_r. This explanation does not appear to be in good greement with our results since they predict in the same cycle some initial overload ·acking, followed by fatigue cracking, followed by a combination of overload and ıtigue cracking. In contrast, the hysteresis loops indicate slow cracking which slowly :celerates and which is followed after slight unloading by rapid propagation, which ıen decelerates and arrests during unloading.

Liu and Chen [53] proposed that their dark bands corresponded to rapid ack propagation, however, our analysis of the relationship between hysteresis loops ıd the geometry of striations and bright zones clearly indicates that the bright zone ırresponds to rapid fatigue crack propagation. It is however clear that our dark ınds correspond to their bright zones and vice versa and our dark bands become ;ht when observed by optical microscopy.

Our results, similar to those of Liu and Chen [53], showed that the bright (as ›served by SEM) zones between striation-like dark bands decreased in size and

came indistinguishable with decreasing stress intensity factor. The dark bands came closer to each other. As well, the slow propagation fatigue fracture surface came darker in the present study than the portion with the presence both of the rk bands and bright zones. This appearance is similar to that of the slow opagation bands, which is clear evidence that fatigue crack propagation still occurs t without causing the occurrence of the rapid propagation portion.

More importantly, a small transformation zone would be produced at low K, d the difference in transformation zone size for two successive cycles will be very all. Moreover, the transformation zones for the successive cycles would overlap mpletely since the crack probably does not propagate out of the transformation ne at the start of the cycle. The transformation zone size at the site of crack arrest uld be very similar to that at K_{max}. Therefore, the differences in surface height (or the amount of material which has bulged out of the surface), caused by the ference in transformation dilation between the propagation and arrest portions a cycle would not be sufficiently visible to result in striation-like bands. As a ult, no distinguishable striations of this type are observed on the fracture surfaces oduced under low K.

As the crack propagates slowly, the stress intensity factor becomes reasingly high, which induces more rapid propagation but also a larger nsformation zone. This results in the deepest (and darkest) portion of the dark

band being at the crack arrest site at the start of this band (which is situated actually lightly within the dark band because the amount of transformation accompanying propagation decreased as the crack decelerated during the decreasing K-portion of the previous cycle). The rapid propagation which was triggered by unloading esulted in an important increase in the transformation zone size. Following this apid propagation, the crack arrests at low K with a small transformation zone resent ahead of the crack tip. It is the difference in the volume change produced etween the large transformation zone associated with rapid propagation and the nall transformation zone produced ahead of the crack tip at crack arrest that esults in the visibility of the striations. The larger this difference in volume increase roduced at the fracture surfaces, the more visible are the striations, i.e. the larger the dark-light contrast.

6 Size of the transformation zone and study of the fatigue crack propagation sequence

No details were known for the crack propagation sequence in ceramics within single load cycle when the study of this thesis was initiated. Cycle-by-cycle studies e however fundamental to understanding fatigue cracking behaviour.

Compared to zirconia stabilized by other oxides, such as ceria, the yttria-abilized zirconia has a very confined transformation zone profile. The amount of

atigue propagation per cycle can then be of the size or even larger than the ransformation zone size, which makes it feasible to study the cycle-by-cycle ropagation behaviour. In contrast, in ceria-stabilized tetragonal zirconia polycrystals Ce-TZP), the stress-induced transformation zone has a long tail shape starting from rack tip and developing in the cracking direction [120-122]. This tail-shaped zone as a usual length from a few hundred micrometers to few millimetres and a depth f a few hundred micrometers. It can be expected that fatigue crack will take many ycles to propagate through the large transformation zone produced by the receding load cycles. Therefore, the investigation of the cycle-by-cycle interaction etween fatigue crack propagation and the transformation zone will be difficult in eria-stabilized zirconia.

7 Some suggestions on further fatigue study in ceramics

According to studies performed in metals, fatigue crack propagation in the gion I is related more to crack closure, crack tip shielding and the microstructure an to loading conditions [123,124]. Preexisting flaws or crack-like defects found mmonly in ceramics [125-128] may affect fatigue crack propagation in this region. rthermore, these preexisting defects are usually small in size, therefore, ceramics ay exhibit strong short crack effects. On the other hand, crack propagation in the reshold region could account for a great portion of fatigue life and is very portant in fatigue life prediction of ceramics. Therefore, fatigue crack propagation

ıould be studied more closely at a low range of the stress intensity factor, ΔK. In articular, the propagation of short cracks should be studied as these will be the pe of cracks initially found in ceramics.

Crack deviation and retardation, which can provide a considerable beneficial fect to fatigue life of a component, were only preliminarily investigated in the esent study. Nevertheless indications were found that the fatigue crack could hibit very complicated behaviour in response to interruptions of load cycling. rack deviation effects were observed with the crack propagation plane oscillation out the plane perpendicular to the tensile stress axis.

In some circumstances, crack acceleration effects were obtained following a ange in load amplitude. Great attention should be paid to such acceleration fects because of considerable negative effect of this acceleration on the fatigue life. ıch behaviour, which is to be expected if the increase in transformation zone size r cycle and crack closure effects behind the crack tip are responsible for good tigue propagation resistance as the present study indicates, requires further study other loading conditions encountered in service, such as variable ΔK and K_{max} lues, to obtain more detailed information on the effect of the load history on the ack propagation behaviour. Such studies should also provide further information the effect of the old transformation zone on the fatigue propagation behaviour.

Ceramics are intended to serve at high temperature for which metallic ıaterials show very limited potential. At the present time, study in this area remains lmost untouched. Therefore, fatigue crack propagation studies at high temperature ıould also be conducted in order to verify the existence of fatigue effect at high mperature and to investigate the fatigue behaviour under such conditions.

CHAPTER 10 CONCLUSIONS

The present study permits to conclude that in ceramics fatigue crack propagation under cyclic compression occurs by detaching particles from the prenotch tip producing a notch-like crack. This notch-like crack becomes sharper as the load cycling continues. In 3Y-TZP, the fatigue fracture surface consists of four different zones: a relatively clean zone produced by fatigue crack initiation; a zone of debris accumulation; a zone in which these debris particles have been flattened into cakes by crack closure effects and a fatigue crack arrest zone which has the form of a sharp notch. The fractographic features of these four zones can be explained by the formation and migration of debris particles and by crack closure.

The numerous debris particles which form on the compression fatigue fracture surface of ceramics migrate towards the prenotch tip, i.e., in the opposite direction of fatigue crack propagation. In the extreme situation of more brittle ceramics tested under high cyclic stress, the debris particles migrate at very high speed and can actually be projected out of the notch.

Spalling sites near the notch-like crack tip and on the lateral surfaces were observed to result from chipping on the lateral surfaces due to rubbing between the two fracture surfaces during compression fatigue cycling. Spalling sites were

bserved also at the prenotch tip on the fatigue fracture surface. Spalling sites never xtended to the fatigue crack tip on the fatigue fracture surface, which indicates that palling occurred after the fatigue crack propagation.

The present study of fatigue crack propagation in 3Y-TZP under cyclic tensile ress produced some important results and an explanation for the formation of riation-like bands during fatigue at high propagation rates in this material.

It is concluded that in tensile fatigue of precracked specimens of 3Y-TZP, the aximum stress intensity, K_{max}, is the factor principally controlling the fatigue crack opagation. The ΔK value had little influence on the fatigue crack propagation.

In tensile fatigue of precracked specimens, striation-like markings, present as ırk bands separated by bright zones, have been obtained in 3Y-TZP. The width the bright zones increased rapidly with increasing stress intensity factor. The width dark bands did not change as much as that of the bright zones. Moreover, the rk bands corresponded to depressions on both fracture surfaces. The occurrence the striation-like markings provided clear evidence for the occurrence of cycle-by-cle fatigue propagation in 3Y-TZP.

Hysteresis loops obtained from a microstrain gage placed at the crack tip on e lateral surface provided particularly important information on the manner in

'hich the striations formed. The present study demonstrated that the dark bands 'ere produced by slow propagation in the loading portion of the load cycle and that ıe bright zones were produced by rapid crack propagation which, except in the last ycle which produced final fracture, was triggered by a small amount of unloading.

These fractographic features can be explained by the stress-induced ansformation playing an important role in producing the dark bands and bright ɔnes. The dark bands were associated with a small transformation zone which ıduced a small amount of volume increase. In contrast, a large transformation zone as produced during the rapid propagation portion of the load cycle. This rapid ropagation produced the bright zone and induced important crack closure stresses :ting on the crack surfaces near the crack tip, resulting in strong crack tip shielding. is this crack-tip shielding which is primarily responsible for the transformation ıughening.

The unloading probably induced reversed transformation or changed the ress distribution in the vicinity of the crack tip, which triggered the rapid 'opagation. At low K, there was no large difference in the transformation zone size ırring fatigue cycling. As well, this transformation zone overlapped with that of the .bsequent cycle. As a result, similar striation-like markings were not visible. The :crease in applied stresses during the load cycle stopped the rapid propagation. As e crack decelerated, the transformed zone size decreased. For this reason, the

rack arrest site can be observed to be within the dark band, although it is situated ear its start and along the deepest portion of this band.

The start of unloading arrests this slow propagation, with the ıicrofractographic observations showing that this arrest site is situated near the end f the dark band. The rapid propagation which is then triggered by a slight amount f unloading initiated either slightly ahead of or at the crack tip (i.e., ahead of the ark band or at the arrest site near the end of this band).

The local slope of fatigue crack propagation curve in the log-log plot of a/dN versus K_{max} exhibited a decrease (except for the last few cycles) with creasing stress intensity factor at high da/dN. This decrease in slope is believed to sult from the crack-tip shielding which increases strongly with increasing stress tensity factor at high da/dN when the fatigue propagation occurs in two stages, ith a slow gradual cracking stage followed by a rapid propagation stage.

In the present study, crack deviation in 3Y-TZP was also observed on fatigue acture surface produced during interruptions of fatigue cycling. Fatigue crack ıanged slightly its propagation direction after each interruption of load cycling. easurements of the topography produced during the interruptions showed that cal directions of crack propagation deviated slightly from the plane which is rpendicular to the loading axis, with the new propagation planes oscillating about

the plane normal to the loading axis. Crack retardation was also observed after the interruption of load cycling. Crack acceleration, where the crack propagated faster than that expected for the new ΔK and K_{max} level, was obtained after decreasing ΔK and K_{max}. This permits to conclude that fatigue crack propagation behaviour of 3Y-TZP is sensitive to load history effects. At low R-ratio (R=0.1), crack closure effects were also observed on the hysteresis loops obtained from the crack tip microstrain gage.

X-ray diffraction on the fracture surface showed clearly the occurrence of stress-induced transformation by the presence of spectral peaks for the monoclinic phase. X-ray diffraction on the lateral surfaces of unnotched samples subjected to compression suggested that compressive stress also induced transformation. Microscopic analyses by Raman spectroscopy provided information on differences of the transformation zone size on different microportions of the fatigue fracture surface and showed the dependence of the amount of stress-induced transformation on the instantaneous stress intensity factor. These analyses indicated that the amount of transformed particles in the dark bands was consistently lower than that in bright zones.

Tensile fatigue of notched specimens without a precrack exhibited only fatigue crack propagation near the crack initiation sites. A through-thickness fatigue crack was not obtained before K_{Ic} was exceeded. The fatigue crack initiation sites

ecreased in number and increased in size with decreasing cycling load. At a very ›w cycling load, a single relatively large fatigue zone was observed to be associated ·ith a single crack initiation site, rather than with small fatigue zones at multiple rack initiation sites.

The fracture toughness measurements resulted in significant differences epending on the manner in which the measurements were performed. The fracture ›ughness measurements on prenotch specimens gave a value of 10.4 MPa$\sqrt{m}$ which approximately two times as large as the true value of the fracture toughness. ompression-precracked specimens tend to give slightly higher fracture toughness ıan indentation and tensile-fatigued specimens. The true value of the fracture ›ughness should be between the measurements obtained from compression- ·ecracked specimens and that from the tensile-fatigued specimens.

REFERENCES

[1] S.M. Wiederhorn, "Subcritical Crack Growth in Ceramics", pp. 613-646 in Fracture Mechanics of Ceramics, vol.2. Proceedings of Symposium on the Fracture Mechanics of Ceramics, Edited by R.C.Bradt, D.P.H.Hasselman and F.F.Lange. Plenum press, New York (1974).

[2] A.G. Evans, "Fatigue in Ceramics", Int. J. of Fracture, **16** [6] 485-498 (1980).

[3] P.F. Becher, "Subcritical Crack Growth in Partially Stabilized ZrO_2 (MgO)", J. Mat. Sci., **21** 297-300 (1986).

[4] A.G. Evans and F.F. Lange, "Crack Propagation and Fracture in Silicon Carbide", J. Mat. Sci., **10** 1659-1664 (1975).

5] S.M. Wiederhorn, "Influence of Water Vapour on Crack Propagation in Soda-Lime Glass", J. Am. Ceram. Soc., **50** [8] 407-414 (1967).

6] T.A. Michalske and S.W. Freiman, "A Molecular Mechanism for Stress Corrosion in Vitreous Silica", J. Am. Ceram. Sco., **66** [4] 284-288 (1983).

7] J.G. Bruce, W.W. Gerberich and B.G. Koepke, "Subcritical Crack Growth in PZT", pp. 687-709 in Fracture Mechanics of Ceramics, vol.2. Proceedings of Symposium on the Fracture Mechanics of Ceramics, Edited by R.C.Bradt, D.P.H.Hasselman and F.F.Lange. Plenum press, New York (1974).

8] Y. Hibino, "Crack Growth in Silica Glass under Dynamic Loading", J. Am. Ceram. Soc., **67** [1] 64-68 (1984).

9] D.A. Krohn and D.P.H. Hasselman, "Static and Cyclic Fatigue Behaviour of a Polycrystalline Alumina", J. Am. Ceram. Soc., **55** 208-211 (1972).

10] K. Noguchi, M. Fujita, T. Masaki and M. Mizushina, "Tensile Strength of Yttria-Stabilized Tetragonal Zirconia Polycrystals", J. Am. Ceram. Soc., **72** [7] 1305-1307 (1989).

11] M.F. Ashby and S.D. Hallam, "The Failure of Brittle Solids Containing Small Cracks under Compressive Stress States", Acta Metall., **34** [3] 497-510 (1986).

12] A. Grossmuller, V. Zelizko and M.V. Swain, "Fatigue Crack Growth in Ceramics Using a Compressive Loading Geometry", J. Mat. Sci. Lett., **8** 29-31

(1989).

[13] A.G. Evans and T.R. Wilshaw, "Quasi-Static Solid Particle Damage in Brittle Solids I. Observations, Analysis and Implications", Acta Metall., **24** 939-956 (1976).

[14] A.G. Evans and E.A. Charles, "Fracture Toughness Determinations by Indentation", J. Am. Ceram. Soc., **59** [7-8] 371-372 (1976).

[15] R.W. Rice, "Pores as Fracture Origins in Ceramics", J. Mat. Sci., **19** 895-914 (1984).

[16] J. Sung and P.S. Nicholson, "The Analysis of the Fracture Origin Types and Severity in Y_2O_3-Partially-Stabilized ZrO_2", pp. 179-189 in Proceedings of the International Symposium on Fracture Mechanics, (Winnipeg, Canada, August 23-26, 1987), Edited by W.R.Tyson and B.Mukherjee. Pergamon Press, (1988).

[17] A.G. Evans, "Structural Reliability: A Processing-Dependent Phenomenon", J. Am. Ceram. Soc., **65** [3] 127-137 (1982).

[18] A.G. Evans, D.R. Biswas and R.M. Fulrath, "Some Effects of Cavities on the Fracture of Ceramics:II", J. Am. Ceram. Soc., **62** [1-2] 101-106 (1979).

[19] F.F. Lange and M. Metcalfe, "Process-Related Origins: II. Agglomerate Motion and Cracklike Internal Surfaces Caused by Differential Sintering", J. Am. Ceram. Soc., **66** 498-406 (1983).

[20] D.J. Barber and N.J. Tighe, "Electron Microscopy and Diffraction of Synthetic Corundum Crystals: II", Phil. Mag., **11** [111] 495-512 (1965).

[21] D.J. Gooch and G.W. Groves, "Prismatic Slip in Sapphire", J. Am. Ceram. Soc., **55** [2] 105 (1972).

[22] T.D. Gulden, "Direct Observation of Nonbasal Dislocations in Sintered Alumina", J. Am. Ceram. Soc., **50** [9] 472-475 (1967).

[23] D. Michel, L. Mazerolles, M. Perez and Y. Jorba, "Fracture of Metastable Tetragonal Zirconia Crystals", J. Mat. Sci., **18** 2618-2628 (1983).

[24] R.F. Firestone, A.H. Heuer, S.H. Moll and R.R. Turnage; Back cover micrograph in J. Am. Ceram. Soc., **56** [10] (1973).

25] S.J. Bennison, "Fracture Modes in Alumina", Back cover micrograph in J. Am. Ceram. Soc., **68** [2] (1985).

26] N. Claussen, "Fracture Toughness of Al_2O_3 with an Unstabilized ZrO_2 Dispersed Phase", J. Am. Ceram. Soc., **59** [1-2] 49-51 (1976).

27] M. Ruhle, A.G. Evans, R.M. McMeeking, P.G. Charalambides and J.W. Hutchinson, "Microcrack Toughening in Alumina/Zirconia", Acta Metall., **35** [11] 2701-2710 (1987).

28] A.G. Evans and K.T. Faber, "Crack Growth Resistance of Microcracking Brittle Materials", J. Am. Ceram. Soc., **67** [4] 255-260 (1984).

29] L. Ewart and S. Suresh, "Dynamic Fatigue Crack Growth in Polycrystalline Alumina under Cyclic Compression", J. Mater. Sci. Lett., **5** [4] 774-778 (1986).

30] M.J. Reece, F. Guin and M.F.R. Sammur, "Cyclic Fatigue Crack Propagation in Alumina under Direct Tension-Compression Loading", J. Am. Ceram. Soc., **72** [2] 348-352 (1989).

31] H.N. Ko, "Fatigue Strength of Sintered Al_2O_3 under Rotary Bending", J. Mater. Sci. Lett., **5** [4] 464-466 (1986).

32] H.N. Ko, "Effect of Grain Size on Fatigue Strength of Sintered Al_2O_3 under Rotary Bending", J. Mater. Sci. Lett., **8** 1438-1441 (1989).

33] H.N. Ko, "Cyclic Fatigue Behaviour of Sintered Al_2O_3 under Rotary Bending", J. Mater. Sci. Lett., **6** 801-805 (1987).

34] J.F. Tsai, C.S. Yu, and D.K. Shetty, "Fatigue Crack Propagation in Ceria-Partially Stabilized Zirconia (Ce-TZP)-Alumina Composites", J. Am. Ceram. Soc., **73** [10] 2992-3001 (1990).

35] D.G. Jensen, V. Zelizko, and M.V. Swain, "Small Flaw Static Fatigue Crack Growth in Mg-PSZ", J. Mater. Sci. Lett., **8** 1154-1157 (1989).

36] R. Kossowsky, "Cyclic Fatigue of Hot-Pressed Si_3N_4", J. Am. Ceram. Soc., **56** [10] 531-535 (1973).

37] L. Ewart and S. Suresh, "Crack Propagation in Ceramics under Cyclic Loads", J. Mat. Sci., **22** [4] 1174-1192 (1987).

38] A.G. Evans and E.R. Fuller, "Crack Propagation in Ceramic Materials under

Cyclic Loading Conditions", Metall. Trans., **5** [1] 27-33 (1974).

9] G. Sines, "Rationalized Crack Growth and Time-to-Failure of Brittle Materials", J. Am. Ceram. Soc., **59** [7-8] 370-371 (1976).

0] A.G. Evans and M. Lines, Int. J. of Fracture, **12** 217-222 (1976).

1] R.C. Garvie and P.S. Nicholson, "Phase Analysis in Zirconia Systems", J. Am. Ceram. Soc., **55** [6] 303-305 (1972).

2] T. Kosmac, R. Wagner and N. Claussen, "X-ray Determination of Transformation Depths in Ceramics Containing Tetragonal ZrO_2", J. Am. Ceram. Soc., **64** [4] c-72-c-73 (1981).

3] C.P. Chen and W.J. Knapp, "Fatigue Fracture of an Alumina Ceramic at Several Temperatures", pp. 691-707 in Fracture Mechanics of Ceramics, vol. 2. Proceedings of Symposium on the fracture mechanics of ceramics, Edited by R.C.Bradt, D.P.H.Hasselman and F.F.Lange. Plenum Press, New York (1974).

4] F. Guin, "Cyclic Fatigue of Polycrystalline Alumina in Direct Push-Pull ", J. Mat. Sci. Lett., **13** 1357-1361 (1978).

5] R.H. Dauskardt, W. Yu and R.O. Ritchie, "Fatigue Crack Propagation in Transformation Toughened Zirconia Ceramics", J. Am. Ceram. Soc., **70** [10] c-248-c-252 (1987).

6] S.Y. Liu and I.W. Chen, "Fatigue of Yttria-Stabilized Zirconia: I, Fatigue Damage, Fracture Origins, and Lifetime Prediction", J. Am. Ceram. Soc., **74** [6] 1197-1205 (1991).

7] A.A. Steffen, R.H. Dauskardt, and R.O. Ritchie, "Cyclic Fatigue Life and Crack-Growth Behaviour of Microstructurally Small Crack in Magnesia-Partially-Stabilized Zirconia Ceramics", J. Am. Ceram. Soc., **74** [6] 1258-1268 (1991).

8] P.C. Paris and F. Erdogan, "A Critical Analysis of Crack Propagation Laws", J. Basic Eng., **85** [12] 528-534 (1963).

9] G. Grathwohl and T. Liu, "Crack Resistance and Fatigue of Transforming Ceramics: I, Materials in the ZrO_2-Y_2O_3-Al_2O_3 System", J. Am. Ceram. Soc., **74** [2] 318-325 (1991).

0] C.K.J. Lin and D.F. Socie, "Static and Cyclic Fatigue of Alumina at High Temperatures", J. Am. Ceram. Soc., **74** [7] 1511-1518 (1991).

1] L.A. Sylva and S. Suresh, "Crack Growth in Transforming Ceramics under Cyclic Tensile Loads", J. Mat. Sci., **24** 1729-1738 (1989).

2] R.M. McMeeking and A.G. Evans, "Mechanics of Transformation Toughening in Brittle Materials", J. Am. Ceram. Soc., **65** [5] 242-246 (1982).

3] S.Y. Liu and I.W. Chen, "Fatigue of Yttria-Stabilized Zirconia: II, Crack Propagation, Fatigue Striation, and Short Crack Behaviour", J. Am. Ceram. Soc., **74** [6] 1206-1216 (1991).

4] R.H. Dauskardt, D.B. Marshall, and R.O. Ritchie, "Cyclic Fatigue-Crack Propagation in Magnesia-Partially-Stabilized Zirconia Ceramics", J. Am. Ceram. Soc., **74** [4] 893-903 (1990).

5] S.Y. Liu and I.W. Chen, "Fatigue Deformation Mechanisms of Zirconia Ceramics", J. Am. Ceram. Soc., **75** [5] 1191-1204 (1992).

6] S. Horibe and R. Hirahara, "Cyclic Fatigue of Ceramic Materials: Influence of Crack Path and Fatigue Mechanisms", Acta Metall., **39** [6] 1309-1317 (1991).

7] R.H. Dauskardt, W.C. Carter, D.K. Veirs and R.O. Ritchie, "Transient Subcritical Crack-Growth Behaviour in Transformation-Toughened Ceramics", Acta Metall. Mater., **38** [11] 2327-2336 (1990).

8] D.L. Davidson, J.B. Campbell and J. Lankford, "Fatigue Crack Growth Through Partially Stabilized Zirconia at Ambient and Elevated Temperatures", Acta Metall. Mater., **39** [6] 1319-1330 (1991).

9] M. Reece and F. Guin, "Indentation Fatigue of High-Purity Alumina in Fluid Environments", J. Am. Ceram. Soc., **74** [1] 148-154 (1991).

0] F. Guin, M.J. Reece, and D.A.J. Vaughan, "Cyclic Fatigue of Ceramics", J. Mat. Sci., **26** [2] 3275-3286 (1991).

1] S. Suresh and J.R. Brockenbrough, "Theory and Experiments of Fracture in Cyclic Compression: Single Phase Ceramic, Transforming Ceramics and Ceramic Composites", Acta Metall., **36** [6] 1455-1470 (1988).

2] Encyclopedia of Chemical Technology, Third Edition, vol.24, John Wiley and

Sons Inc. (1984).

[63] S. Block, J.A.H. da Jornada and G.J. Piermarini, "Pressure Temperature Phase Diagram of Zirconia", J. Am. Ceram. Soc., **68** [9] 497-499 (1985).

[64] G.M. Wolten, "Diffusionless Phase Transformations in Zirconia and Hafnia", J. Am. Ceram. Soc., **46** [9] 418-423 (1963).

[65] H.S. Maiti, K.V.G.K. Gokhale and E.C. Subbarao, "Kinetics and Burst Phenomenon in ZrO_2 Transformation", J. Am. Ceram. Soc., **55** [6] 317-322 (1972).

[66] D.K. Smith and C.F. Cline, "Verification of Existence of Cubic Zirconia at High Temperature", J. Am. Ceram. Soc., **45** [5] 249-250 (1962).

[67] C.H. Perry, D.W. Liu and R.P. Ingel, "Phase Characterization of Partially Stabilized Zirconia by Raman Spectroscopy", J. Am. Ceram. Soc., **68** [8] c-184-c-187 (1985).

[68] J.W. Adams, H. Nakamura, R.P. Ingel and R.W. Rice, "Thermal Expansion Behaviour of Single-Crystal Zirconia", J. Am. Ceram. Soc., **68** [9] c-228-c-231 (1985).

[69] G.K. Bansal and A.H. Heuer, "On a Martensitic Phase Transformation in Zirconia (ZrO_2)-I. Metallographic Evidence", Acta Metall., **20** [11] 1281-1289 (1972).

[70] G.K. Bansal and A.H. Heuer, "On a Martensitic Phase Transformation in Zirconia (ZrO_2)-II. Crystallographic Aspects", Acta Metall., **22** [4] 409-417 (1974).

[71] N. Claussen, "Microstructural Design of Zirconia-Toughened Ceramics (ZTC)", pp. 325-351 in Advances in Ceramics, vol. 12. Science and Technology of Zirconia II, Edited by Nils Claussen, Manfred Ruhle, and Arthur H. Heuer. The American Ceramic Society Inc., Columbus, Ohio (1984).

[72] V.S. Stubian and J.R. Hellmann, "Phase Equilibria in Some Zirconia System", pp. 25-36 in Advances in Ceramics, vol.3. Science and Technology of Zirconia, Edited by A.H.Heuer and L.W.Hobbs. The American Ceramic Society, Inc., Cloumbus, Ohio (1981).

[73] E.C. Subbarao, "Zirconia: An overview", pp. 1-24 in Advances in ceramics,

vol.3. Science and technology of zirconia, Edited by A. H. Heuer and L. W. Hobbs, The American Ceramics Society, Inc., Cloumbus, Ohio (1981).

[74] M. Shimbo, M. Itoh, M. Ueki and Y. Miyano, "Stress-Induced Transformation and Toughening of Yttria-Stabilized Zirconia", pp. 415-422 in Advances in ceramics, vol.24B. Science and technology of zirconia III, Edited by Shigeyuki Somiya, Noboru Yamamoto and Hiroaki Yanagida. The American Ceramic Society, Inc., Weterville, Ohio (1988).

[75] A.J.A. Winnubst and A.J. Burggraaf, "The Aging Behaviour of Ultrafine-Grained Y-TZP in Hot Water", pp. 39-47 in Advances in ceramics, vol. 24A. Science and technology of zirconia III, Edited by Shigeyuki Somiya, Noboru Yamamoto and Hiroaki Yanagida. The American Ceramic Society, Inc., Weterville, Ohio (1988).

[76] H.G. Scott, "Phase Relationships in the Zirconia-Yttria System ", J. Mat. Sci., **10** 1527-1535 (1975).

[77] S. Lio, M. Watanade, K. Kuroda, H. Saka and T. Imura, "Tetragonal-to-Monoclinic Transformation in Y-TZP During Low Temperature Aging and Its Restraint by Coating", pp. 49-54 in Advances in ceramics, vol. 24A. Science and technology of zirconia, Edited by Shigeyuki Somiya, Noboru Yamamoto and Hiroaki Yanagida. The American Ceramic Society, Inc., Weterville, Ohio (1988).

[78] T.K. Gupta, J.H. Bechtold, R.C. Kuznicki, L.F. Cadoff and B.R. Rossing, "Stabilization of Tetragonal Phase in Polycrystalline Zirconia", J. Mat. Sci., **12** 2421-2426 (1977).

[79] V.K. Pujari and I. Jawed, "Effect of Densification Conditions on the Stabilization of the Tetragonal Phase in ZrO_2 Polycrystals", J. Am. Ceram. Soc., **68** [9] c-242-c-243 (1985).

[80] K.K. Srivastava, R.N. Patil, C.B. Chaudhary, K.V. Gokhale, and E.C. Subbarao, "Revised Phase Diagram of System ZrO_2-$YO_{1.5}$", Trans. J. Br. Ceram. Soc., **73** [2] 85-91 (1974).

[81] H.G. Scott, "Phase Relationships in the Yttria-rich Part of the Yttria-Zirconia System", J. Mat. Sci., **12** 311-316 (1977).

[82] C. Pascual and P. Duran, "Subsolidus Phase Equilibria and Ordering in the System ZrO_2-Y_2O_3", J. Am. Ceram. Soc., **66** [1] 23-27 (1983).

83] R. Ruh, K.S. Mazdiyasni, P.G. Valentine, and H.O. Bielstein, "Phase Relations in the System ZrO_2-Y_2O_3", J. Am. Ceram. Soc., **67** [9] c-190-c-192 (1984).

84] M. Matsui, T. Sama and I. Oda, "Stress-Induced Transformation and Plastic Deformation for Y_2O_3-containing Tetragonal Zirconia Polycrystals ", J. Am. Ceram. Soc., **69** [3] 198- 202 (1986).

85] R.R. Lee and A.H. Heuer, "In situ Martensitic Transformation in a Ternary MgO-Y_2O_3-ZrO_2 alloy: I, Transformation in Tetragonal ZrO_2 Grains", J. Am. Ceram. Soc., **71** [8] 694-700 (1988).

86] R.R. Lee and A.H. Heuer, "In situ Martensitic Transformation in a Ternary MgO-Y_2O_3-ZrO_2 alloy: II, Transformation in Tetragonal ZrO_2 Precipitates", J. Am. Ceram. Soc., **71** [8] 701-706 (1988).

87] I.M. Low, "ZrO_2 transformation toughening criteria", J. Mat. Sci. Lett., **7** 297-299 (1988).

88] M.V. Swain, "Factors controlling the strength of transformation toughened zirconia ceramics", pp. 204-213 in Proceedings Australian Fracture Group Symposium, Sydney University (1985).

89] M. Shimbo, M. Ueki, Y. Miyano, S. Ishihara and T. Fujita, "Stress-Induced Transformation During Compression of ZrO_2-4 mol% Y_2O_3", J. Mat. Sci. Lett., **7** 877-878 (1988).

90] R.A. Millier, J.L. Smialek and R.G. Garlick, "Phase Stability in Plasma-Sprayed, Partially Stabilized Zirconia Yttria", pp. 241-253 in Advances in ceramics, vol.3. Science and technology of zirconia, Edited by A.H.Heuer and L.W.Hobbs. The American Ceramics Society, Inc., Columbus, Ohio (1981).

91] V. Lanteri, A.H. Heuer and T.E. Mitchell, "Tetragonal Phase in the System of ZrO_2-Y_2O_3", pp. 118-191 in Advances in Ceramics, vol. 12. Science and Technology of Zirconia II, Edited by Nils Claussen, Manfred Ruhle, and Arthur H. Heuer. The American Ceramic Society Inc., Columbus, Ohio (1984).

92] T. Sakuma, "Development of Domain Structure Associated with the Diffusionless Cubic-to-Tetragonal transition in ZrO_2-Y_2O_3 alloys", J. Mat. Sci., **22** 4470-4475 (1987).

[93] A.H. Heuer, R. Chaim, and V. Lanteri, "Review: Phase Transformations and Microstructural Characterization of Alloys in the System Y_2O_3-ZrO_2", pp. 3-20 in Advances in ceramics, vol.24A. Science and technology of zirconia III, Edited by Shigeyuki Somiya, Noboru Yamamoto and Hiroaki Yanagida. The American Ceramic Society, Inc., Weterville, Ohio (1988).

[94] G.M. Wolten, "Solid Phase Transition in the UO_2-ZrO_2 System", J. Am. Chem. Soc., **80** [18] 4772-4775 (1958).

[95] R.C. Garvie, R.H. Hannink and R.T. Pascoe, "Ceramic Steel", Nature, **258** [5537] 703-704 (1975).

[96] D.L. Porter, A.G. Evans and A.H. Heuer, "Transformation Toughening in Partially Stabilized Zirconia (PSZ)", Acta Metall., **27** [10] 1649-1654 (1979).

[97] M.V. Swain and R.H.J. Hannink, "Metastability of the Martensitic Transformation in a 12 mol% ceria-Zirconia Alloy: II Grinding Studies", J. Am. Ceram. Soc., **72** [8] 1358-1364 (1989).

[98] D.L. Porter and A.H. Heuer, "Mechanisms of Toughening Partially Stabilized Zirconia (PSZ)", J. Am. Ceram. Soc., **60** [3-4] 183-184 (1977).

[99] M.V. Swain, "Inelastic Deformation of Mg-PSZ and Its Significance for Strength-Toughness Relationship of Zirconia Toughened Ceramics", Acta Metall., **33** [11] 2083-2091 (1985).

[100] D.B. Marshall and M.R. James, "Reversible Stress-Induced Martensitic Transformation in ZrO_2", J. Am. Ceram. Soc., **69** [3] 215-217 (1986).

[101] F.F. Lange, "Transformation Toughening Part 2: Contribution to Fracture Toughness", J. Mat. Sci., **17** 235-239 (1982).

[102] J. Adams and B. Cox, "Irradiation-Induced Phase Transformation in Zirconia Solid Solutions", J. Nucl. Energy, Part A, **11** [1] 31-33 (1959).

[103] R.H. Dauskardt, D.K. Veirs, and R.O. Ritchie, "Spatially Resolved Raman Spectroscopy Study of Transformed Zones in Magnesia-Partially-Stabilized Zirconia", J. Am. Ceram. Soc., **72** [7] 1124-1130 (1989).

[104] M. Ishigame and T. Sakurai, "Temperature Dependence of the Raman Spectra of ZrO_2", J. Am. Ceram. Soc., **60** [7-8] 367-369 (1977).

[105] M. Dalhaye and P. Dhamelincourt, "Raman Microprobe and Microscope with

Laser Excitation", J. Raman Spectrosc., **3** [1] 33-34 (1975).

106] Powder Diffraction File (Inorganic Volume), The Joint Committee on Powder Diffraction Standards, Swarthmore, Pennsylvania, U.S.A. (1974).

107] D.R. Clarke and F. Adar, "Measurement of the Crystallographically Transformed Zone Produced by Fracture in Ceramics Containing Tetragonal Zirconia", J. Am. Ceram. Soc., **65** [6] 284-288 (1982).

108] G. Katagiri, H. Ishida and A. Ishitani, "Direct Determination by a Raman Microprobe of the Transformation Zone Size in Y_2O_3 Containing Tetragonal ZrO_2 Polycrystals", pp. 537-544 in Advances in ceramics, vol.24A. Science and technology of zirconia, Edited by Shigeyuki Somiya, Noboru Yamamoto and Hiroaki Yanagida. The American Ceramic Society, Inc., Weterville, Ohio (1988).

109] R.C. Garvie, R.H.J. Hannink and M.V. Swain, "X-ray Analysis of the Transformed Zone in Partially Stabilized Zirconia (PSZ)", J. Mat. Sci. Lett., **1** 437-440 (1982).

110] C.M. Philippi and K.S. Mazdiyasni, "Infrared and Raman Spectra of Zirconia Polymorphs", J. Am. Ceram. Soc., **54** [5] 254-258 (1971).

111] Huberto Balmori-Ramirez, "Élaboration, Propriétés Méchaniques et Resistance au Choc Thermique des Alumines-Zircones", Ph.D Thesis, Ecole Ploytechnique de Université de Montréal, Montreal, Quebec (1990).

112] S. Suresh, L. Ewart, M. Moden, W.S. Slaughter and M. Nguyen, "Fracture Toughness Measurements in Ceramics: Pre-cracking in Cyclic Compression", J. Mat. Sci., **22** [4] 1271-1276 (1987).

113] H.P. Kirchner and R.E. Walker, "Delayed Fracture of Alumina Ceramics with Compressive Surface Layers", Mater. Sci. Engng., **8** 301-309 (1971).

114] B.R. Lawn and D.B. Marshall, "Hardness, Toughness, and Brittleness: An Indentation Analysis", J. Am. Ceram. Soc., **62** [7-8] 347-350 (1979).

115] B.R. Lawn, A.G. Evans, and D.B. Marshall, "Elastic/Plastic Indentation Damage in Ceramics: The Median/Radial Crack System", J. Am. Ceram. Soc., **63** [9-10] 574-581 (1980).

116] V.G. Keramidas and W.B. White, "Raman Scattering Study of the Crystallization and Phase Transformation of ZrO_2", J. Am. Ceram. Soc., **57**

[1] 22-24 (1974).

[117] M. Ishigame and T. Sakurai, "Temperature Dependence of the Raman Spectra of ZrO_2", J. Am. Ceram. Soc., **60** [7-8] 367-69 (1977).

[118] Howard E. Boyer, Atlas of Fatigue Curves, American Society for Metals, Carnes Publication Services, Inc. (1986).

[119] D.G. Jensen, V. Zelizko, and M.V. Swain, "Small Flaw Static Fatigue Crack Growth in Mg-PSZ", J. Mat. Sci. Lett., **8** 1154-1157 (1989).

[120] L.R.F. Rose and M.V. Swain, "Transformation Zone Shape in Ceria Partially-Stabilized Zirconia", Acta Metall., **36** [4] 955-962 (1988).

[121] Cheng-Sheng Yu and Dinesh K. Shetty, "Transformation Zone Shape, Size, and Crack-Growth-Resistance (R-Curve) Behaviour of Ceria-Partially-Stabilized Zirconia Polycrystals", J. Am. Ceram. Soc., **72** [6] 921-928 (1989).

[122] Cheng-sheng Yu and D.K. Shetty, "Transformation Yielding, Plasticity and Crack-Growth-Resistance (R-Curve) Behaviour of CeO_2-TZP", J. Mat. Sci., **25**, 2025-2035 (1990).

[123] N.J. Marchand, J.P. Bailon, and J.I. Dickson, "Near-Threshold Fatigue Crack Growth in Copper and Alpha-Brass: Grain-Size and Environmental Effects", Metall. Trans., **19A** [10] 2575-2587 (1988)

[124] R.O. Ritchie, "Influence of Microstructure on Near-Threshold Fatigue-Crack Propagation in Ultra-High Strength Steel", Met. Sci., **11** [8-9] 368-381 (1977).

[125] F.F. Lange, "Processing-Related Fracture Origins: I, Observations in Sintered and Isostatically Hot-Pressed Al_2O_3/ZrO_2 Composites", J. Am. Ceram. Soc., **66** [6] 396-398 (1983).

[126] F.F. Lange and M. Metcalf, "Processing-Related Fracture Origins: II, Agglomeration Motion and Cracklike Internal Surfaces Caused by Differential Sintering", J. Am. Ceram. Soc., **66** [6] 398-406 (1983).

[127] F.F. Lange, B.I. Davis and I.A. Aksay, "Processing-Related Fracture Origins: III, Differential Sintering of ZrO_2 Agglomerates in Al_2O_3/ ZrO_2 Composite", J. Am. Ceram. Soc., **66** [6] 407-408 (1983).

[128] F.F. Lange, B.I. Davis and E. Wright, "Processing-Related Fracture Origins: VI, Elimination of Voids Produced by Organic Inclusions", J. Am. Ceram.

Soc., **69** [1] 66-69 (1986).

.29] S.W. Wiederhorn and L.H. Bolz, "Stress Corrosion and Static Fatigue of Glass", J. Am. Ceram. Soc., **53** [10] 543-548 (1970).

.30] D.J. Green, R.H.J. Hannink and M.V. Swain, "Transformation Toughening of Ceramics", CRC Press Inc., Boca Raton, Florida, (1989).

.31] D.B. Marshall, M.C. Shaw, R.H. Dauskardt, R.O. Ritchie, M.J. Readey and A.H. Heuer, "Crack-Tip Transformation Zones in Toughened Zirconia", J. Am. Ceram. Soc., **73** [9] 2659-2666 (1990).

APPENDIX 1 THE INTEGRATION FOR SUBCRITICAL CRACK PROPAGATION VELOCITY

The relationship between cracking velocity in the bright zone and the instantaneous stress intensity factor for specimen YSG2 has been obtained as

$$da/dt = 1.97x10^{-9}(K)^{12} \qquad (A1.1)$$

where da/dt is the cracking velocity in mm/s, K is the stress intensity factor in MPa√m.

Zone B, which has a width of approximately 200 μm (Figure 7.62), is believed to be produced during the unloading of the cycling interruption. This unloading proceeded linearly from 4.3 to 0.43 MPa√m in 30 seconds. An integration can be made on equation (A1.1) to estimate the increment in crack length during this 30 seconds of interruption unloading, which gives

$$da = 1.97x10^{-9}(K)^{12}dt \qquad (A1.2)$$

$$\Delta a = \int_0^{30} 1.97\times10^{-9}(K)^{12}dt \qquad (A1.3)$$

However, the stress intensity factor is a function of both the applied load and the crack length, the former was decreased linearly from 150 N to 15 N in 30 seconds, the latter kept increasing. From the measurement made on the fracture surface, the total increase of crack length is 0.2 mm, but the entire crack length at that moment was 2.83 mm. A change of 0.2 mm on a base of 2.83 mm will lead a very small difference in the associated stress intensity, which will be less than 5%. As a result, we can take the crack length as a constant in calculating the instantaneous stress intensity. By taking the crack length as 2.8 mm, the instantaneous stress intensity factors K were 4.3 and 0.43 MPa$\sqrt{m}$ for the beginning and the end of the interruption unloading, respectively. The unloading was performed linearly in 30 seconds. Therefore, the instantaneous stress intensity factor K during this unloading can be given as:

$$K = -0.13t + 4.3 \qquad \text{(A1.4)}$$

where K is in MPa$\sqrt{m}$ and t, the unloading period, is from 0 to 30 seconds.

Substituting equation (A1.4) for K in equation (A1.3) and proceeding with the integration yields

$$\Delta a = 0.20 \text{ mm} \qquad \text{(A1.5)}$$

APPENDIX 2 THE DEVELOPMENT OF EQUATIONS FOR CALCULATING THE CRACK PLANE DEVIATION ANGLE

When the specimen stage is tilted a certain angle, the projected distance etween two features on a crack surface will change by an amount which depends n the inclination of the crack surface to the specimen stage. Combined with the tilt ngle, the change of the projected distances before and after the tilting can be mployed to calculate the deviation angle between two cracking planes of interest, s long as after tilting the two interested features are still in focus at the suitable ıagnification employed.

If scanning electron microscopy is operated at a large magnification and at large working distance, the condition of parallel projection is approximated. This an assumption that illumination rays are parallel to each other. In this case, a mple rotation of rectangular Cartesian coordinate system will apply to the tilting peration on the SEM.

Let (x, y, z) and (x', y', z') be the coordinates of point R in the coordinate 'stems O(X, Y, Z) and O'(X', Y', Z'), respectively, where the coordinate system ı'(X', Y', Z') is obtained by rotating the coordinate system O(X, Y, Z) an angle β ɔout the axis X. The transformation equations can be written as follows

$$x' = x; \qquad (A2.1)$$

$$y' = y\cos\beta + z\sin\beta; \qquad (A2.2)$$

$$z' = -y\sin\beta + z\cos\beta. \qquad (A2.3)$$

For two point features P and Q, their coordinates in the original and the econd systems will be P (x_p, y_p, z_p), P (x'_p, y'_p, z'_p) and Q (x_q, y_q, z_q), Q (x'_q, y'_q, z'_q), espectively.

To facilitate calculation, the intersection between the two cracking planes of ıterest is chosen parallel to the tilt axis. The tilt axis is chosen as the X axis, the X, ', and Z axes are mutually perpendicular, with the Z axis also perpendicular to the ıicrograph.

It is preferable to choose a reference plane, and to calculate the angles etween the two cracking planes of interest and this reference plane. When the ngles between the reference plane and both cracking planes are known, the eviation angle between two cracking planes can be easily obtained. Now, this roblem can be considered as simply to choose a reference plane and to obtain the ngles between this reference plane and two cracking planes of interest.

The plane perpendicular to the beam axis of SEM is the logical reference lane for a chosen inclination of the specimen. Two images of the same area are

then taken with some angular difference between them. A line segment is drawn on one of the crack planes. This line segment should be perpendicular to the intersection line of the two crack planes of interest. Two prominent features on this line will be chosen in order to obtain the height difference (ΔZ) between these two features with respect to the reference plane and to obtain the projected distance (ΔY) between these two features. The ratio of ΔZ to ΔY will be the tangent of the angle between the crack plane and the reference plane. Now, the problem becomes that of obtaining the values of ΔZ and ΔY. ΔY will be easily measured directly on the micrograph obtained before tilting the specimen stage. However, ΔZ can not be measured directly. To obtain ΔZ, a calculation on the measurements obtained after the tilting will be required. This calculation can be carried out by virtue of the transformation of the coordinate system.

According to the coordinate transformation equations (A2.1-A2.3), after tilting an angle β, the Y coordinates of the two features P and Q will be written as;

$$y'_p = y_p\cos\beta + z_p\sin\beta \qquad \text{(A2.4)}$$

$$y'_q = y_q\cos\beta + z_q\sin\beta. \qquad \text{(A2.5)}$$

Subtracting equation (A2.5) from equation (A2.4) yields the following equation:

$$\Delta Z = z_p - z_q = \frac{(y'_p - y'_q) - (y_p - y_q)\cos\beta}{\sin\beta} \qquad (A2.6)$$

Equation (A2.6) can also be written as:

$$\Delta Z = z_p - z_q = \frac{\Delta Y' - \Delta Y \cos\beta}{\sin\beta} \qquad (A2.7)$$

where $\Delta Y = (y_p - y_q)$ and $\Delta Y' = (y'_p - y'_q)$.

The projected distances between the two features, will be measured directly on the micrographs obtained before and after the tilting operation. Finally, the angle between the cracking plane and the reference plane will be obtained from

$$\alpha = Arctg\,\frac{\Delta Z}{\Delta Y} = Arctg\,\frac{\Delta Y' - \Delta Y \cos\beta}{\Delta Y \sin\beta} \qquad (A2.8)$$

ÉCOLE POLYTECHNIQUE DE MONTRÉAL
3 9334 00290451 2